The Microstructure and Phase Evolution of Pseudomorphic Polymer-derived Ceramic Papers

Die Mikrostruktur und Phasenevolution Pseudomorpher Polymer-abgeleiteter Keramischer Papiere

vom Fachbereich Material- und Geowissenschaften der Technischen Universität Darmstadt genehmigte Dissertation zur Erlangung des Grades Doctor rerum naturalium (Dr. rer. nat.)

von Johannes Mauricio Peter, geboren in Mannheim

Berichterstatter: Prof. Dr. Hans-Joachim Kleebe
Mitberichterstatter: Prof. Dr. Leopoldo Molina-Luna

Darmstadt 2023

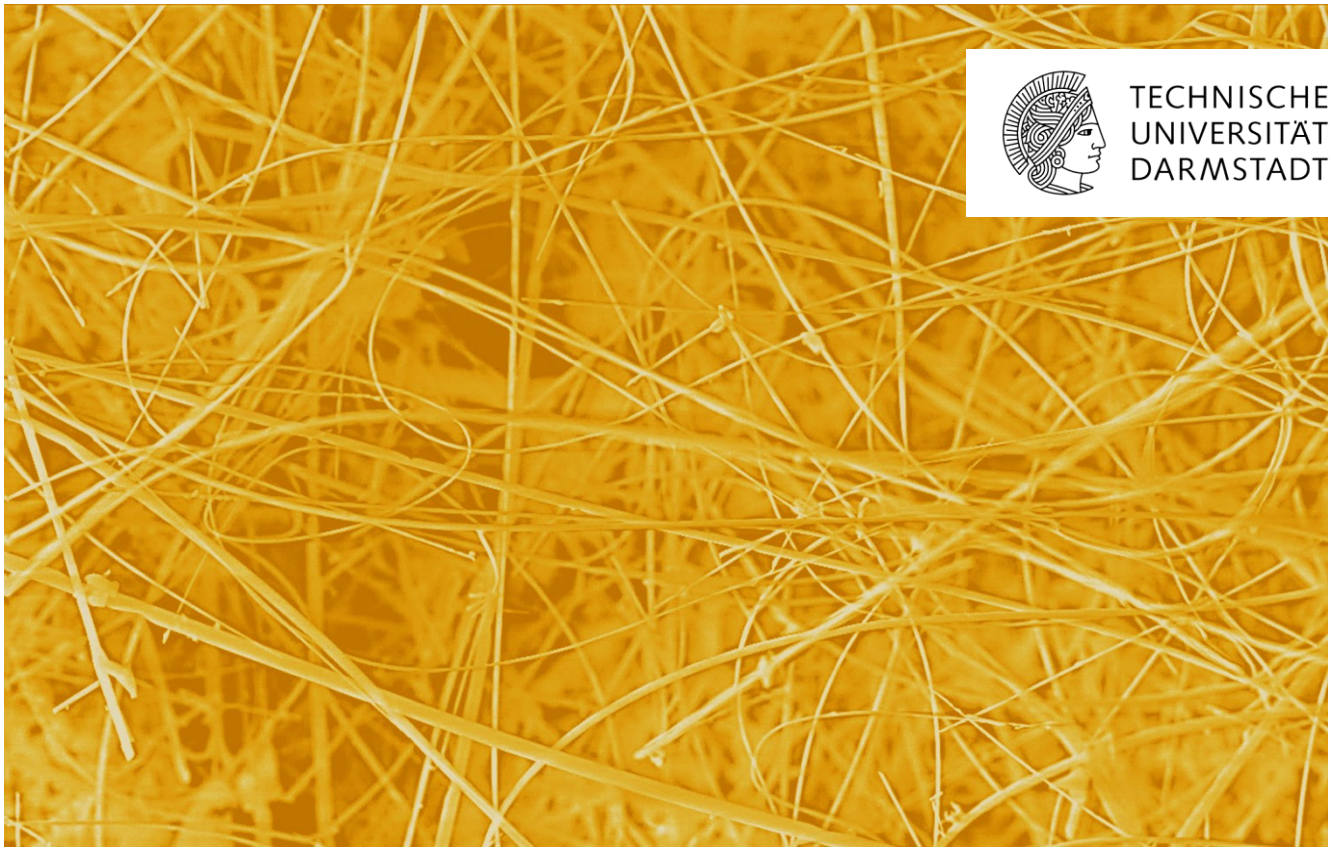

Approved doctoral thesis by Johannes Peter

The Microstructure and Phase Evolution of Pseudomorphic Polymer-derived Ceramic Papers

Darmstadt, Technische Universität Darmstadt

Year of publication on TUprints: 2024

Date of thesis defense: 05.09.2023

Technische Universität Darmstadt
Department of Material and Geosciences
Institute of Applied Geosciences
Schnittspahnstraße 9
64287 Darmstadt

Erklärungen laut Promotionsordnung

§ 8 Abs. 1 lit. c PromO

Ich versichere hiermit, dass die elektronische Version meiner Dissertation mit der schriftlichen Version übereinstimmt.

§ 8 Abs. 1 lit. d PromO

Ich versichere hiermit, dass zu keinem vorherigen Zeitpunkt eine Promotion versucht wurde.

§ 9 Abs. 1 PromO

Ich versichere hiermit, dass die vorliegende Dissertation selbstständig und nur unter Verwendung der angegebenen Quellen und Hilfsmittel verfasst wurde.

§ 9 Abs. 2 PromO

Die vorliegende Arbeit hat zu keinem vorherigen Zeitpunkt zu Prüfungszwecken gedient.

Darmstadt, 26.07.2023

_____

Johannes Peter

dedicated to my dear family and friends

Content

Abbreviations & Symbols

Abbreviations

AC	Amorphous carbon
ADF	Annular dark field
ALD	Atomic layer deposition
ATR	Attenuated total reflection
BF	Bright field
BSE	Backscattered electrons
CBED	Convergent beam electron diffraction
CCD	Charge-coupled device
CMS	Carbon molecular sieve
CTEM	Conventional TEM
CTF	Contrast transfer function
CVD	Chemical vapor deposition
CVI-R	Reactive chemical vapor infiltration
DF	Dark field
ED	Electron diffraction
EDS	Energy-dispersive X-ray spectroscopy
EM	Electron microscopy
Euc	Eucalyptus
$Fe(acac)_3$	Iron(III)acetylacetonate
FFT	Fast Fourier transformation
FT-IR	Fourier-transform infrared spectroscopy
GC	Graphitic carbon
HAADF	High-angle annular dark field
HAP	Hydroxyapatite
HAPNW	Hydroxyapatite nanowires
HRSTEM	High-resolution scanning transmission electron microscopy
HRTEM	High-resolution transmission electron microscopy
Lin	Cotton Linters
MAS-NMR	Magic-angle spinning nuclear magnetic resonance spectroscopy
nano-ED	Nano-beam electron diffraction
NC	Nanocomposite

$Ni(acac)_2$	Nickel(II)acetylacetonate
NP	Nanoparticle
$Pd(acac)_2$	Palladium(II)acetylacetonate
PDC	Polymer-derived ceramic
PDCP	Polymer-derived ceramic paper
PDC-NC	Polymer-derived ceramic nanocomposite
PHPS	Perhydropolysilazane
PXRD	Powder X-ray diffraction
QMID	Quasi-multiple ion detection
SAED	Selected area electron diffraction
Sar	Sartorius filter paper
SAXS	Small-angle X-ray scattering
SE	Secondary electrons
SEM	Scanning electron microscope, scanning electron microscopy
SSP	Single-source precursor
TC	Turbostratic carbon
TDS	Thermal diffuse scattered electrons
TEM	Transmission electron microscope, transmission electron microscopy
TGA	Thermogravimetric analysis
UHTC	Ultra-high temperature ceramics
UM	Ultramicrotomy
XRD	X-ray diffraction

Symbols

a, b, c	Lattice parameters along the crystallographic [100], [010], and [001] axes
α	Convergence angle of the electron probe
$Å$	Ångström, 10^{-10} m
β_1, β_2, β_3	Inner collection angle of BF, inner and outer collection angle of DF detector, respectively
C_C	Chromatic aberration
C_S	Spherical aberration
d	Lattice spacing
d_f	Defocus of the objective lens
ΔE	Energy spread of beam electrons
ΔG	Gibbs free energy change
ΔG^0_f	Gibbs free energy change of formation
E, E_0	Energy, energy of the incident electron beam

g, g_{hkl}	Reciprocal lattice vector
hkl	Miller indices
[hkl]	Specific crystallographic direction
⟨hkl⟩	Set of symmetry-equivalent crystallographic directions
(hkl)	Specific crystallographic plane
{hkl}	Set of symmetry-equivalent crystallographic planes
k	Vector of the incident wave
keV	Kiloelectronvolt; the kinetic energy of accelerated electrons
k_D	Vector of the diffracted wave
kJ	Kilojoule
kV	Kilovolt; acceleration voltage applied in an electron microscope
λ	Electron wavelength
$mrad$	Milliradians
n	Integer number
s	Excitation error
T	Temperature
Θ	Diffraction angle
τ	Collection semi-angle
Z	Atomic number

Abstract

Polymer-derived ceramics (PDCs) and their nanocomposites (NCs) are a class of materials accessed through the pyrolytic decomposition of suitable molecular precursors. In contrast to traditional powder sintering techniques, the composition, microstructural characteristics and, consecutively, the performance of PDCs can be conveniently adjusted through the design of the preceramic polymer, which has attracted sustained interest of researchers in the last decades. Most molecular precursors possess exceptional processability in their polymeric state, allowing the employment of advanced fabrication techniques, such as extrusion, coating, infiltration, and even additive manufacturing. Quite recently, heat-treating regular cellulose-based paper templates infiltrated with preceramic polymers have been successfully deployed to conveniently generate polymer-derived ceramic papers (PDCPs) exhibiting structural characteristics closely resembling that of the template. Ceramic papers combine the unique structure of organic papers with the composition and properties of various ceramic materials making them predestined for a wide range of applications, such as filtration, refractories, or as catalyst support. A key concept of the PDCP approach is to unite the processability of cellulose-based papers with the exceptional property design of PDC materials, paving the way for component preform of tailorable ceramics with paper-like structures and complex morphologies. The present dissertation deals with the microstructure and phase characterization of various PDCPs obtained from cellulose paper templates infiltrated with transition metal-modified polysilazane precursors upon heat treatment. The focus lies on assessing the impact of individual synthesis parameters on the structure and phase evolution of the ceramic papers to attain a better understanding of the means applicable to tailor their properties and ultimately, enable future application of this exciting novel material class.

For the present study, various single-source precursors (SSPs) were prepared from modification of either perhydropolysilazane (Durazane 2250) or poly(vinyl)silazane (Durazane 1800) with one of three transition metals. Several different cellulose-based paper templates were dip coated with the SiMN(O,C)-based SSPs (M = Fe, Ni, Pd) prepared from reacting polysilazanes with metalorganic acetylacetonate compounds ($Fe(acac)_3$, $Ni(acac)_2$, $Pd(acac)_2$) and subjected to pyrolysis at up to 1000 °C in Ar or reactive NH_3 atmosphere. In a second step, the as-pyrolyzed ceramic papers were annealed at 1300 °C in flowing Ar or N_2 to investigate their high-temperature evolution and the impact of the atmosphere employed on the phase assemblage generated. Detailed investigation of the interactions between template and precursor, phase evolution, and microstructural characteristics upon heat-treatment of the preceramic composites was conducted employing scanning electron microscopy (SEM) imaging and energy-dispersive X-ray spectroscopy (EDS) analyses in combination with X-ray diffraction (XRD) and Fourier-transform infrared (FT-IR) spectroscopy. In addition, ultra-thin fiber cross-sections were prepared from each sample and investigated via transmission electron microscopy (TEM) imaging and electron diffraction, allowing the in-situ generated micro- and nanostructure to be elucidated in great detail.

In all cases, upon pyrolysis, ceramic composites with a paper-like structure were obtained, consisting of cellulose-derived carbon fibers coated with a SiMOC(N)-based PDC layer. The transition from a SiN(O,C)- towards a SiOC(N)-based ceramic is attributed to the interaction between the pyrolysis products of the H_2O-rich cellulose with the polymer during heat-treatment. As revealed by electron microscopic imaging, the coating generated exhibits excellent bonding to the carbon fibers, which was further investigated via FT-IR analyses, indicating that this likely stems from chemical reactions of the polysilazanes with the hydroxyl groups of cellulose during surface modification of the templates. The template-assisted synthesis leads to pseudomorphic PDCPs faithfully reproducing the morphological characteristics of the respective paper template used, whereas other synthesis parameters were found to have a negligible effect.

Upon pyrolysis at 1000 °C, the transition metal-modified precursor has separated into X/SiOC(N) ceramic nanocomposites (X = metal, metal carbide, metal silicide) consisting of nanosized metal-based precipitates

dispersed within an amorphous SiOC(N) matrix. The phase assemblages generated, microstructural characteristics, and even macroscopic properties of the PDCPs were found to vary notably with the transition metal introduced. For instance, while both Ni- and Pd-modified papers encompass metallic and metal silicide phases, they exhibit a remarkably distinct micro- and nanostructure. The former features highly graphitized carbon fibers containing most of the metal-based phases, whereas the latter consists of entirely amorphous pyrolytic carbon encased by a Pd_XSi/SiOC-based NC layer. By using Fe for precursor modification, metallic Fe and carbides are generated and the microstructure is somewhat intermediate between the other two systems, with graphitic carbon fibers enveloped by a Y/SiOC layer (Y = α-Fe, Fe_3C) coating and some oxide phases present and the fiber-coating interface. Also, both the Fe- and Ni-modified papers exhibited noteworthy ferromagnetic behavior due to the abundance of ferromagnetic precipitates. To investigate the low-temperature evolution of PDCPs and the effect of a reactive atmosphere on the phase assemblage generated, Fe-modified papers were subjected to pyrolysis in NH_3 at 500-1000 °C. While the ceramic papers are devoid of any crystalline phases upon 500 °C treatment, Fe_XO nanocrystals have precipitated within the coating upon ammonolysis at 700 °C. Increasing the temperature further led to a reduction of the oxides towards α-Fe throughout the sample without any Fe_3C present upon pyrolysis at 1000 °C. Moreover, Fe_XN phases are generated exclusively along the fiber-coating interface at 700 °C, which withstand reduction and grow considerably towards higher temperatures. Both the suppression of carbide formation and generation of metal nitrides is traced back to reactions between the ceramic papers and NH_3 atmosphere and shows that the phase evolution of PDCPs can be effectively controlled via the pyrolysis atmosphere. Conversely, neither the type of polysilazane used nor the kind of paper template had a notable effect on the microstructure and phase assemblage observed in any of the ceramic papers.

Annealing of the as-pyrolyzed samples at 1300 °C led to profound changes across all systems investigated; most notably, the surface and macropores of the papers were found covered with in situ generated nanowires and whisker structures. Tempering in Ar induced crystallization of β-SiC from the amorphous SiOC matrix and growth of α-SiC whisker structures with aspect ratios of up to 50:1. In N_2, ultra-long α-Si_3N_4 nanowires with aspect ratios of around 1000:1 are produced. Quite often, these nanostructures are decorated with metal silicide tips, suggesting that their growth is facilitated via a transition metal-catalyzed vapor-liquid-solid (VLS) mechanism. The number, morphology, and aspect ratios of the wires were found to vary depending on the transition metal introduced, indicating that precursor modification enables control over these aspects. Apart from generating Si-based nanostructures, tempering led to the conversion of any metal-based phase towards the thermodynamically most stable silicide in the respective system, i.e. Fe_3Si, Ni_2Si, and Pd_2Si, and the ferromagnetism observed in the Fe- and Ni-based papers upon pyrolysis, vanishes in the tempered samples. Also, the graphitization of the cellulose-derived carbon fibers increases significantly with even the formerly amorphous fibers in the Pd-modified papers found to be composed of graphitic nanostructures to a large extend, with Pd_2Si now predominately occurring dispersed throughout the fibers. This indicates that the graphitization of the fibers also is catalyzed by the transition metals, presumably via a solution-precipitation mechanism and within a different temperature range for the three metals introduced, opening additional pathways to tailor micro- and nanostructural attributes of PDCPs.

The results show that the PDC route is a feasible approach to accessing ceramic paper composites exhibiting a variety of microstructural characteristics and interesting properties adjustable to some extend through controlling individual synthesis parameters. While using cellulose-based materials as templates potentially restricts the generation of non-oxide ceramics, their morphological characteristics are precisely transferred onto the ceramic composite, facilitating convenient access to ceramic materials with complex morphologies. Moreover, the data show that besides temperature and atmosphere, precursor modification with transition metals is especially promising to tailor certain features and properties of PDCPs to the needs of a variety of potential applications.

Zusammenfassung

Polymer-abgeleitete Keramiken (PDCs) und Nanokomposite (NC) sind Materialien, die durch die pyrolytische Zersetzung geeigneter molekularer Präkursoren zugänglich sind. Im Gegensatz zu herkömmlichen Pulversinterverfahren können Zusammensetzung, Mikrostruktur und Eigenschaften von PDCs gezielt durch die Anpassung des präkeramischen Polymers beeinflusst werden, was zu anhaltendem Interesse in der Forschung der vergangenen Jahrzehnte geführt hat. Aufgrund ihrer Eigenschaften, können die meisten präkeramischen Polymere auf vielfältige Weisen verarbeitet oder geformt werden, wodurch sie sich beispielsweise für Extrudieren, Beschichtung, Infiltration oder additive Fertigung eignen. Vor kurzem wurde gezeigt, dass die Pyrolyse von Zellulose-basierten Papieren, die mit präkeramischen Polymeren infiltriert wurden, eine einfache Herstellung von keramischen Materialien mit Papier-ähnlicher Struktur ermöglichen. Dass keramische Papiere die einzigartige Struktur von Papier mit den Eigenschaften von verschiedenen keramischen Systemen vereinen, macht sie für eine Reihe von Anwendungen wie beispielsweise in Filtern, Hochtemperaturmaterialien oder als Trägermaterial in Katalysatoren interessant. Das Konzept Polymer-abgeleiteter keramischer Papiere (PDCPs) ist die Synergie zwischen der guten Verarbeitbarkeit von Papier und der Anpassbarkeit von PDCs, um die Herstellung von keramischen Bauteilen mit komplexen Strukturen durch Vorformen zu ermöglichen. Die vorliegende Dissertation befasst sich maßgeblich mit der Charakterisierung der Mikrostruktur und Phasen, die in verschiedenen PDCPs während des pyrolytischen Umwandlungsprozesses gebildet werden. Dabei wird insbesondere der Einfluss einzelner Syntheseparameter auf die Charakteristika der Papiere untersucht, um zu verstehen, womit die Eigenschaften dieser neuartigen Materialien gezielt für zukünftige Anwendungen eingestellt werden können.

Hierfür wurden verschiedene Single-Source-Präkursoren (SSPs) durch die Reaktion von Perhydropolysilazan (Durazane 2250) oder Poly(vinyl)silazan (Durazane 1800) mit je einem von drei organischen Übergangsmetall-Acetylacetonaten hergestellt. Verschiedene Zellulose-basierte Papier Template wurden mit dem SiMN(O,C)-basierten SSP (M = Fe, Ni, Pd) oberflächenmodifiziert und bei bis zu 1000 °C in Ar oder reaktivem NH_3 pyrolysiert. In einem zweiten Schritt wurden die pyrolysierten Papiere bei 1300 °C in Ar oder N_2 gesintert um den Einfluss hoher Temperaturen und verschiedener Atmosphären auf die Materialien zu ermitteln. Der Einfluss der einzelnen Syntheseparameter, die Wechselwirkung zwischen den Templaten und Präkursoren, sowie die Phasen- und Mikrostrukturentwicklung während der einzelnen Syntheseschritte wurde mittels Rasterelektronenmikroskopie (SEM), Energy-dispersive Röntgenspectroskopie (EDS) in Kombination mit Röntgenbeugung (XRD) und Fourier-Transformations-Infrarotspektrometrie (FT-IR) im Detail untersucht. Zusätzlich konnte die in situ erzeugte Mikro- und Nanostruktur der verschiedenen PDCPs mittels Transmissions-Elektronenmikroskopie (TEM) an ultradünnen Faserquerschnitten studiert werden.

In allen Fällen führte die Pyrolyse zu keramischen Kompositen mit Papier-ähnlicher Struktur, aufgebaut aus karbonisierten Zellulosefasern, die von einer SiMOC(N)-basierten Beschichtung ummantelt sind. Dabei ist die Umwandlung der SiN(O,C) Polymere in SiOC(N)-basierte Keramiken wahrscheinlich auf Reaktionen mit den Pyrolyseprodukten der H_2O-haltigen Zellulose zurückführbar. Die TEM Untersuchungen zeigen eine feste Anbindung der keramischen Beschichtung an die Fasern, was durch chemische Reaktionen der Polymere mit den Hydroxylgruppen der Zellulose unter Ausbildung von kovalenten Si-O Bindungen ermöglicht wird, wie komplementäre FT-IR Analysen andeuten. Die hier eingesetzte Syntheseroute führte in allen Fällen zu pseudomorphen PDCPs, deren morphologische Charakteristika maßgeblich durch das jeweils eingesetzte Papier bestimmt wird, während andere Syntheseparameter keinen nennenswerten Einfluss hierauf zu haben scheinen.

Nach der Pyrolyse bei 1000 °C hat sich aus jedem der Metall-modifizierten SSPs ein keramisches X/SiOC(N) NC (X = Metall, Metallkarbid, Metallsilizid) bestehend aus Metall-basierten Nanokristalliten in einer amorphen SiOC(N) Matrix gebildet. Dabei können die Phasenzusammensetzung, Mikrostruktur und sogar manche

makroskopischen Eigenschaften der Papiere deutlich in Abhängigkeit vom eingesetzten Übergangsmetall variieren. Beispielsweise wurden sowohl in den Ni- als auch in den Pd-modifizierten Proben Metall- und Metallsilizidphasen gebildet, unterschieden sich sonst jedoch deutlich: Während die Fasern in ersteren überwiegend aus graphitischem Kohlenstoff aufgebaut sind und den Großteil der Ni-Phasen beinhalten, sind die Fasern in Pd-modifizierten Papieren vollständig amorph und die Metall-basierten Phasen treten ausschließlich innerhalb der keramischen Beschichtung auf. Mit Fe-modifizierten Präkursoren entstanden wiederum andere Phasen und die Mikrostruktur zeigte Merkmale der beiden anderen Systeme, mit graphitisierten Fasern, die von einer Y/SiOC Schicht (Y = α-Fe, Fe_3C) eingehüllt sind sowie Fe-Oxiden, die nur an der Grenze zwischen Faser und Beschichtung auftreten. Dabei zeigten sowohl Fe- als auch Ni-modifizierte Papiere deutlichen Ferromagnetismus durch die Bildung metallischer Nanophasen. Um die Entwicklung der Fe-modifizierten PDCPs bei niedrigen Temperaturen und den Einfluss der Atmosphäre zu untersuchen, wurden sie bei 500-1000 °C in reaktivem NH_3 pyrolysiert. Während nach der Ammonolyse bei 500 °C noch keine kristallinen Phasen auftraten, beginnt die Kristallisation der Beschichtung bereits bei 700 °C mit der Ausscheidung von Fe_XO Nanopartikeln. Bei höheren Temperaturen wurden die Oxide zu α-Fe reduziert, wobei kein Fe_3C gebildet wurde. Zusätzlich entstanden während der Ammonolyse bei 700 °C Fe_XN Kristallite entlang des Faser-Beschichtung-Kontakts, die nach Behandlung bei 1000 °C deutliches Wachstum zeigten, anstatt reduziert worden zu sein. Sowohl das Fehlen von Karbiden als auch die Bildung von Metalnitriden resultiert aus den Reaktionen von NH_3 mit den Kompositen während der Pyrolyse und zeigt, dass die Phasenentwicklung von PDCPs maßgeblich durch die Atmosphäre beeinflusst werden kann. Das eingesetzte Polysilazan sowie die Art der Papiertemplate zeigte hingegen keinerlei nennenswerten Einfluss auf die Mikrostruktur und Phasenzusammensetzung in den keramischen Papieren.
Nach dem Tempering der pyrolysierten Proben bei 1300 °C zeigten sich grundlegende Veränderungen in allen untersuchten Papieren, wie zum Beispiel, dass die Oberflächen und Porenräume der Papiere mit in situ gebildeten Nanodrähten und Whiskerstrukturen überzogen sind. Die Behandlung in Ar führte zu Fasern, die mit kristallinem β-SiC und zusätzlichen α-SiC Whiskern mit einem Längenverhältnis von bis zu 50:1 beschichtet sind. In N_2 gesinterte Papiere wiesen eine Vielzahl von ultralangen α-Si_3N_4 Nanodrähten mit einem Längenverhältnis von etwa 1000:1 auf, was den maßgeblichen Einfluss der Prozessatmosphäre demonstriert. An den Spitzen der Nanostrukturen können gelegentlich Metallsilizidpartikel beobachtet werden, was einen Dampf-Flüssigkeits-Feststoff (VLS) Wachstumsmechanismus anzeigt, der durch die Übergangsmetalle katalysiert wird. Die Anzahl, Morphologie und Dimensionen der Strukturen unterscheiden sich abhängig vom eingesetzten Metall, was darauf hindeutet, dass diese mittels Modifikation der Polymere gesteuert werden können. Neben der Bildung von Si-basierten Nanostrukturen führte das Sintern der Papiere zur Umwandlung der verschiedenen Metallphasen in das jeweils thermodynamisch stabilste Silizid, Fe_3Si, Ni_2Si und Pd_2Si, wodurch die ferromagnetische Eigenschaften der pyrolysierten Fe- und Ni-basierten Papiere verloren gehen. Die Graphitisierung der Kohlenstofffasern stieg außerdem deutlich und auch die vorher amorphen Fasern in den Pd-modifizierten Papieren bestehen nun zu großen Teilen aus graphitischen Nanostrukturen, in denen die Pd_2Si-Partikel eingeschlossen sind. Dies zeigt an, dass die Graphitisierung ebenfalls durch die Übergangsmetalle katalysiert wird, was möglicherweise auf einen Lösungs-Ausscheidungs-Mechanismus zurückführbar ist, der je nach Metall in unterschiedlichen Temperaturbereichen beginnt, was zusätzliche Möglichkeiten bietet die Nano- und Mikrostruktur von PDCPs zu beeinflussen.
Die vorliegende Arbeit zeigt, dass der PDC Ansatz für die Herstellung von Papier-ähnlichen keramischen Kompositen geeignet ist, deren Struktur und Eigenschaften maßgeblich durch die Kontrolle der Syntheseparameter beeinflusst werden kann. Während der Einsatz von Zellulose-Templaten die Herstellung von nicht-oxidischen PDCs erschwert, lässt sich ihre Morphologie hervorragend auf PDC Systeme übertragen, was eine einfache Herstellung von keramischen Kompositen mit komplexer Struktur ermöglicht. Neben der Temperatur und eingesetzten Atmosphäre, spielt besonders die Übergangsmetall-Modifikation der Präkursoren eine entscheidende Rolle bei der Anpassung bestimmter Eigenschaften der PDCPs auf verschiedene potenzielle Anwendungsgebiete.

1 Introduction

1.1 Motivation & Concept

Uniting the unique structure of organic papers with the properties of various ceramic materials, ceramic papers are of interest for a wide range of application fields, such as refractories, insulation, filtration, catalysis, electromagnetic interference, and many others. In contrast to traditional cellulose-based papers, ceramic papers can be tailored to be extremely resistant to heat, oxidation, and degradation, making them predestined for employment in harsh environments and possibly, as a sustainable alternative for long-term physical data storage. Consequently, inorganic materials with a paper-like structure have attracted the attention of numerous researchers in recent years and were extensively studied regarding their characteristics and applicable processing techniques related to their present and future utilization [1,2].

Typically, ceramics with paper-like morphology are accessed by processing fibrous or wire-like compounds into two-dimensional sheets comparable to the traditional paper-making process. Nanowires and -whiskers composed of, for instance, SiC, SiO_2, MnO_2, hydroxyapatite, and many others, have been successfully assembled into ceramic papers, which however, requires ceramic fibers with suitable properties and processability. An entirely different approach to preparing ceramics with well-defined morphologies is the use of structural templates, as it was employed for several so-called biomorphic ceramics. Carbonized wood and cork templates infiltrated with inorganic precursors can be converted into ceramics with cellular pore structures inherited from the biocarbon template. Similarly, paper-like ceramics, based on, for instance, SiC, Si_3N_4, or TiC, were obtained via gas-phase infiltration of carbonized cellulose fibers. A more recent study also reports on the production of fibrous AlN/C composites through sol-gel infiltration of pristine cellulose-based papers and subsequent thermal treatment [3]. Within the context of template-assisted processing, the use of liquid preceramic polymers is a highly promising approach, as it offers intriguing possibilities for the production of ceramic materials with freely designable morphologies. Not only do such molecular precursors feature excellent processability in their preceramic state, but the properties of the resulting polymer-derived ceramics (PDCs) can also easily be adjusted by tailoring the composition and structure of the polymers. Quite recently, proof of concept was delivered by a study by Zhou et al. reporting on the successful preparation of a C/SiFeN(O) composite with paper structure from cellulose-based templates infiltrated with an iron-modified polysilazane precursor [4,5]. This triggered consecutive investigation of the underlying principles of the conversion mechanism and processing parameters that could be exploited to adjust the microstructure and phase assemblage of such polymer-derived ceramic papers (PDCPs) and explore potential functionalization routes as well as application fields of this exciting new material class [6–8].

As summarized in Fig. 1-1, an analogy exists between the experimental concept of PDCP synthesis and the naturally occurring mineral conversion mechanism known as 'pseudomorphosis' (ancient Greek: ψσευδής – false, μορφή – shape). If a primary mineral A with a certain composition, crystal structure, and morphology (e.g. quartz, SiO_2, trigonal, pseudohexagonal prismatic habit) is subjected to hydrothermal alteration, the mineral may be converted into another, via a process called metasomatosis. While this inevitably leads to a change in the minerals' composition and (most often) crystal structure, the morphology may be retained, completely or partially. The resulting mineral B (e.g. talc, $Mg_3Si_4O_{10}(OH)_2$, triclinic) inherits the habit of the primary phase, as depicted in the famous example from the Johanniszeche in Bavaria. Although generally a rather uncommon phenomenon, a multitude of mineral pseudomorphoses are known, and several distinct subtypes have been identified and studied [9,10]. During the pseudomorphic conversion, the primary mineral essentially acts as a morphological template, imparting shapes to the newly formed mineral, it otherwise could never attain.

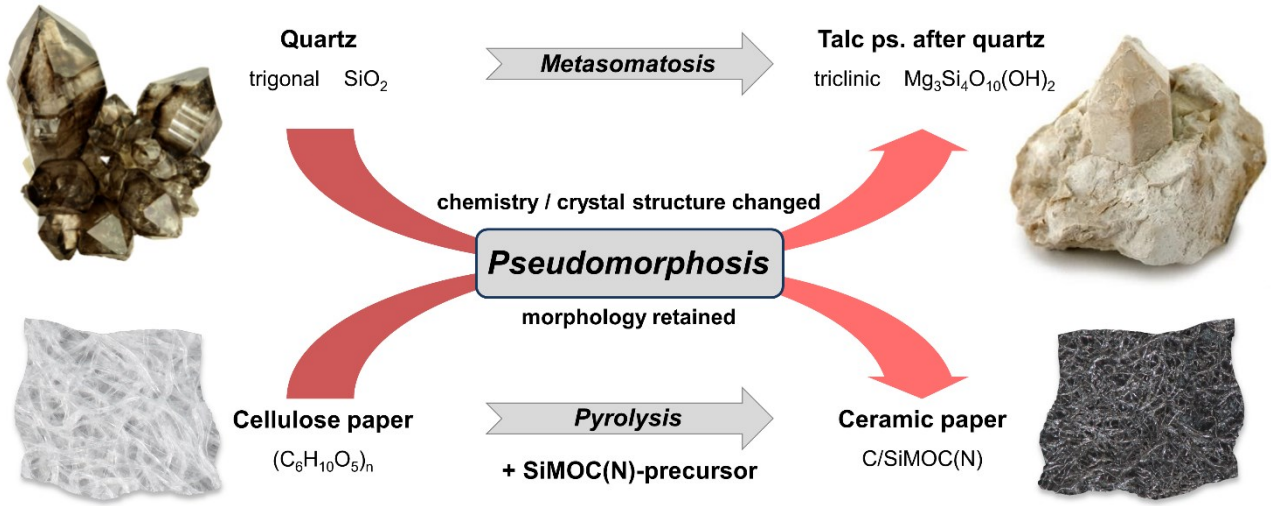

Figure 1-1: Schematic depiction of the experimental concept for the template-assisted synthesis of pseudomorphic polymer-derived ceramic papers in analogy to the naturally occurring phenomenon of 'pseudomorphosis'. A regular cellulose paper is surface-modified with a SiMOC(N) precursor (M = transition metal) and pyrolyzed to obtain a ceramic composite with a paper-like morphology inherited from the template [images reproduced from *https://www.mindat.org/photo-320341.html* (quartz) and *https://commons.wikimedia .org/wiki/File:Quartz-Talc-tmix07-127a.jpg* (talc)].

The basis of the present research is to apply this principle as a PDC processing technique to access highly adaptable ceramic composites with paper-like morphology by infiltration of a regular cellulose paper template with a suitable polymeric precursor followed by high-temperature treatment. Although the feasibility of this approach was proven by preceding studies, little has been reported on the in situ generated microstructure and phase evolution as well as the parameters that could be used to tailor their properties to the needs of potential uses. Hence, systematic investigation of the synthesis and processing parameters, such as the type of paper template and precursor, the pyrolysis atmosphere, and processing temperature is required to understand the underlying synthesis principles, explore functionalization, and ultimately enable the application of PDCPs.

1.2 Objectives

Accessing ceramic materials via the PDC route encompasses dealing with various synthesis parameters ranging from adjusting the polymeric structure and composition to precisely controlling processing conditions. While this clearly holds tremendous potential for the targeted design of high-performance ceramic materials, a broad understanding of the key aspects involved is paramount for the successful employment of this approach. According to these requirements, the present work aims to address the following questions within the context of the template-assisted synthesis of polymer-derived ceramic papers:

- How does the preceramic polymer bond to the cellulose-based substrate prior to pyrolysis?
- How do precursor and cellulose interact during polymer-to-ceramic conversion? How does this affect the composition, structure, and phase evolution of PDCPs?
- How do the characteristics of the paper templates, their fiber structure and porosity, impact the morphology, microstructure, and phase assemblage of the resulting ceramics?

Moreover, as one of the key aspects of the PDC route, the influence of varying certain characteristics of the preceramic polymer is a subject of interest, and the following questions arise:

- How do adjustable attributes of the polymeric precursor, such as the composition and molecular structure, impact the morphology, microstructure, and phase distribution of PDCPs?
- How does the modification of the precursor with different transition metals influence the microstructural and phase evolution? What are the implications for potential functionalization routes?

Finally, controlling processing parameters, such as temperature and atmosphere play a pivotal role during PDC synthesis and thus have to be investigated with respect to the following aspects:

- How does the pyrolysis temperature affect PDCPs? What are the effects of high-temperature annealing?
- How are the chemistry, phase assemblage, and microstructure affected by alternating the processing atmosphere during pyrolysis and/or annealing?

While the few preceding studies have addressed these questions through bulk analysis methods, localized investigation of the in situ generated microstructure and its evolution according to varying the above-mentioned parameters has not yet been achieved. Transmission electron microscopy (TEM) is a widely applied method for the microstructure characterization of ceramic materials. Uniting a unique combination of individual analysis techniques within one instrument, TEM allows imaging and accessing structural and compositional information down to the atomic scale. In particular, when paired with complementary methods, such as scanning electron microscopy (SEM), X-ray diffraction (XRD), and Fourier-transform infrared spectroscopy, TEM excels at conveying a comprehensive understanding of a material and thus, is chosen as the principal method for elucidating the objectives outlined.

2 Literature Review

2.1 Polymer-derived Ceramics (PDCs)

Employing preceramic polymers as precursors for the production of ceramic materials is a comparably new yet promising approach to manufacturing advanced ceramics with highly designable morphologies, compositions, and properties. In recent years, the polymer-derived ceramics (PDCs) route has enabled important advances in ceramic science owing to the discovery of a wide range of useful and unique features associated with this processing method. As a consequence, exploration of potential applications fields, such as in high-temperature materials, coatings, catalyst support, or in biotechnology, just to name a few, has been ongoing relentlessly, which is expected to continue in the future due to the highly designable nature of PDCs.

Published in the 1960s, the works of Ainger and Herbert [11] as well as Chantrell and Popper [12] are generally considered to have broken ground on the synthesis of Si-based non-oxide ceramics from polymeric precursors. A few years later, the conversion of different organosilicon polymers into Si_3N_4 and SiC-based ceramic fibers was reported by Verbeek et al. [13], which was also the subject of interest in the research group around Yajima, successfully preparing SiC-based ceramics derived from polycarbosilane precursors [14,15]. In the following years, various ceramic materials with tailored compositions have been explored and successfully prepared, typically belonging to the binary systems Si-N, Si-C, Al-N, or B-N, the ternary systems SiCN, SiCO, and BCN, or quaternary materials.

Compared to traditional powder-sintering methods, the PDC route allows the production of additive-free ceramic materials with easily accessed specialized morphologies by employing conventional polymer-processing techniques, such as coating, extrusion, injection molding, infiltration pyrolysis, and even additive manufacturing [16–18]. The preformed polymer components can then be heated to induce polymer-to-ceramic conversion, resulting in ceramics or ceramic composites with well-defined structures that are hardly realized using other techniques. Meanwhile, they can be processed at comparably low temperatures of around 1000-1300 °C, as opposed to the 1700-2200 °C typical for powder sintering techniques, offering economic potential for lowering energy consumption [19].

The adaptable molecular structure of the precursors and controlling the nanostructural arrangement of the resulting ceramics is another key aspect of PDCs. Generally, PDCs with covalent bonds are characterized by exceptional creep-, oxidation-, and decomposition resistance up to high temperatures, making them interesting for application in harsh environments [19,20]. Moreover, by using suitable preceramic polymers, (covalently) mixed-bonded SiCN or SiCO ceramics can be obtained [21], which has not been achieved by traditional methods so far. This is due to the low solubility of carbon in Si_3N_4 and SiO_2 as well as nitrogen and oxygen in SiC, making such ternary

compositions only accessible through the molecular preparation approach. Furthermore, even combinations of these systems are possible, facilitating the synthesis of some interesting quaternary systems, such as SiCNO, SiBCO, or SiBCN. The latter were found to have significantly improved resistance to decomposition and crystallization at temperatures as high as 2200 °C compared to their boron-free counterparts, which is attributed to kinetic inhibition due to the increased structural disorder [22]. This highlights that the properties of PDC materials can be decisively modified by adjusting the chemical composition and molecular structure of the polymer precursor, as well as the effect of chemical modification on the performance of the resulting material.

Even though research on PDCs is comparably young, a multitude of different polymer precursors and corresponding ceramics have been produced and their structure and properties investigated. Unsurprisingly, silicon-based precursor systems in particular have received a great deal of attention from researchers due to the widespread importance of silicon-based compounds in scientific and industrial applications. In addition to the above-mentioned desirable thermo-mechanical properties, which make them predestined for use as structural materials or protective coatings, Si-based PDCs can exhibit or be imparted with functional properties enabling application as, for example, magnetic, semiconducting, or electromagnetic wave absorbing materials [23–25]. Also, due to the coupling of such functionalities to the micro- and nanostructural arrangement of a material, PDC technology offers attractive ways of tuning performance via the design of the molecular precursor and precise control of the synthesis parameters. For instance, giant piezoresistivity observed in both SiCN- and SiCO-based PDCs can be attributed to the formation of percolation paths along segregated carbon domains, which are predominately formed at high pyrolysis temperatures. Hence, the piezoresistive response can be effectively modified by adjusting carbon content and (or) processing temperature [26,27]. Very recently, this led to the successful prototyping of cost-efficient multifunctional PDC-based strain gauges, exploiting the piezoresistive response of SiOC thin films [28]. Some relevant application fields of Si-based PDCs are summarized in Fig. 2-1.

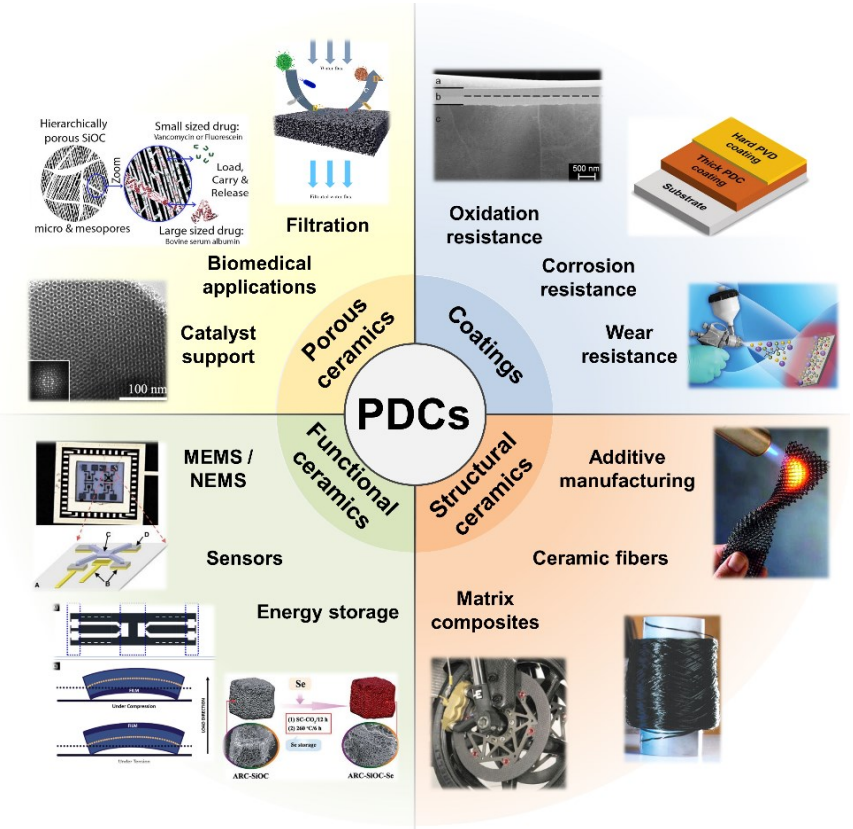

Figure 2-1: Overview of some important application fields for Si-based PDC materials, including porous, functional, and structural ceramics as well as ceramic coatings. Images reproduced from [18,28–37].

Lately, the focus of PDC research has gradually shifted towards modification of preceramic polymers with metalorganic compounds opening even more pathways for creating highly versatile advanced ceramic components. Homogeneously introducing metal species into the polymeric structure typically leads to the precipitation of nanosized metal-based particles upon polymer-to-ceramic conversion, which is an attractive feature for various utilization fields [24]. Concerning heterogeneous catalysis, for instance, the PDC route provides means of generating an inert, highly porous support through polymer processing (foaming or fillers), while simultaneously enabling the formation of nanosized catalytic centers with high surface-to-volume ratios [29]. In addition, the metals may lead to interesting interactions within the polymer itself, such as improved cross-linking or generation of Si- and C-based nanostructures [19,30,31].

In summary, PDC technology, uniting many intriguing features within a simple concept, enabled significant advancements in the field of ceramic science and holds tremendous potential for accessing a wide range of adaptable high-performance ceramic materials in the future. However, many aspects of the PDC route are not yet well-understood, owing to the complexity of multicomponent ceramic systems and the variety of processing parameters that may be adjusted [19,24]. In the following chapters, the fundamentals of the research field are briefly described, focusing on the processing techniques, microstructural characteristics, and potential application fields of PDC materials.

2.1.1 Synthesis and Processing of Polymer-derived Ceramics

Compared to traditional synthesis approaches, the fundamental advantage of the PDC route lies in the fact that critical parameters, such as composition, phase assemblage, phase distribution, and microstructure of the resulting material can be effectively adjusted by designing the preceramic precursor. Hence, targeted modification of the polymer structure gives a convenient way of tuning the physical and chemical properties of the ceramics produced [24]. This, however, appoints a central role to the development of suitable precursors as well as understanding the means of engineering their molecular structure and optimizing processing routes to make use of their potential. For employment as a ceramic precursor, polymers have to meet some key requirements, such as being resistant to volatilization during thermal treatment, possessing reactive functional groups for cross-linking, and exhibiting adequate viscosity and solubility for the preceramic processing steps [19].

Although various preceramic polymers have been explored for preparing PDC materials in the past decades, silicon-based systems in particular have attracted the attention of researchers owing to the desirable properties of organosilicon compounds and the relevance of silicon-based materials for industrial applications. Fig. 2-2 displays the most important preceramic organosilicon polymers as summarized by Colombo et al., classified according to the Si-X linkages (X = O, C, N, B) present in the polymeric backbone [19]. In addition, a variety of substituents, denoted by R^1 to R^5, may be attached to the monomers (most often Si-sites) providing further options for adjusting

the polymer on the molecular level. This represents an effective way of modifying the rheological, optical, and electronic properties of the precursor, as well as their solubility, chemical and thermal stability. Moreover, as besides hydrogen, commonly aliphatic or aromatic organic side groups are added, the carbon content of the resulting ceramics can be tuned precisely, which plays a pivotal role in the microstructural evolution and property design of PDC materials [19,20,32].

The elemental classes of Si-based polymers are poly(organo)silanes (Si-Si backbone), poly(organo)carbosilanes (Si-C), poly(organo)siloxanes (Si-O), and poly(organo)silazanes (Si-N), as well as hybrid compositions, such as polycarbosiloxanes (Si-O-Si-C) or polysilylcarbodiimides ((Si-N=C=N). Precursors containing boron within their polymeric backbone (i.e. polyborosiloxanes, polyborosilanes, etc.) have attracted a lot of interest lately due to the significantly improved temperature stability of the corresponding ceramics compared to boron-free PDCs making them predestined for ultra-high-temperature applications [19,22]. The structure, synthesis, and processing of each of these polymers has been subject of intensive research for decades owing to their manifold desirable properties.

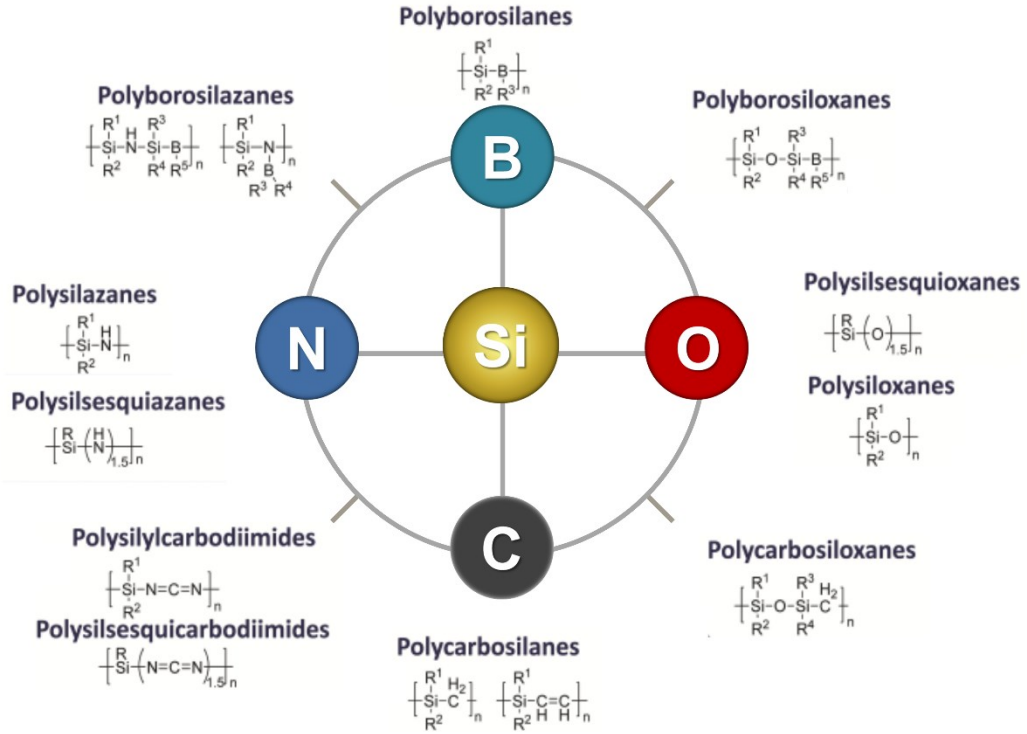

Figure 2-2: Overview of the fundamental classes of organosilicon polymers employed in PDC synthesis, classified according to the elements in the Si-X (X = B, C, N, O) polymeric backbone. Redrawn from [19].

The synthesis of Si-based molecular precursors generally relies on widely available chloro-, hydro-, or organosilanes, which can undergo polymerization. For instance, reacting chloro(organo)silanes with water typically results in the formation of polysiloxanes, which are widely employed in construction purposes due to their excellent chemical and physical properties, while being important precursors for SiCO ceramics [33,34]. Meanwhile, reaction with ammonia is the usual way of synthesizing poly(organo)silazanes, which primarily are

used as precursors for Si-N-based ceramic materials. Due to their comparably low molecular weight, modification of polysilazanes with organic substituents and catalyst-aided cross-linking plays an important role in reducing their volatility and increasing the ceramic yield [35,36]. Commercially available polysilazane derivatives are typically used as precursors for dielectric materials, protective coatings, or SiCN-based ceramics with desirable high-temperature resistance [19].

Apart from introducing different organic side-groups, chemical modification of molecular precursors with metalorganic compounds provides a powerful pathway for engineering the composition, microstructure, and properties of PDC materials. Through the reaction with compounds, such as metal alkoxides or metal acetylacetonates, covalent Si-O-M or Si-M bonds (M = e.g. Al, Fe, Zr, Hf) form at specific sites of the polymeric backbone or functional groups, depending on the type of organosilicon polymer [37–39]. The chemical modification of the precursors leads to a uniform incorporation of the metal species into the polymeric structure resulting in metal-modified SSPs, which, upon pyrolysis at intermediate temperatures, typically are converted into nanocomposite materials with metal-based precipitates homogeneously dispersed within an amorphous ceramic matrix. This approach enables PDCs to be imparted with various interesting functional properties, such as magnetism or electrical conductivity, while also providing means of improving the thermo-mechanical properties of the material as, for instance, in ultra-high temperature ceramics (UHTCs) [40–42].

In their polymeric state, most molecular precursors can be easily processed into their desired shape employing various well-established techniques, setting the PDC route apart from traditional ceramic processing approaches. Many preceramic polymers can be cast, pressed, foamed, and drawn to fiber shape, they can be injection molded, applied as a coating, and impregnate other materials [17,43–46], offering unprecedented possibilities for producing ceramic materials with highly specialized morphologies. Some shaping techniques applicable to preceramic polymers are exemplarily depicted in Fig. 2-3. To produce preceramic green bodies that can retain their shape upon heat treatment, cross-linking processes facilitated by functional groups, such as Si-H or Si-vinyl, are essential. Curing of the polymers is typically achieved thermally at moderate temperatures (< 200 °C), which comes at the cost of some evaporation leading to the formation of bubbles and reduced ceramic yield [19,47]. Catalysts can reduce the temperature needed for curing offsetting these drawbacks and other approaches have been explored, such as oxidative, laser, plasma, and UV curing, which, however, are often limited in their applicability and come with certain drawbacks or expenses [48–51].

The cross-linked polymers are converted into PDCs via pyrolysis at elevated temperatures, usually in the range of 600-1400 °C, typically resulting in amorphous covalently bonded ceramics. The resulting composition is predominately determined by that of the polymeric precursor, that is SiC for polycarbosilanes, SiC_xO_y for polysiloxanes, and SiC_xN_y for polysilazanes and polysilylcarbodiimdes. However, as pointed out above, both tailoring the precursor chemistry and controlling processing parameters can be used to affect the composition of the derived ceramics, by adjusting the Si/X (X = C, O, N) ratios [19]. The ceramization process is accompanied by the evolution of organic sidegroups from the precursor, causing the release of volatile species such as CH_4, H_2, H_2O, or NH_3, which was shown to be highly dependent on the type and modification of the preceramic polymer

and results in substantial mass-loss [52,53]. Upon subsequent annealing at higher temperatures, i.e. > 1300 °C, most PDCs undergo phase separation and crystallization giving rise to multiphasic poly-crystalline materials [54]. Hence, the processing temperature plays a pivotal role in tailoring the phase composition and microstructural arrangement of PDCs, as summarized in Fig. 2-4.

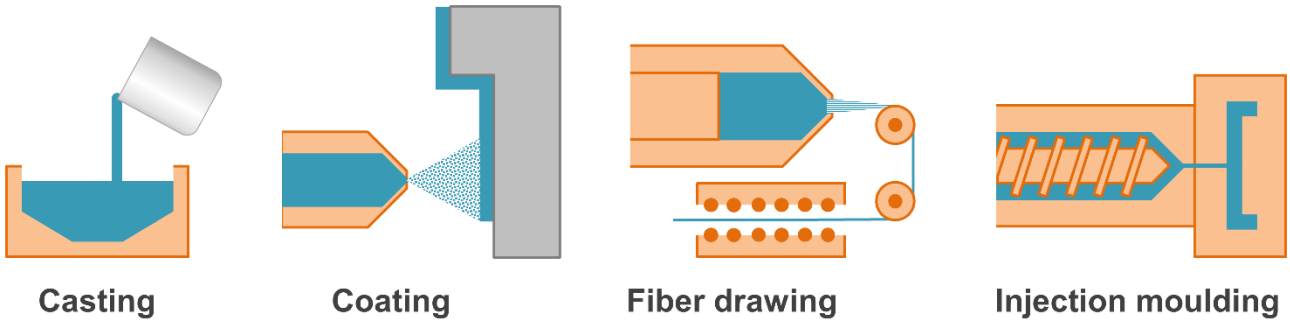

Figure 2-3: Schematic illustration of some shaping techniques applicable to preceramic polymers. Based on [19].

Similarly, the pyrolysis atmosphere provides means to modify the composition of the resulting ceramics. Pyrolysis in nitrogen atmosphere, particularly at high pressures, has been shown to lead to nitrogen incorporation into the ceramics; which is even more pronounced in NH_3. The reactive ammonolysis can be used to effectively shift the composition of polysiloxane-derived SiCO ceramics towards SiON via the removal of free carbon and simultaneous nitridation [55–57]. Moreover, the highly reactive ammonia allows in situ generation of metal nitrides such as Fe_XN or VN instead of metallic or silicide phases, which is an interesting tool to adjust the functional properties of the ceramics [58,59]. Another critical parameter is the oxygen activity in the pyrolysis atmosphere, particularly for non-oxide ceramic thin films and other geometries with low volume-to-surface ratios. The presence of oxygen, even in small quantities, can result in carbon and nitrogen removal from the material and the generation of oxide phases and grain coarsening, which, depending on the desired application, may be detrimental to the material's performance [57,60,61].

Upon polymer-to-ceramic conversion, the release of gas-phase compounds generally results in either linear volume shrinkage (usually 20-30 %) or the generation of (micro to macro) pores, severely restricting the ability to obtain dense ceramics from preceramic objects. Typically, this process is associated with the formation of cracks, especially in larger volume bodies, while being much less pronounced for ceramic coatings, fibers, and foams. The most common approach to overcome this challenge is the introduction of filler materials into the preceramic polymer, which can have additional beneficial effects besides reducing shrinkage. A multitude of distinctly composed fillers, such as ceramic, metallic, and polymeric compounds can be used, which also come in various shapes and sizes, including but not limited to powders, fibers, platelets, or nanotubes. In Fig. 2-5, a selection of some filler types used in PDC processing along with their effects on the resulting ceramics is displayed.

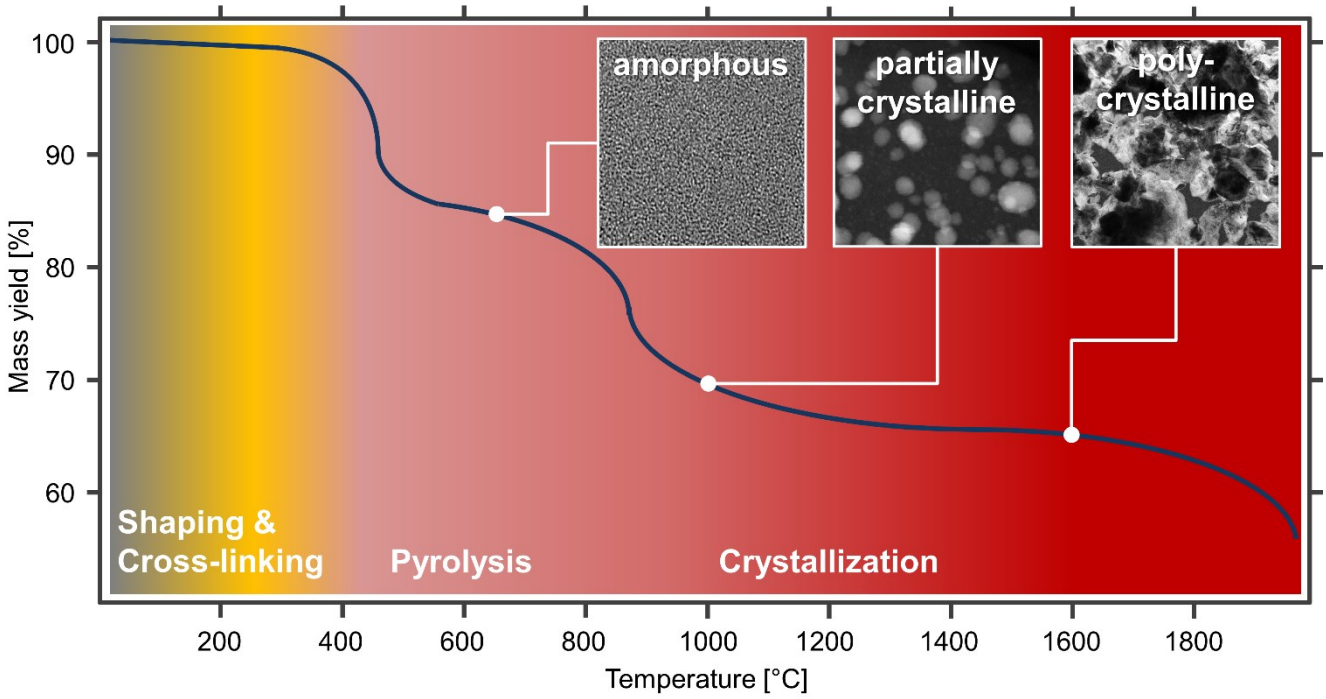

Figure 2-4: Schematic depiction of the temperature evolution of (metal-modified) polymer precursors accounting for mass changes and microstructural arrangement at the different processing stages. Upon pyrolysis, the SSPs are initially converted into amorphous monophasic ceramics, which undergo phase separation and crystallization during high-temperature annealing. Based on [19,62].

Passive fillers, that is substances that do not react with the precursor at any point during processing, such as SiC and Si_3N_4 powders, mainly provide shrinkage reduction and avoidance of macrodefect formation. Metallic and intermetallic compounds, on the other hand, are typically referred to as 'active' fillers, due to reactions with gases or the (pre)ceramic matrix during heat treatment. Similar to polymer modification with metalorganic compounds, this usually results in the generation of silicide, carbide, oxide, or nitride precipitates exhibiting interesting and useful characteristics that can be used to impart functional capabilities to the ceramic material, adjust its mechanical, thermal, and optical properties, or induce metal-catalyzed reaction processes [41,63,64]. In addition, the formation of intermetallic phases can come with significant volume expansion, further counteracting shrinkage and defect formation [65]. The reaction of metallic powder fillers with preceramic polymers has been successfully employed to produce PDCs with well-defined microstructures and interesting phase assemblages, based on, for instance, mullite [66], wollastonite [67], and SiAlON [68]. The introduction of carbon-based fillers into a preceramic polymer provides another interesting way of tailoring its properties. While carbon fibers and nanotubes can be used to adjust the electrical and mechanical attributes of the resulting ceramics, graphite powder can shift composition towards SiC formation via carbothermal reduction [69,70].

Another useful technique is the use of polymeric fillers that undergo decomposition upon heat treatment, acting as 'sacrificial' templates for the formation of pores with controllable shape and size [19,71]. This can not only reduce crack formation considerably but also provides means of engineering well-defined (hierarchical) porosity within the ceramic body and achieving high specific surface areas, which is of interest for various application

fields, such as in gas filters or as catalyst support [72]. Besides merely controlling porosity, both sacrificial and hard templates can be used to confer specific morphologies onto PDC materials. Polymer-infiltration of, for instance, synthetic sponges, silica, and biological templates, such as natural and carbonized wood, cellulose fibers, and carbonate corals, has been successfully employed as a way to create ceramic materials with pore architectures and morphologies that are difficult or impossible to achieve using other methods [73–75].

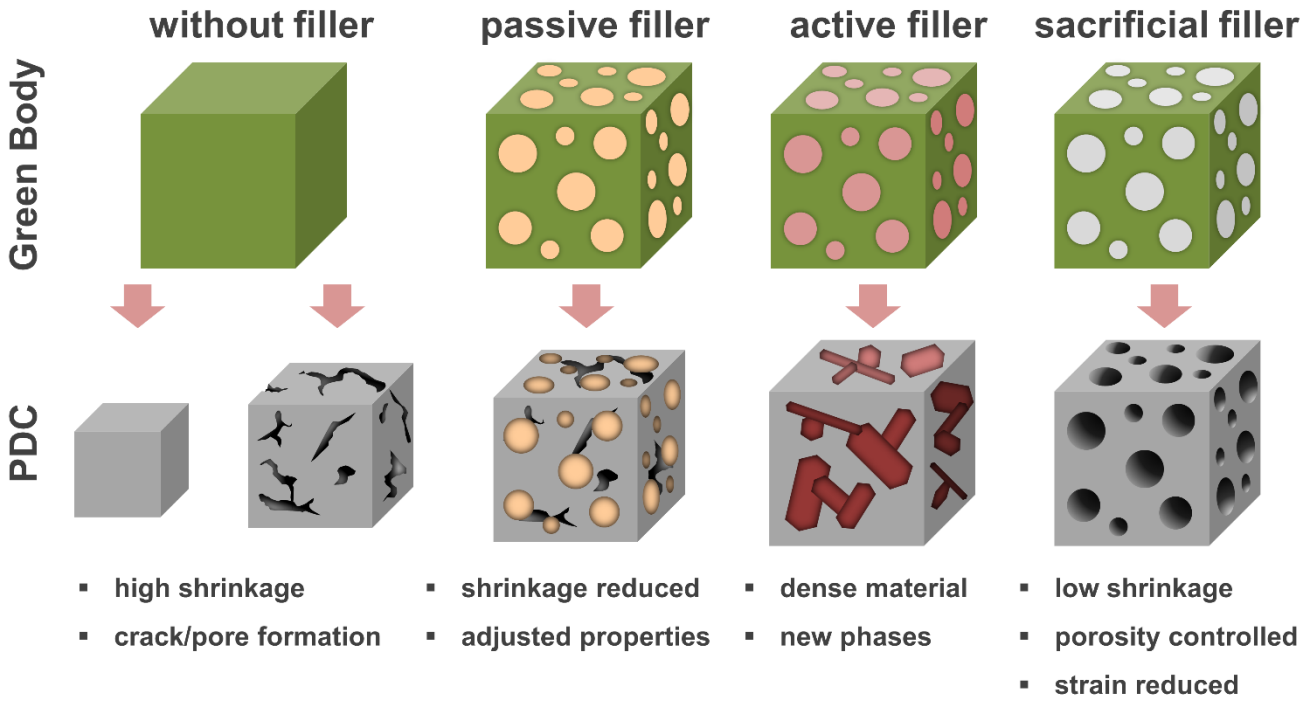

Figure 2-5: Schematic of some filler types employed in preceramic polymer processing and their effect on shrinkage, formation of pores, and phase composition of the resulting PDC materials. Based on [76].

2.1.2 Microstructure of Polymer-derived Ceramic Nanocomposites (PDC-NCs)

The term nanocomposite (NC) denotes a material encompassing two or more distinct Gibbsian phases from which at least one is nanoscaled. In his fundamental research on nanocrystalline materials, Gleiter recognized that size reduction of the components within a composite plays a pivotal role in engineering material properties [77], setting the stage for the development of a wide range of polymer-, metal-, and ceramic-based NCs over the following decades. Originally used for describing multiphasic piezo- and pyroelectrics, the connectivity concept introduced by Newnham gives a tool to classify the microstructures of composites, relating connectivity patterns between the phases present in a material to variations of its properties [78]. The same thought was revisited by Niihara, who suggested classifying diphasic NCs as being either intra- or intergranular, a hybrid mixture thereof, or a composite of two nanophases, as depicted in Fig. 2-6 [79]. According to both contributions, engineering the microstructural

arrangement of the components decisively affects the resulting properties and thus potentially enables dramatic improvement of a material's performance.

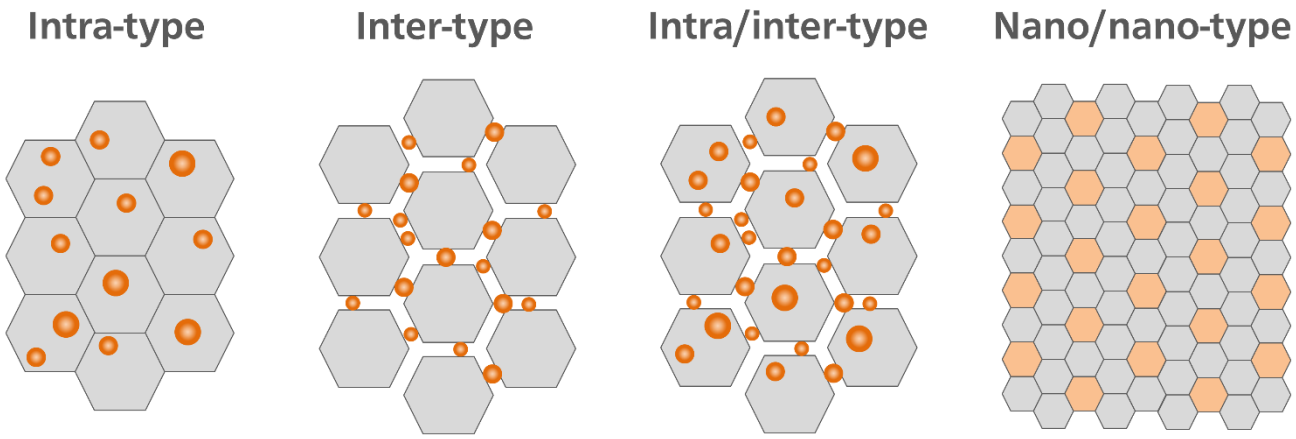

Figure 2-6: Different structural arrangement types of nanocomposite materials according to the classification of Niihara. Redrawn after [79].

Unsurprisingly, the molecular preparative approach of PDC technology and the inherent control over the micro- and nanostructural setting of the produced ceramic has been recognized to have immense potential for the production of nanocomposite ceramics. While the thermal treatment of suitable SSPs initially leads to amorphous and monophasic ceramics (compare Fig. 2-4), many PDCs undergo phase separation at higher temperatures, which results in the nucleation and growth of crystalline phases [52]. Compared to amorphous PDCs, some of these fully crystallized micro-/nanocomposites exhibit significantly altered properties, such as improved high-temperature stability or dramatically increased electrical conductivity. Detailed investigation of polymer-derived nanocomposites revealed that this often is not only related to the formation of crystalline phases but also to their microstructural arrangement. For instance, enhanced high-temperature oxidation resistance of Si_3N_4/SiC composites derived from amorphous SiCN was found to be caused by the formation of a passivating SiO_2 surface layer encasing the bulk [80]. Similarly, the electrical conductivity of some PDCs may be increased by several orders of magnitude upon high-temperature annealing through the formation of continuous crystalline carbon networks that act as percolation paths [81,82].

In the last years, in-depth characterization of various PDC(-NC)s has been conducted employing a range of sophisticated techniques, such as MAS-NMR, SAXS, FT-IR, TEM, and complementary simulations, to elucidate the micro- and nanostructure present within the materials generated. This led to the realization that some PDCs, which were assumed to be single-phasic, in fact, are composed of small domains featuring compositional variations on the nanometer scale. For instance, within SiOC-based PDCs, the segregation of a “free” carbon phase was found to affect the arrangement of mixed-bonded SiO_xC_y tetrahedral units considerably, leading to the formation of O- and C-rich nanodomains [83,84]. Likewise, within polysilazane-derived SiCN ceramics, excess carbon is initially homogeneously dispersed within the amorphous matrix but segregates to form sp^2-hybridized carbon at sufficiently high temperatures. This again is associated with the formation of nanodomains that at first,

span just around 1-3 nm, but grow with increasing annealing temperature [19,85]. The structural arrangement of segregated carbon domains decisively affects the chemical durability, crystallization resistance, and electric properties of PDCs and, as a consequence, is of major interest for a variety of applications [19,53,86,87].

The molecular architecture of the polymeric precursor was shown to play an important role concerning the microstructural and nanodomain evolution of PDCs, even for identically composed polymers. In the case of SiCN ceramics, profound differences in the nanostructural arrangement, depending on the type of precursor used, have been revealed via solid-state NMR and other techniques. Upon pyrolysis at 1000 °C, polysilazane-derived ceramics consist of mixed-bonded amorphous SiC_xN_y, whereas polysilylcarbodiimides are converted into a three-phasic nanocomposite consisting of amorphous Si_3N_4, carbon, and SiC domains, as displayed in Fig. 2-7 [20,21,88,89]. The same was concluded from TEM investigations of the glass-network structure of amorphous SiCN ceramics derived from four different polymeric precursors. Detailed electron diffraction studies revealed notable differences in the nanostructure of the glasses upon pyrolysis and more pronounced upon annealing at 1400-1540 °C, at which some showed crystalline precipitates, while others did not. Thus, the onset of crystallization and the temperature resistance of PDCs is decisively affected by the initial polymer architecture of the precursors [90]. Moreover, these examples highlight that some monophasic amorphous PDCs may be more accurately described as intrinsic nanocomposites [24] and that understanding the processes operating during the thermal evolution of a polymer precursor on the nanoscale is paramount to be able to utilize the vast potential of the PDC approach.

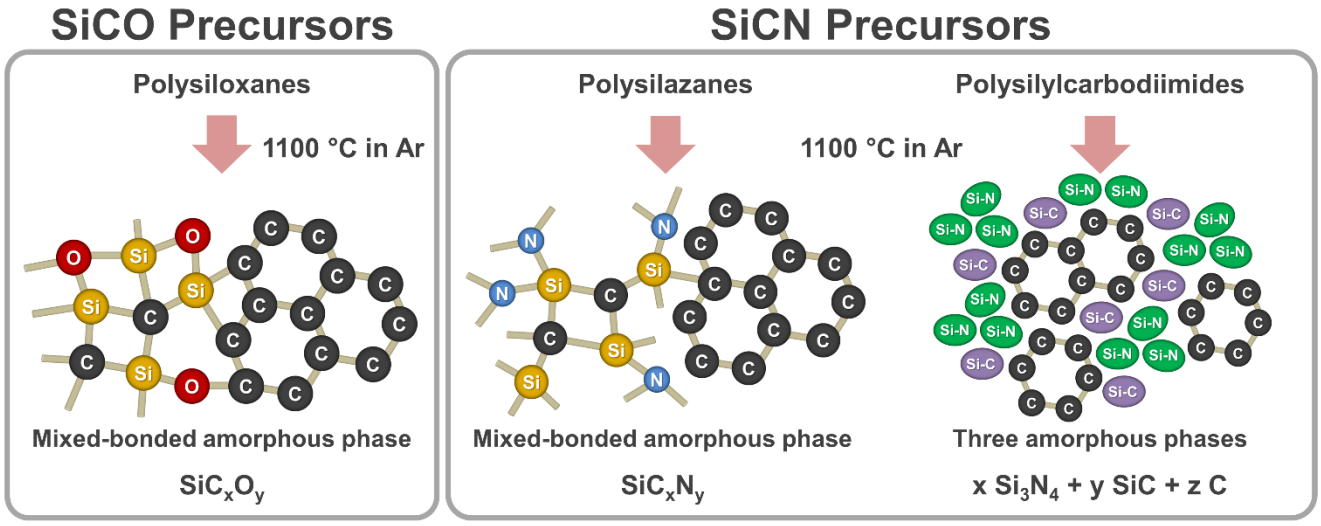

Figure 2-7: Nanostructural arrangement of SiCO- and SiCN-based PDCs derived from polysiloxanes, polysilazanes, and polysilylcarbodiimides upon pyrolysis at 1100 °C in Ar atmosphere. In the case of the two SiCN polymers, two distinct nanodomain architectures are generated, one containing primarily single-phase amorphous SiC_xN_y with mixed bonds (polysilazanes), the other consisting of three discrete amorphous phases without mixed bonding. Based on [19,21].

Modification of polymer precursors with metallic or intermetallic compounds plays a central role in the production of PDC-NCs and has led to the creation of various interesting ceramic materials in the last decades. As described

above, one way of accomplishing this is physically blending the preceramic polymers with metals or intermetallic compounds, the other involves chemical modification of the polymer with metal-organic compounds, such as metal alkoxides or amido complexes. Utilizing the latter approach, for instance, SiHfOC- and SiHfCN(O)-based preceramic polymers have been successfully prepared and their temperature evolution during polymer-to-ceramic transition has been studied in detail. In both cases, upon heat treatment at 800 °C, an entirely monophasic and amorphous material is obtained, whereas at higher temperatures (i.e. 1100 and 900 °C, respectively), nucleation of a nanosized Hf-containing phase is observed. An additional temperature increase to 1300 °C induces the crystallization of HfO_2 nanoparticles dispersed within an amorphous matrix, leading to the formation of SiOC/HfO_2 and SiCN(O)/HfO_2 PDC-NCs, respectively [39,91,92]. Similarly, various other PDC-NCs, such as Fe_3Si/SiOC, ZrO_2/SiCN, and VN/Si_3N_4, have been synthesized by precursor modification with different metal species [23,59,93]. Some of these materials exhibit significantly improved properties, such as enhanced corrosion resistance, ultra-high temperature stability, or reduced mass loss compared to metal-free PDCs [94–96]. Also, they can feature attractive functional capabilities, such as (soft)magnetic properties, electromagnetic shielding, or improved electrical conductivity [23,40]. In most cases, this can not only be related to the generation of metal-based species but rather to the microstructural setting and phase distribution. For instance, enhancement of electrical conductivity typically results from the formation of percolation paths along intermetallic grains and networks of segregated carbon. As a consequence, other interesting properties, such as microwave absorption or sensing capabilities, may be improved considerably [97,98].

The ability to generate nanosized metal-based particles dispersed within a high-surface porous ceramic matrix makes PDC-NC materials attractive for catalytic applications. By design of the polymeric structure and control of the processing parameters, some pivotal microstructural attributes, such as the size of the catalytically active particles and pore architecture of the ceramic, can be tuned precisely. Hence, various metal-modified PDC systems have been investigated for employment in energy-related heterogeneous catalytic application fields, such as Ni/SiOCN for CO_2 methanation (Sabatier-reaction), Co/SiOC for Fischer-Tropsch reaction, and MoSiC/SiC/C for hydrogen evolution reaction, just to name a few [99–102]. Many of these systems were shown to exhibit promising activity and exceptional stability for their respective reactions, which could let them emerge as a genuine alternative to well-established, yet costly, precious-metal-based catalyst materials in the future [29].

2.2 Cellulose-based Organic Papers

The use of paper has been recorded since ancient times, with the earliest known example being papyrus used by the Egyptians around 3000 BC. The use of other plant matter for producing papers was first documented in China between around 20 BC and 105 AD using techniques that are quite comparable to the ones employed today [103]. However, the processing and use of paper have undergone significant advancements since then, as today, paper is a ubiquitous material used in a variety of applications, including books, magazines, packaging, printing, filtration, construction materials, and many others, due to its low cost, lightweight, flexibility, and processability. Despite the ever-increasing prevalence of digital communication and computer-based work profiles, the global market for cellulose-based papers is growing rapidly, driven by surging demand from the packaging and printing industries. According to a 2023 report by the Statista Research Department, the global market for pulp and papers was valued at $351.53 billion in 2021 and is expected to reach about $373 billion by 2029 [104].

Paper is made primarily from cellulose fibers, which are derived from plant sources such as different types of wood, cotton, and agricultural waste. The molecular arrangement of cellulose and macroscopic structural features of paper are of great interest due to their importance in understanding the properties and potential applications of these materials. Cellulose, the main component of paper, is a complex polysaccharide made up of repeating glucose units connected by β-1,4-glycosidic linkages. Additionally, papers may also contain hemicellulose, lignin, and other minor components that can vary depending on the wood type used [103].

The industrial paper-making process is rather complex, involving several consecutive processing steps, including pulping, refining, and drying, each of which can influence the properties of the final product [103,105]. The first step in paper production is the preparation of pulp, which can be done by either mechanical or chemical means. Mechanical pulping involves grinding wood chips or other raw materials into fibers, whereas during chemical pulping, the raw materials are cooked with chemicals to break down the fibers [106]. The choice of wood type and pulping method can greatly impact the properties of the resulting paper, as, for example, papers made from hardwood fibers tend to have a higher density and stiffness than those made from softwood or cotton [107]. Similarly, papers produced using chemical pulping methods such as kraft or sulfite pulping tend to have higher strength and durability than those produced via mechanical pulping methods [108]. Once the pulp is prepared, it is mixed with water to form a slurry and spread out onto a moving screen to form a web-like sheet of paper, which is then dried, pressed, and cut into the desired size and shape. In addition to the raw materials and processing techniques, additives such as fillers, dyes, and sizing agents can be added to the paper during production to modify its properties [103]. These additives can affect the strength, porosity, and printability of the paper, among other characteristics. For example, the addition of calcium carbonate can improve the whiteness and opacity of the paper, while the addition of alumina trihydrate can enhance its flame resistance and ink adhesion [103,109,110].

Printing and publishing are perhaps the most well-known applications of paper, as virtually all print media, such as books, magazines, newspapers, and the like are produced using paper. The quality of the paper has a significant impact on the final product, as it can affect the readability, durability, and overall aesthetic appeal of the printed

material. Paper is also widely used in packaging materials, including cardboard boxes, paper bags, and wrapping paper, for which the strength and durability of paper, along with its low cost and lightweight make it an ideal material for protecting and transporting goods. Moreover, paper is used in the construction industry as a component of building materials, such as insulation, drywall, and roofing. These materials are often made by combining paper fibers with other materials, such as gypsum, asphalt, or cement, to create products with fire and moisture resistance or soundproofing properties [111,112]. Also, paper is a popular medium for artists and designers, who use it to create a wide range of artworks, including drawings, paintings, sculptures, and installations. The versatility of paper allows artists to experiment with different techniques and textures, and the availability of different types of paper means that artists can choose a paper that best suits their particular needs and preferences.

Furthermore, cellulose-based materials are of great importance in the field of material sciences due to their unique set of properties. A particularly interesting attribute of cellulose-based papers is their flexibility, which allows for convenient shaping by rolling or folding into morphologically complex objects, such as corrugated cardboard. Moreover, the hierarchically structured cellulose fibers can provide high strength and stiffness, when incorporated into a composite material [113] and the mechanical properties of cellulose-based materials can be further enhanced by the addition of other materials such as nanocellulose, polymers, and inorganic compounds, improving the material's strength, stiffness, and toughness [114,115]. In addition, cellulose-based papers have low toxicity, biodegradability, and renewability, making them an attractive alternative to many traditional materials [116]. These properties make cellulose-based materials ideal for use in various applications, including composites, coatings, and sensors [117,118]. Cellulose has also been used as a substrate for the deposition of thin films, providing a renewable and sustainable alternative to traditional substrates such as silicon [119]. Even the development of cellulose-derived electronics has been explored utilizing, for example, printing techniques to generate structured electrodes or employing cellulose as dielectric thin-film in transistor technology with tremendous potential for energy applications [120,121].

2.2.1 Composition and Structure of Cellulose-based Papers

The exceptional properties of cellulose-based papers primarily stem from the unique attributes, structure, and arrangement of their principal constituent the cellulose fibers. Cellulose is a complex polysaccharide and the main component of plant cell walls and thus the most abundant polymer in the world. The structure of cellulose fibers is highly hierarchical as shown in Fig. 2-8. Each fiber contains numerous bundles of microfibrils built up by several elementary fibrils, which consist of linear molecular cellulose chains. The chains can contain up to 15,000 alternately rotated glucose monomers, the fundamental unit of cellulose, connected by β-1,4-glycosidic linkages [122]. Due to the abundance of hydroxy-groups in glucose, intra-, and intermolecular hydrogen bridges form,

resulting in exceptional bonding between the fibrils, which contributes to the extraordinary mechanical properties of cellulose fibers. The fibrils are very well organized and aligned into a crystalline arrangement across the fibers, additionally affecting the mechanical attributes of the higher-level structure (i.e. wood, paper, and the like) [122,123]. Distinct structural settings result in significantly altered properties, as, for instance, toughness or density may vary considerably between individual types of wood. Moreover, the dimensions of cellulose fibers play a pivotal role in the paper-making process, as longer fibers tend to result in enhanced properties of the product, such as increased flexibility and resistance to tearing [124].

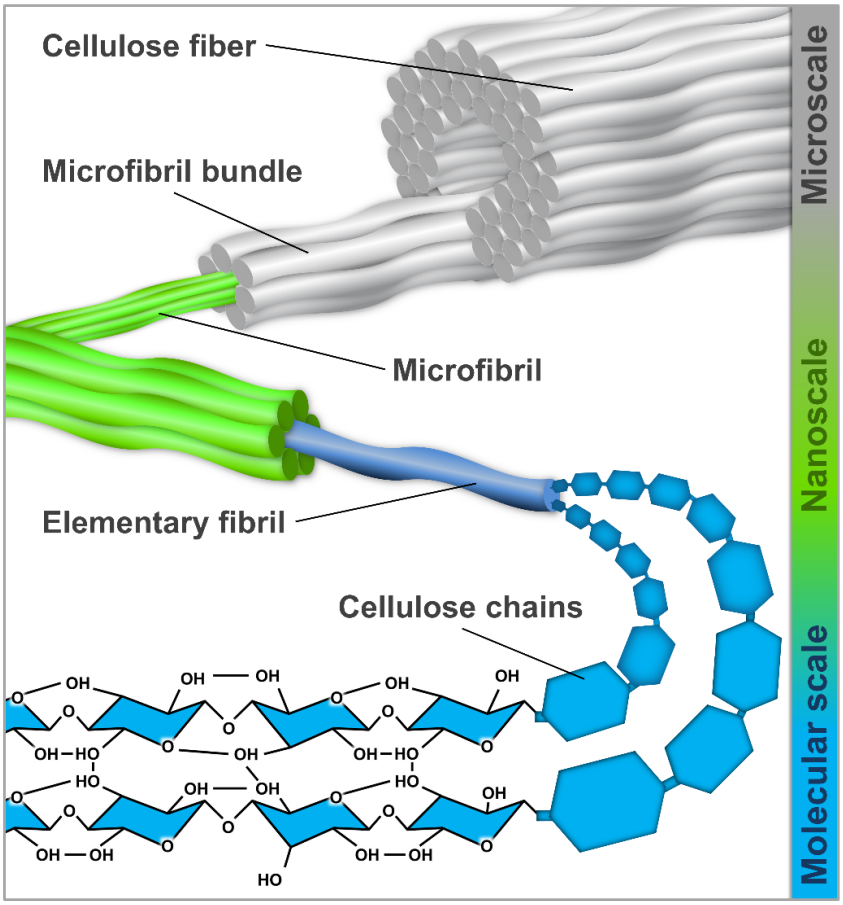

Figure 2-8: Schematic illustrating the hierarchical structure of cellulose fibers. Each fiber contains several microfibril bundles, which themselves are organized from individual microfibrils. The nanosized elementary fibrils consist of linear cellulose molecule chains, containing several thousands of alternately oriented glucose units, which are linked to each other by β-1,4-glycosidic bonds. Due to the abundance of hydroxy-groups in glucose, hydrogen bonds form between the molecular chains and fibrils, causing the strong adhesion and unique mechanical properties of cellulose fibers. Based on [123].

Besides cellulose, comprising up to 90 % of papers, the most important components are hemicellulose, lignin, and accessories, such as waxes, resins, and inorganic compounds. The content of these substances varies across the different wood types used for papermaking and affects various important properties of the resulting papers. Thus, controlling their residuals in the pulp during processing is paramount to obtaining high-quality paper products. Hemicelluloses are a group of relatively short-chained amorphous polysaccharides spanning several hundred to a few thousand monomer units. In contrast to cellulose, the chains may be branched and can be divided into different structural types which are discussed in detail elsewhere [125]. Within plant cell walls, the macrofibrils consist of crystalline cellulose fibrils embedded within a matrix of hemicellulose and lignin [126]. Lignin, a complex polymer consisting of heterogeneously bonded phenylpropane units, can account for up to 30 % of the mass and is primarily found in the outer layers of plant cell walls [103,127]. The content of lignin within paper decisively affects its properties, as lignin can interfere with the bonding of cellulose, leading to increased rigidity, but reducing strength and durability. Also, within plant cells, it binds the cellulose fibrils

together, which can impede pulping, and, when exposed to air, lignin attains a yellow stain. Hence, to obtain pure cellulose pulp for high-quality paper, most of the lignin has to be removed during processing [103]. Depending on the source wood, the pulp may also contain small amounts of resins and waxes, which are generally not desired in the final product and can interfere with lignin removal [128]. Finally, some inorganic compounds, such as CaO, MgO, K_2O, silicates, and sulfates, are typically found in wood, usually comprising 0.5-1.5 %. Upon combustion, they are the only substances to remain, which is why they are referred to as ash. Similar to the other components of plant matter, the ash content is highly variable across different parts of a plant, between distinct species, and with the location of growth [103,129]. Consequently, the intrinsic ash content of a paper depends on the type and origin of pulp source used. Overall, a high content of α-cellulose fibers with high aspect ratio and low contents of other compounds is beneficial to producing papers, which is why some raw materials are more suitable than others. An important example are the seed hairs of the cotton plant, which are almost pure high aspect-ratio cellulose fibers with exceptional mechanical properties.

On the macroscopic level, the attributes of papers are defined by the arrangement of the cellulose fibers, that is their orientation, the packing density, and the porosity between them. As stated above, various kinds of additives are deployed during paper processing, which can be roughly divided into mineral additives, such as carbonates, clay, and gypsum, and chemical additives, such as starch, polymers, resins, and dyes, providing means to adjust and enhance the properties of the product. Hence, most papers contain up to large amounts of filler substances, depending on the intended application.

2.2.2 Thermal Decomposition of Cellulose-based Papers

Pyrolysis denotes the thermal decomposition of a substance in the absence of an oxidizing agent and hence, without the occurrence of combustion processes. The thermal decomposition of cellulose-based organic papers is a complex process that involves a series of reactions leading to the formation of a variety of products [130]. The compounds generated upon decomposition depend on a variety of factors, including the heating rate, duration, temperature, pressure, and the type of cellulose.

The pyrolytic decomposition of cellulose can be divided into three stages: dehydration, depolymerization, and decomposition [131]. In the first stage, dehydration of cellulose leads to the release of water due to the breaking of hydrogen bonds between the cellulose molecules, which typically occurs between 100 and 200 °C associated with a significant mass loss [132]. The second stage of cellulose decomposition is the depolymerization of polymeric cellulose chains. Here, the glycosidic bonds between the glucose units of cellulose are broken, leading to the formation of smaller molecules such as levoglucosan, which is a major product of cellulose pyrolysis [133]. The depolymerization temperature of cellulose is typically between 200 and 350°C [130]. The final stage is the decomposition of the depolymerized products, which are further degraded to form a variety of volatile and non-

volatile compounds, including gases, tar, and char, generally needing temperatures between 350 and 500 °C to take place [132]. The gases produced include carbon monoxide, carbon dioxide, and some hydrocarbons, such as methane, ethylene, and acetylene, while tar is a complex mixture of several organic compounds, such as phenols, aldehydes, ketones, and furans [133]. Finally, char is the solid residue that remains after the volatile gases and tar have been released, mainly composed of pyrolytic carbon and any inorganic substances present in the paper. An overview of the different carbon-containing pyrolysis products of cellulose is displayed in Fig. 2-9.

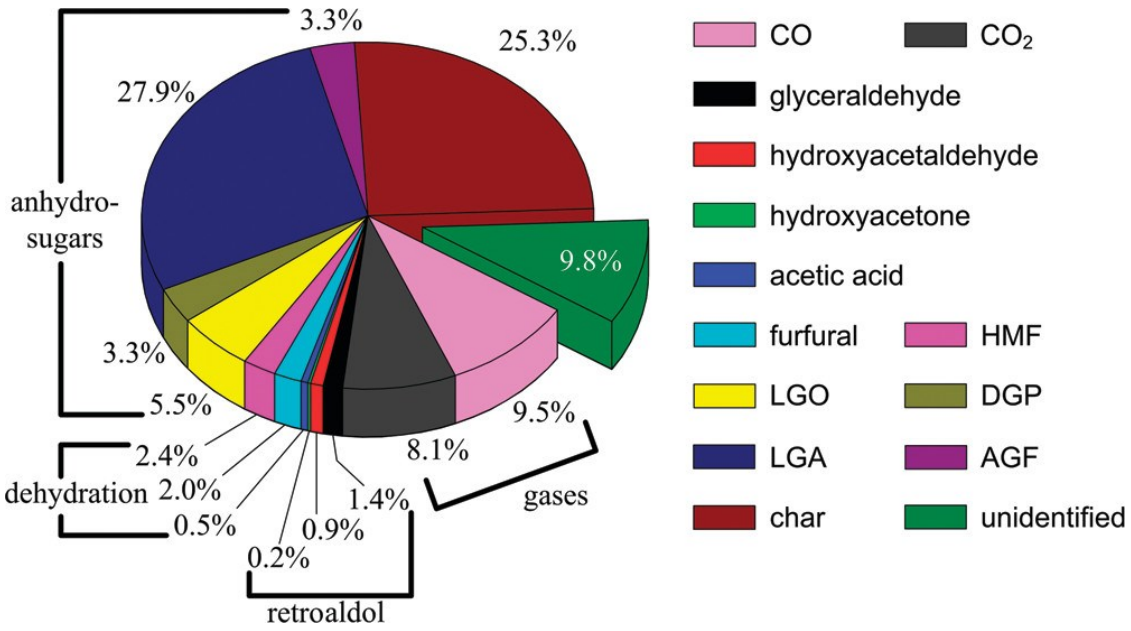

Figure 2-9: Detailed quantification of the carbon-containing pyrolysis products of cellulose as detected via pyrolysis-coupled gas chromatography-mass spectrometry (GC-MS). Besides char (25.3 %), mainly CO_X gas (17.6 %), and various anhydrosugars (40 %) form upon pyrolysis with a heating rate of 150 K min^{-1} [HMF = hydroxymethylfurfural; LGO = levoglucosenone; DGP = dianhydroglucopyranose; LGA = levoglucosan; AGF = anhydroglucoforanose]. Reproduced from [130].

The heating rate can have a significant impact on the pyrolytic products of cellulose. At higher heating rates, the cellulose undergoes rapid pyrolysis, resulting in the generation of more gaseous compounds. Conversely, slower heating rates can lead to more extensive decomposition of the cellulose, producing more tar and char [134,135]. Also, the maximum temperature plays a critical role in the pyrolysis of cellulose, with higher temperatures promoting rapid decomposition, resulting in the release of more volatile gases and less char. Likewise, lower temperatures can lead to more extensive decomposition of the cellulose, favoring the formation of tar and char. Moreover, the maximum temperature affects the composition of the pyrolytic products. For example, at higher temperatures, there is a greater likelihood of cracking reactions, leading to the production of smaller, more volatile compounds [136]. Also, longer heating times can lead to more extensive decomposition of the cellulose, resulting in the production of more tar and char. However, longer heating times can also lead to the degradation of pyrolytic products, resulting in the formation of smaller, more volatile compounds [137].

Furthermore, other components in the paper matrix, such as lignin and hemicellulose, may also affect the composition of the pyrolytic products of cellulose. For instance, lignin is known to promote the formation of polycyclic aromatic hydrocarbons (PAHs), whereas the less stable hemicellulose typically is the first compound to undergo decomposition [138] resulting in the generation of acetic acid, which in turn promotes levoglucosan formation [133]. Hence, the source and quality of the cellulose can have a significant impact on the pyrolytic process, as cellulose derived from different plants can have varying chemical compositions, resulting in different products. For instance, softwood-derived papers tend to yield more tar than hardwoods, while cellulosic cotton fibers release more carbon monoxide during pyrolysis [139]. Finally, impurities can have a significant impact on the pyrolytic decomposition of cellulose-based papers; for example, the presence of inorganic materials, such as clay minerals or calcium carbonate, can act as a catalyst, promoting the formation of char and reduce the yield of volatile gases [140,141].

The pyrolysis of cellulose-based organic papers has several practical applications. One important application is the production of biofuels, including gasoline, diesel, and jet kerosene, for which levoglucosan, a major product of cellulose pyrolysis, is an attractive precursor [133]. Additionally, as the carbon resulting from the pyrolysis of cellulose can exhibit high porosities and surface area, the process is an important way of producing activated carbon that is used in a variety of applications, such as water treatment, air purification, and energy storage [142,143]. Furthermore, the nanostructural characteristics of the carbon product can be affected by adjusting the pyrolysis parameters. Low-temperature pyrolysis, for instance, was shown to result in less porous amorphous residue, whereas higher temperatures promote graphitization and micropore formation.

2.3 Ceramic Papers

As described above, cellulose-based organic papers possess an extraordinary set of properties, which conferred a revolutionary role in certain aspects of cultural, social, and technological development upon them. However, the intrinsic properties of cellulose-based papers entail fundamental weaknesses with respect to many application fields. For instance, their high flammability and hydrophilicity make them susceptible to damage and degradation in some environments, which, although measures are explored, are hardly overcome. Unsurprisingly, developing paper-like materials composed of non-organic substances, with a similar set of properties but offset drawbacks has attracted the attention of many researchers. Materials composed of inorganic components such as glass, metal, or ceramic fibers, possessing a paper-like structure are generally referred to as inorganic papers. Uniting the unique structure of regular organic papers with the properties of a wide range of materials such as carbon fibers and nanotubes, mullite, silica, and others, within the context of this exciting material class, various interesting two-dimensional materials have been developed in recent years.

Papers produced from ceramic compounds are often employed as refractory insulators due to their excellent temperature stability and chemical resistance, while some can exhibit desirable mechanical properties reminiscent of cellulose-based papers, such as flexibility or high tensile strength [1,144,145]. Moreover, like their monolithic counterparts, the capabilities of ceramic papers can be tuned via their compounds, allowing functionalization such as for electromagnetic shielding, sensing purposes, and even energy storage to be imparted to the material [146–148]. The inherently high surface area and hierarchical architecture of paper-like materials result in excellent adsorption and filtration behavior, which makes them predestined for use in air and water purification, or as catalyst support materials [144,149–151]. Some typical compounds from which ceramic papers have been successfully produced are SiC, SiO_2, manganese oxides, and hydroxyapatite nanowires (HAPNW) [148,152–154]. HAPNW-based papers in particular were shown to have intriguing properties, such as pronounced mechanical flexibility, flame resistance, and biocompatibility [144,155]. Moreover, such papers are processed from abundant and non-toxic resources, are ideal to be written and printed on due to their white color, and can act as adsorbents for organic pollutants [144].

Producing papers from two or more raw materials has been subject of intensive research and led to the creation of various interesting composite papers with engaging properties and multifunctionality. Many different components, such as HAP, SiC, glass, and cellulose fibers as well as carbon nanotubes, and graphene or graphene oxide sheets have been successfully combined within hybrid paper-like materials, exhibiting interesting properties and unique structures. For instance, papers consisting of glass fibers coated with a network of ultralong HAPNW were shown to have exceptional flexibility, tensile strength, and thermal stability, compared to pure glass fiber papers [155]. Other interesting examples are HAPNW/graphene oxide papers with thermosensitive capabilities [154], thermally stable and insulating HAPNW/silica aerogel composites [156], hierarchically structured SiC/graphene papers for heat dissipation [157], and even paper-like composites utilizing 2D-materials such as a Ti_2C/carbon nanotube paper with promising electrochemical properties for battery technology [158]. Moreover,

concerning pollutant remediation and catalysis, ceramic (composite) papers provide ideal support for catalytically active compounds, due to their hierarchical porous structure. For example, catalytic degradation of toxic chemicals has been realized by HAPNW-based papers loaded with different active nanoparticles, such as Au or Ag_3PO_4.[159,160]. A highly designed flexible ceramic paper composite consisting of SiO_2/Al_2O_3 ceramic fibers strengthened through the addition of cellulose fibers and a CeO_2 binder was shown to be a promising support material for Co-catalyzed diesel soot combustion [161]. In each case, a key feature of ceramic papers in this context is their unique hierarchical pore structure, which enables controlling permeation and transportation rates of fluids and gases, while also providing a high surface area [162].

Clearly, ceramic paper research provides diverse directions for functionalization and deployment in several application fields. However, while the process of making organic cellulose-based papers has been perfected over the course of centuries, the synthesis of ceramic (composite) paper-like materials is comparably young and can differ considerably depending on the raw materials processed and the structural settings desired. Hence, in the following, a brief introduction to some established and novel approaches to accessing ceramics with paper structure is presented.

2.3.1 Classic Approaches to the Fabrication of Ceramic Papers

Manufacturing paper-like ceramics usually involves processing fibrous or wire-like ceramic compounds into sheets, often aided by the addition of binders, pressing, or calcination. As pointed out above, ceramic papers have been successfully produced from various components. However, a restricting factor is the availability of ceramic materials with a wire-like morphology, which is often challenging and costly to achieve. Since ceramic fibers are compulsory for many advanced composite materials, intensive research has been conducted on synthesis procedures and property optimization. Most studies are concerned with fibers composed of simple oxides, carbides, and nitrides, such as SiO_2, Al_2O_3, MnO_2, SiC, ZrC, BN, or Si_3N_4, but also more complex compositions, such as mullite, SiAlON, or $SiBN_3C$. To obtain ceramic fibers and nanowires, a range of techniques such as centrifugal-, solution blow-, and electrospinning are established, but also chemical vapor- (CVD), and atomic layer deposition (ALD) have been successfully deployed. Some compounds can be processed into ceramic fibers via self-assembly, while a comparably novel, yet capable approach is via the PDC route. Each processing method comes with certain advantages and drawbacks, as summarized in Tab. 2-1 [163]; for instance, centrifugal spinning allows for high-throughput fiber preparation from ceramic melts but is highly energy-intensive and can only produce fibers with relatively high (> 1 µm) diameters. Electro- and solution blow spinning of preceramic fibers and subsequent calcination enables precise control over the fiber properties but has a low rate of production. Combined with PDC technology, spinning methods can be used to access homogeneous complex fiber compositions, which can exhibit properties highly attractive for technical application in ceramic composites

[164,165]. CVD is capable of producing SiC and Si_3N_4 nanowires with very small diameters, self-assembly of certain molecule species is an elegant way of preparing homogeneous nanoribbon-based aerogel-type materials and ceramic membranes [153,166], and ALD can generate hollow fibers through coating and subsequent removal of the template material. These three approaches, however, are limited with respect to the material system they can be applied to and are too complex and inefficient to meet industrial requirements at present. Also, the properties of ceramic papers are inevitably coupled with those of the ceramic fibers used. For instance, the diameter and aspect ratio of HAPNWs or SiC-NWs strongly affects the flexibility of corresponding papers [144,167,168]. Hence, both the applicability of further processing, such as compression, and certain performance criteria of the resulting ceramic paper require fibers with adequate properties to be available.

Table 2-1: Overview of different techniques used to prepare ceramic fibers including advantages, disadvantages, typical fiber diameters achieved, and their industrial prospect. Redrawn from [163].

Method	Type	Advantages	Disadvantages	Fiber diameter	Industr. prospect
Centrifugal spinning	Melt	High efficiency	Poor flexibility	> 1 µm	High
	Solution	Efficiency / broad material choice	Polymer removal	Tens of nm to a few µm	Relatively high
	Sol	Efficiency; yield, polymer-free	Varying diameter	Hundreds of nm to several µm	Relatively high
Electrospinning	Solution	Versatility, uniformity	Low efficiency, polymer removal	Tens of nm to a few µm	Relatively low
	Sol	High yield, polymer-free	Varying diameter	Tens of nm to a few µm	Relatively low
Solution blow spinning	Solution	Simple & safe; efficient, versatile	Polymer removal	Tens of nm to a few µm	Relatively high
Self-assembly	Solution	Ribbon structures	Limited material choice	Tens of nm to a few µm / few nm	Low
Atomic layer deposition	Solution	Hollow well-defined structures	Complicated; limited material	Tens of nm to a few µm	Low
Chemical vapor deposition	Gas	Uniform; non-oxide components	Inefficient; limited material choice	Tens to hundreds of nm	Low
Polymer conversion	Solution	Non-oxide components	Low efficiency; inert atmosphere.	Tens of nm to a few µm	Relatively low

Regardless of the fiber synthesis technique used, to obtain ceramic papers, typically additional processing steps have to be employed. In some cases, a paper-like arrangement of the compounds can be achieved without extra steps, as exemplarily shown in Fig. 2-10 for ZrO_2-based papers prepared via solution blow spinning [151]. In this study, the preceramic fibers were deposited on a roller collector, and the resulting fabric was converted into a ceramic paper via calcination. Another example is a flexible multifunctional membrane prepared from self-assembling ultralong MnO_2 nanowires, which merely have to be vacuum filtrated to obtain a paper-like arrangement kept together by hydrogen bonding [153]. In the majority of cases however, the addition of binder additives [161], compression [148], high-temperature calcination [157], or combinations thereof [150,169] is necessary to achieve cohesion between the ceramic fiber compounds. Hence, to access ceramic materials with paper-like morphology, usually, a series of preparative steps have to be executed, which drives up production costs limiting their attractiveness for application.

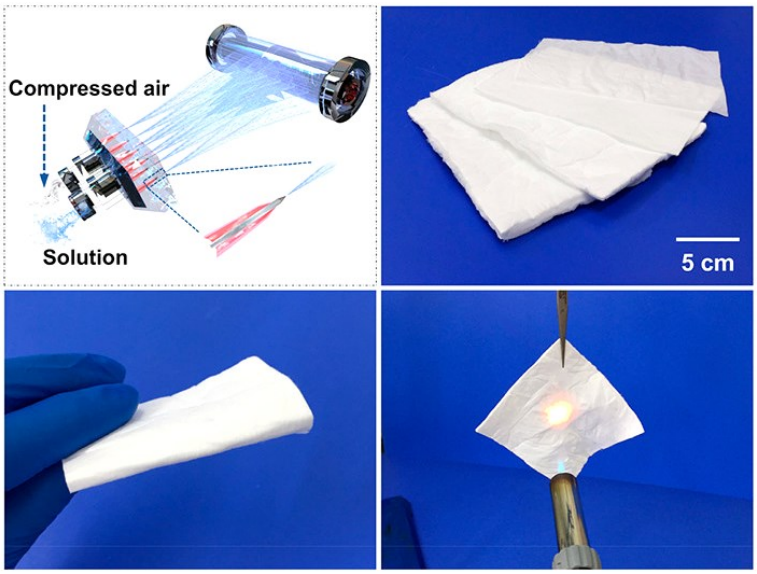

Figure 2-10: Example of a foldable all-ceramic Al_2O_3-stabilized ZrO_2 filter paper prepared via solution blow spinning. The thermal stability of the paper enables it to be deployed as high-temperature air particle filter, for instance, within exhaust gas purification systems. Reproduced from [151].

2.3.2 Template-assisted Synthesis of Ceramic Papers

A fundamentally different approach to accessing ceramics with paper-like structures is the use of morphological templates. The general idea of templating is to transfer a certain structure or morphology from one material onto another, which, as outlined at the beginning of this work, is closely related to the naturally occurring phenomenon of pseudomorphosis.

In mineralogy, the umbrella term denotes several distinct mechanisms that lead to the conversion of one mineral into another while fully or partially retaining the original morphology. Most famous is the so-called substitution pseudomorphosis (compare Fig. 2-11 a) being the allochemical transformation of one mineral into another, often realized by the dissolution of the primary phase alongside simultaneous replacement with a newly formed phase [9,10]. Intriguingly, not only minerals can be replaced, but also other objects have been reported to have conferred their morphology and structural attributes onto mineral phases. This often is observed in fossils, such as silicified

wood, pyritized ammonites, and opalized bones, in which fine microstructural features can be preserved during replacement by the respective mineral. For instance, silicification of wood, that is replacement of the plant tissue by amorphous SiO_2, sometimes results in conserved cell structures, as shown in Fig. 2-12 a, down to a sub-micrometer scale [170]. Many chemical compounds can exist in more than one single stable crystal structure depending on the physicochemical conditions. The different modifications are called allotropes (for elements) or polymorphs (for any compound) and can exhibit immensely different properties and macroscopic morphologies. Examples of famous (and industrially important) polymorphous substances are the two principal structures of carbon, graphite ($P6_3/mmc$) and diamond ($Fd\bar{3}m$), or the three modifications of TiO_2, rutile ($P4_2/mnm$), anatase ($I4_1/amd$), and brookite ($Pbca$). Changing temperature or pressure results in an isochemical change of the crystal structure towards the corresponding stable modification. In some cases, this does not lead to a simultaneous change of the morphology, resulting in a so-called paramorphosis (ancient Greek: παρά – besides). In nature, paramorphs are rather common, and many mineral specimens, although appearing as a distinct polymorph, in fact, are the variant stable at ambient conditions. For instance, aragonite ($CaCO_3$, $Pmcn$) is metastable at atmospheric pressure and slowly forms a paramorphosis by transforming into calcite ($CaCO_3$, $R\bar{3}c$), without changing its typical pseudohexagonal morphology (Fig. 2-11 b). Another interesting type is the so-called peri- or epimorphosis (περί - around; επί- on top of) which describes the incrustation of a mineral A with a mineral B and consecutive dissolution of A. As a result, a hollow structure mimicking the original morphology of mineral A is left behind that may or may not be subsequently filled with another mineral (Fig. 2-11 c). Many examples of quartz coatings encasing various minerals such as baryte, fluorite, or calcite are known, sometimes closely resembling the original morphology [9,10].

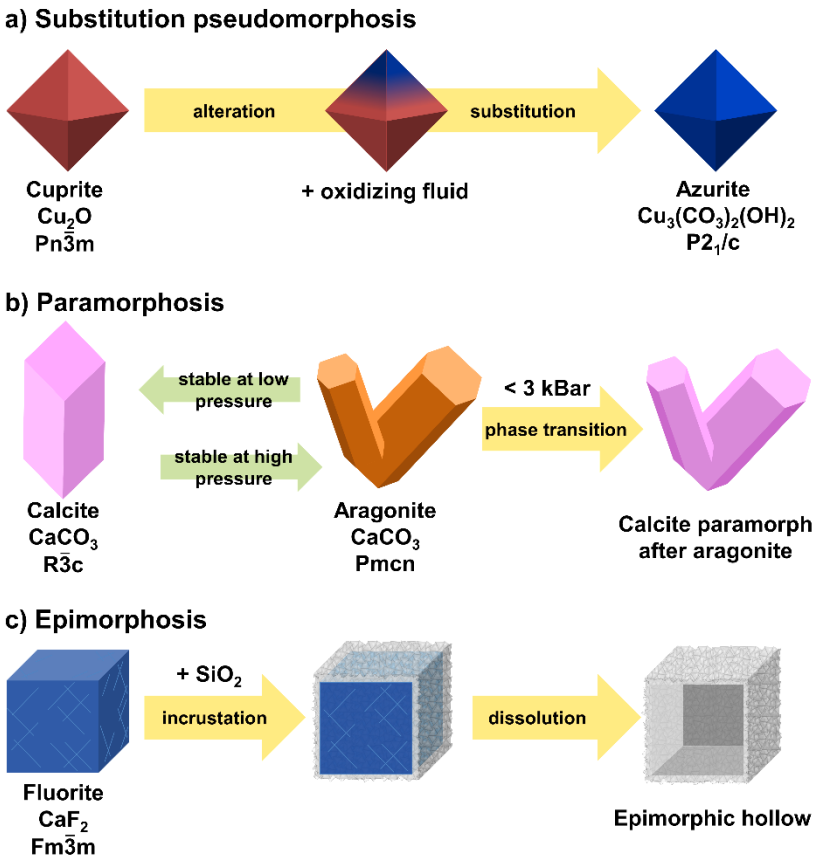

Figure 2-11: Schematic illustrating the types of pseudomorphous mineral conversion mechanisms substitution pseudomorphosis (a), paramorphosis (b), and epimorphosis (c).

The mechanisms of pseudomorphosis have attracted the interest of researchers seeking convenient and applicable ways of imparting specific structures and morphologies onto various material systems, which are difficult or even impossible to obtain using conventional techniques. Templating has proven feasible for the preparation of porous ceramics with

well-defined pore architectures. As some biological substances exhibit unique and complex structures accounting for highly attractive material properties, a whole class of materials revolves around transferring the architecture of some biological substances, such as wood or cork, onto ceramic systems. Several 'biomorphic' ceramics have been prepared by liquid- or gas-phase infiltration of biocarbon templates obtained from pyrolysis of different wood types. The method is applicable to access ceramics composed of, for instance, SiC, Si/SiC, TiC, TiO_2, Al_2O_3, ZrO_2, and complex compositions, such as hydroxyapatite (compare Fig. 2-12 b-d), with a cellular hierarchical pore structure inherited from their respective template [171–177]. The infiltration method is an important tool to tailor the composition and phase assemblage of biomorphic ceramics. Liquid melt infiltration typically leaves pores filled with material, which has to be etched in an additional treatment step, whereas gas-phase infiltration results in unconfined pores and can be used to precisely adjust the molar ratios of resulting phases and microstructural parameters [178,179]. Moreover, sol-gel infiltration of biocarbon templates with suitable precursors can be used to obtain biomorphic carbide or oxide ceramics, depending on whether carbothermal reduction or calcination in air is applied [180–182].

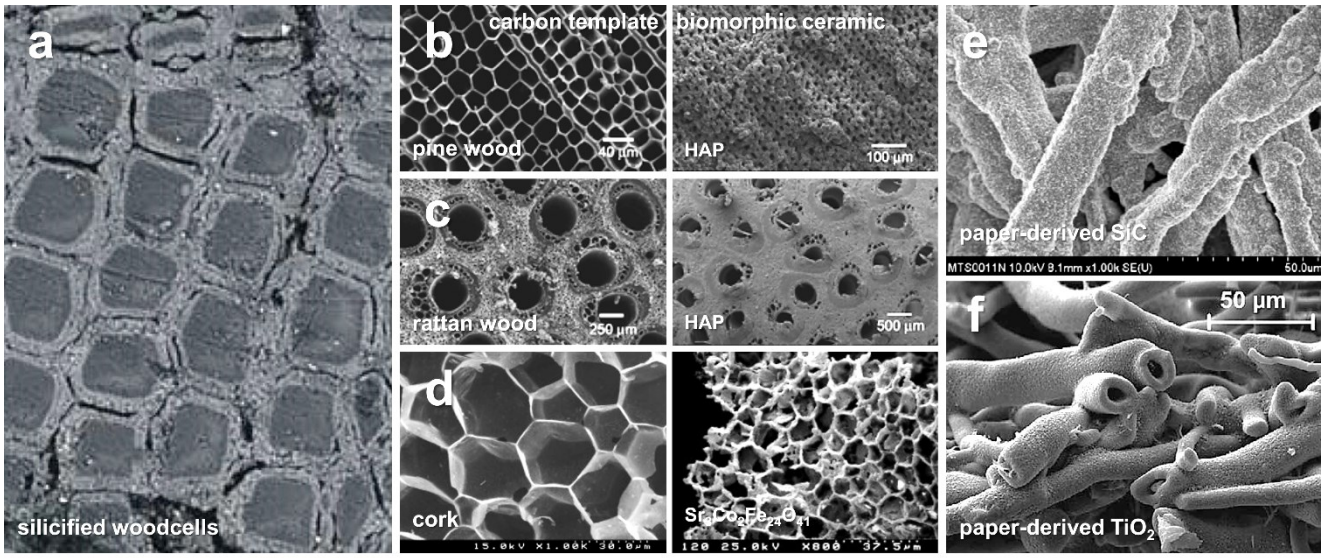

Figure 2-12: Examples of some pseudomorphic materials with their structure inherited from biological matter. SEM image of naturally silicified cells in a fossil wood specimen (a). Two examples of biomorphic HAP ceramics prepared from pine (b) and rattan wood-derived carbon templates (c), respectively. Complex magnetic SrCoFeO-hexaferrite ceramic with cellular microporous structure synthesized from sol-gel infiltrated carbonized cork (d). SiC- (e) and TiO_2-based (f) fibrous ceramics accessed through reactive gas-phase infiltration of carbonized paper templates. Images reproduced from [170,177,183–185].

Similarly, the production of fibrous ceramics has been reported in several cases via infiltration of biocarbon templates derived from wood pulp or cellulosic fibers. The principles applied are the same in that a specific structure, i.e. the fiber morphology of the paper template, can be conveniently transferred onto a ceramic system without the need for the above-mentioned elaborate ceramic fiber preparation routes. For instance, SiC-based ceramics prepared from paper-derived carbon templates have been successfully produced via chemical vapor

infiltration reaction (CVI-R) with methyltrichlorosilane [184,186]. After a consecutive heat-treatment step, the carbon fibers are entirely converted into a porous SiC ceramic with a fiber structure inherited from the paper-derived template, shown in Fig. 2-12 e. Employing the same procedure, TiC-based ceramics with paper structure were prepared, which could be converted into TiO_2 papers (shown in Fig. 2-12 f) simply by high-temperature oxidation [185,187]. In the same group, SiC/Si_3N_4-based paper-like composites have been successfully produced by thermal treatment of methylchlorosilane-infiltrated carbonized paper templates and subsequent heat treatment in nitrogen atmosphere [188]. Depending on the temperature, either β-Si_3N_4 or α-Si_3N_4 whiskers were generated on a SiC matrix, affecting the flexibility and oxidation resistance of the paper-like ceramics, thus offering ways to adjust the material properties with respect to high temperature applications.

The use of pristine (non-carbonized) paper fibers for templating, has been less popular among researchers in the past but has attracted great attention recently. Inspired by traditional paper-making processes, preceramic papers have been investigated as a method to prepare paper-like ceramics with adaptable structures and properties. Greil and Travitzky et al. coined the term denoting a hybrid material class consisting of organic paper fibers loaded with inorganic filler materials, which, upon thermal treatment, can be converted into ceramic materials [145]. Resembling the preparation process of organic papers, preceramic papers are produced from a suspension of cellulose fibers containing large quantities of inorganic fillers, to which polymeric binders are added. Then, continuous preceramic paper sheets are produced from the solution by dewatering, pressing, and drying in a paper sheeting machine (compare Fig. 2-13 a-b). The properties of the hybrid material, such as porosity, smoothness, stiffness, and others, highly depend on the bonding between the fibers and are thus designable through the inorganic filler content, which also decisively affects the ceramic yield and porosity of the resulting ceramics. Various paper-like ceramic materials based on, for instance, Al_2O_3, ZrO_2, SiC, and HAP, have been successfully synthesized employing the preceramic paper approach [189–191]. The attractive processability and designability of preceramic papers coupled with the use of well-established paper processing technologies were shown to offer outstanding potential for economical manufacturing of ceramic objects with complex morphologies, such as corrugated structures and multilayer components, as shown in Fig. 2-13 c-f [145].

Similar to biocarbon templates prepared from paper, regular organic papers have been successfully employed as morphological templates for producing paper-like ceramic materials in recent years. Many studies are concerned with sol-gel infiltration of cellulose-based templates, which can then be calcined to obtain morph-genetic ceramics. A rather early study reports on the synthesis of biomorphic Al_2O_3 ceramics from alumina sol infiltrated cotton fibers upon calcination at 800 °C and subsequent functionalization with Ag nanoparticles [192]. The authors recognized that the organic fibers almost exclusively composed of cellulose provide numerous anchoring sites for the oxide precursors due to the abundance of functional -OH surface groups. Almost simultaneously, the preparation of an AlN/C composite paper from alumina-infiltrated filter paper and subsequent carbothermal nitridation was reported [3]. Again, the high amount of hydroxyl groups present on the surface of cellulose fibers was reported to provide suitable adhesion of the sol, resulting in the generation of a well-defined core-shell structure composed of graphitic carbon coated with a thin AlN layer. Other materials prepared via sol-gel

infiltration of organic fibers are anatase (TiO_2), SnO_2/C, SiO_2/C, Ag/Si/C, TiO_2/Si, and many others, most of them within the last decade and aimed towards being deployed in battery technology [193–197].

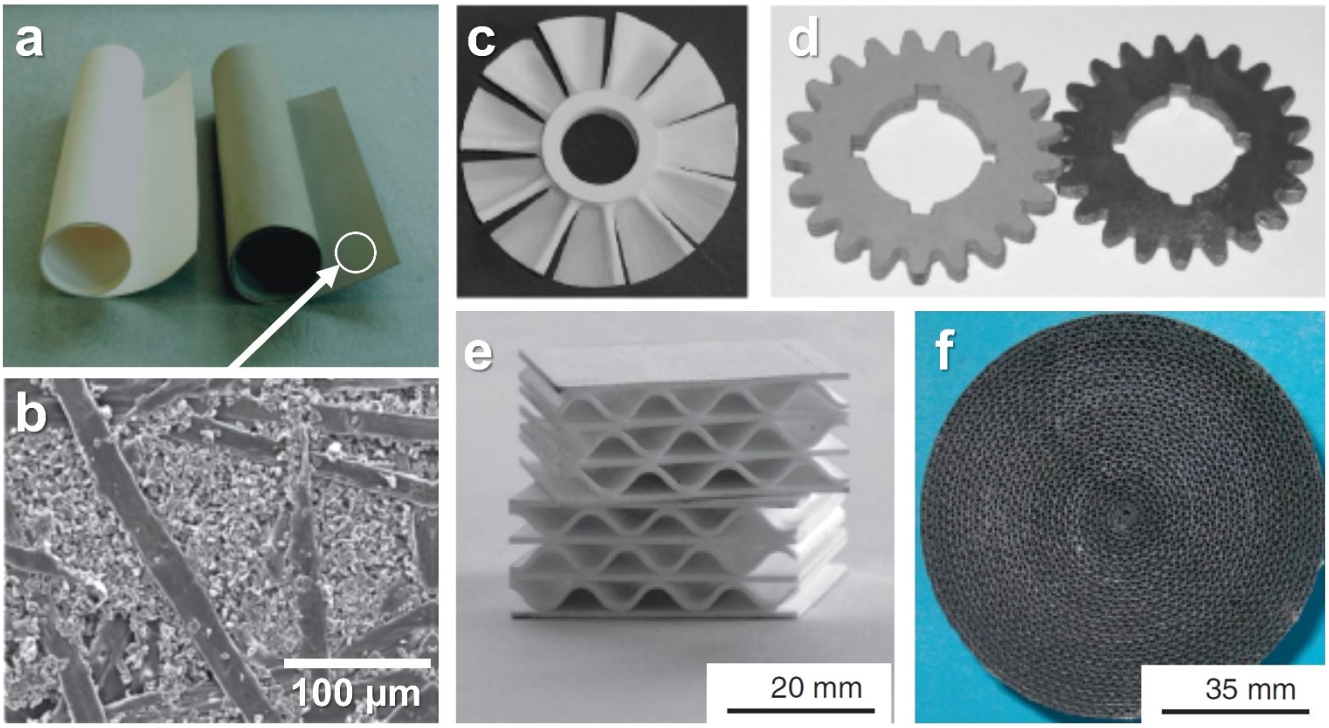

Figure 2-13: Photograph of Al_2O_3 (left) and SiC-filled (right) preceramic paper rolls (a). The SEM micrograph (b) shows the corresponding microstructure of the hybrid papers with inorganic filler particles in between cellulose fibers. Several examples of ceramic objects with complex morphologies derived from multilayer preceramic papers: an Al_2O_3 turbine rotor (c), SiC-based gear wheels (d), corrugated Al_2O_3 heat-exchanger (e), and SiC catalyst carrier roll (f). Reproduced from [145].

Using preceramic polymers instead of sols is a similar, yet much less investigated approach to preparing ceramic materials from infiltrated cellulose-based papers. Very early works were conducted in the working group around Greil, exploring the possibility of generating ceramics with corrugated structure from cardboard dip-coated in a polymer/metal filler slurry and subsequent pyrolysis [198,199]. The resulting SiAlON/SiC and $SiO_2/Al_2O_3/Al_6Si_2O_{13}$ ceramics retained the macroscopic morphology of the cardboard template, which was recognized to have immense potential for accessing ceramics with unique cellular pore architecture. However, the fibrous paper structure of the template was not found to be preserved, hence the resulting ceramics do not exhibit the typical characteristics of ceramic papers. Much later, the concept of producing ceramic papers from organic paper templates infiltrated with a polymeric single-source precursor (SSP) was revisited reporting on the successful synthesis of a C/SiFeN(O)-based ceramic composite [4]. Upon reactive ammonolysis at 1000 °C, the cellulose-based filter paper impregnated with a Fe-modified perhydropolysilazane (PHPS) precursor was converted into a ceramic material exhibiting the hierarchical morphology of the template. Subsequent annealing at 1200-1400 °C in N_2 atmosphere led to the generation of ultra-long Si_3N_4 nanowires on the paper surface, which was attributed to an Fe-catalyzed VLS process. These results highlight that chemical modification of the molecular

precursor and varying certain processing parameters may provide facile options for producing functionalized ceramic papers with a well-defined structure and adaptable phase composition, being of interest for various potential applications. However, while the study provided interesting insights into the phase evolution and microstructure of such polymer-derived ceramic papers (PDCPs), some fundamental questions remained, triggering consecutive investigations of the underlying principles. Specifically, the mechanisms of the morphology transfer, the temperature-dependent microstructure evolution of the ceramic composites, and the impact of varying certain synthesis parameters, such as precursor composition and pyrolysis atmosphere, on the characteristics of the ceramic papers need to be understood. Hence, the present research aims to address these and other questions in order to develop a comprehensive understanding of the decisive parameters that can be used to tailor the structure and properties of PDCPs to the needs of future applications. Within the context of this and the complementary thesis associated with the same project [8], three publications report on and discuss the results concerning synthesis, microstructure characterization, phase assemblage, and functionalization of various PDCPs [6,7,200].

3 Experimental Procedures

3.1 Synthesis of Polymer-derived Ceramic Papers

All samples investigated in the present research project were synthesized by Alexander Ott in the working group Dispersive Solids of the Technische Universität Darmstadt under the supervision of Prof. Dr. Ralf Riedel. For the preparation of the polymer-derived ceramic papers (PDCPs), a one-pot synthesis approach was employed, in line with the procedure utilized during preceding studies of this novel material class [4,5].

The PDCPs are prepared by dip-coating regular cellulose-based paper templates with polysilazane-based preceramic polymers followed by thermolysis, as schematically depicted in Fig. 3-1. First, a pristine paper is dipped into a transition metal-modified single-source precursor (SSP) and dried to yield a polymer-coated preceramic paper. Subsequently, polymer-to-ceramic conversion is facilitated via pyrolysis at up to 1000 °C, leading to the formation of pseudomorphic ceramic composites with a morphology inherited from the paper template. Finally, annealing at 1300 °C of the as-pyrolyzed ceramic papers is carried out, to induce the formation of functional crystalline phases. In the following, the materials and parameters applied to the individual synthesis steps are briefly described.

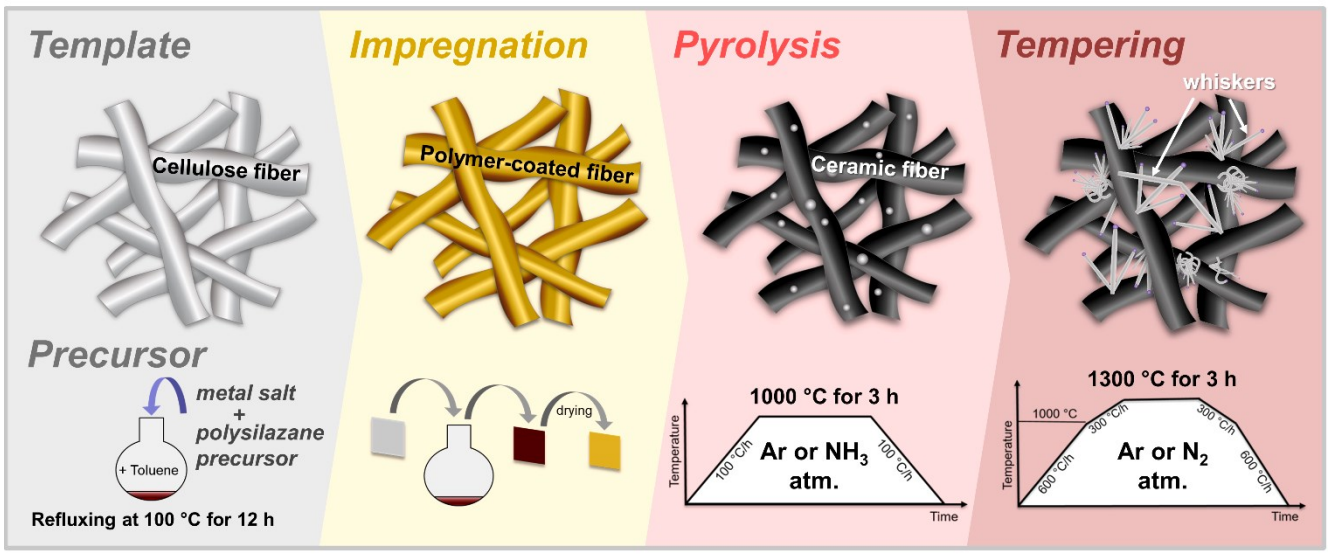

Figure 3-1: Schematic depiction of the synthesis approach to access polymer-derived ceramic papers employed in this study. A preceramic polysilazane polymer is refluxed with a metalorganic compound to yield a transition metal-modified crosslinked SSP. Dip-coating of a precut cellulose paper template with the precursor solution leads to polymer-coated preceramic papers, which are dried and subsequently pyrolyzed at up to 1000 °C in either Ar or NH_3 atmosphere, with the heat-treatment inducing polymer-to-ceramic conversion, leading to pseudomorphic ceramic composites. In the last step, the PDCPs are functionalized with crystalline phases via tempering at 1300 °C in either Ar or N_2 atmosphere. Adapted and expanded from [6,7].

3.1.1 Synthesis of the Metal-modified Single-Source Precursors

For the synthesis of the preceramic SSPs, two different organosilicon polymers, Durazane 2250 and Durazane 1800 (Sigma-Aldrich, St. Louis, USA) were used. As depicted in Fig. 3-2, the former is a pure perhydropolysilazane (PHPS) consisting exclusively of the $[H_2Si\text{-}NH]_n$ backbone, while the latter is an organopolysilazane, with additional methyl and vinyl groups attached to Si sites. In order to homogeneously incorporate transition metals into the polymer, modification of the precursors is done in their polymeric state by the addition of metalorganic acetylacetonate compounds. For each polysilazane, one of the three transition metals Fe, Ni, and Pd was introduced in the form of iron(III)acetylacetonate (Fe(III)$acac_3$), Ni(II)$acac_2$, or Pd(II)$acac_2$ (Merck KGaA, Darmstadt, Germany). Detailed information on the materials used is given in [8].

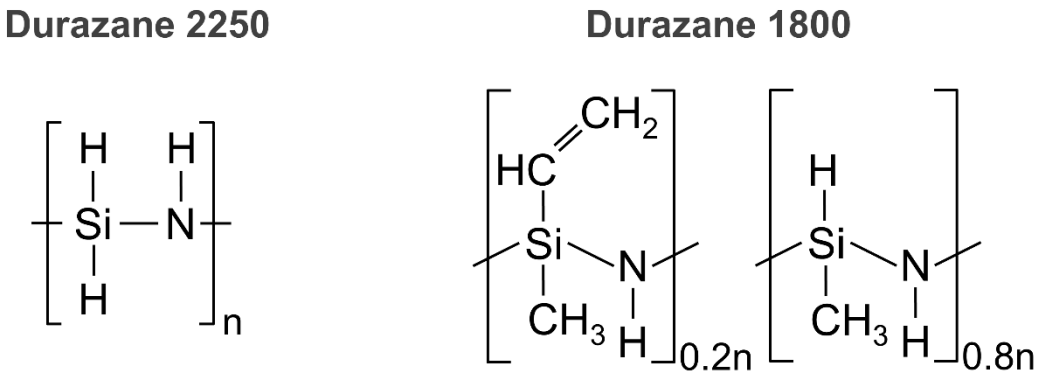

Figure 3-2: Simplified depiction of the perhydropolysilazane (Durazane 2250) monomer and an organopolysilazane (Durazane 1800) comonomer structure. While the former has only hydrogen attached to the Si-N backbone, the latter contains additional -CH_3 (methyl) and -$CH{=}CH_2$ (vinyl) groups at the Si sites.

The preparation of the SSP was done after the following scheme: As Durazane 2250 readily reacts with ambient moisture, it comes dissolved in di-n-butylether as a 20 wt.-% solution. Filled into a round-bottom flask, the solvent is removed via Schlenk technique in Ar atmosphere for 3 h. In the case of Durazane 1800, this step is omitted. The pure precursor is dissolved in anhydrous toluene (99,8 %, Merck) and one of the three metalorganic compounds is added. Solubility in toluene varies considerably between the different acetylacetonates hence, solvent amounts and polysilazane/acetylacetonate ratios were adjusted accordingly, as thoroughly described in the doctoral thesis of Alexander Ott [8]. Finally, the mixture is refluxed at 100 °C for several hours to improve homogenization through crosslinking reactions. Nevertheless, even upon crosslinking for 12 h, the reaction in each precursor system was found to be incomplete, particularly when Ni(II)$acac_2$ and Pd(II)$acac_2$ were added, with some unreacted metalorganic compounds suspended within the precursor.

According to the literature, two distinct mechanisms may facilitate molecular bonding between PHPS and a metal acetylacetonate. As displayed in Fig. 3-3, either a substitution reaction at the Si-H groups takes place (A) forming Si-Fe, or in the presence of moisture traces, Si-O-Fe linkages accompanied by the release of an acetylacetonate

ligand, or hydrosilylation of the C=O groups (B) is catalyzed by the metal species, resulting in the formation of Si-O bonds. Previous studies have found experimental evidence of both possible reaction pathways, yet did not provide a conclusive statement on the exact nature of the reaction [4,6]. Therefore, it is assumed that both interactions will occur, potentially affecting the carbon and oxygen content of the resulting metal-modified SSP. As it was proposed that only the Si-H sites will be involved in the above-mentioned reactions, while N-H will not, in the case of the Si-C bond containing Durazane 1800, generally fewer sites per fundamental unit can take part in the modification with the metal acetylacetonates. This could affect precursor composition and homogeneity, which, however, was not evidenced by existing results [6,8].

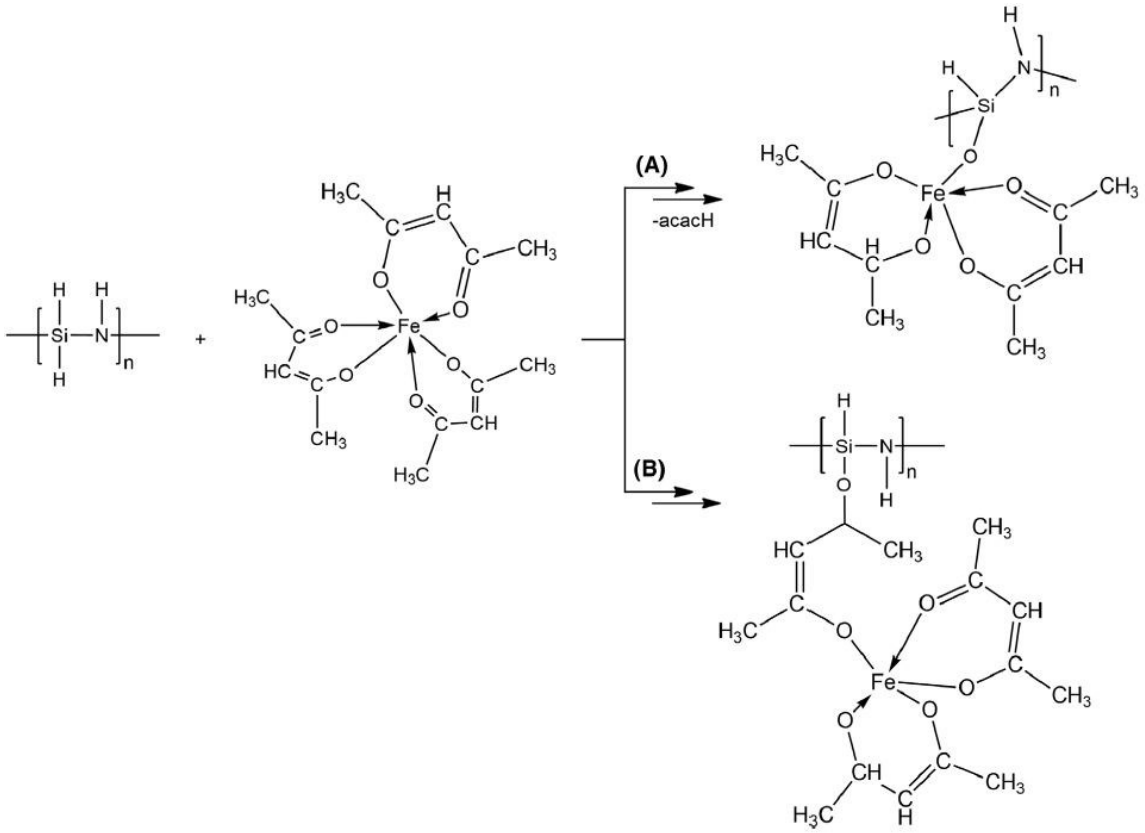

Figure 3-3: Proposed pathways of the reaction between PHPS and Fe(III)acac$_3$ during single-source precursor synthesis: (A) substitution at the Si-H sites of the polymeric backbone, leading to the formation of Si-Fe or Si-O-Fe bonds accompanied by the release of an acetylacetonate group; (B) hydrosilylation of C=O within acetylacetonate ligands. Reproduced from [6].

3.1.2 Cellulose-based Paper Templates

Three cellulose-based papers were employed as templates in this study, of which one is a commercially available laboratory (grade 3hw) qualitative filter paper (Sartorius, Göttingen, Germany). According to its data sheet, the paper is made from refined pulp and cotton linters with an α-cellulose content of > 95 % and has a grammage of 65 g/m^2. Moreover, the paper is declared as wet-strengthened through the addition of certain compounds, which are not further specified in the datasheet. As per personal correspondence with customer service, a chlorine-

containing polyaminoamide-epichlorohydrin resin is added to ensure the stability of the filter paper during water contact. In the present work, the paper is dubbed ‘Sartorius’ (‘Sart’). The other two papers were manufactured in the Paper Technology and Mechanical Process Engineering department of the Technische Universität Darmstadt by Andreas Striegel and Christiane Helbrecht. Utilizing eucalyptus pulp and cotton linters, respectively, the papers designated ‘Eucalyptus’ (‘Euc’) and ‘Cotton Linters’ (‘Lin’) were fabricated using the Rapid Köthen Method according to DIN EN ISO 5269-2 with the help of an automated sheeting machine. Both papers were processed into round sheets with a grammage of 65 g/m^2. In contrast to the commercially available ‘Sartorius’, no wet-strength agents or other additives are introduced into the papers. As shown in the micrographs of Fig. 3-4, the three papers exhibit differing fiber diameters and curvature. Also, the ‘Sartorius’ paper has a distinct appearance due to a pronounced luster of the fibers, likely originating from the wet-strength additive.

Prior to impregnation with the polymeric precursors, the papers are cut into small rectangular pieces (1.5 x 1.5 cm) and dried at 80 °C for at least 24 h. Using a tweezer, the templates are dipped into the precursor solution for approximately 1 s in inert Ar atmosphere, and the excess solvent is removed by vacuum drying, leading to polymer-coated preceramic papers.

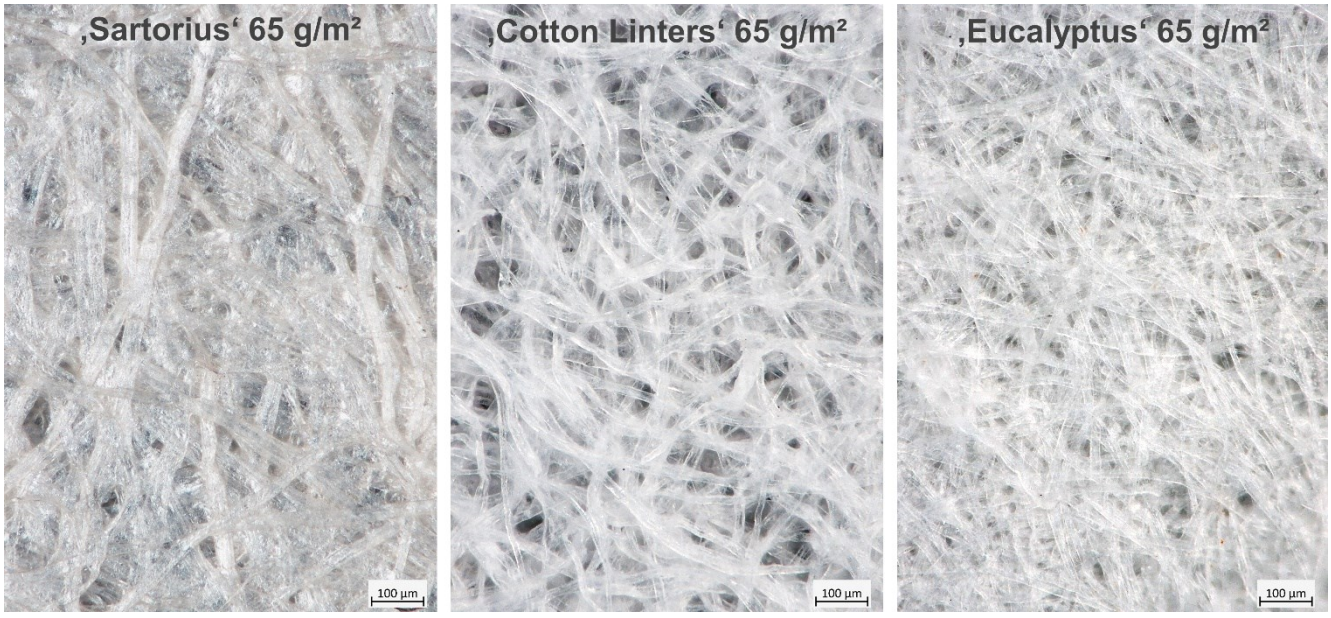

Figure 3-4: Optical micrographs of the three cellulose-based papers employed for templating the ceramic papers investigated. Focus-stacked composite images were acquired with a Zeiss AxioZoom.V16 using annular illumination and high dynamical range (HDR) processing.

3.1.3 Pyrolysis & Annealing

To convert the preceramic polymer-cellulose composites into ceramic papers, the samples were pyrolyzed at 1000 °C, as per the temperature program depicted in Fig. 3-1. Heating and cooling rates were 100 K/h for all samples, with the designated target temperature maintained for 3 h. Most of the samples were pyrolyzed in inert

Ar atmosphere, whereas some of the Fe-modified 'Sartorius' papers were processed using reactive NH_3 (ammonolysis) to assess the impact of different atmospheres on the structure and composition of the resulting ceramics. For the ammonolysis, the samples were placed in a quartz crucible inside a Schlenk tube and heated in a high-temperature oven (Carbolite Gero GmbH & Co. KG, Neuhausen, Baden-Württemberg, Germany) with constant ammonia (99.999 vol.-%; H_2O < 5 ppmv; O_2 + Ar < 1 ppmv, Air Liquide S.A., Paris, France) flow of 0.05 L/min, while pyrolysis in flowing Ar atmosphere was conducted within a LOBA tube furnace (HTM Reetz GmbH, Berlin, Germany).

Finally, some of the as-pyrolyzed ceramic papers were treated with an additional tempering step at 1300 °C in either flowing N_2 (99.999 %; Air Liquide S.A.) or Ar atmosphere with a flow rate of 0.05 l/min. The samples were placed within graphite crucibles and heated inside a graphite furnace (GT Advanced Technologies, Hudson, USA), according to the adjusted temperature program depicted in Fig. 3-1. Heating and cooling rate was 600 K/h until 1000 °C was reached and then reduced to 300 K/h, with the maximum temperature of 1300 °C held for 3 h.

3.2 Specimen Preparation

Owing to the various synthesis parameters employed, more than 40 distinct ceramic papers were produced and investigated in the present study. Moreover, numerous additional samples, such as pure ceramics derived from the different precursors (without the use of a paper template) or the papers themselves upon high-temperature treatment, have been examined to assess the impact of individual synthesis parameters on the resulting materials. Appendix A comprehensively lists the samples investigated in this study, along with the materials and parameters applied during processing.

3.2.1 TEM Sample Preparation

As the principal characterization technique employed in this study, a particular focus was laid on the preparation of electron transparent samples with a preserved microstructure from the as-prepared ceramic papers for transmission electron microscopy (TEM) investigation. Generally, electron microscopy demands materials to be stable in a vacuum, resistant to beam damage induced by high-energy electron irradiation, and sufficiently conductive. Moreover, a fundamental condition for TEM imaging is an extremely thin specimen, usually not exceeding a few tens of nanometers. A comparably easy way of achieving this is to produce fine powders of the materials and suspend them on a sample grid, with very small grains and grain edges allowing for electron transmission. Clearly, although this method is simple and straightforward, the destruction of the samples' original microstructure renders its investigation impossible. Traditionally, a combination of polishing and ion thinning is used for obtaining thin foils from bulk ceramics and many other inorganic substances, whereas chemical etching

is typically employed for metals. More recently, focused ion beam (FIB) has emerged as a useful and versatile technique for the preparation of electron transmissible sample lamellae, which can be selectively cut from the region of interest within a bulk sample, thinned to the desired thickness using an ion beam, and precisely transferred to a certain position on a holder. Moreover, even sample modification by deposition of atomic species (e.g. Pt or C) or connection to electronic devices, is possible, opening unprecedented possibilities for in situ experiments conducted in the (sub)nanometer regime. While this makes FIB an indispensable tool for pushing the frontiers of, for instance, semiconductor research, the comparably high expenses associated with it typically limit its use to specific questions and materials and make it less attractive for preparing large quantities of specimens.

Two approaches to the preparation of TEM samples with intact microstructure from the polymer-derived ceramic papers have been investigated and assessed in a preceding study associated with this thesis [201]. It was shown that, if elaborate measures were applied, polishing and thinning could be used to prepare TEM samples from the ceramic papers. The brittle and filigree ceramic composites could be stabilized and lapped with diamond abrasive when sandwiched between $SrTiO_3$ platelets. Followed by Ar ion milling, a few electron transmissible fibers could be obtained, which, however, was inconsistent, time-consuming, and generated only low-quality results and hence, was deemed inadequate. Conversely, ultramicrotomy slice-cutting, a classic preparation technique established for biological or polymeric specimens but seldom used for ceramic materials, produced exceptional TEM samples from the PDCPs. The method was found to offer compelling advantages, such as a homogeneous sample thickness, large electron transparent areas, high reproducibility, extremely good time and cost efficiency, and a lack of ion implantation artifacts, all while leaving the in-situ generated microstructure of the ceramic papers mostly undisturbed. As this meets the requirements for the production of highly representative samples from the numerous ceramic papers of interest, ultramicrotomy preparation was chosen as the primary preparation approach in the present study.

A schematic of the ultramicrotomy cross-sectioning procedure is presented in Fig. 3-5. In advance, small stripes are carefully cut from the ceramic papers, embedded within a casting mold using a two-component epoxy resin (EpoFix, Struers GmbH, Willich, Germany), and let cure at 70 °C for 24 h. The sample blocks are trimmed to a four-sided truncated pyramid (A), with the sample material cropping out centered within the resulting flat-top with an area of roughly 100 x 200 µm, as shown in the figure. For the sectioning procedure, either a Micro Star Technologies (Bruker Co., Billerica, USA) or a Diatome Ultra (Diatome Ltd, Nidau, Switzerland) diamond knife was used, each mounted within a boat holder, at an angle of 55° and 45°, respectively. The sample blocks were clamped into the holding arm, which passes the diamond knife according to the depicted motion scheme (B). Through the addition of a predefined forward increment after each cycle, ultra-thin slices are cut from the blocks cutting face and left floating on the water surface in the boat holder. Cross-sections with a suitable thickness (< 70 nm) can be selected by their characteristic interference color and are carefully transferred to a TEM sample grid (copper, 300 mesh, ‘lacey’ carbon film) using a specialized catching loop (Perfect Loop, Diatome) tool (C). As shown in the visual light micrographs, each grid holds multiple sample slices with uniform thickness, containing numerous ceramic fiber cross-sections suitable for TEM imaging (D).

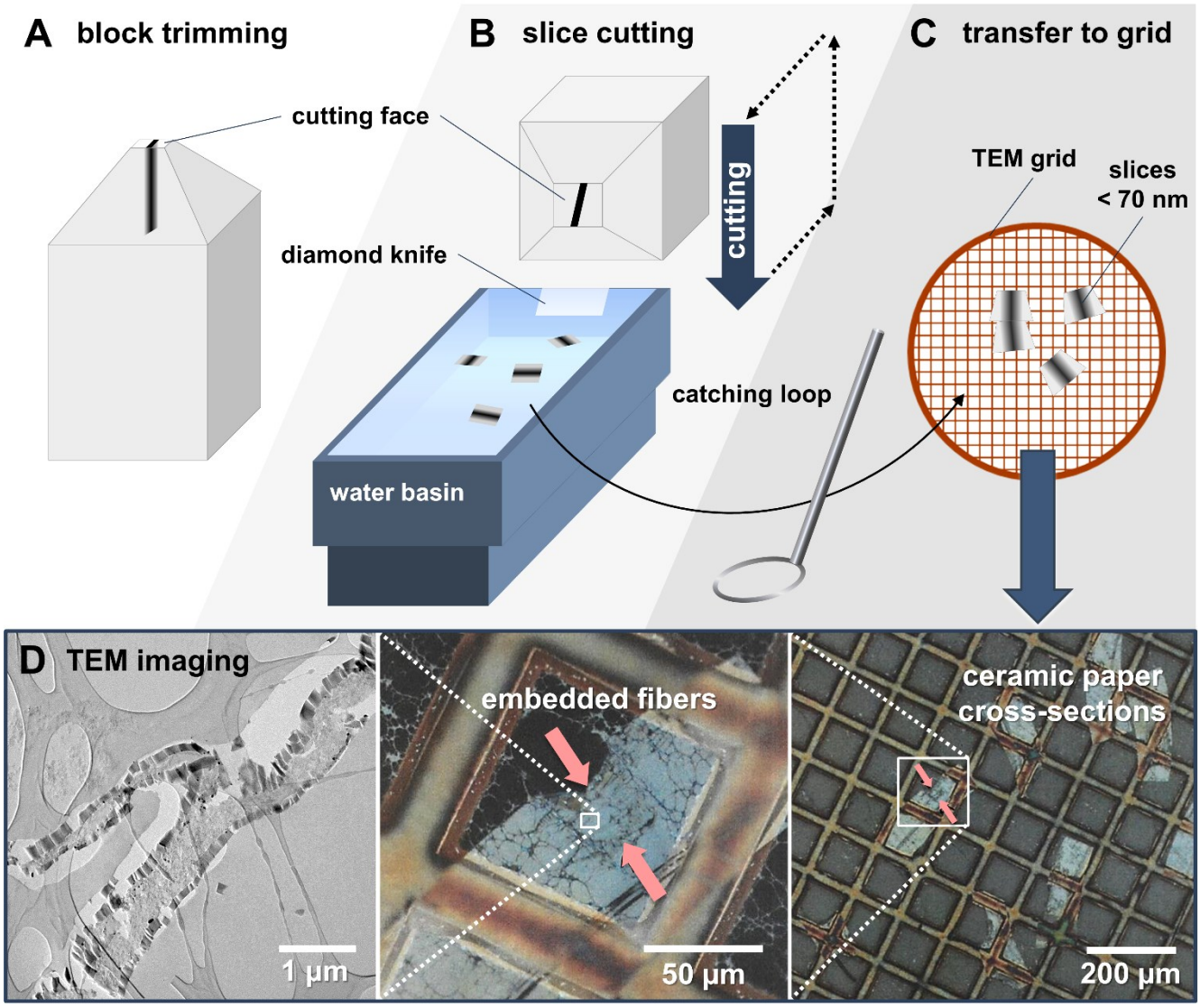

Figure 3-5: Schematic illustration of the ultramicrotomy sample preparation procedure employed for obtaining electron transparent cross-sectional samples of the ceramic papers for TEM investigation. (A) The sample is embedded within an epoxy resin sample block and trimmed to a pyramidal shape. (B) Ultra-thin slices a cut with a diamond knife via the incremental forward motion of the sample holder. (C) The resulting slices are transferred to a TEM sample grid with a catching loop, resulting in numerous electron-transmissible ceramic paper cross-sections of homogeneous thickness (< 70 nm) ideal for (D) TEM imaging. Own work, adapted and expanded from [7]; light micrographs taken by Birgit Bußmann, Max Planck Institute for Solid State Research, Stuttgart.

Please note that the mechanical stress applied by the diamond knife during sectioning may introduce preparation artifacts into the sample, which can result in a compressed, sheared, textured, or fractured microstructure [202]. Indeed, as it is displayed in the TEM BF image of a typical ceramic fiber cross-section (Fig. 3-5 D) obtained via ultramicrotomy slice-cutting, in many cases, the fibers were found to be encased by a severely fragmented ceramic coating. As described in the aforementioned study [201], a comparison with the distinctly prepared samples demonstrated that this is an artifact introduced by the sectioning procedure itself and not an intrinsic feature of the ceramic papers. Careful optimization of the preparation parameters (cutting face area, slice thickness, cutting speed, two different diamond knives) and ultrasonic-assisted cutting was applied in the present study aiming to

prevent fracture during ultramicrotomy sectioning, which however, did not reliably result in fiber cross-sections with intact ceramic coating. While the fragmentation does disturb the microstructure notably, the fragments of the ceramic coating generally remained attached to its substrate, giving an unmistakable impression of the in situ generated composite structure of the ceramic papers and even allowed for examination of the coating-substrate interface, which was found to satisfy the requirements of this research project.

For a comparative investigation of the pure polymer-derived ceramics, standard preparation of TEM powder samples was employed. For this, the freshly prepared coarse-grained ceramic powders were mildly ground using a mortar and suspended in ethanol, followed by ultrasonic dispersion to deagglomerate the particles. A few droplets of the suspension were deposited on a TEM sample grid (copper, 300 mesh, 'lacey' carbon film) and the solvent was let to evaporate. Finally, the samples were sputtered with carbon (approximately 5 nm layer thickness) to minimize charging effects during electron microscopic examination.

3.2.2 SEM Sample Preparation

For SEM analyses, the as-synthesized ceramic papers were mounted on carbon-based conducting tape and mildly sputtered with carbon (approximately 10 nm layer thickness) to reduce charging artifacts induced by the incident electron beam. The pure polymer-derived ceramics were first ground to produce fresh fracture surfaces followed by the deposition of a small amount of the powder on a sample carbon tape, followed by carbon coating. The pristine cellulose-based paper templates were dried for 24 h at 60 °C to remove adsorbed water and a carbon layer with increased thickness was applied due to their poor conductivity.

3.2.3 PXRD Sample Preparation

For powder X-ray diffraction (PXRD) data acquisition of the ceramic papers, for each sample, one as-prepared paper sheet (approx. 2.25 cm^2) was ground to obtain a fine powder. The samples were each placed in the center of a free-rotation Zero Diffraction Plate sample holder (oriented silicon crystal, B-doped) and brought to a uniform height by carefully leveling the powder with a glass plate.

3.2.4 FT-IR Sample Preparation

As-prepared samples of the preceramic polymers and freshly impregnated papers were analyzed in attenuated total reflection (ATR) mode requiring no additional sample preparation. For FT-IR studies conducted in transmission geometry, ceramic samples were pressed into KBr pellets.

3.3 Transmission Electron Microscopy (TEM)

The conventional TEM data presented in this study were acquired with a JEM 2100F (JEOL Company, Tokyo, Japan) field emission electron microscope operated at 200 kV. Sample orientation along two axes was realized via a JEOL double-tilt beryllium holder with a nominal tilting range of +/- 25°. Images were recorded with an UltraScan 1000 (Gatan, Pleasanton, USA) charge-couple device camera using the Gatan Microscopy Suite software. Phase determination from electron diffraction patterns was carried out manually or aided by the specialized diffraction data analysis tools Program for Interpreting Electron Diffraction Patterns (PIEP) [203] and ReciPro [204].

3.3.1 Fundamentals of TEM

Although originally developed to allow microscopic imaging beyond the resolution limit of optical microscopes, modern TEMs unite the capabilities to access various material characteristics, such as local composition, phase assemblage, and atomic structure, in a single instrument. Hence, over the past decades, TEM has emerged as an indispensable tool for micro- and nanostructure characterization, with a constantly expanding suite of techniques. As the primary analytical technique employed in the present study, in the following chapter, some theoretical aspects and the fundamentals of the methods used are briefly outlined. More details on the subject are available in the literature [205,206].

Electron microscopic investigation relies on the interaction of primary electrons with a sample resulting in scattering and generation of secondary signals, which can be analyzed to obtain various kinds of spatially resolved

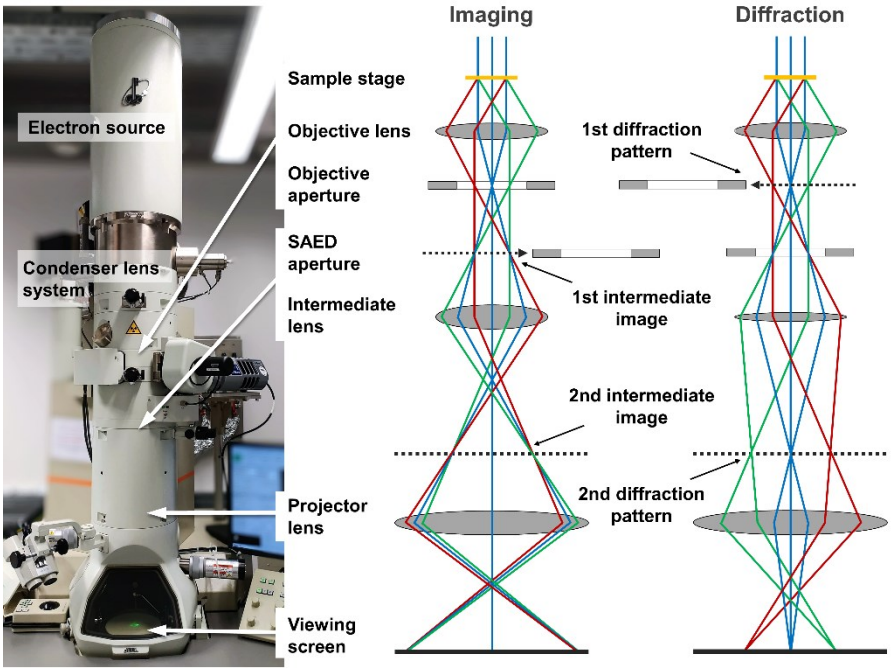

Figure 3-6: Display of the JEM 2100F microscope showing the typical setup of a TEM, with the elctron gun on top of the column followed by the condenser lens system used to adjust the beam properties. The ray paths after interaction with the specimen for both imaging and diffraction mode are depicted, along with the lens systems and apertures used. In the back focal plane of the objective lens, a diffraction pattern is generated and, depending on the excitation of the intermediate lens, either it or the real space image is projected onto the screen [205].

information. In a TEM, a high-intensity electron beam (typically 60–300 keV) is generated in the illumination system atop the instrument and traverses the microscopic column and several electromagnetic lens systems. To allow electron transmission through a sample, it has to be very thin, typically less than 100 nm. The condenser lens system right below the gun is used to adjust the spot size and convergence of the beam. The objective lens system is usually split into an upper and lower polepiece, housing the specimen in between and decisively affecting the image quality in conventional TEM operation. A key feature of TEM is that diffraction of the electron beam inevitably results in the formation of a reciprocal space image (diffraction pattern) in the back focal plane of the objective lens. Thus, varying excitation of the intermediate lens allows to conveniently switch between imaging and diffraction mode. The general setup of a TEM instrument is depicted in Fig. 3-6, showing one of the microscopes used in the present research along with the ray paths for imaging and diffraction mode after interaction with the specimen. Finally, the projector lens system is responsible for controlling the magnification of the image projection onto the phosphor screen or detector.

As is the case for light in optical microscopes, the theoretical resolution limit of a TEM is determined by the wavelength of the electrons, which in turn is controlled through the acceleration voltage. In contrast to visible light waves that range between 380 nm (blue) and 750 (red), electron waves at 200 keV exhibit a wavelength of $\lambda \approx 2.5$ pm, theoretically allowing to resolve subatomic structures. However, the achievable resolution limit is governed by the aberrations of electromagnetic lenses, which have historically been putting constraints on the performance of electron microscopes as some require significant efforts to be overcome. The magnetic field strength of electromagnetic lenses increases with deviation from the optical axis leading to different focal lengths, which is called spherical aberration. Its amplitude is described by

$$\boldsymbol{d_s = \frac{1}{2} C_s \tau^3} \qquad \text{Eq. 3-1}$$

where C_s is the spherical aberration coefficient, τ the collection semi-angle of the lens, and d_s is the diameter of the blurred focus disc resulting from imaging a point source affected by spherical aberration. Dispersion of electrons with a certain energy spread intrinsically caused by the electron source and further increased by inelastic interactions, leads to a deviation from a uniform focal point in a similar manner. The chromatic aberration also blurs the focus point to a disc with diameter d_c expressed through

$$\boldsymbol{d_c = \frac{1}{2} C_c \tau \frac{\Delta E}{E_0}} \qquad \text{Eq. 3-2}$$

with the chromatic aberration coefficient C_c, the energy spread ΔE, and the nominal beam energy E_0. Moreover, elliptical distortion of the image, so-called astigmatism, is introduced through the lenses, which, however, is effectively corrected through a quadrupole stigmator during operation. Finally, the diffraction of electron waves at apertures gives rise to an Airy pattern, affecting the optimal point resolution achievable. The diffraction error

only plays a role during imaging with small apertures and cannot be corrected. The radius of the Airy disc, d_B, determines the resolution limit between two points according to

$$d_B = 0.61 \frac{\lambda}{\tau}. \qquad \text{Eq. 3-3}$$

With the implementation of sophisticated spherical and chromatic aberration correctors in the early 2000s, the resolution of TEMs has increased significantly. Present-day uncorrected TEM instruments typically achieve a point resolution of around ≈ 1 Å, whereas state-of-the-art C_s- and C_c-corrected microscopes were shown to resolve distances just short of 0.5 Å [207].

The primary source of image contrast in TEM is the elastic scattering of electron waves through interaction with the sample volume, which can result in a change of amplitude and phase. The prevalence of incoherent elastic scattering events depends on the mean free path of the electron waves, which is determined by the mass of the atomic nuclei and the thickness of the sample. Hence, heavier elements and thicker sample areas lead to more scattering giving rise to mass-thickness contrast. Another type of amplitude contrast, diffraction contrast, is based on coherent elastic scattering at the lattice planes of crystalline phases. The relationship between the electron wavelength, lattice spacing, d, and diffraction angle, Θ, is approximated by Bragg's law according to

$$n\lambda = 2d \sin\Theta = \left|\overrightarrow{k_D} - \vec{k}\right| \qquad \text{Eq. 3-4}$$

where n is the order of diffraction, $\overrightarrow{k_D}$ the wavevector of the diffracted, and $\vec{k}$ of the incident beam. Given that the orientation of the diffracting lattice planes satisfies the Bragg condition, interference of the scattered waves gives rise to a diffraction pattern consisting of intensity maxima and minima reflecting the periodicity of the crystalline phase. As both contrast mechanisms scatter intensity away from the optical axis, the objective aperture may be

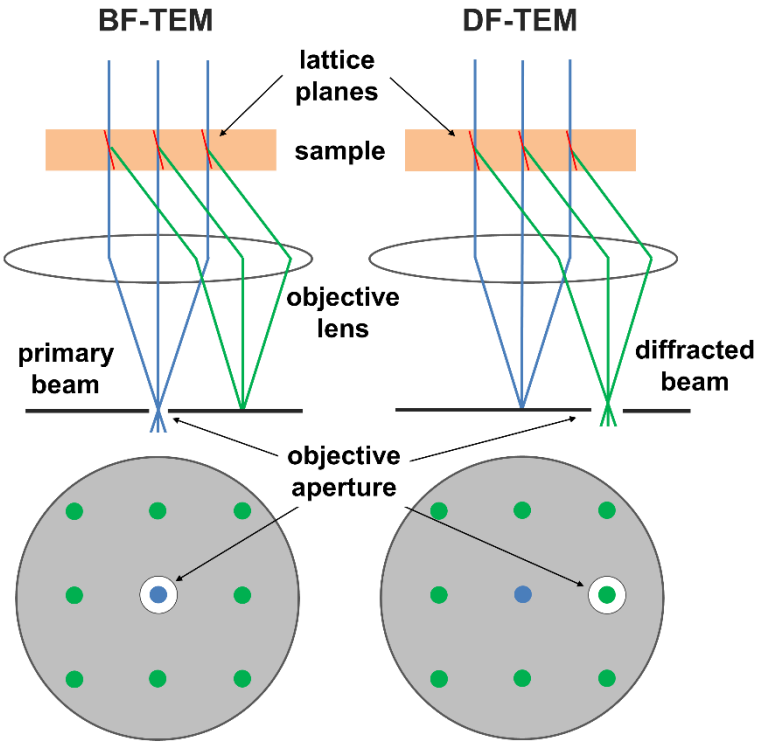

Figure 3-7: Ray diagram and objective aperture setting during BF imaging (left), using only the primary beam for image generation. For DF imaging (right), the aperture is used to block all but a single diffracted beam resulting in an image in which only regions contributing to the selected beam's intensity are displayed bright. Redrawn after [205,206].

used to exclude diffraction maxima or incoherently scattered electrons from contributing to the image, increasing the amplitude contrast. Bright-field (BF) image formation mainly involves the intensity of the transmitted (i.e. unscattered) beam causing highly scattering regions (thick, high atomic number, crystalline phases in Bragg condition) to be dark, whereas weakly scattering areas (e.g. vacuum) appear bright. Smaller apertures may be used to increase contrast, which is an important tool during lower-magnification imaging. For generating dark-field (DF) images, on the other hand, the transmitted beam is excluded by the aperture, and at least one diffracted beam (or incoherently scattered intensity) is selected. In the corresponding image, only regions contributing to the selected reflection will appear bright. The ray paths and objective aperture settings of both imaging modes are schematically depicted in Fig. 3-7.

Upon interaction of the incident electron beam with the specimen, the original plane and coherent electron waves are modulated by the atomic potential of the sample atoms resulting in the so-called phase contrast, which forms the basis of high-resolution (HRTEM) imaging. The associated phase shift enables interference between modulated direct and diffracted waves, which converts phase contrast into amplitude contrast allowing detection by the viewing screen or camera. At high magnifications, and given a sufficiently thin sample region, the phase contrast generated during coherent illumination for a certain reciprocal lattice vector, or spatial frequency u, is expressed through the contrast transfer function (CTF)

$$\boldsymbol{T(u) = 2A(u)\sin\chi(u)} \qquad \text{Eq. 3-5}$$

where $T(u)$ is the resulting phase contrast, $A(u)$ the aperture function, and $\chi(u)$ the phase-distortion function. The latter is dependent on the microscopic setup as shown by

$$\boldsymbol{\chi = \pi\Delta f\lambda u^2 + \frac{1}{2}\pi C_s\lambda^3 u^4} \qquad \text{Eq. 3-6}$$

with Δf being the defocus, λ the electron wavelength, u the spatial frequency, and C_s the spherical aberration coefficient. Hence, the CTF and, as a consequence, the obtainable resolution in HRTEM imaging, is determined by the applied focus, quality of the electron optics, acceleration voltage, and spatial frequency imaged. Defocusing the objective lens can slightly counteract spherical aberration, which is used to finetune the CTF and achieve optimum resolution. The Scherzer defocus

$$\boldsymbol{\Delta f_{Sch} = -1.2(C_s\lambda)^{0.5}} \qquad \text{Eq. 3-7}$$

denotes the focus setting at which maximum spatial frequencies may be resolved, thus representing the performance of the microscope. The thickness of the sample also affects phase contrast and beyond the resolution limit (at $\boldsymbol{\Delta f_{Sch}}$), contrast inversions occur. Hence, image interpretation generally has to be aided by image simulations to fully extract information, such as atomic column positions. Nevertheless, HRTEM allows to access

important structural information, such as local crystallinity, determine phases and orientations, characterize defects and grain boundaries, and much more, appointing it a central role during TEM operation.

3.3.2 Electron Diffraction

As described above, upon incidence of electron waves onto a crystalline specimen, given the Bragg condition is satisfied, diffraction, a special case of coherent elastic scattering, occurs. A plane wave incident on a crystal lattice is modified by its periodic arrangement and interference of the resulting secondary wavelets with each other nets several coherent beams scattered to specific angles. This leads to the formation of a diffraction pattern, in which the length of each reciprocal lattice vector, g_{hkl}, is inversely proportional to the lattice plane spacing, d_{hkl}, of the diffracting crystal. A commonly applied visualization of the diffraction pattern formation is the Ewald sphere concept used to relate the reciprocal lattice to the wave vectors of the incident (k) and diffracted ($\boldsymbol{k_D}$) beams, as depicted in Fig. 3-8. The radius of the sphere constructed in the reciprocal space is defined by the reciprocal wavelength of the incident radiation ($|\boldsymbol{k}| = \boldsymbol{\lambda^{-1}}$). From the origin of the sphere, any reciprocal lattice point may be described by the diffracted wave vector $\boldsymbol{k_D = k + g_{hkl}}$ and any point intersected by the Ewald sphere meets the Laue criterion (and Bragg's law) resulting in a diffraction maximum. The orientation of the lattice with respect to the incident beam defines which points will be intersected and which maxima appear in the pattern. However, when considering a crystal perfectly oriented along a certain zone-axis (e.g. in Fig. 3-8), not a single reciprocal lattice point precisely meets the

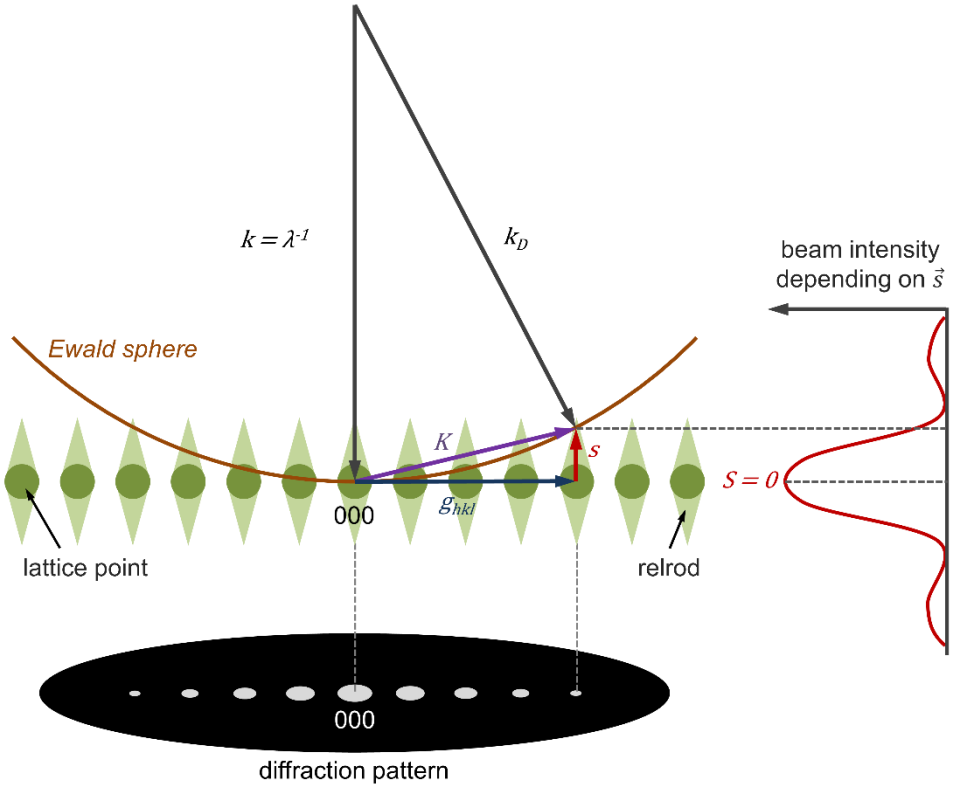

Figure 3-8: Schematic of the Ewald sphere construction for a 2D cross-section of the reciprocal lattice oriented perpendicular to the wave vector of the incident electron beam, k. Intersection of the Ewald sphere and a reciprocal lattice point ($\vec{g}_{hkl}$) is assigned a diffracted wave vector (k_D) and leads to an intensity maximum in the corresponding diffraction pattern. The lattice points are elongated to a rod-like shape (relrod) introducing the excitation error $\vec{s}$, which gives the true diffraction vector ($\vec{K} = \vec{g}_{hkl} + \vec{s}$) and affects the diffracted beam intensity. Based on [205,206].

Bragg condition, and only a single diffraction maximum (i.e. 000) should be produced. However, the extremely small thickness of a TEM specimen causes a phenomenon called the thin-foil effect, which results in a finitely elongated spindle-shaped zone (oriented normal to the thin-foil surface) in which the conditions for diffraction are met [205]. These reciprocal lattice rods ("relrods") derived from their corresponding points are a conceptual necessity to explain the pattern formation and intensity distribution of an electron diffraction pattern by introducing the excitation error, $\vec{s}$. As shown in Fig. 3-8, $\vec{s}$ describes the deviation from the exact reciprocal lattice point (i.e. Bragg condition) at which the Ewald sphere intersects the relrod giving the true diffraction vector $\vec{K} = \vec{g}_{hkl} + \vec{s}$ and determining the effective intensity of the resulting diffraction spot. In contrast to X-ray diffraction, using highly accelerated electrons equals a sphere of immense diameter, which is why the surface of the Ewald sphere may be considered almost flat. This results in numerous reciprocal lattice points being intersected simultaneously thus forming a diffraction pattern in a single illumination.

The capability to acquire both highly localized diffraction patterns and real space images of a region of interest, represents a powerful feature of TEM, allowing detailed characterization of microstructure, phases, and defects of a wide range of materials. Moreover, electron diffraction in itself is a highly versatile technique that can be used to access various kinds of information from a sample. The principal approach of diffraction pattern acquisition is the selected area electron diffraction (SAED), for which the sample is illuminated with a parallel beam and a region is chosen with the SAED aperture (compare Fig. 3-6) and all electrons originating from other source regions are excluded from the pattern. The size of the aperture limits the area observed and allows diffraction from very small features down to about 200 nm in size. During conventional TEM operation, SAED is one of the most important tools to assess the crystallinity of a sample by examining the features present in the diffraction pattern. Amorphous materials generally show no discrete reflections due to the missing long-range order and only display a Gaussian intensity distribution or diffuse broad rings and halos, originating from a certain degree of short-range ordering (compare Fig. 3-9 a,b). While this can be used to extract information about the glass structure, and hence, characterize the atomic structure of amorphous phases, its use is limited without complementary techniques or

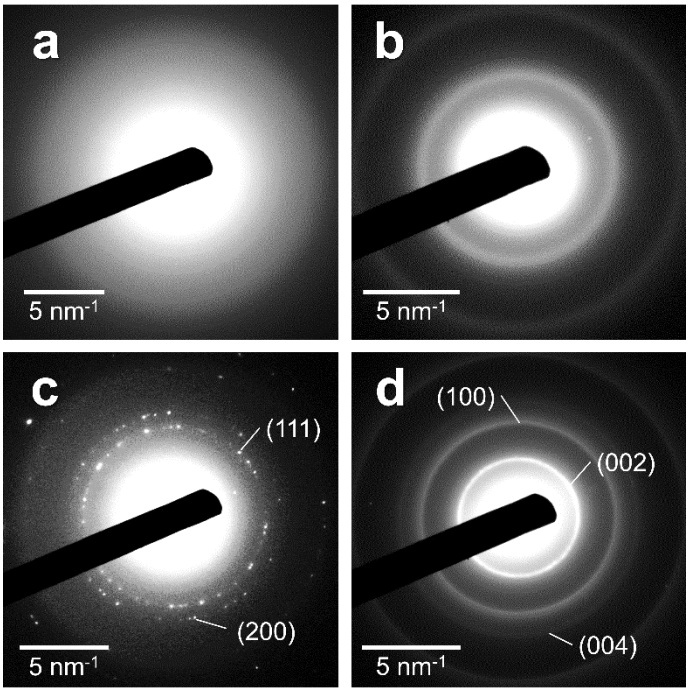

Figure 3-9: Examples of typical SAED patterns observed in the ceramic paper samples. Amorphous PDCs feature a Gaussian intensity distribution (a), while amorphous carbon shows broad rings and halos due to short-range ordering (b). Crystallization of nanosized Ni_XSi leads to discrete reflection rings assignable to certain lattice spacings (c). Diffraction from semicrystalline turbostratic carbon yields a diffuse ring pattern, reflecting its partial disorder (d).

simulations. Diffraction from crystalline substances on the other hand, as we have seen above, generates discrete intensity maxima representing the periodic arrangement of the phase, which can be used to identify phases, determine their orientation, assess defects, investigate special grain boundaries (e.g. twinning), and characterize superstructures, among other uses. Diffraction from a polycrystalline material consisting of numerous randomly oriented crystallites gives a characteristic concentric pattern of reflection rings, in which each ring can be assigned a specific lattice plane distance (compare Fig. 3-9 c). Such ring patterns are similar to X-ray diffraction patterns obtained from crystalline powders and can be used to identify phases and determine the crystallinity of the grains. The sharpness of the reflection rings correlates with the ordering of the lattice as even slight deviations in the lattice constant lead to a broadening of the maxima in the pattern, often observed for very small crystallites (<10 nm) or semicrystalline (partially disordered) phases, such as turbostratic carbon (Fig. 3-9 d). SAED from a single crystal results in the formation of a point pattern in reciprocal space, representing the periodicity and spacing of the lattice planes oriented along the zone-axis imaged. Each maximum corresponds to a specific lattice plane spacing (and diffraction angle) which can be indexed to identify phases and zone-axis orientations (Fig. 3-10 a). Instead of using parallel illumination, the beam can also be focused onto the sample at a certain convergence angle α, which is then called convergent beam electron diffraction (CBED). Instead of spot maxima, the beam convergence results in the formation of diffraction discs with their diameter controlled by the α setting. For large angles, a Kossel pattern is generated, consisting of wide overlapping discs that can carry additional information useful to extract the crystal symmetry or characterize dislocations. Using narrower condenser apertures results in an α smaller than the diffraction angle θ, forming patterns of non-overlapping discs termed Kossel-Möllenstedt diagram. The patterns obtained from this "quasi-parallel" setting are in principle equivalent to regular SAED (in fact, they can contain a lot more information) but due to the focused beam setting, they allow probing of much smaller sample areas (Fig. 3-10 b). This enables diffraction from minuscule features, such as individual nanocrystals or line defects only a few nanometers in size [208] commonly referred to as μ- or nano-diffraction.

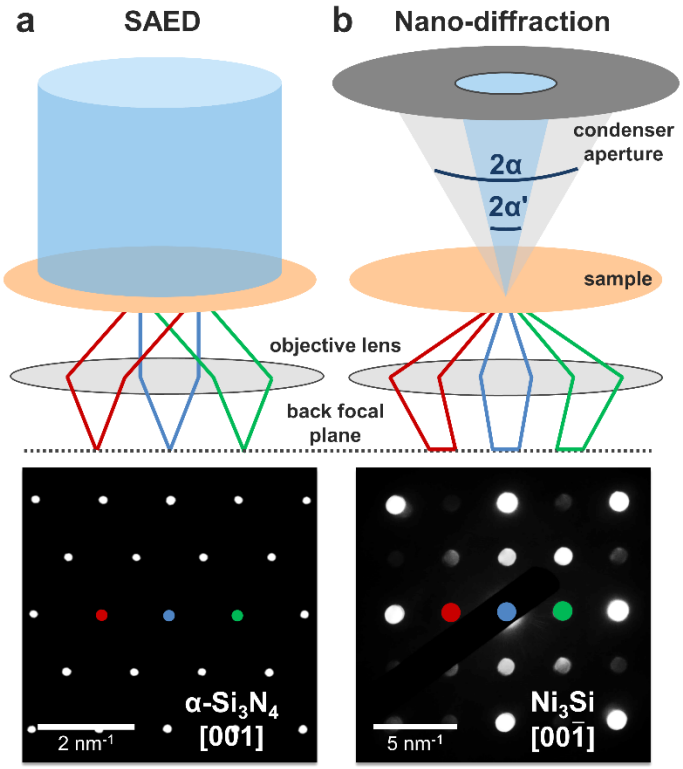

Figure 3-10: Comparison of the setup, ray paths, and result of SAED (a) and nano-diffraction (b) pattern acquisition. With parallel illumination, a point pattern is formed in the back focal plane and the region of interest is selected with an aperture below the sample. For nano-diffraction, the beam is focused on a small feature, and a diffraction disc pattern is formed. To avoid overlapping of the discs, the convergence angle (α) has to be adjusted (α') using a small condenser aperture. Based on [205,206].

3.3.3 Scanning Transmission Electron Microscopy (STEM)

Within the present research, analytical scanning transmission electron microscopy (STEM) data were primarily acquired with the JEM-2100F, whereas atomic resolution (HRSTEM) images were obtained with a JEOL JEM ARM-200F, equipped with a condenser system C_S-corrector (CEOS GmbH, Heidelberg, Germany), facilitating a nominal optimum resolution of 0.8 Å. For atomic resolution HAADF imaging, a camera length of 6 cm was used, corresponding to an acceptance angle range of 90-370 mrad. Both microscopes were operated at 200 kV and are equipped with double-tilt beryllium sample holders for specimen orientation.

During STEM operation, instead of using parallel beam illumination, a focused electron probe is formed in the condenser system and scanned over the sample surface. In contrast to conventional TEM (CTEM), the image is not obtained from a single illumination but rather built up by assigning signal intensity detected at each probe position to the corresponding pixel. Although the image formation mechanism differs fundamentally, the contrast observed in STEM images is approximately equivalent to CTEM imaging, considering only elastic scattering, which is described by the principle of reciprocity. As the same beam-sample interactions take place, at each probe position, mass-thickness and diffraction determine the transmitted intensity incident on the detectors. Consequently, STEM allows for both BF and DF imaging analogous to CTEM, which, however, is realized differently owing to the distinct illumination principle. The image formation mechanism neither requires an objective lens nor the respective aperture. Instead, the signals generated by the scanning electron probe are directly collected by different detectors, concentrically centered around the optical axis at a certain (variable) camera length (compare Fig. 3-11).

A central circular detector is used for BF imaging, that is detecting unscattered electrons and such scattered to low angles, as is the case in CTEM. In addition, electrons scattered to higher angles, are collected by an annular DF detector within a range limited by its inner and outer acceptance angles. The resulting annular dark field (ADF) images exhibit a contrast similar to conventional DF images but receive intensity from all diffracted beams falling within the defined angular range, rather than a selected beam. By adjusting the camera length,

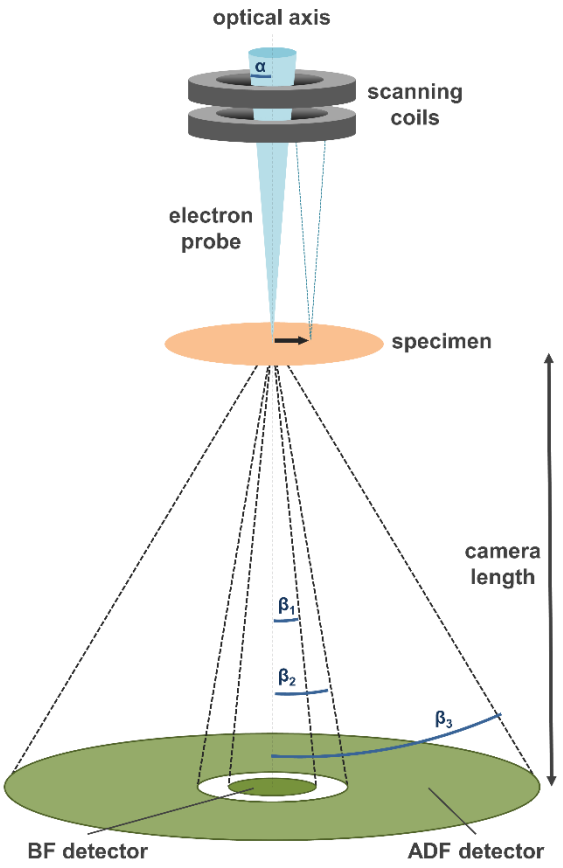

Figure 3-11: Illustration showing the typical setup of a STEM system. An electron probe with convergence angle α is scanned across the sample and the scattered electrons collected by detector plates, concentrically arranged around the optical axis. Depending on the adjustable camera length, the angular range of the detectors can be varied. β_1 denotes the outer acceptance angle of the BF detector; β_2 the inner and β_3 the outer acceptance angle of the ADF detector.

the acceptance angles of both detectors can be conveniently modified, allowing control of the contrast generated. With decreasing the camera length, only electrons scattered at increasingly higher angles are collected by the DF detector, which is called high-angle annular dark field (HAADF) and is considered one of the most useful and widely applied imaging modes in STEM. With an acceptance angle of > 50 mrad, predominately thermal diffuse scattered (TDS) electrons are incident on the detector, whereas electrons scattered to small angles, that is by diffraction or incoherent elastic scattering, are excluded. TDS mainly depends on the inelastic scattering probability, which is an element-specific property proportional to the mean atomic number (Z) of the material. The relation is approximated by $\boldsymbol{I \propto Z^{1.7}}$, meaning that during HAADF imaging, contrast is determined (almost) exclusively by the element species in the sample, sometimes referred to as Z-contrast-imaging. Hence, compositional information with very high (down to atomic scale) spatial resolution is accessible via HAADF STEM, without significant contributions from elastic scattering contrast effects. Also, as this mode does not rely on phase contrast, the contrast transfer function (CTF) does not feature inversions, meaning that atoms will always be displayed bright on dark background for the whole range of spatial frequencies, enabling image interpretation without the need for complementary simulations.

The resolution of STEM primarily depends on the diameter of the electron probe and, to resolve atom columns, it is necessary to achieve a subatomic spot size while maintaining sufficient beam currents. Hence, HRSTEM typically can only be realized with instruments equipped with a C_s-corrected condenser system. Also, the imaging technique is very sensitive to many factors, such as lattice orientation, sample thickness, and probe alignment.

3.3.4 Energy-dispersive X-ray Spectroscopy (EDS)

Spatially resolved compositional data analyses were carried out with an XMAX 80 energy-dispersive X-ray (EDS) detector attached to each electron microscope used in the present study. Acquisition and interpretation of the resulting spectra was performed employing the corresponding INCA software (Oxford Instruments, Abingdon, UK).

Provided sufficient kinetic energy of the electrons, irradiation of the specimen with an electron beam may cause expulsion of inner-shell electrons from sample atoms generating electron holes. Such holes will be immediately filled with an electron from a higher energy level accompanied by the emission of an X-ray quantum with an energy characteristic for the specific energetic transition and thus be unique to the respective element it is emitted from. Collected by a detector, these characteristic X-rays represent the information used for EDS analyses and allow spatially resolved element determination in an electron microscope. EDS is a standard technique in electron microscopy, as it enables accessing characteristic signals of almost any element ($_4$Be – $_{92}$U) simultaneously and fast. During STEM and SEM operation, the scanning image formation enables acquisition of EDS line profiles and even element maps, offering a capable tool for visualization of a specimen's chemical structure, even down to the atomic scale. Also, the technique is fairly insensitive to moderate specimen thickness variations and features

a high peak-to-background ratio. A concurring process to characteristic electron emission is the generation of Auger electrons, which is inversely proportional to Z. Hence, EDS analyses are best suited for detecting heavier elements, which can even be quantified rather accurately. Lighter elements, such as $_5$B or $_7$N, have a low yield of characteristic X-rays and thus, do not allow precise element quantification. Generally, EDS analyses are considered a semi-quantitative method, capable of quickly and accurately assessing the main elements but lacking the ability to provide exact quantifications of minor and trace elements. In typical commercial EDS systems, a spectral resolution of approximately 120 eV is achieved, preventing the resolution of some overlapping peaks. With increasing atomic numbers, higher voltages are needed to generate characteristic X-rays, which is not a concern in TEM (140-300 kV) but has to be considered during SEM analyses (1-30 kV), depending on the specimen composition.

3.4Scanning Electron Microscopy (SEM)

SEM investigation of the ceramic papers was conducted using a JSM-7600F (JEOL Company) high-resolution field emission scanning electron microscope. Secondary electron (SE) and backscattered electron (BSE) images of the ceramic papers and ceramic powders were acquired with an acceleration voltage of 10-15 kV, whereas imaging of the cellulose-based paper templates was conducted at 3-5 kV.

Analogous to STEM operation, in SEM, an electron probe scanned over the sample surface is used for image formation, assigning an intensity value to each position and corresponding image pixel. However, instead of electron transmission, secondary signals arising from the interaction of the electron beam and sample volume are collected by detectors, enabling different information to be accessed. Upon incidence of the probe onto the (bulk) specimen, within the excitation volume of the beam, various signals are generated, such as secondary and Auger electrons, continuum and characteristic X-rays, as well as light quanta from cathodoluminescence. An overview of the most important signals and the detector arrangement of a typical SEM setup is displayed in Fig. 3-12.

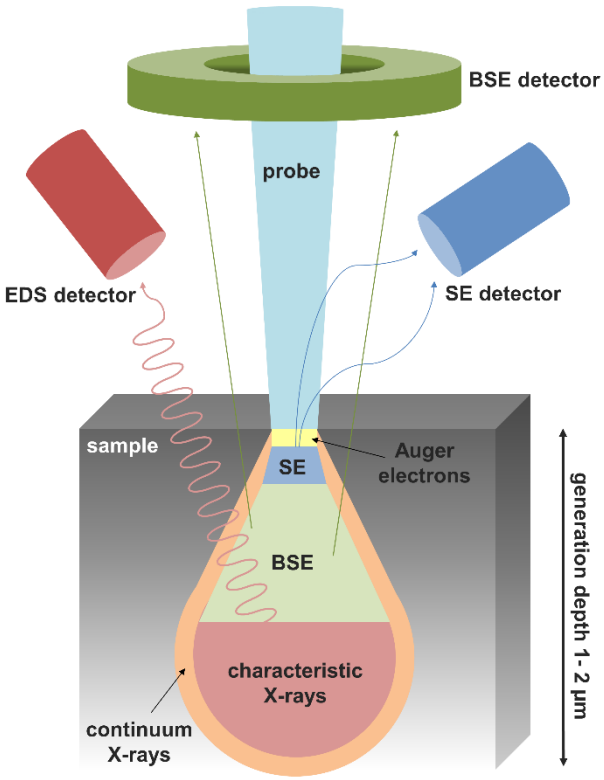

Figure 3-12: Schematic showing the most important signals generated upon electron probe interaction with a bulk sample and arrangement of detectors in a typical SEM setup. Signal generation depth and shape of the excitation volume depend on both the acceleration voltage used and the density of the material.

Secondary electrons (SE) are loosely bound charge carriers in the valence or conduction band of a material and are easily expelled by the incident beam. As their kinetic energy is rather low, only SE generated near the sample surface do not get reabsorbed and may be collected by a detector. SE imaging is one of the fundamental modes in SEM and is particularly useful for imaging the sample surface with high resolution. Contrarily, primary beam electrons can undergo elastic Rutherford scattering at high angles and conserved momentum. As the scattering probability is highly dependent on the atomic number and local density, images generated from backscattered electrons (BSE) display a distinct elemental contrast. Due to their high kinetic energy ($\approx \boldsymbol{E_0}$) they can come from greater depths and multiple scattering results in widening of the signal generation region, resulting in a noticeably reduced resolution compared to SE imaging. Additionally, grain orientation in crystalline materials can affect image contrast due to electron-channeling effects and backscatter diffraction. As in TEM, the generation of characteristic X-rays is used to obtain localized compositional information of the specimen via EDS analyses. Due to the large generation depth and associated absorption, secondary fluorescence, and matrix effects, however, spatial resolution and accuracy of quantification are generally much lower in an SEM.

3.5 Powder X-ray Diffraction (PXRD)

Complementary to the spatially resolved electron microscopy data, integrated information on the crystalline phases generated within the PDCPs was obtained via powder X-ray diffraction (PXRD) analyses. Finely ground, non-oriented powders of the freshly prepared ceramic papers were analyzed in a PANalytical Empyrean (Malvern Panalytical Ltd., Malvern, UK) diffractometer operated in Bragg-Brentano geometry. Sample analyses were performed at standard conditions using Co Kα emission (≈ 1.7902 Å) at 40 mA and 40 kV for a Bragg angle (2θ) range of 10-75° with a scanning speed of 0.006°/s and a step size of 0.013°. The diffraction patterns obtained were analyzed using the HighScore Plus software (Malvern Panalytical) with the inorganic crystal structure database (ICSD, FIZ Karlsruhe, Germany).

3.6 Fourier-transform Infrared Spectroscopy (FT-IR)

To access information about the molecular bonding within the samples, Fourier-transform infrared spectroscopy (FT-IR) studies were conducted using a VARIAN 670-IR (Bruker, Billerica, USA) spectrometer. The air-sensitive preceramic polymer samples and impregnated papers were analyzed in attenuated total reflection (ATR) mode for a wavenumber range of 4000 – 400 cm^{-1}.

4 Results & Discussion

4.1 Interaction of Polysilazanes with Cellulose-based Templates

Employing templates as a tool to transfer morphological characteristics onto ceramic material systems has attracted considerable attention from researchers in the past. Utilizing this approach, well-defined morphologies, porosities, and microstructures have been successfully generated in various materials that otherwise would have been difficult or even impossible to obtain.

In this chapter, the use of regular cellulose-based papers as a template material for the generation of PDCs with morph-genetic paper-like morphology is presented and the underlying principles relevant for the successful morphological feature transfer are discussed in detail. Moreover, the bonding mechanism of the preceramic polymer to the cellulose fibers and the interactions between them arising during polymer-to-ceramic conversion are explored. Finally, the processing parameters that may decisively affect the morphological characteristics of the PDCPs, such as the type of cellulose fibers or carbon content of the preceramic organosilicon polymer are evaluated.

4.1.1 Bonding Mechanism between Polysilazane-based Polymers and Cellulose Substrates

As described in Chapter 3.1, the pristine paper templates are dip-coated with the freshly prepared SSP, leading to preceramic papers surface modified with a metal-containing SiMOC(N)-based (M = Fe, Ni, Pd) polymer coating. Fig. 4-1 displays SEM overviews of the untreated “Sartorius” paper template (a), the same paper coated with a SiFeOC(N) polymer (b), and the corresponding ceramic paper upon pyrolysis at 1000 °C in ammonia atmosphere (c). In addition to C and O signals from the cellulose fibers, distinct Si and Fe signals are evident in the EDS spectrum of the preceramic paper, showing the successful surface modification of the template with the preceramic polymer. Upon pyrolysis, a polymer-derived ceramic paper is obtained with the paper morphology of the template clearly retained. The fiber morphology represents that of the cellulose fibers rather faithfully, with fine details of the paper structure being transferred to the ceramic system. Meanwhile, the fibers have undergone extensive shrinkage during pyrolysis exhibiting less than 50 % of their original volume, which will be further discussed in the next chapter (Chapter 4.1.2). EDS analysis demonstrates that the preceramic polymer has been converted into a SiFeO(C)-based ceramic layer that is, according to the uniform contrast in the BSE image, homogeneously encasing the fibers. Notably, no N signal is evident in the PDCPs suggesting that it was removed from the polysilazane-based system during the polymer-to-ceramic conversion.

The results show that the template-assisted PDC route is a feasible way to obtain ceramics with paper-like morphology; however, questions concerning the intrinsic structure and bonding of the PDC layer to the fibers arise that have to be addressed by cross-sectional SEM and TEM examination. For this purpose, ultra-thin sample slices suitable for electron transmission were prepared from the ceramic papers by ultramicrotomy sectioning as described in the experimental section.

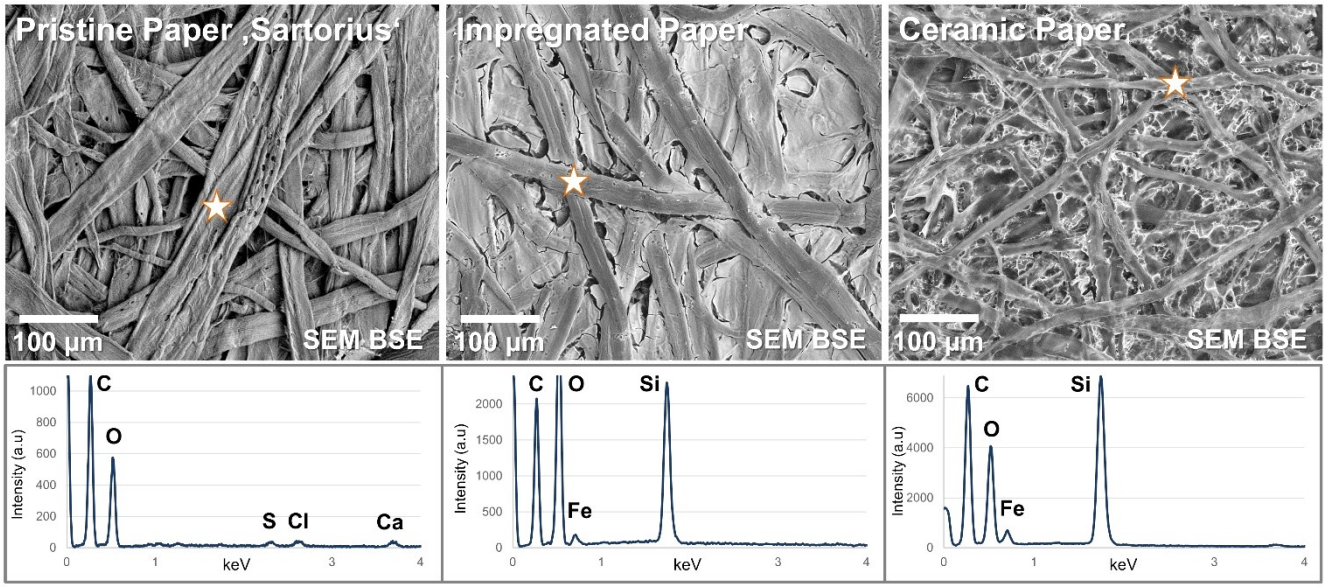

Figure 4-1: SEM images of the pristine commercially available filter paper "Sartorius" (a) showing the typical paper structure of randomly interwoven cellulose fibers primarily composed of C and O according to EDS analysis. Surface modification with a SiFeOC(N)-based polymer leads to a uniformly coated paper template showing distinct Si and Fe signals in the EDS spectrum (b). Upon pyrolysis at 1000 °C, a ceramic paper with a morphology inherited from the template is obtained (c). EDS spectra were acquired at the locations marked.

In Fig. 4-2, a TEM BF image of an ultramicrotomy sample prepared from the SiFeOC(N)-modified ceramic paper upon ammonolysis at 1000 °C is displayed (a). The PDCP is shown to be composed of cellulose-derived carbon fibers coated with a SiFeOC-based ceramic layer. Accordingly, the ceramic papers produced can be denoted as C/SiFeOC ceramic microcomposites. The coating exhibiting a relatively homogeneous width of around 100–300 nm continuously encases the fibers, closely representing their surface morphology, and is easily distinguishable from the carbon by the amplitude contrast in the BF images. Clearly, the sample prepared via UM sectioning has ideal characteristics for TEM-based microstructure analysis as it provides vast sample areas (basically the extent of an individual slice being 100x200 µm) with a relatively uniform thickness of approximately 50-80 nm. However, as shown by the fragmented ceramic coating (b), artifacts introduced by the slicing procedure are a major concern of UM preparation. It is well established that the mechanical stress applied by the diamond knife can result in compressed, sheared, or fractured samples depending on the materials' mechanical properties [202]. Consequently, it is paramount to have complementary preparation pathways to assess artifacts and gain a reliable understanding of the undisturbed microstructure of the sample. As described earlier, a preceding study proved that the fractured ceramic layer is not an intrinsic feature of the in situ-generated

microstructure of the PDCPs [201]. Since conventional MultiPrep polishing of the same ceramic paper results in samples with an intact PDC coating encasing the fibers (c), the fragmentation can be attributed to the ultramicrotomy slice-cutting procedure.

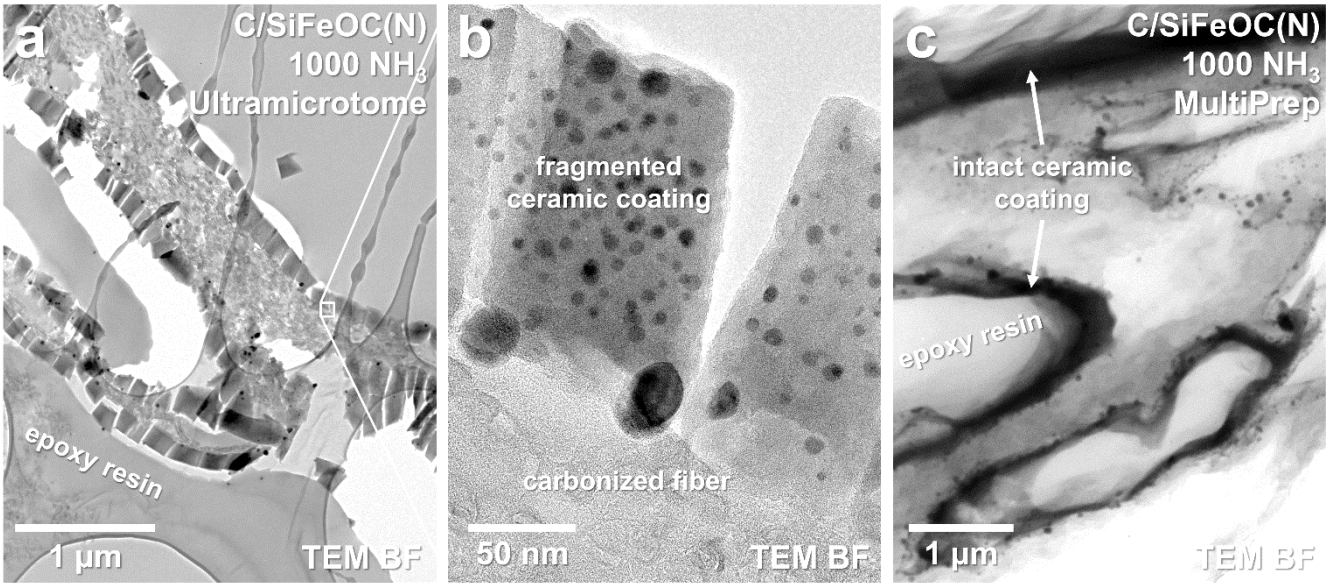

Figure 4-2: TEM bright-field image of a fiber cross-section in the SiFeOC(N)-modified ceramic paper ammonolysis at 1000 °C prepared via ultramicrotomy slice-cutting (a). The cellulose-derived carbon fiber is entirely encased by a SiFeO(C,N)-based ceramic coating exhibiting a rather uniform thickness. The high-magnification BF image of the interface between the cellulose-derived carbon and the PDC layer (b) shows numerous nanosized precipitates dispersed within the coating. Please note that the ceramic layer has been fractured during the UM preparation with the fragments remaining attached to the substrate. Complementary MultiPrep polishing reveals an intact coating encasing the fibers confirming that the fragmentation is an artifact of the sectioning procedure, not an intrinsic feature of the PDCPs (c).

Notably, although the coating has been fractured during sectioning, most fragments remained attached to the carbon fibers, displaying the firm adhesion between the ceramic coating and its substrate. Polysilazanes in their polymeric state exhibit outstanding properties that make them predestined for application as a coating material. In addition to their high thermal and chemical stability, compared to typical organic coatings, polysilazanes can display superior adhesion to their substrate, as reactions with -OH surface groups may lead to the formation of strong chemical bonds. Fig. 4-3 displays the three adhesion mechanisms that facilitate covalent Si-O bonding between silazanes and their substrates, as summarized by others [209–211]. First, the interaction of Si-H bonds with -OH surface groups results in the formation of a single oxygen bridge accompanied by the release of molecular hydrogen gas (a). Secondly, two Si-O bonds may result from Si-N-Si bonds interacting with -OH, breaking the silazane backbone chain to form Si-NH_2 groups and a Si-O linkage to the substrate. In a second step, Si-NH_2 interacts with an additional -OH group, creating another oxygen bridge and simultaneously releasing ammonia gas (b). Finally, silanol groups may form in the polymer chain if water is present, which then can react with the substrates' functional groups to form Si-O bonds and release water, a process called hydrolysis (c).

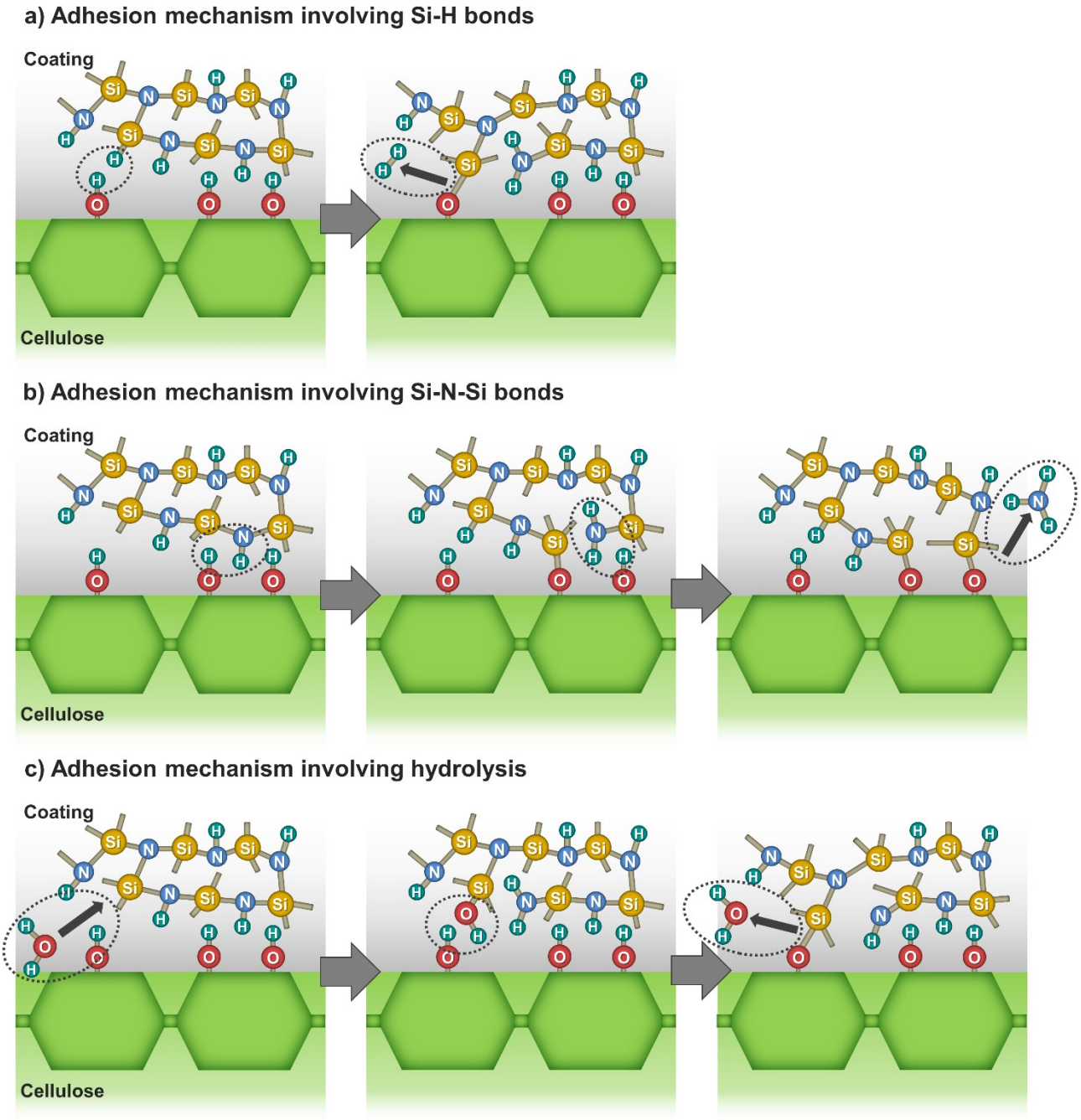

Figure 4-3: Schematic depiction of the three adhesion mechanisms proposed to be responsible for the strong covalent bonding between polysilazane-based polymers and -OH surface groups of the substrate. Based on [209,211].

As hydroxy-groups are a principal component of the cellulose structure (that is six -OH units per glucose dimer), the use of cellulose as a template material offers a decisive synergy with polysilazane precursors by facilitating strong adhesion of the polymeric precursor via the depicted mechanisms. The polymer coating remains linked to the fibers during ceramization, leading to a ceramic layer that uniformly encases the cellulose-derived carbon and remains attached to the substrate, even under applied mechanical stress.

Further indications for chemical bonding of the SSPs to the cellulose template were accessed via FT-IR analyses, as depicted in Fig. 4-4. Here, three measurements acquired from the as-prepared SiFeN(O,C) precursor, the pristine 'Sartorius' paper template, and the impregnated preceramic paper are displayed. As expected, the pristine template exhibits distinct O-H vibrational bands (3600 – 3100 cm^{-1} and 1650 cm^{-1}), while the SSP shows a rather sharp Si-H band (2145 cm^{-1}). In the preceramic paper surface modified with the SiFeN(O,C) polymer, both the O-H and Si-H bands have been notably reduced in intensity and a small N-H band visible in the polymer precursor (1180 cm^{-1}) has vanished in the impregnated paper. Please note, however, that the intensity reduction of the Si-H and N-H bands may be affected by the lower volume fraction of the polymeric coating compared to the pure precursor. Nevertheless, both observations substantiate that the reactions described above contributed to the strong adhesion of the polysilazanes to the cellulose substrate and thus, are believed to be a requirement for the formation of a resilient ceramic layer encasing the carbonized fibers completely. Accordingly, using polysilazane-based preceramic polymers for the modification of cellulose-based templates is a synergistic combination for the fabrication of PDC microcomposites with specialized morphologies.

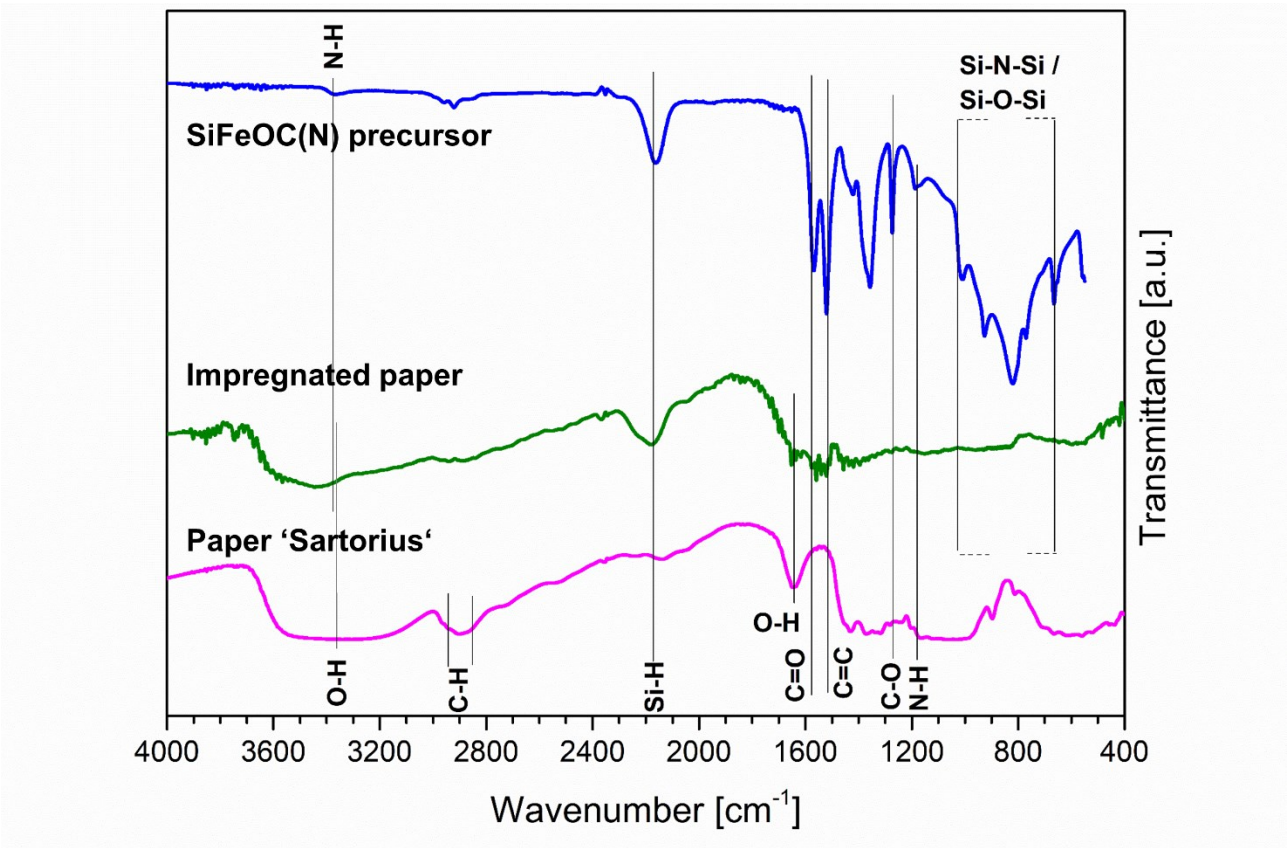

Figure 4-4: FT-IR spectra of the as-prepared SiFeOC(N) precursor, the pristine Sartorius paper, and the impregnated template. In the surface-modified paper, O-H bands are drastically reduced in intensity, compared to the untreated template. At the same time, sharp Si-H and N-H bands observed in the preceramic polymer are less pronounced, together indicating that covalent bonding between the polymer and the substrate took place by the reactions described in the text. Data were acquired in ATR mode; courtesy of Alexander Ott.

4.1.2 Impact of Varying the Paper Template

To assess the effect of the different papers on the morphological features, composition, phase assemblage, and microstructure of the PDCPs, samples derived from each of the templates, with all other synthesis parameters held constant, were comparatively investigated.

Scanning electron microscopy (SEM) imaging of the two papers produced for use as templates in the present research reveals their typical structure of randomly interwoven cellulose fibers, as depicted in Fig. 4-5 a,b. Some morphological differences are evident in the images, with 'Eucalyptus' ('Euc') consisting of relatively straight and flat fibers with an average (in-plane) diameter of 13 µm, whereas 'Cotton Linters' ('Lin') predominately accommodates rounded and curved fibers averaging at a slightly larger diameter of 16.5 µm. Also, some specific features unique to the respective paper can be observed, such as fibers with a regular pattern of macropores reminiscent of wood cells, which are only found in 'Euc', and fine cellulose fibrils (50-500 nm diameter) scattered throughout the cotton-derived 'Lin'.

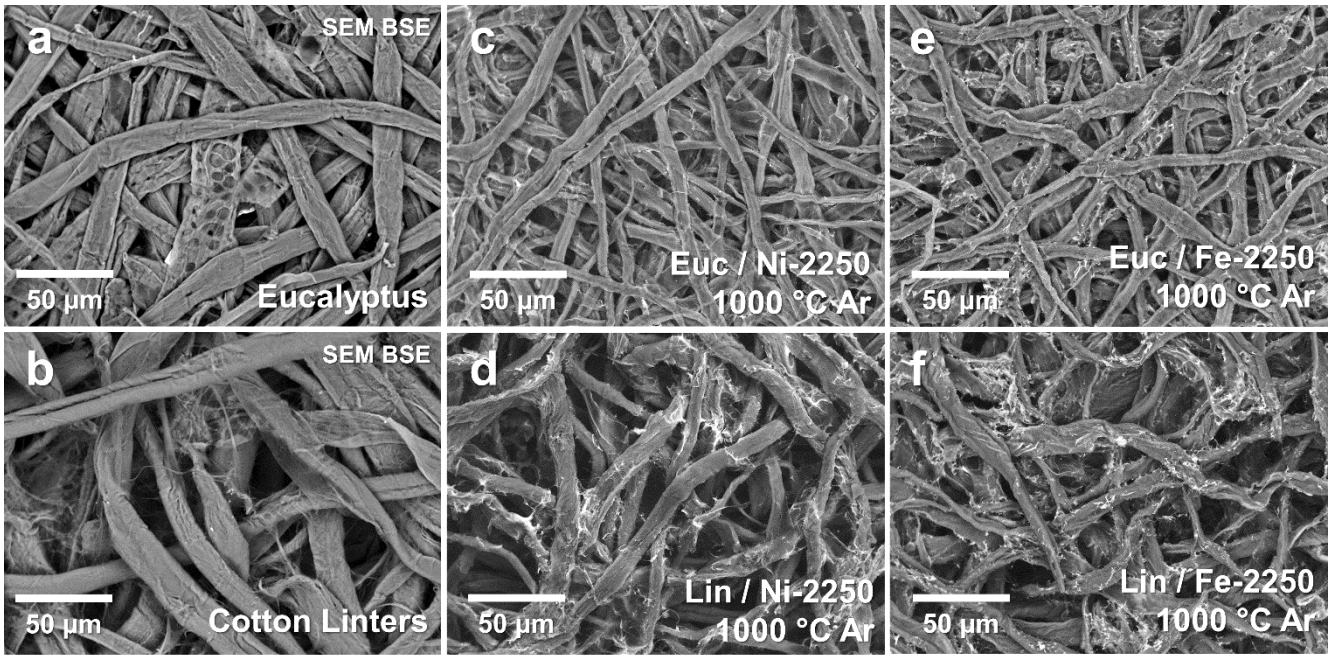

Figure 4-5: SEM BSE images of the cellulose-based paper templates 'Eucalyptus' (a) and 'Cotton Linters' (b). Images c-d show Ni-modified PDCPs upon pyrolysis at 1000 °C, produced from each of the two paper templates. The morphology accurately resembles that of the respective template employed, without other notable differences apparent. The use of an Fe-modified precursor leads to identical results (e-f). Own work, adapted from [200].

Upon impregnation with the Ni-modified Durazane2250 (PHPS) preceramic polymer and consecutive pyrolysis at 1000 °C in Ar atmosphere, two PDCPs are generated (c-d) faithfully resembling the overall morphology of the paper employed. Structural details, such as the flatter fibers and pore structures in 'Euc' or microfibrils in 'Lin', have been transferred onto the SiNiOC-based ceramic papers, allowing for easy distinction between the two PDCPs. Meanwhile, considerable shrinkage is evident in both papers. The (in-plane) fiber diameter in Euc/Ni-PHPS averages at just over 6 µm, whereas the fibers in Lin/Ni-PHPS have shrunk to around 8.5 µm, corresponding

to approximately 50 % (54 % and 49 %, respectively) volume shrinkage. The same can be observed for Fe-PHPS papers (e-f), which are also easily distinguished by their characteristic morphology and exhibit a similar degree of shrinkage. Apart from the morphological features accurately resembling that of the template, no notable differences between the two PDCPs in either system are evident at this scale of observation.

To investigate the impact of the paper templates on the phase assemblage generated, powder X-ray diffraction (PXRD) studies of the ceramic papers were conducted as depicted in Fig. 4-6. The spectra of the three Fe-PHPS-modified papers processed in ammonia atmosphere at 1000 °C are rather similar to each other, being predominately amorphous. Regardless of the template used, only small and broad reflexes tentatively assignable to α-Fe (*Im*$\bar{3}$*m*) or Fe_3C (*Pnma*) occur at ≈52.6° and ≈50.2°, respectively. Although unambiguous phase identification is not possible based on these data alone, the results highlight that the (bulk) phase assemblage generated is independent of the paper used as template. PXRD analyses conducted on Pd-PHPS-modified PDCPs upon pyrolysis at 1000 °C in Ar atmosphere show the same trend, with identical reflexes detected for both 'Lin' and 'Euc' templates at ≈44.4° assignable to Pd_2Si (*P*$\bar{6}$2*m*) and at ≈46.9° and ≈54.8° matching metallic Pd (*Fm*$\bar{3}$*m*). As the intensity of the maxima is fairly identical and no additional reflexes occur, again, no impact on the phase assemblage through variation of the paper template is indicated.

It is concluded that the choice of the paper templates employed in this study does not affect the microstructure and phase assemblage of the PDCPs investigated, which has also been substantiated by detailed transmission electron microscopy (TEM) studies (compare Fig. 4-8 and reference [200]). Hence, the distinction between the ceramic papers generated from different paper templates will not be made for the remaining chapters and only notable discrepancies are displayed, if applicable.

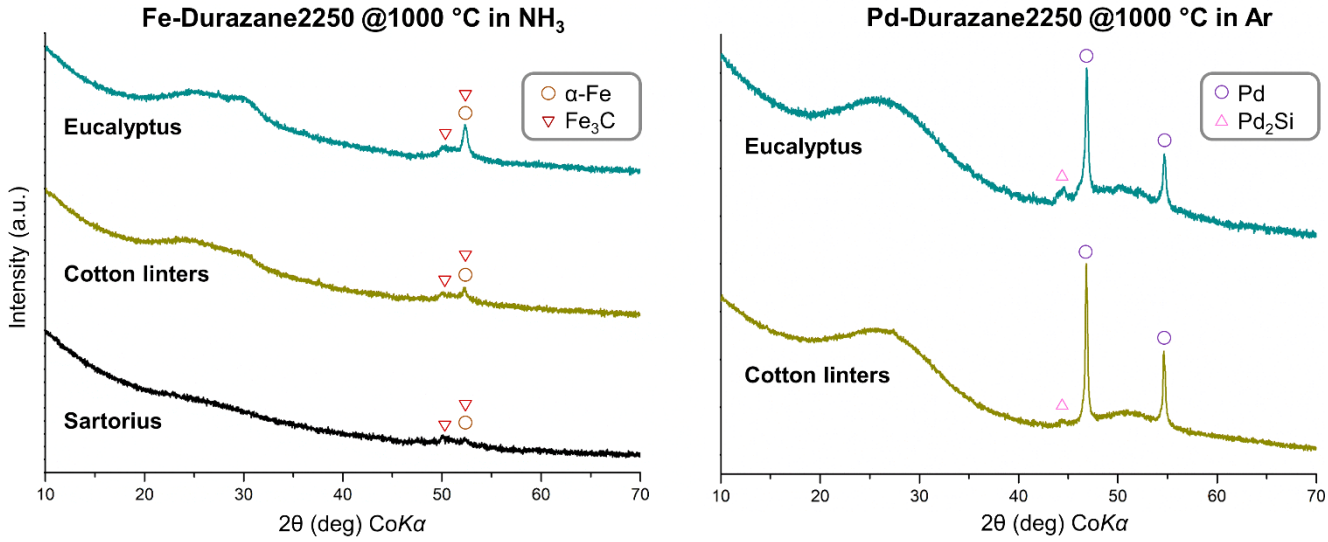

Figure 4-6: PXRD spectra of C/Fe-2250 ceramic papers (left) upon ammonolysis at 1000 °C templated with the three papers 'Sart', 'Lin', and 'Euc'. PXRD spectra of C/Pd-2250 papers (right) upon pyrolysis at 1000 °C in Ar, templated with 'Lin' and 'Euc', respectively. The analyses suggest that no notable variations of the phase composition arise from using different paper templates.

4.1.3 The Characteristics of Polymer-derived Ceramic Papers Upon Interaction of Cellulose with two different Polysilazane Precursors

Apart from the beneficial adhesion behavior between the template and the SSP, the chemical reaction of the organic (and oxygen-rich) cellulose with the oxidation-sensitive polysilazane coatings during pyrolysis may affect the composition, microstructure, and phase assemblage of the resulting ceramic composite.

Two polysilazane-based precursors, Durazane 2250 and Durazane 1800, were employed in the SSP synthesis to assess the impact of their molecular structure on the resulting ceramic composites. Durazane 2250 is a pure perhydropolysilazane (PHPS) composed only of Si, N, and H, whereas, the polyorganosilazane Durazane 1800 contains additional methyl and vinyl side groups attached to the -Si-N- backbone chain [212]. Consequently, for each Si (or N) atom, Durazane 1800 accommodates two C in its fundamental dimer. However, modification with the metalorganic compound Fe(III)acac$_3$ after the possible reaction pathways illustrated in Fig. 3-3 (Chapter 3.1.1) introduces additional C into the polymer. Given that some of the acetylacetonate ligands are released during the formation of Si-M bonds (M = metal) [4,24,213], the resulting C:Si (C:N) ratios are 10:1 for Durazane 2250 and 7:1 for Durazane 1800. Accordingly, in the case of Ni(II)acac$_2$ and Pd(II)acac$_2$, the ratios are 5:1 and 9:1, respectively. If, however, predominately hydrosilylation of the C=O groups catalyzed by the metal sites took place [213,214], the ratios change (i.e. 15:1 and 9.5:1 for Fe(III), as well as 10:1 and 7:1 for Ni(II) and Pd(II)) as no acetylacetonate is released. That is under the assumption that only Si-H bonds are involved in the reaction of polysilazanes with the acetylacetonate compounds, as was concluded in earlier works [4,5]. If the N-H bonds of the polymers or the methyl and vinyl groups of the Durazane 1800 were contributing to the modification process, the ratios could change considerably, which, however, has not been verified by earlier studies. In any case, due to the precursor modification, all SSPs prepared throughout this study contain notable amounts of C and O. Depending on the exact reactions taking place during the modification process, either the Durazane 2250 or the Durazane 1800 exhibit higher C:N ratios. Comprehensive FT-IR studies conducted on both the as-prepared precursors and corresponding PDCs upon pyrolysis revealed only subtle differences, such as indications of a slightly different arrangement of the ceramic network structure, and XRD analyses showed no variations of the phase assemblage generated [8]. Hence, the two SSP systems are overall very similar and their effect on the attributes of the PDCPs is hardly predictable, demanding detailed investigations.

To determine whether the choice of the base precursor affects the morphological and microstructural characteristics of the PDCPs, the different ceramic paper samples were comparatively investigated via electron microscopic imaging and elemental analyses. Fig. 4-7 depicts low-magnified SEM images of ‘Euc’-templated samples prepared using Pd- (a & b), Ni- (c & d), as well as Fe-modified (e & f) Durazane 2250 (top row) and Durazane 1800 (bottom row) SSPs, respectively. Regardless of the metal or precursor utilized, the overall morphology of the papers is identical, without any notable differences evident, and closely resembling the attributes of the paper template employed. Also, the degree of shrinkage was found to be identical for either precursor, and comparative EDS analyses (not shown here) revealed no compositional variance across the

different samples. Thus, concerning the morphology, composition, and general structural characteristics, no impact of alternating between the two different polysilazanes utilized could be observed, with either SSP facilitating the synthesis of pseudomorphic PDCPs with paper structure.

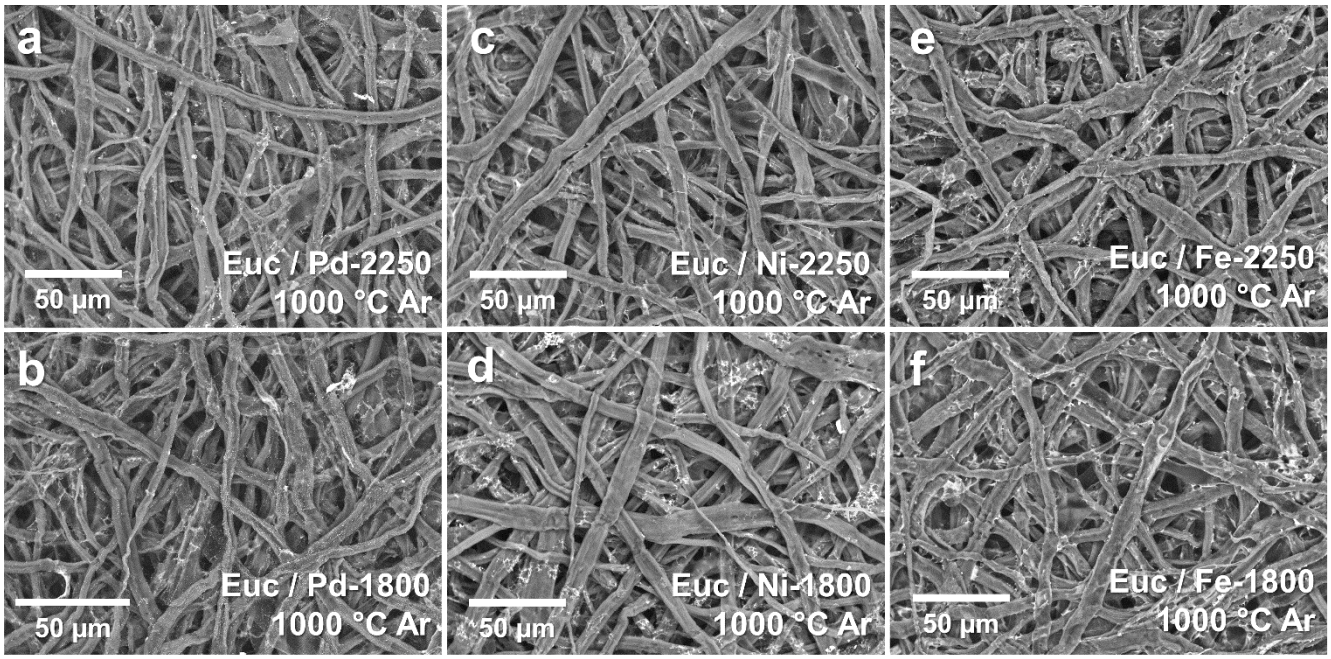

Figure 4-7: Overview of different PDCPs prepared from surface-modification of 'Eucalyptus' paper templates and consecutive pyrolysis at 1000 °C in Ar. Independent of whether Pd (a & b), Ni (c & d), or Fe (e & f) was used for precursor modification, no morphological differences were observed between the papers prepared with Durazane 2250 (top row) or Durazane 1800 (bottom row).

The effect of using different precursors was further investigated concerning possible smaller discrepancies within the ceramic composites, such as distinct phase assemblages, intrinsic microstructural, or localized compositional variations. Fig. 4-8 displays TEM BF images of four cross-sectional samples prepared from Ni-modified papers with alternating template-precursor combinations. In each case, an almost identical microstructure has been generated with cellulose-derived carbon fibers encased by a PDC layer of varying width. Locally, numerous small Ni-based precipitates are dispersed within the ceramic layer, whereas in other sections, none are observable. The fibers have undergone extensive graphitization, as indicated by the characteristic contrast, and also accommodate several Ni-based precipitates, which exhibit larger diameters than the ones found in the coating. Generally, the microstructural characteristics observed, such as the width of the ceramic layer, the degree of graphitization, or the occurrence of precipitates, display more variation within a single sample than across the different ceramic papers. Even the composition of the SiOC-based PDC coatings was shown to be identical, regardless of the template or precursor used (compare the corresponding EDS analyses). This was also found to be the case in the Fe- and Pd-modified samples, and the PXRD analyses presented in the following chapters reveal no notable variations concerning the phase assemblage within each of the three transition metal systems; especially in the samples upon high-temperature annealing. Hence, any major effect of the SSP investigated on the characteristics of the PDCPs generated can be excluded based on the results of the present research (see also reference [200]).

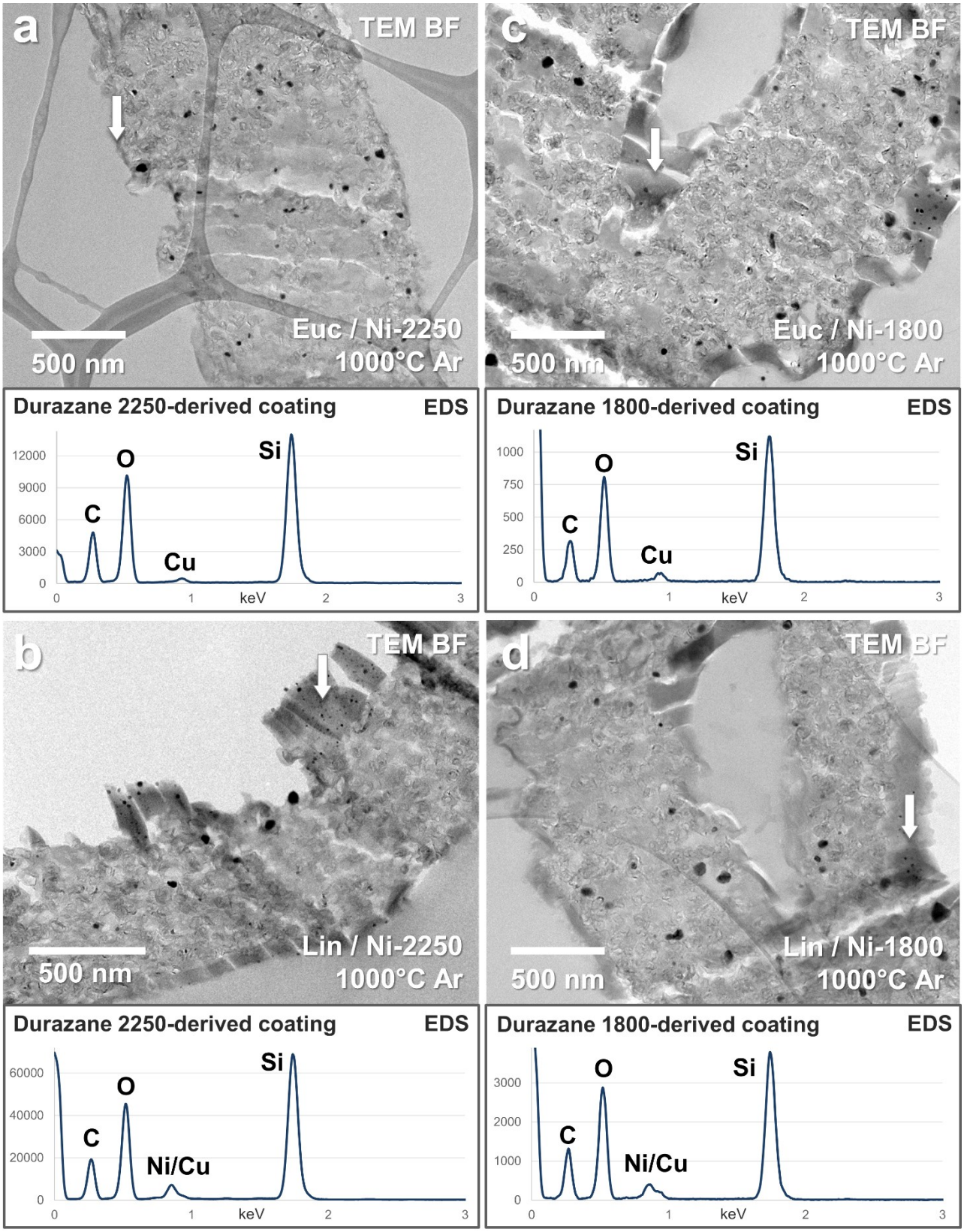

Figure 4-8: TEM BF images of the four cross-sectional samples prepared from the Euc/Ni-PHPS (a), Lin/Ni-PHPS (b), Euc/Ni-Durazane (c), and Lin/Ni-Durazane (d) papers upon pyrolysis at 1000 °C in Ar atmosphere. As shown in the EDS spectra, cellulose-derived carbon fibers were found to be encased by a continuous Si(Ni)OC-based coating, with close to identical elemental ratios across all four ceramic papers. EDS locations are indicated by arrows. Own work, adapted from [200].

Finally, it is important to note that upon pyrolysis of the SSP-modified papers, a pure SiOC-based ceramic layer is generated regardless of the precursor utilized. The removal of N from the system can be attributed to the interaction of the oxidation-sensitive precursors with reactive pyrolysis products originating from the cellulose template. Similar mechanisms apply as proposed for the bonding between the SSP and the cellulose, creating Si-O-Si linkages at the expense of Si-N-Si bonds [215,216]. As presented later in this work, this even applies to PDCPs processed in a nitriding (NH_3) atmosphere, which implies that the generation of non-oxidic PDCs may be difficult or even impossible to achieve if a cellulose template is utilized. Also, the results show that the carbon content of the SiOC matrix generated is independent of the precursor used. Neither the present EDS data nor intensive FT-IR characterization of the samples revealed compositional differences or pronounced formation of Si-C bonds in either precursor system [8]. Again, this might be an effect of the cellulose template releasing hydrocarbons during pyrolysis that can react with the PDC layer as well as the acetylacetonate ligands introduced via precursor modification.

Interaction of Polysilazanes with Cellulose-based Templates - Summary

- Upon pyrolysis of cellulose-based paper templates surface-modified with SiMOC(N)-based (M = Fe, Ni, Pd) single-source precursors, pseudomorphic ceramic composites with a morphology inherited from the paper template are generated:
    - The polymer-modified fibers are converted into ceramic composites consisting of cellulose-derived carbon fibers encased by a PDC layer exhibiting strong adhesion to the substrate
    - Bonding is facilitated by interactions between the polysilazanes and hydroxy groups abundant at the surface of the paper fibers, as indicated by FT-IR analyses.
- The morphology of the ceramic papers generated is directly and faithfully inherited from the respective paper template utilized:
    - Conversely, an impact of the paper template on the phase assemblage and microstructure generated could not be concluded from the TEM and XRD results.
- Regardless of the type of polysilazane employed, the PDC coating generated is SiOC-based upon pyrolysis at 1000 °C and nitrogen has largely been removed from the system, attributed to:
    - The precursor modification with the metalorganic acetylacetonate compounds
    - The reaction of the precursors with oxidizing pyrolysis products from the cellulose fibers.
- The morphology, composition, microstructure, and phase assemblage of the ceramic papers showed no variation with using different types of polysilazanes.

4.2 SiFeOC(N)-based Ceramic Papers

In this project, three different transition metals, Fe, Ni, and Pd, were used for the modification of the polysilazane-based polymers. Depending on the transition metal utilized, distinct assemblages, distributions, and particle sizes of metal-based precipitates can be generated, while also different interactions with the cellulose-derived carbon fiber and PDC coating may arise. Consequently, introducing specific metalorganic compounds into the preceramic polymer is a powerful tool to modify the phase composition and microstructural characteristics of the resulting ceramic papers, which in turn, may decisively affect their properties. The focus of the following chapters lies on the phase evolution of the transition metals and the ceramic matrix with respect to the temperature and atmosphere applied during pyrolysis and the consecutive tempering step.

Being one of the most important transition metals, Fe is used in countless application fields such as structural, electrical, magnetic, and catalytic materials just to name a few. Most notably, Fe-based alloys and its numerous intermetallic compounds are of great industrial and scientific interest as they exhibit very desirable and unique properties making them indispensable for modern society. Thus, introducing Fe phases into ceramic material systems offers intriguing possibilities for functionalization and property design that have been utilized in various cases.

4.2.1 Pyrolysis in Reactive Ammonia Atmosphere

The following section presents the low-temperature evolution of SiFeOC(N)-based ceramic papers treated in reactive ammonia atmosphere, as it was published in [7]. Within this subsection, the commercially available filter paper 'Sartorius'paper was used as the template for the PDCPs generated. Applying a reactive ammonia atmosphere during the pyrolysis of organosilicon polymers directly affects the composition of the resulting PDCs. As it was shown for both polysiloxanes and poly(organo)silazanes, beyond 750 °C, NH_3 is very effective in removing free carbon from the system through the formation of HCN gas and, simultaneously, leads to nitridation of Si-R groups (R = H, Me, $CH_2CH_2Si\equiv$, etc.), shifting the composition of the resulting ceramic from SiO_xC_y towards SiO_xN_y [217,218]. Moreover, in the case of Fe-modified ceramic papers, ammonia serves the purpose of generating iron nitrides that are considered interesting for various potential applications, such as for magnetic materials, electrocatalysis, and electromagnetic interference studies [219–221].

Fig. 4-9 displays a TEM BF image of a fiber cross-section prepared from the SiFeOC(N)-based ceramic paper after treatment in ammonia atmosphere at 500 °C. During the ammonolysis, the cellulose fiber has been carbonized (A) and incorporated some N as indicated by the corresponding EDS spectrum. Both the SAED pattern and HRTEM image, along with the FFT inset, reveal that the carbon is entirely amorphous with only some near-range order present as implied by the diffuse concentric discs marked. The fiber is encased by a SiFeOCN coating (B) that is fragmented from the sectioning procedure, but still attached to the fiber and is shown to be monophasic and entirely amorphous by the SAED pattern that reveals no discrete reflexes and a Gaussian intensity distribution.

At higher magnifications, numerous pores are visible in the ceramic layer, predominately mesopores with diameters of 2-8 nm.

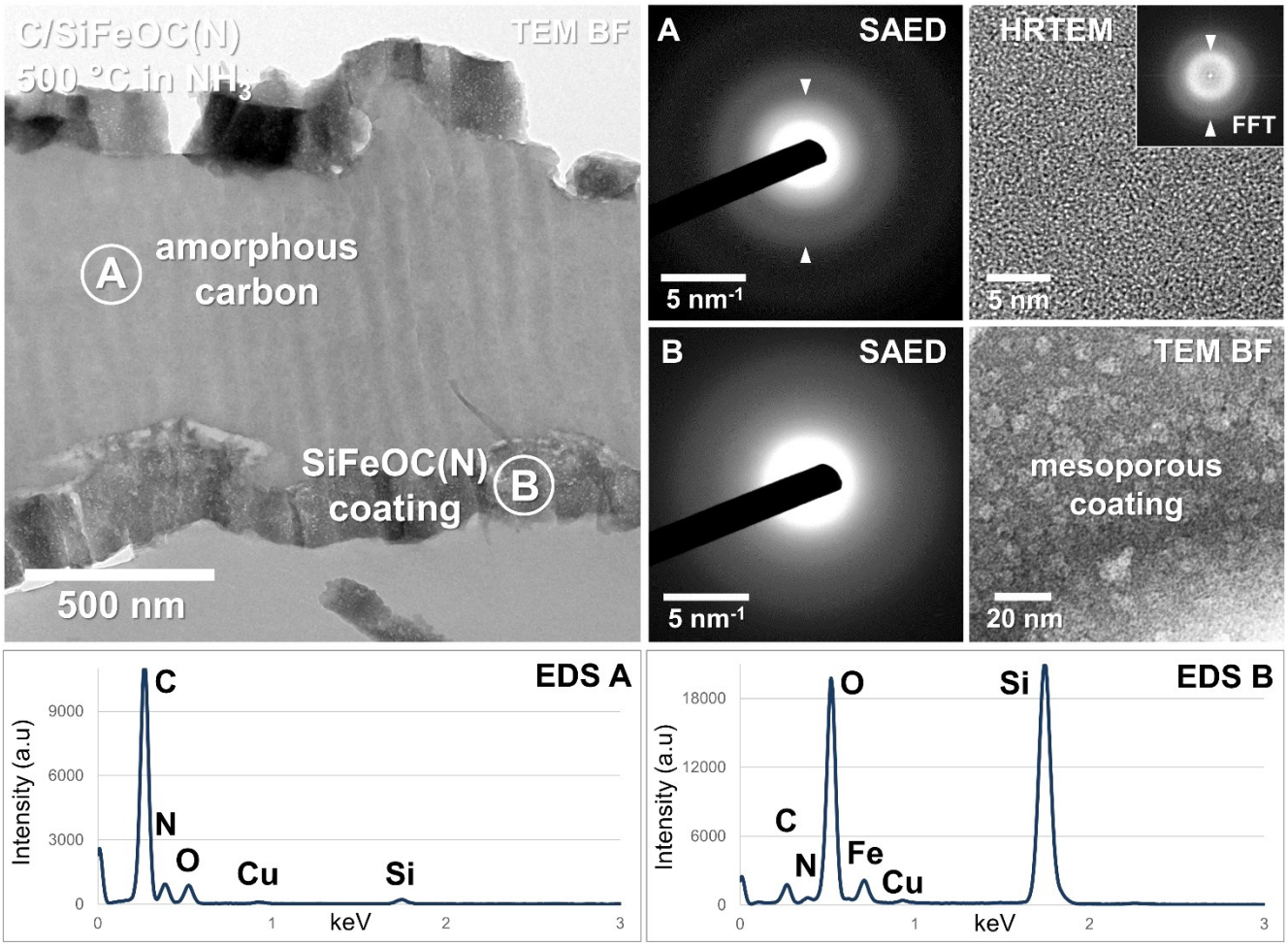

Figure 4-9: TEM BF image of a fiber cross-section in the ceramic paper ammonolyzed at 500 °C. The cellulose-derived carbon fiber (A) is amorphous as shown by electron diffraction and HRTEM imaging, with diffuse concentric discs in the SAED and fast Fourier transformation (FFT) indicating some near-range order present in the pyrolytic carbon. The SiFeOC(N) coating (B) exhibits numerous mesopores in the high-magnification BF image while being monophasic and amorphous according to the SAED pattern. Own work, reproduced from [7].

Upon ammonolysis at 500 °C, the results show the state of the monophasic PDC coating before phase separation of Fe-based precipitates. Clearly, the polymer-to-ceramic conversion is incomplete at this point, as revealed by the porosity visible in the ceramic layer indicating ongoing degassing of volatile species from the coating. Moreover, significant beam damage was observed during TEM imaging with sputtering and associated redeposition of sample matter occurring constantly.

The microstructure of the SiFeOC(N) papers obtained upon ammonolysis at 700 °C is depicted in Fig. 4-10. Apart from the formation of some pores, the cellulose-derived carbon fiber (A) has not changed much compared to the sample prepared at 500 °C, since it was still found to be entirely amorphous by SAED and HRTEM imaging. According to the EDS spectrum, the composition is almost identical, but with less nitrogen incorporated.

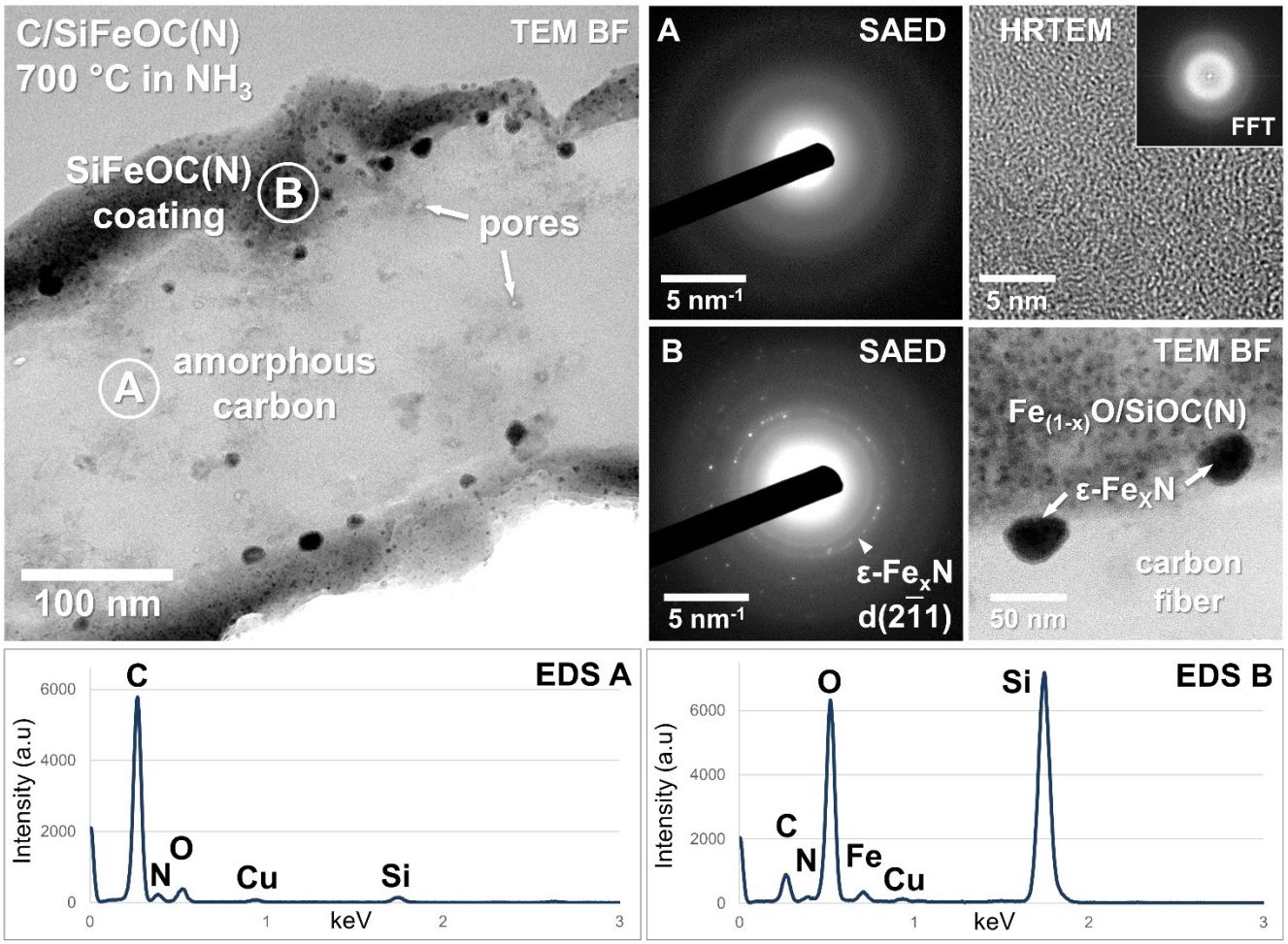

Figure 4-10: TEM BF image of a fiber cross-section in the ceramic paper upon ammonolysis at 700 °C. The carbon fiber (A) is still entirely amorphous, as revealed by the SAED pattern and the HRTEM image, but contains some minor pores indicated by arrows. In the SiFeOC(N) coating (B), precipitation of Fe-based phases has taken place, as shown by the high magnification BF image and the corresponding SAED pattern, with nanosized precipitates finely dispersed within the ceramic layer and another population of larger crystallites mainly occurring along the fiber-coating interface. Own work, reproduced from [7].

The PDC coating (B) on the other hand, shows significant structural changes now containing numerous nanosized precipitates within it and considerably declined in thickness from over 300 nm to around 100 nm. Also, please note that it remained intact during UM sectioning, which might indicate distinct mechanical properties compared to the sample prepared at lower temperatures. While the overall chemistry has not changed notably, the SAED pattern now shows discrete reflections that can be assigned to an ε-Fe_XN phase, i.e. Fe_3N ($P312$), $Fe_3N_{1.2}$ ($P6_322$), Fe_2N ($P\bar{3}m1$), and Fe_2N ($P312$), differing from each other only by occupancy and ordering of N sites in their structure and being difficult to reliably distinguish by X-ray and electron diffraction techniques alone [222]. As the high-magnification image of the fiber-coating contact reveals, two populations of precipitates exist; one being very small particles with diameters of up to 8 nm finely dispersed within the ceramic layer and the other being much larger with around 20-50 nm mainly occurring at the fiber-coating interface.

Fig. 4-11 displays HRTEM images of both phases, along with the corresponding electron diffraction and compositional data. Evidently, the larger precipitates (a) are the ε-Fe_XN crystallites, according to SAED (b) and

EDS (c) analysis, with the Si, O, and C signals stemming from the surrounding amorphous ceramic matrix and the carbonized fiber. Also, the particle exhibits a crystalline shell that is poorly ordered and causes additional faint reflections to occur in the SAED pattern, which however, could not be assigned to a distinct phase unequivocally. According to the EDS spectrum, several Fe-based phases such as Fe_3C, other ε-Fe_XN variants, oxides, or intermediate Fe-O-C-N phases are conceivable. The poor ordering and somewhat polycrystalline appearance of the shell structure suggest that it nucleated on preexisting ε-Fe_XN particles rather than a conversion mechanism, as, for instance, carbothermal reduction, took place, which however, cannot be resolved from the existing data.

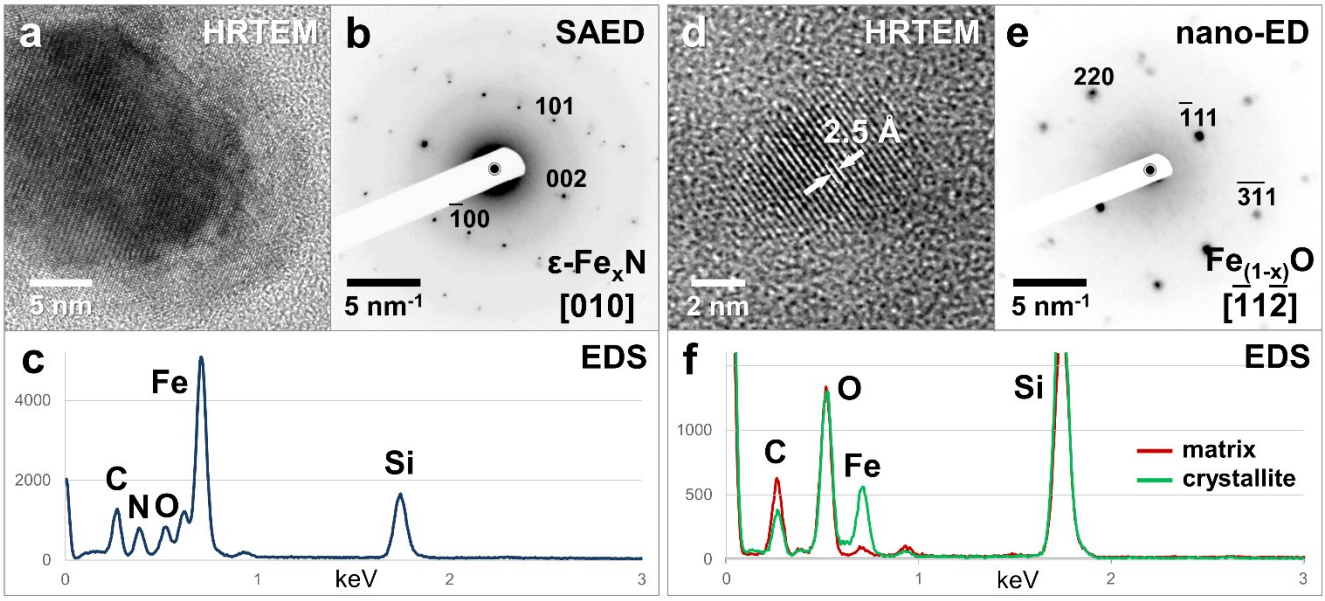

Figure 4-11: Display of the crystalline phases observed upon ammonolysis at 700 °C. The larger precipitates (a) are found along the fiber-coating contact zone and were identified as trigonal/hexagonal ε-Fe_XN via SAED (b) and EDS analysis (c). A multitude of smaller particles (d) is found dispersed within the otherwise amorphous SiOC(N) coating and are shown to be iron oxides with wustite ($Fe_{(1-X)}O$) structure via nano-ED (e) and EDS analyses (f). Own work, reproduced from [7].

The smaller precipitates occurring within the SiOC(N)-based coating (d) were identified as the iron oxide wustite ($Fe_{(1-x)}O$, $Fm\bar{3}m$) using nano-ED (e) and comparative EDS analyses of the particles and the ceramic matrix (f) due to their minuscule size. Please note that no reflexes of Fe-based oxides were found in corresponding XRD measurements [6], which can be rationalized by their extremely small cluster size making them essentially X-ray amorphous. Even with localized SAED methods, only very faint reflexes were generated, usually overshadowed by the diffuse background. Therefore, HRTEM imaging combined with nano-ED is the only method capable of verifying the occurrence of iron oxide particles that are believed to be the first precipitation step of metal-based phases during the separation of monophasic Fe-modified SiOC ceramics [23].

Fig. 4-12 displays a fiber cross-section in the C/SiFeOC(N)-modified paper upon ammonolysis at 1000 °C. Any nitrogen incorporated into the carbon fiber (A) has been removed upon heat treatment at 1000 °C, as is indicated by the missing N signal in the EDS analysis of the fiber, while the spectrum features a rather small O signal

compared to the sample prepared at 700 °C, suggesting a completed carbonization process of the cellulose. As indicated by the heterogeneous contrast in the TEM BF image, the carbon fiber has been partially graphitized, giving rise to discrete concentric ring patterns in the SAED. Most notably, the innermost ring corresponds to the d(002) spacing of graphitic carbon and exhibits a distinct modulation along the fiber direction, indicating a preferential orientation of the lattice planes, likely inherited from the cellulose molecular chains [223]. In the HRTEM image, curved sets of lattice planes characteristic of turbostratic carbon (TC), a semicrystalline intermediate between AC and graphite ($P6_3mc$), are revealed. The lattice fringes exhibit a spacing of just under 3.5 Å being notably higher than the d(002) spacing of 3.34 Å of planar graphite [224], being in close agreement with the 3.44 Å of TC given in the literature [225].

The ceramic layer (B) encasing the cellulose-derived TC fiber is fragmented from the UM sectioning procedure but still attached to the substrate, as was the case in the sample prepared at 500 °C. According to EDS analysis, its composition has not changed much compared to the sample ammonolyzed at 700 °C, with Si, O, C, and Fe being its principal components, but, as in the carbon fiber, without any N signal present. Exclusively along the fiber-coating interface, large crystallites occur, as in the ceramic paper prepared at 700 °C (Fig. 4-10), and, likewise, numerous nanosized precipitates are homogeneously dispersed within the ceramic layer. In the corresponding SAED pattern, several concentric Scherrer rings are visible, which are typical for polycrystalline materials with random grain orientations. The pattern matches the lattice planes of elemental iron, with the innermost ring, relating to the d(110) spacing (2.022 Å) of α-Fe. As displayed in the HRTEM image, the precipitates exhibit a spherical shape and a rather uniform size distribution of around 6-12 nm.

The characteristics of the two crystalline phases present are shown in Fig. 4-13. In the HRTEM image, one of the small precipitates with a diameter of 8 nm contained within the coating is displayed (a). According to nano-ED (b) and comparative EDS analyses (c), the small crystallites were unequivocally identified as metallic α-Fe, surrounded by an amorphous SiOC-based ceramic matrix. Although the presence of Fe-Si phases is conceivable from the EDS spectrum alone, the diffraction data allows excluding Fe_2Si ($P\bar{3}m1$) and Fe_5Si_3 ($P6_3/mcm$), due to their trigonal/hexagonal symmetry and Fe_3Si ($Fm\bar{3}m$), as the {110} reflexes would be absent at this reciprocal position of the ⟨001⟩ zone axis according to the extinction rules in the face-centered Bravais lattice.

In contrast to the papers prepared at lower temperatures, the PDCPs obtained upon ammonolysis at 1000 °C are highly ferromagnetic and become noticeably attracted by an external magnetic field, owing to their high content of metallic iron. This gives a convenient way to macroscopically confirm the TEM results regarding phase composition and highlights the ability to effectively tune the phase composition of PDCPs by merely adjusting pyrolysis temperature.

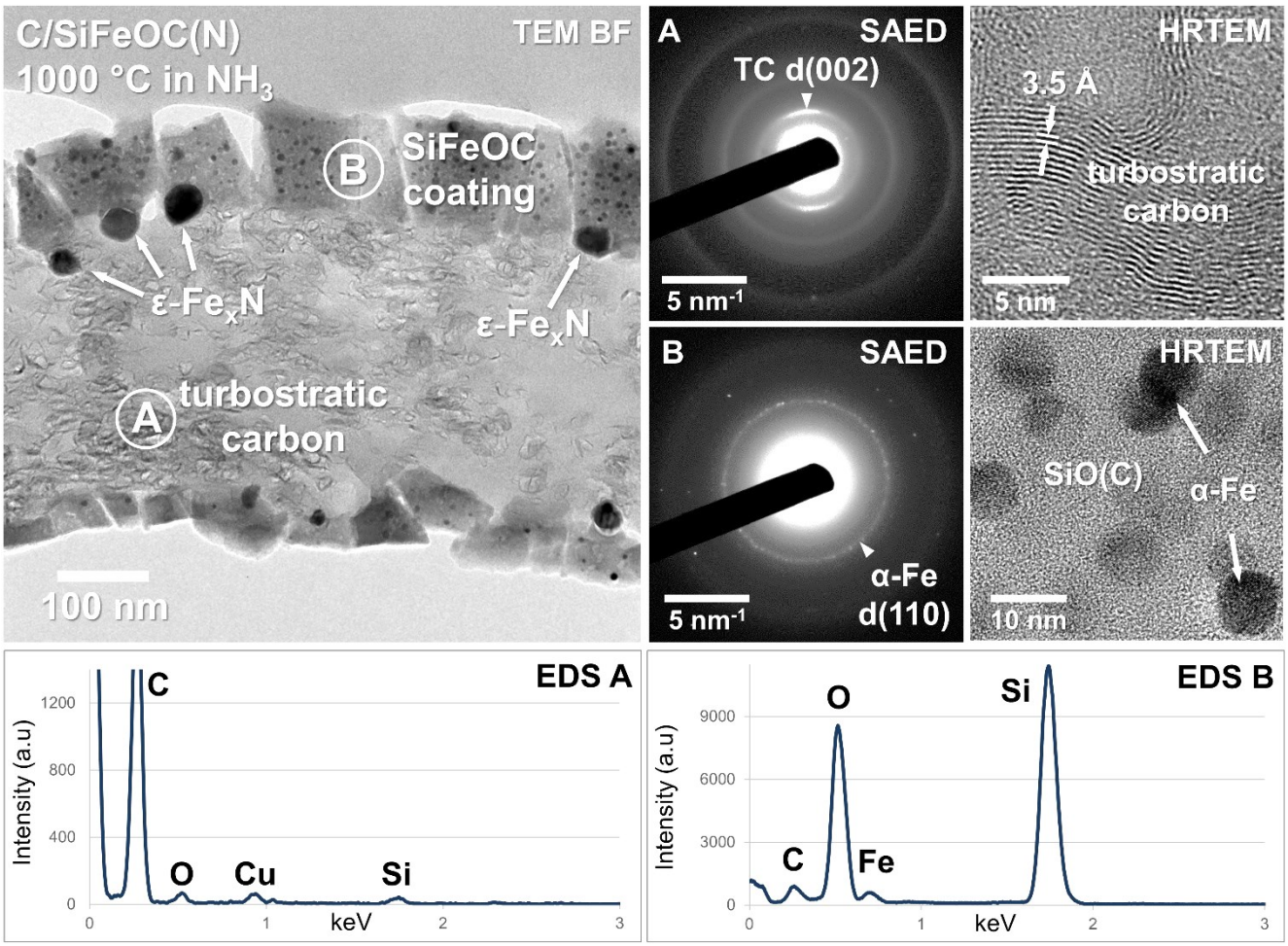

Figure 4-12: Cross-sectional TEM BF image of a fiber in the ceramic paper obtained upon ammonolysis at 1000 °C. The cellulose-derived carbon fiber (A) has been partially graphitized as indicated by discrete reflex rings arising in the corresponding SAED pattern. The HRTEM image shows curved sets of lattice planes with a spacing of just under 3.5 Å, typical for semicrystalline turbostratic carbon. Dispersed within a SiOC-based ceramic matrix (B), numerous nanosized precipitates occur, giving rise to discrete reflections in the corresponding SAED pattern, which are assignable to metallic α-Fe, while the larger ε-Fe$_X$N precipitates are exclusively observed along the fiber coating interface. Own work, reproduced from [7].

As in the paper prepared at 700 °C, larger crystallites (d) were observed intermittently occurring along the fiber-coating interface. Despite their size of up to more than 100 nm, they exhibit spherical crystal shapes with only rudimentarily developed crystal facets, while even the largest are single-crystalline, according to SAED (e). Via diffraction and EDS analysis (f), the phase could be identified as ε-Fe$_X$N with a composition close to stoichiometric Fe_3N; however, superlattice reflections along various directions can occasionally be observed in the diffraction patterns, which has been attributed to the ordering of N vacancies in the literature, indicating intermediate compositions between Fe_3N and Fe_2N [226]. As ε-Fe$_X$N was only observed along the fiber-coating contact zone and not within the ceramic layer, a higher nitridation potential in the cellulose-derived carbon fiber compared to the bulk crucible atmosphere is assumed.

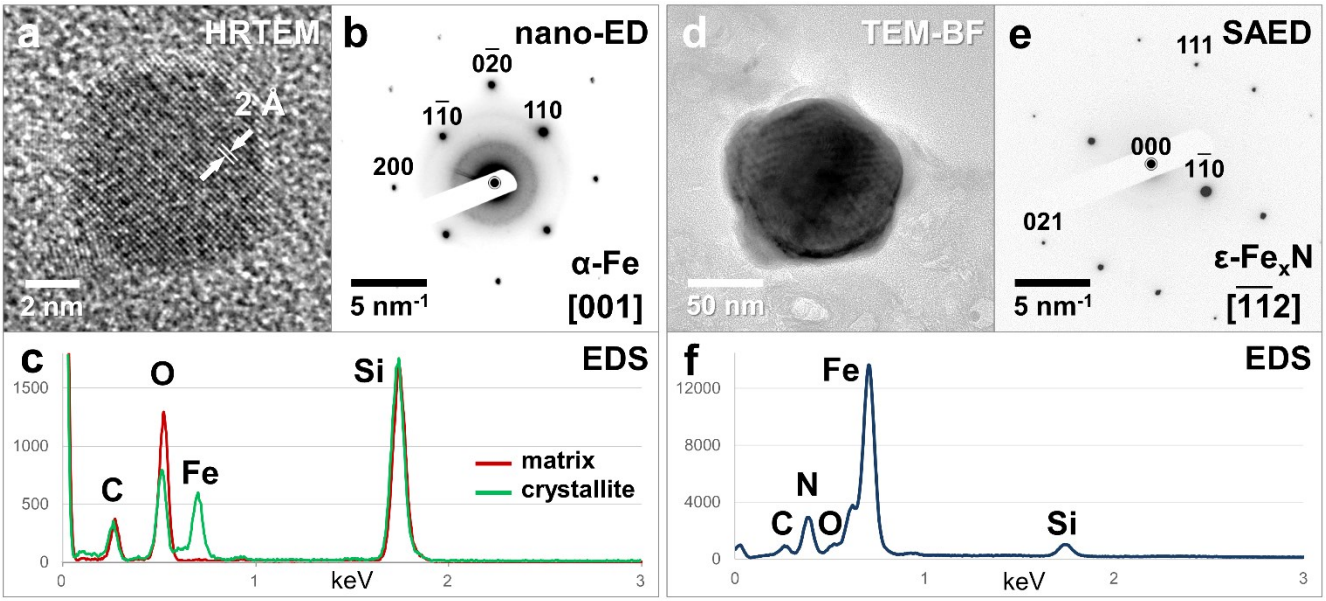

Figure 4-13: Fe-based phases identified in the SiFeOC(N)-modified ceramic paper upon ammonolysis at 1000 °C. One of the nanosized precipitates contained in the ceramic coating is shown in the Fourier-filtered HRTEM image (a) and was identified to be α-Fe via nano-ED (b) and EDS analyses (c). Along the fiber-coating interface, as in the sample prepared at 700 °C, much larger ε-Fe$_X$N crystallites occur (d), revealed by the corresponding SAED pattern (e) and EDS spectrum (f). Own work, reproduced from [7].

4.2.2 Low-Temperature Evolution of SiFeOC(N) PDCPs Upon Ammonolysis

From the results shown, the low-temperature evolution of the SiFeOC(N)-modified ceramic papers treated in ammonia atmosphere can be deduced, as summarized in Fig. 4-14. The figure displays the microstructures and phase assemblages observed in the SiFeOC(N)-modified ceramic papers upon ammonolysis at 500, 700, and 1000 °C as well as the processes that were found to take place between each temperature step.

Upon pyrolysis at 500 °C, a monophasic SiFeOC(N)-based ceramic is generated encasing the cellulose-derived carbon fiber, without any crystalline phases detected. While ammonolysis of PHPS-based precursors usually results in SiCN-based ceramics, in this case, only minor N contents were detected. The cellulose template contains large quantities of oxygen, which are released during pyrolysis (e.g. as -OH or H_2O) and can react with the polymer to form Si-O bonds via hydrolysis or are accompanied by the release of NH_3 as described in Chapter 4.1.3 [215,216]. Indeed, TGA analysis has shown that the main mass loss of the SiFeOC(N)-modified papers takes place between 240–400 °C, where over 45 wt.-% are lost due to the liberation of H_2O, NH_3, and organic compounds. This substantiates that the interaction of the template with the SSP is responsible for shifting the composition of the PDC layer towards SiOC. Between 400–1180 °C, mainly CO and CO_2 are released, resulting in another 22 wt.-% being lost [8]. At 500 °C, it is assumed that a significant portion of the CO_X results from the decomposition of acetylacetonate ligands containing the Fe before phase separation. The multitude of micro-and

mesopores within the ceramic matrix revealed in the TEM images, give additional indication of the ongoing release of gases from the coating.

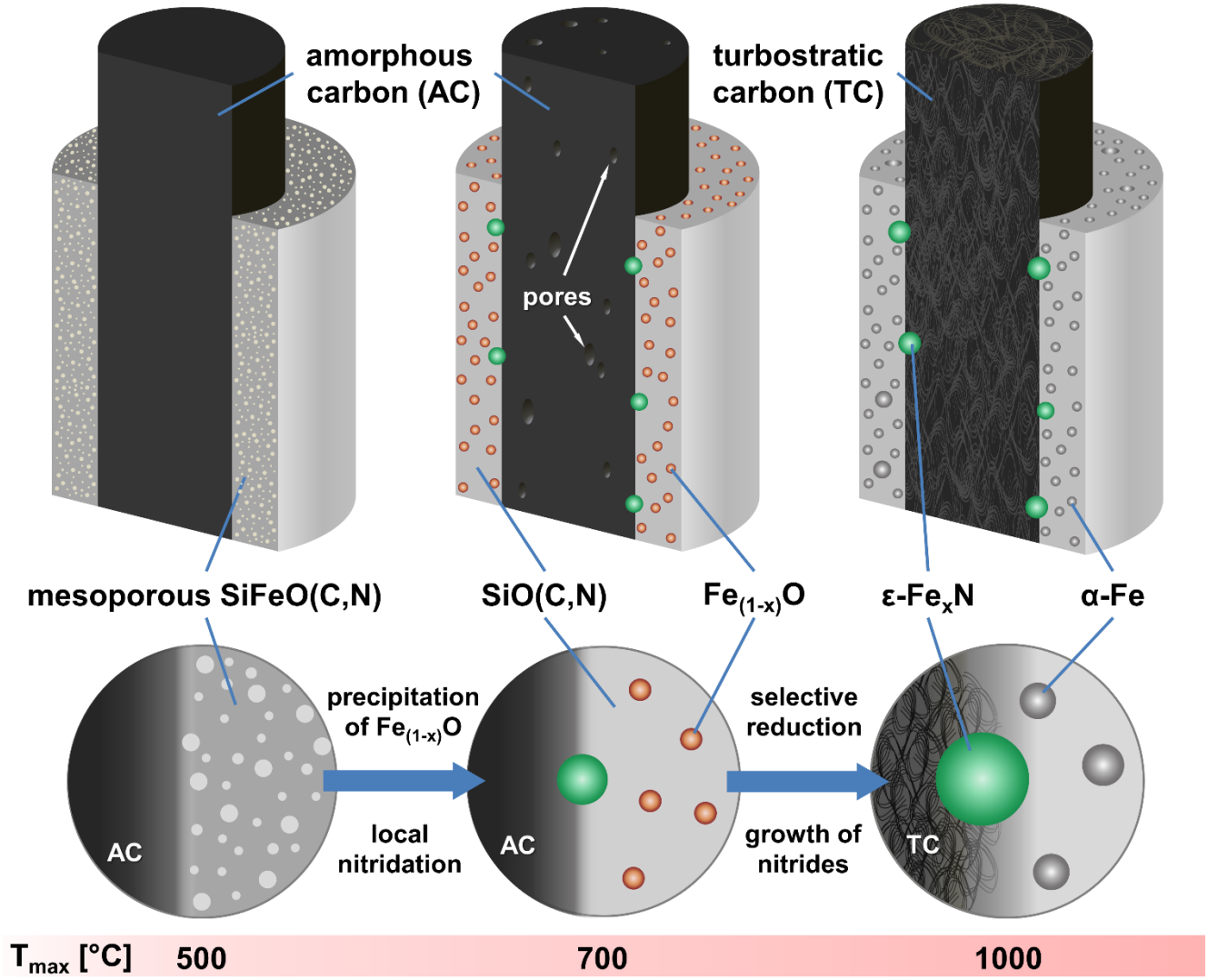

Figure 4-14: Summary of the low-temperature evolution of the C/SiFeOC(N)-based ceramic papers showing the microstructure and phase assemblage observed after 500, 700, and 1000 °C treatment in NH_3 atmosphere. Until temperatures of at least 500 °C, the PDC layer is entirely monophasic with some of the polymeric structure retained. Phase separation has taken place in the sample prepared at 700 °C, resulting in the in situ precipitation of $Fe_{(1-X)}O$ particles within the coating, which were observed to be nitridated along the fiber coating interface forming ε-Fe_XN. Upon ammonolysis at 1000 °C, the cellulose-derived carbon fiber has been partially converted into turbostratic carbon, while the iron oxides have been reduced to metallic α-Fe. Meanwhile, the nitrides along the fiber-coating contact zone have grown considerably, indicating a distinct nitridation potential within the porous carbon fiber. Own work, reproduced from [7].

Upon ammonolysis at 700 °C, a multitude of nanosized Fe-oxides precipitate within the ceramic coating. As proposed in an earlier study, they are formed due to the oxygen-rich environment of the Fe atoms in the Fe(III)$acac_3$-modified polymer and resulting monophasic SiFeOC(N) coating [23]. According to the TEM results, the non-stoichiometric oxide wustite is the prevailing Fe-based phase, as verified via electron diffraction. In the

Fe-O phase diagram, the stability window of $Fe_{(1-x)}O$ without magnetite ($Fe^{2+}Fe^{3+}{}_2O_4$, $Fd\bar{3}m$) or metallic α-Fe present requires a narrow oxygen content range of around 23-24 wt.-% at 700 °C. However, within the two-phase fields α-Fe + $Fe_{(1-x)}O$ (0-23 w.-%) and $Fe_{(1-x)}O$ + Fe_3O_4 (24-27.7 w.-%), wustite is stable over a broad compositional range [227,228]. While no α-Fe or Fe_3O_4 precipitates could be identified, it is reasonable to assume that at least some exist among the numerous crystallites. Above around 710 °C, $Fe_{(1-x)}O$ will be reduced to Fe or Fe_3C in the presence of carbon [229] and below 560 °C, wustite is metastable and will decompose to form metallic iron and magnetite [227]. However, if the temperature falls below 300 °C, the decomposition process becomes extremely slow, presumably leading to the preservation of the metastable particles due to the comparably fast cooling of the ceramic papers. The detection of nanosized wustite in the ceramic coating is quite notable as, on the one hand, it gives general insights into the phase evolution and separation process of the preceramic SiFeOC(N) polymer, and on the other, $Fe_{(1-x)}O$ is recognized as an active compound in catalysis [230], which recently has been explored for potential application in experimental battery concepts [228].

With ε-Fe_XN, the sample features another Fe-based compound predominately occurring along the interface between the ceramic layer and the amorphous cellulose-derived carbon fiber. Exhibiting diameters between 20-50 nm, they are much larger than the Fe-oxides and their predominant generation along the fiber-coating contact zone implies distinct chemo-physical conditions compared to the ceramic matrix. The porosity generated within the cellulose-derived carbon fiber upon pyrolysis enables the diffusion of gas molecules along the pore volume to take place. In principle, this should selectively promote fast diffusion of smaller species, such as H_2 (kinetic radius: 289 pm), NH_3 (260 pm), and H_2O (265 pm)), whereas larger gases, such as CO_2 (330 pm) or N_2 (364 pm) are retained. Hence, ammonia diffusing through the pyrolytic carbon can react with Fe-oxides along the interface with the ceramic coating to either directly form Fe-nitrides or allow carbothermal reduction nitridation reaction via

$$N_{(g)} + C_{(s)} + Fe_XO_{(s)} \rightarrow Fe_XN_{(s)} + CO_{(g)} \qquad \text{(Eq. 4-1)}$$

to take place [231,232]. Moreover, EDS analyses of the carbon fibers revealed distinct N signals upon ammonolysis at 500–700 °C, which indicates transport of nitriding species within the porous carbon fiber. Permeation of gases through the dense ceramic coating, on the other hand, should be much slower, rationalizing why almost no ε-Fe_XN crystallites are generated here.

Upon ammonolysis at 1000 °C, the microstructure of the ceramic papers has changed considerably, featuring highly graphitized carbon fibers encased by a SiOC-based ceramic layer containing numerous nanosized a-Fe crystallites. While the phase separation of the monophasic PDC coating into a FeO/SiOC(N) nanocomposite between 500 °C and 700 °C is recognized in the literature, questions remain regarding the exact formation mechanism of the α-Fe nanoparticles upon pyrolysis at 1000 °C. Their homogeneous distribution and occurrence solely within the PDC layer suggest that they have directly formed from the in situ reduction of $Fe_{(1-x)}O$. Meanwhile, the crystallites have notably decreased in number and grown in size, presumably via Ostwald ripening. Grain coarsening in HfO_2/SiOC PDC-NCs has been attributed to local carbon loss near surfaces leading

to lower viscosities and thus increased diffusivities of the ceramic matrix [91]. In the PDCPs, the entire ceramic layer encasing the carbon fibers can be considered a surface-near zone, as it is only up to a few hundred nm thick. Moreover, compared to the sample prepared at 700 °C, less carbon has been detected within the coating, substantiating the assumption that carbon loss is contributing to the observed grain coarsening.

As iron oxides are known to be thermodynamically unstable at high temperatures with respect to carbothermal reduction and carbon being abundant in the SiOC-based coating, two possible reactions of wustite with the ceramic matrix may arise, as it was thoroughly discussed for Fe-modified SiOC ceramics in the literature [23,229]. Either the direct formation of metallic Fe takes place via

$$FeO + C \rightarrow Fe + CO \qquad \text{with } \Delta G = -43.3 \text{ kJ/mol at } 1000\ ^\circ C \qquad \text{(Eq. 4-2)}$$

or cementite (Fe_3C, *Pnma*) results from the reaction

$$FeO + 4/3\ C \rightarrow 1/3\ Fe_3C + CO \quad \text{with } \Delta G = -44.1 \text{ kJ/mol at } 1000\ ^\circ C. \qquad \text{(Eq. 4-3)}$$

As the latter reaction is slightly favored at 1000 °C, generation of Fe_3C should be predominately occurring, which also was described for Fe-modified SiOC ceramics [229]. Yet, the prevalence of metallic Fe in our samples indicates that, if cementite is indeed generated upon carbothermal reduction, it will decompose rapidly, which is known to occur at temperatures exceeding 750 °C [233]. However, this would cause precipitation of a graphitic carbon phase from the crystallites, which was not observed within the ceramic layer, suggesting that the carbide phase does not form in the first place. Besides free carbon, CO is another conceivable option for the reduction of wustite, as it should be readily available from the decomposing cellulose fiber and acetylacetonate ligands, particularly, as the Boudouard equilibrium is shifted above around 700 °C, favoring CO over CO_2 formation [234]. This, in turn, could enable the reactions

$$FeO + CO \rightarrow Fe + CO_2 \qquad \text{with } \Delta G = 2.09 \text{ kJ/mol at } 800\ ^\circ C \qquad \text{(Eq. 4-4)}$$

$$3\ FeO + 5\ CO \rightarrow Fe_3C + 4\ CO_2 \qquad \text{with } \Delta G = 25.1 \text{ kJ/mol at } 800\ ^\circ C \qquad \text{(Eq. 4-5)}$$

to take place, consuming available CO gas [235]. Here, Fe formation would be favored over Fe_3C, given low CO concentrations (i.e. < 20 vol.%) and higher reaction temperatures (i.e. > 670 °C), as was observed in other studies [235,236]. Thus, it is concluded that CO is, at least partially, responsible for the in situ conversion of the primary wustite precipitates into nanosized Fe crystallites.

Finally, with molecular hydrogen, another powerful reducing agent exists in the system, originating from the pyrolytic decomposition of ammonia after the reaction

$$2\ NH_3 \rightarrow 3\ H_2 + N_2 \quad \text{with } \Delta G = 150.340 - 0.2306\ T\ (kJ/mol). \qquad \text{(Eq. 4-6)}$$

As this process is temperature-dependent (featuring a highly negative ΔG of -143.21 kJ/mol at 1273 K), it was shown that a significant portion of the NH_3 molecules will decompose at temperatures of 1000 °C, resulting in a gaseous mixture of N_2, NH_3, and almost 50 vol.-% H_2 [237]. While the fact that a flowing ammonia atmosphere is employed during pyrolysis should considerably mitigate the effect of H_2 accumulation, gaseous species could be retained within the macropores between the fibers, consequently enabling the reaction of free hydrogen with wustite according to

$$FeO + H_2 \rightarrow Fe + H_2O \qquad \text{(Eq. 4-7)}$$

to form Fe and water, which again, is more favorable at a higher temperature, with ΔG = 4.18 kJ/mol at 600 °C compared to ΔG = -1.26 kJ/mol at 800 °C [235].

The ε-Fe_XN crystallites formed along the fiber-coating interface upon ammonolysis at 700 °C did not only withstand their reduction at 1000 °C but they also grew considerably, reaching diameters of up to 80 nm. This indicates an increased nitriding potential within the fibers at this temperature, which may stem from the decomposition of NH_3 (Eq. 4-6) due to elevated temperature (and catalytically at existing ε-Fe_XN sites [231]). Ammonia readily diffuses through the fibers due to its small kinetic radius and decomposes, with the resulting large N_2 molecules being retained. This presumably results in nitrogen accumulation within the fiber stabilizing ε-Fe_XN along the contact between the carbon and ceramic layer. Conversely, the H_2 generated can leave the fiber and is available as a reducing agent. The structural transformation of the amorphous carbon fiber towards a partially graphitized carbon fiber upon ammonolysis at 1000 °C may also play a role here, as it increases the free pore volume. Several studies have shown that carbon membranes can act as molecular sieves (CMS) for H_2 separation from gas mixtures, which is a complex mechanism relying mainly on the size of the pores in the membrane and the diameter of the permeating molecules [238–240]. The gaps between individual graphene layers in turbostratic carbon act as ultra-micropores (< 6 Å), which facilitate enhanced H_2 selectivity in CMS membranes [238].

The occurrence of TC itself is peculiar, as thermal graphitization of amorphous carbon (precursors) is typically realized only at much higher temperatures of around 2000-2800 °C, implying that the process is somehow catalyzed in the SiFeOC(N)-modified ceramic papers. It is well established in the literature that various transition metals and iron in particular are effective catalysts for the graphitization of amorphous carbons [241]. Thus, it stands to reason that the structural transformation of the fiber is facilitated by the interaction of the cellulose-derived carbon with the Fe-containing ceramic coating, drastically lowering the temperature at which graphitic carbon may be formed, which will be discussed in detail later in this work (Chapter 4.5).

4.2.3 Pyrolysis in Inert Argon Atmosphere

To assess the impact of different pyrolysis atmospheres on the microstructure generated, SiFeOC(N)-modified ceramic papers were pyrolyzed in Ar atmosphere at 1000 °C and comparatively investigated. With the use of inert Ar gas instead of NH_3, reactions occurring during pyrolytic conversion are limited to interactions between the preceramic polymer and the cellulose template.

In Fig. 4-15, the PXRD data of the Fe-modified ceramic papers upon treatment in Ar atmosphere and subsequent tempering is displayed. Upon pyrolysis at 1000 °C, ceramic papers with overall low crystallinity are generated; solely in the spectrum of the Durazane 2250 sample, a sharp intense reflex at ≈31° is visible, which, along some other minor peaks, can be unequivocally assigned the high quartz (SiO_2; $P6_222$) structure. SiO_2 phases, such as high quartz and cristobalite ($P4_12_12$), can form in SiOC-based PDCs upon oxidation [242,243]. In the case of the ceramic papers investigated, this is believed to be a consequence of localized oxygen contamination and does not reflect the phase evolution of the bulk material. Apart from this exception, only minor maxima are evident, from which the most intense reflex located at ≈52.5° can be assigned to either α-Fe or Fe_3C in both cases. Due to the slightly better crystallinity in the Durazane 2250 sample, some additional low-intensity maxima are present, which also fit the Fe_3C structure. The remaining minor reflexes can be tentatively ascribed to the iron oxide magnetite. Finally, a broad maximum at ≈30° is visible in both spectra, which resembles the typical shape of the d(002) maximum of semi-crystalline turbostratic carbon. Upon tempering at 1300 °C in Ar atmosphere, the crystallinity of the PDCPs has increased significantly, and intense sharp reflexes (≈41.8°, ≈48.6°, and ≈71.2°) are visible matching cubic β-SiC. The crystallinity of the graphitic carbon phase has developed considerably according to the much sharper and more intense d(002) reflex. Moreover, in both cases, a Fe-Si phase instead of metallic Fe or carbide has been detected, which can be identified as Fe_3Si. In the Durazane 2250 sample, also a minor amount of Fe_5Si_3, and, in the case of the Durazane 1800, small amounts of cristobalite appear to be present. Employing a flowing N_2 atmosphere during high-temperature treatment results in the formation of α-Si_3N_4 ($P3_1c$) and subordinate β-Si_3N_4 ($P6_3$) instead of SiC, while Fe_3Si again is the prevailing Fe-based phase generated, while graphitization is fairly comparable to the samples treated in Ar.

Fig. 4-16 displays a TEM BF image of a fiber cross-section in a SiFeOC(N)-based paper obtained upon pyrolysis at 1000 °C in Ar atmosphere. The overall structure closely resembles that observed in the sample upon ammonolyzed at 1000 °C (compare Fig. 4-12) with a partially graphitized fiber encased by a ceramic layer fragmented from the UM sectioning procedure. As both the SAED pattern and HRTEM image reveal, the fiber has undergone partial graphitization leading to the formation of turbostratic carbon, while being devoid of Fe-based precipitates (A). The degree of graphitization is comparable to that observed in the ammonia-treated sample, as only the d(002) ring with a lattice spacing between 3.45-3.55 Å appears sharp, again with a noticeable intensity modulation indicating a preferential orientation of the TC lattice planes. Other lattice plane reflection rings such as the (100), (004), and (110) remain diffuse revealing a poor degree of ordering of the graphitic clusters. Please note that the larger carbon fibers, such as the one shown here, are not homogeneously converted into TC but rather

maintain a core composed of amorphous carbon. This leads to a layered structure with an AC core, enveloped by a layer of TC, which itself is encased by the PDC coating.

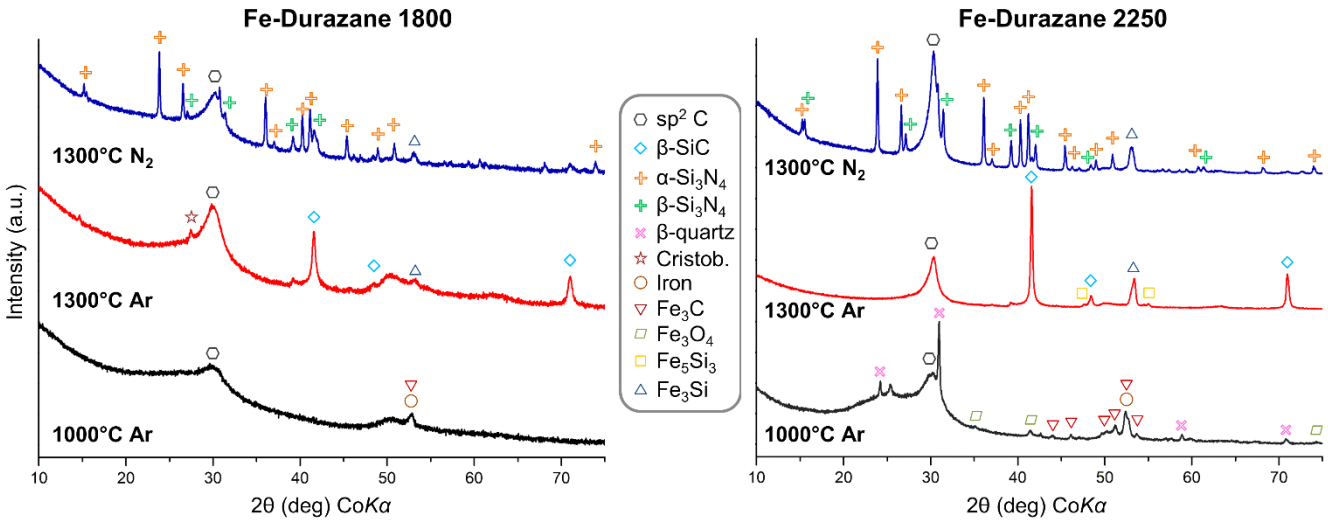

Figure 4-15: Comparison of the PXRD spectra of the Fe-modified PDCPs prepared from either precursor system and upon pyrolysis in Ar and consecutive high-temperature treatment in Ar or N_2.

Within the SiOC-based matrix (B), numerous crystalline precipitates are observed exhibiting a spherical shape and diameters of around 10-50 nm. Their occurrence gives rise to discrete reflection rings in the corresponding SAED pattern, which can be assigned to both α-Fe and Fe_3C, but do not allow for unambiguous phase determination. The overall composition of the coating is similar to that in the ammonolyzed sample, albeit with a notably higher carbon content (EDS B). Moreover, in contrast to the sample upon ammonolysis, locally, some small segregated carbon domains have been generated within the PDC layer during pyrolysis in Ar. Also, the size range of the Fe-based precipitates is larger, which could indicate pronounced grain coarsening via Ostwald ripening. Within the a-SiOC coating, pores can be observed, which provide free volume promoting fast diffusion. In addition to the crystallites enclosed within the ceramic matrix, several larger precipitates are observable occurring exclusively along the fiber-coating interface, which exhibit inhomogeneous contrast and irregular, sometimes polygonal to irregular shapes.

Characterization of the phase assemblage was conducted via HRSTEM imaging with the results summarized in Fig. 4-17. The ADF overview of the fiber-coating contact zone (a) shows a multitude of the smaller crystallites dispersed within the a-SiOC layer. HAADF imaging revealed that α-Fe (b) and Fe_3C (c) nanoparticles are coexistent, both exhibiting the same spherical shape and size range. It is not clear from the results to which extent the phase assemblage varies locally, but both the SAED patterns of the coating and single-crystal determination suggest that the phases can coexist in direct vicinity, sometimes even adjacent to each other (compare Fig. 4-16). This in turn may indicate very localized variations of the carbon content within the coating. The larger crystalline aggregates present along the interface between the cellulose-derived carbon and the ceramic layer were identified to be the spinel-type iron-oxide magnetite (d). Single-crystals of magnetite with up to 100 nm diameter were found

to exhibit comparably well-developed crystal facets, whereas the much more common polycrystalline aggregates (as the one shown in Fig. 4-17 a) are mostly irregularly shaped clusters with inhomogeneous contrast and reaching sizes of more than 400 nm.

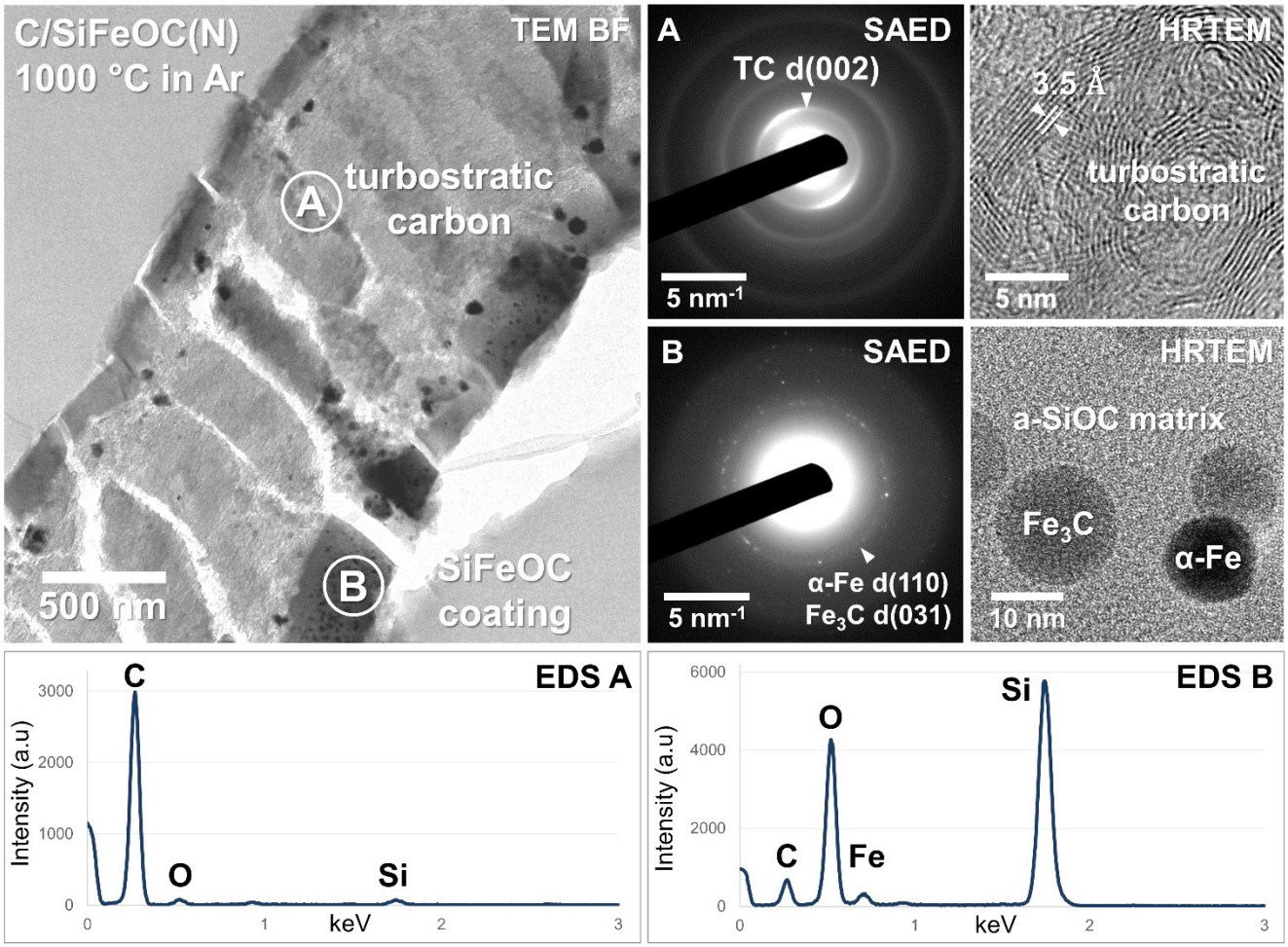

Figure 4-16: TEM BF image of a fiber cross-section in a SiFeOC(N)-modified paper obtained upon pyrolysis in Ar atmosphere at 1000 °C. The cellulose-derived carbon fiber (A) is partially graphitized, as shown by both the d(002) ring of turbostratic carbon in the SAED pattern and the characteristic curved lattice fringes in the HRTEM image. The fiber is encased by a continuous SiOC-based ceramic layer (B) containing numerous Fe-based precipitates that give rise to discrete reflex rings in the SAED pattern.

While the microstructure of the Fe-modified PDCPs upon pyrolysis in Ar is very similar to that observed in the ammonolyzed samples featuring a partially graphitized turbostratic carbon fiber encased by a SiFeOC(N) NC layer, the results show that the phase assemblage generated and the composition vary depending on the atmosphere employed. The generation of Fe_3C and segregated carbon within the a-SiOC layer might be the effect of the Ar atmosphere, which is not capable of removing carbon from the system as ammonia does via HCN formation [217]. Moreover, instead of nitride formation at the fiber-coating interface, large oxides are present, which is peculiar in that they are surrounded by carbon. This may point to a drastically increased oxidative potential within the fibers during pyrolysis, presumably originating from the diffusive transport of oxygen and hydroxy groups along the

free volume of the porous fibers. Also, despite the distinct phases generated, the Fe-based PDCPs prepared in Ar exhibit a ferromagnetic response comparable to that of the sample upon ammonolysis at 1000 °C. In the present case, it stems from the presence of the ferromagnetic magnetite and metallic α-Fe. The results suggest that the pyrolysis atmosphere severely affects the phase evolution of the SiFeOC(N)-based ceramic papers, which could be used to tailor the phase assemblage to the requirements of certain applications.

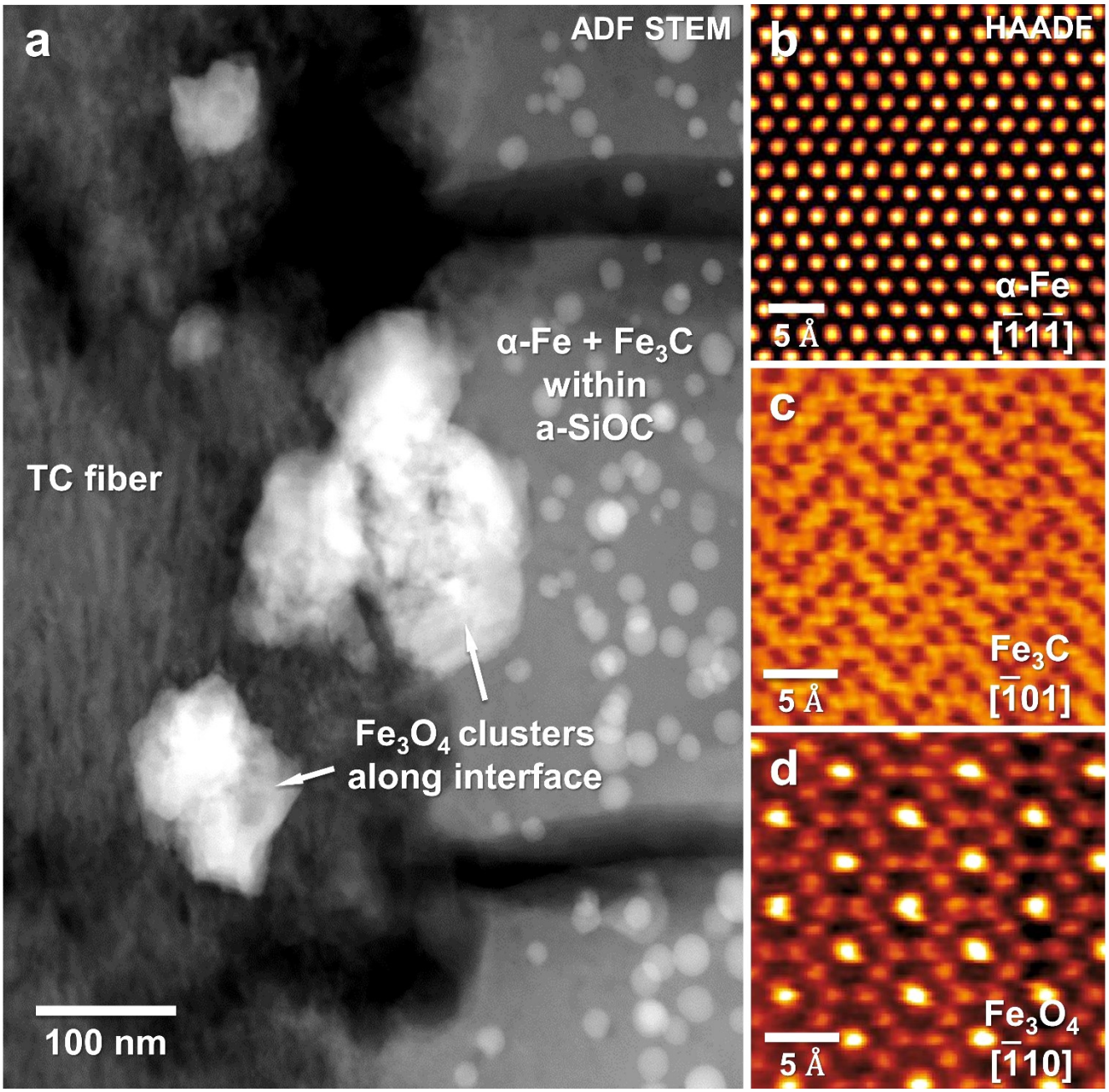

Figure 4-17: ADF STEM image of the fiber-coating interface in the SiFeOC(N)-modified paper obtained upon pyrolysis in Ar atmosphere at 1000 °C (a). In addition to the small precipitates dispersed within the SiOC coating that were identified via HAADF imaging to be α-Fe and Fe_3C (b,c), much larger polycrystalline aggregates exclusively occurring in contact with the turbostratic carbon fiber were observed and determined to be the ferromagnetic Fe-oxide magnetite (d). Own work, adapted from [200].

4.2.4 Tempering at 1300 °C in Argon Atmosphere

To pave the way for future application of PDCPs, it is pivotal to establish a fundamental understanding of the synthesis parameters that affect the microstructure and composition of the ceramic papers investigated. Most PDCs are well-known to maintain an amorphous ceramic matrix up until high temperatures and typically only form crystalline phases well above 1000 °C. Thus, controlling temperature offers a decisive tool for tailoring phase composition and properties of the resulting ceramics, which naturally is expected to apply to PDCPs as well. Moreover, the atmosphere employed during tempering also plays a major role as it affects phase equilibria and may or may not facilitate reactions between the ceramic and the gas phase. For this study, following pyrolysis, each ceramic paper was treated at 1300 °C in either Ar or N_2 atmosphere, as described in Chapter 3.1.1, and comparatively investigated in order to assess the influence of the high-temperature heat treatment on the microstructural evolution and phase assemblage of the ceramic composites.

A SiFeOC(N)-modified ceramic paper upon pyrolysis at 1000 °C and consecutive tempering at 1300 °C in Ar atmosphere is depicted in Fig. 4-18. The SEM image shows that the fiber morphology of the paper template is well-preserved even upon high-temperature treatment and the fibers exhibit a rather uniform, somewhat grainy contrast in the BSE image. As depicted in the STEM image, investigation of cross-sectional samples reveals extensively graphitized and highly porous cellulose-derived carbon fibers (A) containing numerous Fe-based precipitates finely dispersed within them. The corresponding SAED pattern indicates a high degree of graphitization, as in addition to the d(002) ring of TC, rather sharp (100), (004), and (110) rings are visible, whereas the diffuse intensity background declined, compared to the SiFeOC(N)-paper upon pyrolysis at 1000 °C. Moreover, no intensity modulation along a particular direction is observed, implying that the TC lattice planes are statistically oriented, which may indicate that the mechanism of graphitization is slightly different from that in the pyrolyzed samples.

As the fiber cross-section shows, the continuous SiOC-based PDC coating formed upon pyrolysis has transformed significantly during the tempering step. The fiber is now encased by a layer of roughly equiaxial grains (B) that are highly crystalline with random grain orientations as seen in the corresponding diffraction pattern. The lattice spacing of the innermost reflection ring can be assigned to the d(111) spacing of cubic β-SiC ($F\bar{4}3m$), which agrees with the XRD results presented above and compositional data acquired via EDS analysis, revealing the grains to be exclusively composed of Si and C. No sharp boundary between the polycrystalline coating and the cellulose-derived carbon fiber is maintained, as the grains do not form a continuous layer but are rather in loose contact to each other, frequently overlapping but mostly with TC or pores in between them, as shown in the high magnification ADF image. Also, while the majority of Fe-based precipitates are contained within the SiOC coating upon pyrolysis, here, most of them are dispersed throughout the carbon fiber, which implies that a mechanism is present causing their relocation during tempering.

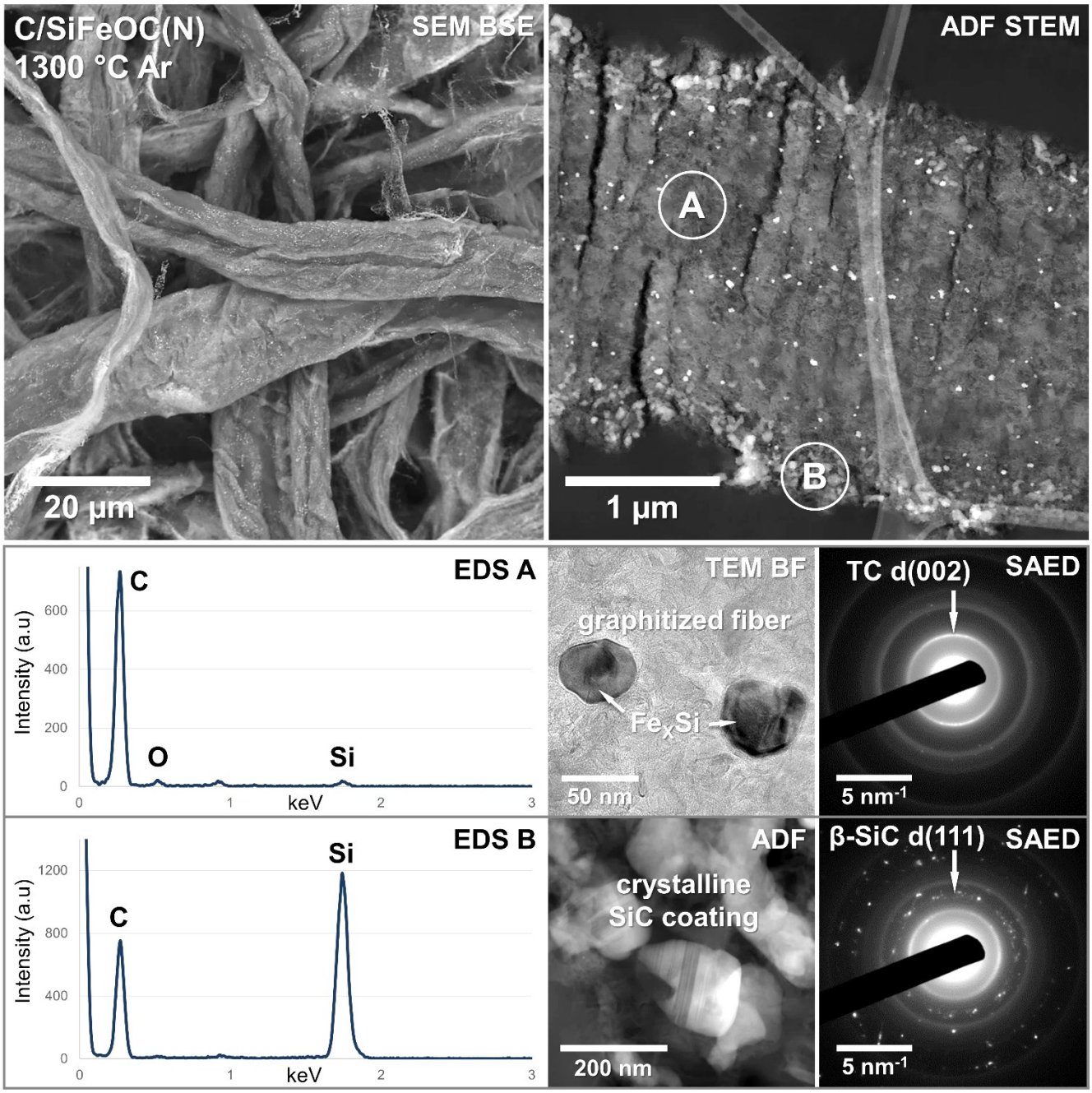

Figure 4-18: SEM overview of the SiFeOC(N)-modified paper obtained upon tempering at 1300 °C in Ar atmosphere showing that the paper morphology is retained even upon high-temperature treatment. The corresponding cross-sectional STEM image displays a carbonized fiber (A) containing numerous Fe-based precipitates, with EDS analysis, BF imaging, and electron diffraction indicating that extensive graphitization of the cellulose-derived carbon has occurred. The fiber is coated with a ceramic layer (B) composed solely of Si and C and is polycrystalline according to the corresponding SAED pattern revealing discrete reflexes assignable to β-SiC.

An overview of the crystalline phases identified in the SiFeOC(N) paper upon heat treatment at 1300 °C in Ar atmosphere is given in Fig. 4-19. HRTEM imaging and electron diffraction reveal the occurrence of two distinct Fe-Si compounds being Fe_3Si (a) and Fe_5Si_3 (b), verifying the XRD results, both found predominately within the graphitized carbon fiber. In most cases, they are between 15-80 nm in diameter and exhibit rounded irregular

shapes, occasionally elongated, droplet- or dumbbell-like, rarely with developed crystal facets. As exemplarily shown (a), the precipitates are always enveloped in a graphitic carbon shell, which often is aligned with the crystallites' edges, thus typically forming onion-like core-shell structures or ribbon- to coil-like graphitic clusters that appear to originate from the iron silicides.

Fig. 4-19 c shows a HRTEM image of one of the crystallites constituting the polycrystalline coating; the corresponding SAED pattern can be assigned to cubic β-SiC, with characteristic streaking features stemming from the disordered polytypic layers running along ⟨111⟩. The crystallites are roughly equiaxial, rarely prismatic, with irregularly developed crystal facets and exhibiting sizes of around 20-100 nm. The SiC is primarily found at the surface of the fibers, with only a few crystallites located surface-near, while none are present closer to the fiber core, implying in situ formation from the amorphous SiOC-based PDC layer.

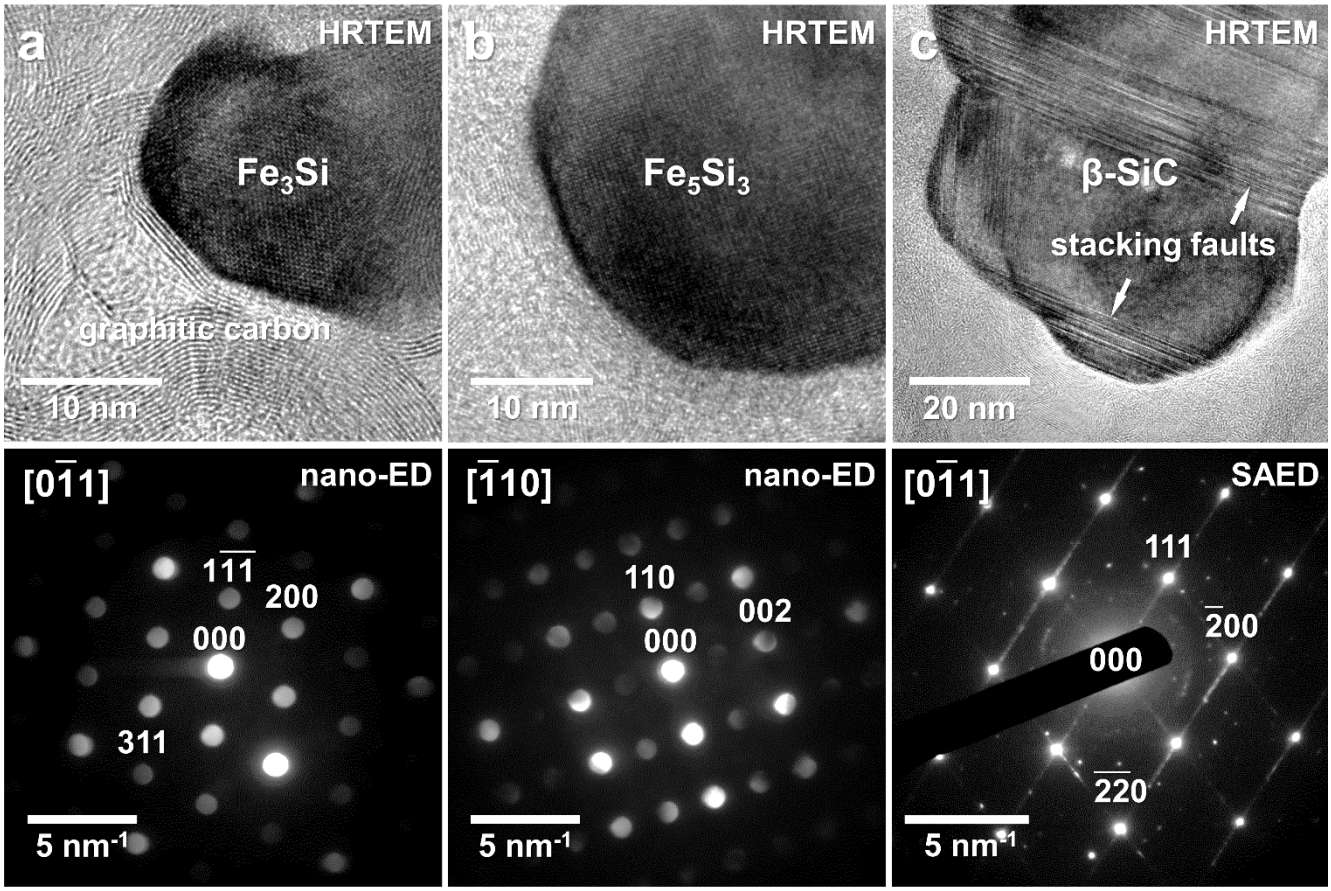

Figure 4-19: Overview of the crystalline phases identified in the SiFeOC(N)-modified paper obtained upon tempering at 1300 °C in Ar atmosphere. Almost exclusively dispersed within the graphitic fiber, Fe_3Si (a) and Fe_5Si_3 (b) precipitates occur. The crystalline coating encasing the fiber consists of close to equiaxial β-SiC crystallites, often containing characteristic stacking faults that cause streaking in the corresponding electron diffraction patterns (c).

4.2.5 Tempering at 1300 °C in Nitrogen Atmosphere

Employing different atmospheres during heat treatment can have a profound impact on the composition, phase assemblage, and properties of PDCs, which can be exploited to tailor the characteristics of such materials. The use of N_2 during high-temperature annealing was shown to affect certain aspects of PDCs differently compared to Ar; for instance, the reaction of N_2 with the ceramic matrix can alter the composition, reduce porosity, affect shrinkage, and result in the formation of new phases [244,245].

In Fig 4-20, an SEM image of an Fe-modified paper upon pyrolysis and consecutive tempering in N_2 atmosphere is depicted, with the fibers and paper structure still clearly visible. In contrast to the sample processed in Ar atmosphere, a multitude of wire structures have been generated scattered over the whole sample surface and in the macropores between the fibers. This has significantly altered the macroscopic appearance of the paper, now exhibiting a light-gray to white hue. As shown in the inset, the in situ generated wires are mostly straight, sometimes slightly curved, kinked, and occasionally branched. They typically possess extremely high aspect ratios, with diameters of only around 50-500 nm compared to lengths of up to a few mm, which is characteristic of such one-dimensional nanostructures. Please note that some whiskers are decorated with spherical Fe-based globules reaching diameters of up to 1-2 µm (compare the inset), which indicates an Fe-catalyzed vapor-liquid-solid (VLS) growth mechanism, as proposed in earlier studies [4]. However, the majority of wires do not exhibit such tips, raising questions about whether their generation could also be, at least partially, ascribed to other processes not relying on catalysts for nanowire generation.

As shown in the ADF STEM image of a fiber cross-section, the internal structure of the ceramic paper depicted is quite similar to that of the samples annealed in Ar. The cellulose-derived carbon fibers (A) primarily consist of turbostratic graphitic nanostructures accommodating numerous Fe-based precipitates, as depicted in the high-magnification BF image. They exhibit sizes between 10-50 nm, rounded irregular, rarely polygonal shapes, and are mostly found enclosed by a shell of graphitic carbon aligned with its edges. The corresponding EDS spectrum and SAED pattern presented are practically indistinguishable from those obtained from the Ar-treated papers, with almost pure carbon that shows typical diffuse reflection rings assignable to disordered graphitic carbon and some faint reflections matching the structures of either α-Fe or Fe_3Si.

No residual a-SiOC coating is observable in the sample upon tempering in N_2 and, in contrast to the samples annealed in Ar, a (semi-)continuous crystalline coating is also absent. Instead, large clusters of crystalline fragments and wire-like structures are found locally attached to the fibers (B). Please note that their distribution is very heterogeneous over the ceramic papers, which can also be seen in the ADF overview, in which most of the fiber depicted is bare and devoid of any coating or surface modification with other phases. The corresponding BF image shows such an agglomerate with a single kinked wire terminated by a crystalline globule. According to the EDS spectrum showing Si and N to be the main components, with only some subordinate C and O present, and the SAED pattern revealing a multitude of discrete reflexes, crystalline Si_3N_4 structures have been generated upon tempering in N_2.

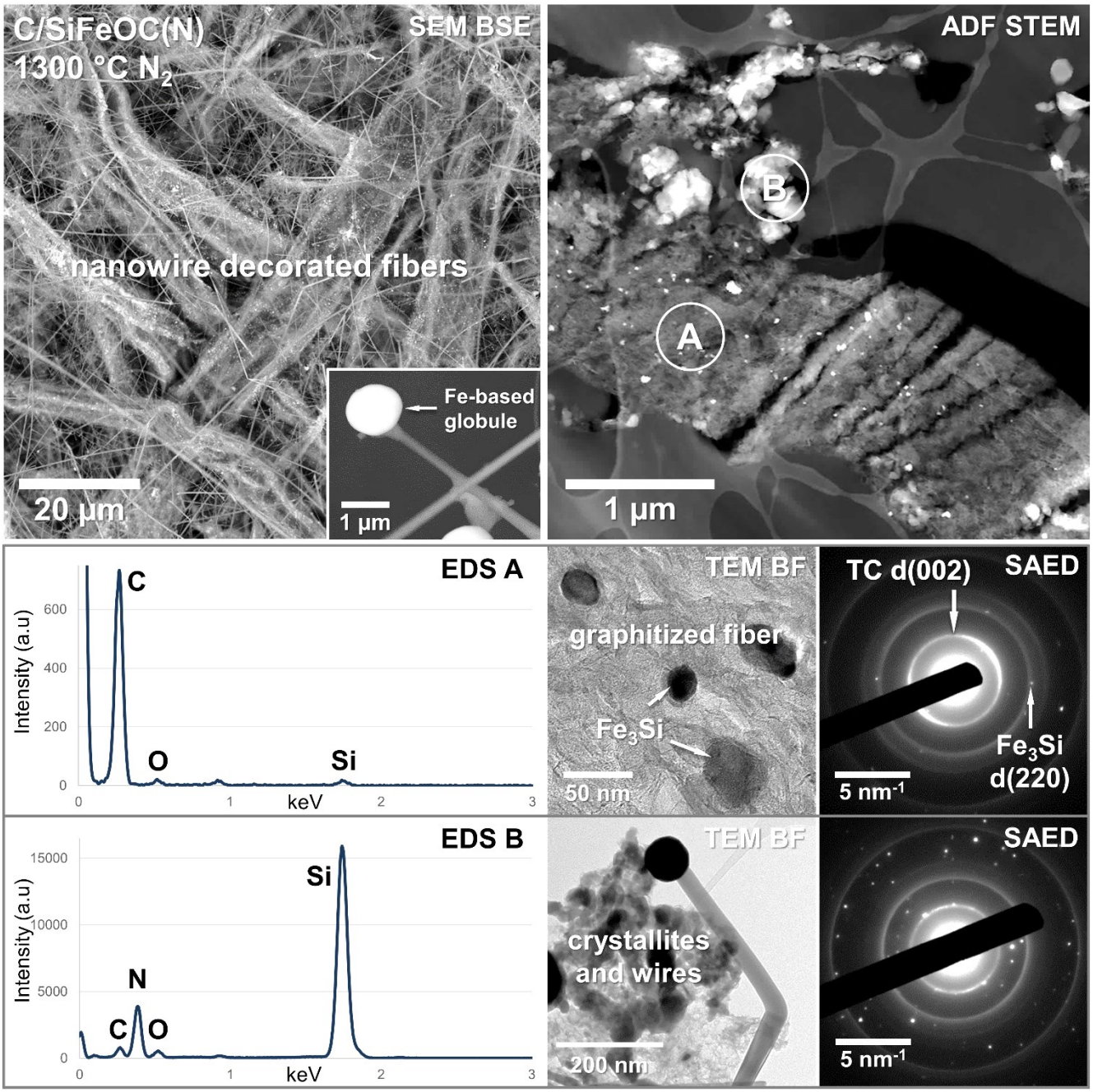

Figure 4-20: SEM overview of the SiFeOC(N)-modified paper obtained upon tempering at 1300 °C in N_2. The morphology of the paper template is still clearly visible and numerous nanowires with exceptionally high aspect ratios have formed on the fibers and in the macropores between them. In the cross-sectional STEM image, a cellulose-derived carbon fiber (A) is displayed, which has undergone considerable graphitization according to the high-magnification BF image and the corresponding SAED pattern and contains numerous Fe-based crystallites. Along the fiber surfaces, large crystalline grains composed of Si and N occur (B), which are fragments of the nanowires, which are occasionally decorated with Fe-based tips (also shown in the SEM inset).

A closer investigation of the crystalline phases present was conducted by a combination of TEM techniques with the results displayed in Fig. 4-21. In the BF image, one of the nanowires is depicted terminated by an Fe-based tip with rudimentary-developed crystal facets and exhibiting a relatively constant width of around 80 nm. As indicated by the EDS analysis, HRTEM imaging confirmed the wires to be single-crystalline α-Si_3N_4 (a) typically

grown along the ⟨100⟩ direction. While pyrolysis at 1000 °C led to the formation of various Fe-based phases, upon tempering in N_2, exclusively Fe_3Si has been generated within the cellulose-derived carbon fibers and decorating some of the Si_3N_4 nanowires; the presence of other silicides such as Fe_5Si_3 could not be verified, which agrees with the XRD data. Interestingly, the Fe_3Si tips were found to be enveloped by well-ordered graphitic carbon shells (b) typically aligned with the crystal facets and giving rise to some discrete reflections in the corresponding SAED pattern (white arrows). HRTEM imaging of the wire-globule contact (c) reveals a planar interface over a length of around 50 nm although no specific orientation relationship is present. The Fe-based tips always showed rotation with respect to the wire to some degree and no coherent crystallographic boundary was found in any case.

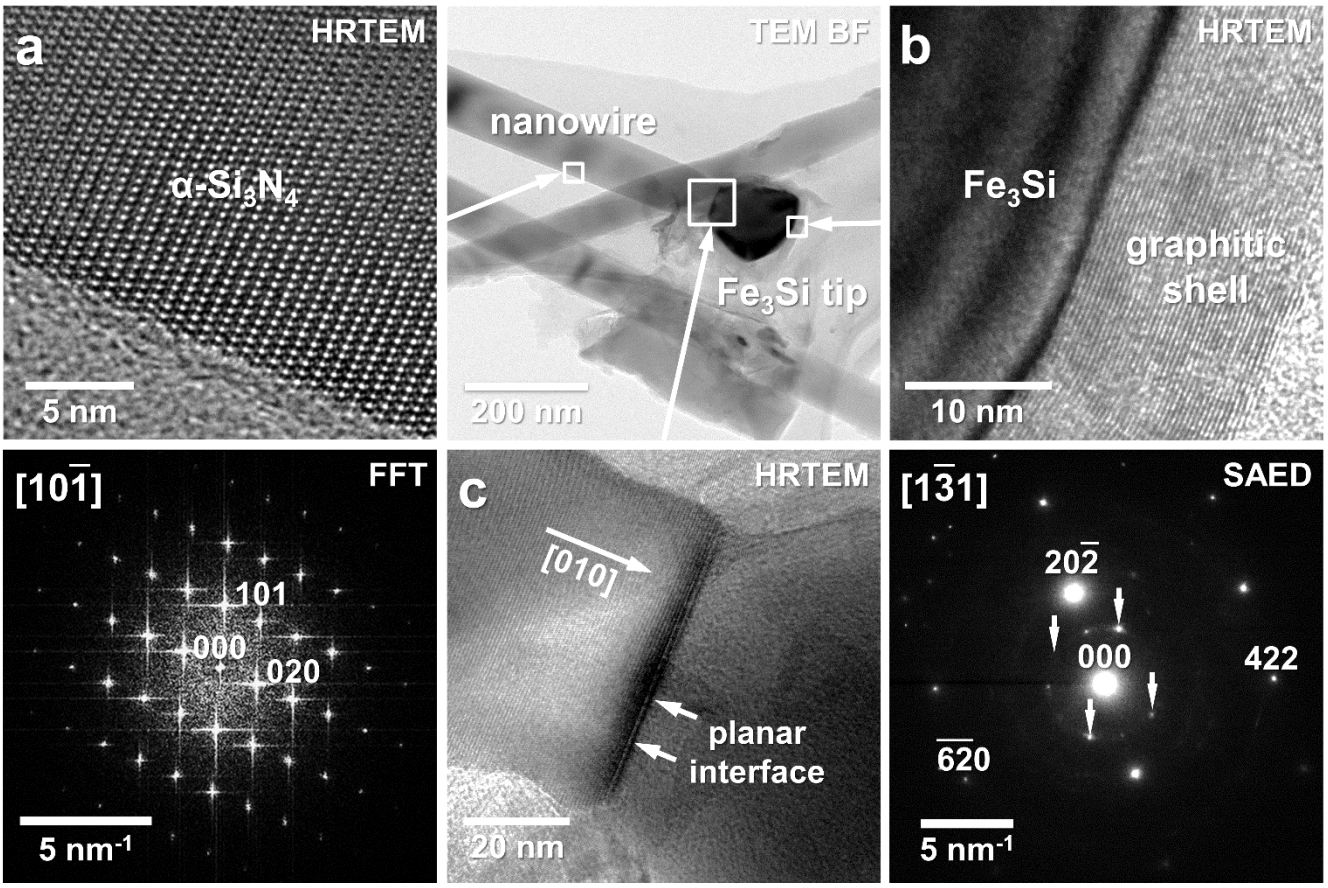

Figure 4-21: TEM BF image of a crystalline nanowire decorated with a Fe-based tip and corresponding phase investigation conducted via HRTEM imaging and electron diffraction. The nanowire (a) is composed of single-crystalline α-Si_3N_4 that, in this case, has grown along the [010] direction. The tip is a Fe_3Si single-crystal with irregular crystal facets encased by a shell of graphitic carbon (b) that gives rise to discrete reflections in the corresponding SAED pattern (white arrows; $d_{(002)} \approx 3.4$ Å). The interface between the wire and tip appears planar in the HRTEM image (c), although no specific crystallographic interface is present.

4.2.6 Microstructure & Phase Evolution of SiFeOC(N)-based PDCPs

Investigation of SiFeOC(N)-based PDCPs upon reactive ammonolysis at temperatures between 500 °C and 1000 °C revealed the complex transition from the SSP-modified paper templates towards hierarchical ceramic composites. The microstructural characteristics and phase assemblages generated were shown to be highly dependent on the pyrolysis temperature and, based on the results presented, the processes operating during polymer-to-ceramic conversion and the evolution of Fe-based phases could be rationalized.

To assess the impact of the processing atmosphere utilized, C/SiFeOC(N) papers were subjected to pyrolysis in inert Ar, and their microstructural attributes were examined in detail. According to the TEM results, the microstructure generated upon pyrolysis at 1000 °C is certainly similar to that resulting from ammonolysis at the same temperature, featuring a partially graphitized cellulose-derived carbon fiber encased by a SiFeOC(N)-based ceramic layer. However, the phase assemblage turned out to be considerably different featuring nanosized Fe_3C in addition to α-Fe precipitates dispersed within the amorphous SiOC matrix. It is reasonable to assume that this is a direct consequence of the processing atmosphere, as ammonia is well known to remove carbon from the system at elevated temperatures according to

$$C_{(s)} + NH_{3\,(g)} \rightarrow HCN_{(g)} + H_{2\,(g)} \qquad \text{(Eq. 4-8)}$$

during polymer-to-ceramic conversion, before the carbon is incorporated into the SiCO network [217,218]. This is supported by the fact that the PDC layers generated in the samples upon pyrolysis in inert Ar exhibit a notably higher carbon content, which favors local carbide formation and rationalizes the abundance of segregated carbon within the coating. Moreover, instead of Fe_XN, large magnetite clusters have formed along the fiber-coating interface in an Ar atmosphere, which indicates increased oxidative potential within the porous carbon fiber compared to the ceramic layer. Similar to the mechanisms proposed to lead to nitridation in reactive NH_3, fast diffusion of oxidizing species along the free volume of the carbon fibers could cause a distinct phase composition in this zone. The formation of different Fe-based phases, varying locally within each sample and with the processing atmosphere, demonstrates the complexity of PDCPs as well as their variability with changing certain processing parameters. Also, it implies that thermodynamic equilibrium has probably not been established upon pyrolysis at 1000 °C, which could also be attributed to the short duration and hence, reaction kinetics. With respect to the comparably homogeneous phase assemblage and microstructure generated upon tempering of the as-pyrolyzed ceramic papers, this assumption is substantiated.

It is well-established in the literature that above 1200 °C, amorphous mixed-bonded SiOC undergoes devitrification and phase separation to form amorphous multiphase systems [24,83] of a-SiO_2 and segregated carbon domains that can subsequently react with each other to initiate nucleation and growth of β-SiC nanocrystallites after the reaction

$$SiO_2\ (s) + 3\ C\ (s) \rightarrow SiC\ (s) + 2\ CO\ (g).$$ (Eq. 4-9)

This is generally considered to proceed in two consecutive steps via

$$SiO_2\ (s) + C\ (s) \rightarrow SiO\ (g) + CO\ (g)$$ (Eq. 4-10)

$$SiO\ (g) + 2\ C\ (s) \rightarrow SiC\ (s) + CO\ (g)$$ (Eq. 4-11)

and is highly dependent on the volume fraction of free carbon in the system. If carbon availability is limited, Eq. 4-10 is favored and excess SiO gas will not be converted into SiC [246,247]; conversely, it was shown for carbon-rich SiOC that in addition to the crystallization of β-SiC, continuous sp^2-hybridized carbon networks (i.e. TC) will form, enveloping SiC precipitates [246]. In this study, as not only the SiFeOC(N)-based preceramic polymers employed contain high fractions of carbon but also the cellulose-derived carbon of the template may react with the coating, the SiOC produced upon pyrolysis at 1000 °C can clearly be considered carbon-rich. Thus, no residual a-SiO_2 or a-SiOC was observed in the annealed samples, being entirely converted into crystalline β-SiC and TC. Please note that this process causes oxygen to be removed from the system almost entirely, as it is indicated by the EDS spectra displayed in Fig. 4-18, significantly changing the composition of the ceramic papers towards being SiFeC-based.

Meanwhile, both the XRD and TEM results show that all Fe-based phases (i.e. α-Fe and Fe_3C precipitates dispersed within the SiOC-based layer and magnetite along the interface) have been converted into two different iron silicide phases and, interestingly, occur deep within the carbon fiber. Overall the PDCPs generated can be described as C/Fe_XSi/SiC microcomposites and exhibit a comparably high degree of crystallinity. According to studies conducted on Fe-modified SiOC ceramics, the formation of Fe_3Si and subordinate Fe_5Si_3 might be realized by the reaction of Fe_3C (and α-Fe) with the a-SiOC matrix forming a transient Fe-Si-C alloy [23]. It was proposed that between 1000 and 1300 °C, and given low concentrations of Si in the alloy, primarily Fe_3Si along with GC will crystallize, whereas, at higher temperatures, the formation of Fe_5Si_3 and β-SiC takes place without the generation of GC [23]. In the SiFeOC(N)-based ceramic papers, all four phases (Fe_3Si, Fe_5Si_3, graphite, and β-SiC) were found to be coexistent upon tempering at 1300 °C, thus both processes are conceivable depending on the local composition of the alloy. Around carbon-rich domains within the SiOC and along the contact to the carbon fiber in particular, Fe_3Si formation is promoted, while at SiO_2-rich regions, Fe-Si-C alloys with higher Si content would favor Fe_5Si_3 nucleation along with SiC, which could then continue growth after the above-discussed mechanism. As the results clearly show, the majority of iron silicides have been relocated from the coating into the cellulose-derived carbon fiber upon tempering, while fiber graphitization has progressed notably compared to the pyrolyzed sample. Catalytic graphitization is a well-known peculiarity of various transition metals with iron being particularly effective in generating sp^2-hybridized carbon from AC and various carbon precursors. According to several authors, this process is facilitated by the dissolution of amorphous carbon in Fe-based alloy

droplets at high temperatures (i.e. > 800 °C) and subsequent layer-wise exsolution as GC [241]. It is widely accepted in the literature that the driving force for this phenomenon is energy minimization through the crystallization of the carbon atoms that it is typically accompanied by a 'liquid-like' movement of the Fe-based phases through the AC (or carbon precursor), which was shown to result in a wide range of graphitic carbon nanostructures such as multi-wall carbon nanotubes, nanocoils, nanocones and the like [241]. While this will be the main subject of a later chapter in this work (Chapter 4.5.1), it is important to note here that the Fe-Si-C alloy droplets are believed to move through the fiber via this process. With the alloy droplets becoming separated from the PDC coating, they can dissolve more carbon, while their Si content remains constant. This could explain why two distinct Fe-Si phases are coexistent and exclusively found within the fiber, whereas β-SiC formation is limited to the fiber surface. Moreover, as the phase assemblage transitions from metallic α-Fe towards Fe-based silicides and due to the increased temperature during annealing, the capabilities to dissolve amorphous and precipitate graphitic carbon may have changed compared to the samples upon pyrolysis. The fact that the TC lattice planes are found statistically oriented only upon tempering can be attributed to an increased graphitization rate, which may be caused by the pronounced mobility of the catalyst particles at elevated temperatures [248,249].

The samples prepared in nitrogen atmosphere are similar concerning the structure of the cellulose-derived carbon and Fe-based phases; hence, iron silicide generation and graphitization of the fiber are assumed to proceed via the same mechanisms proposed for the samples tempered in inert Ar. Here, exclusively Fe_3Si has formed according to XRD and TEM analysis and, in line with preceding studies, in situ generation of ultra-long one-dimensional Si_3N_4 nanowires was observed on the surface of the PDCPs [4,5], resulting in C/Fe_3Si/Si_3N_4 microcomposite papers with overall high crystallinity. The presence of Fe-based globules at the end of the wires indicates a metal-catalyzed VLS process to be responsible for their growth according to the reaction

$$3\ SiO_{(g)} + 2\ N_{2\ (g)} + 3\ CO_{(g)} \xrightarrow{Me_{(l)}\ cat} Si_3N_{4\ (s)} + 3\ CO_{2\ (g)} \qquad \text{(Eq. 4-12)}$$

at Fe-Si-C catalyst droplets, with the SiO and CO gas required generated via Eq. 4-10. However, the initial nucleation may be facilitated by a simple vapor-solid (VS) mechanism at free carbon sites after

$$3\ SiO_{(g)} + 2\ N_{2\ (g)} + 3\ C_{(s)} \longrightarrow Si_3N_{4\ (s)} + 3\ CO_{(g)} \qquad \text{(Eq. 4-13)}$$

as proposed by others [30,250]. The CO_2 resulting from Eq. 4-12 can then react with available free carbon to produce additional CO and, consecutively, SiO gas, allowing the continuation of nanowire growth [250] at the expense of the a-SiOC matrix, which is consumed by these reactions. According to the literature, the type of Si_3N_4 generated depends on the local composition of the amorphous SiOC(N), with N_2-rich sites favoring β-Si_3N_4 growth, while pure Si-C-O matrices result in the generation of α-Si_3N4 [250]. The fact that mostly the latter was generated along some minor β-phase aligns with the results that the PDC coating generated upon pyrolysis is mostly free of nitrogen but exhibits some compositional variations leading to the phase assemblage observed.

SiFeOC(N)-based Ceramic Papers - Summary

- SiFeOC(N)-based PDCPs treated in reactive NH_3 at 500, 700, and 1000 °C were investigated via TEM and their low-temperature microstructural and phase evolution studied:
  - Upon 500 °C ammonolysis, the cellulose fibers have been converted into amorphous carbon encased by a continuous monophasic and amorphous SiFeOCN PDC layer with high porosity
  - Precipitation of $Fe_{(1-X)}O$ nanocrystals dispersed within an a-SiOC(N) layer was observed upon pyrolysis at 700 °C, along with the generation of Fe_XN precipitates exclusively at the fiber-coating interface, which is the result of nitriding species diffusing through the porous carbon fiber
  - After treatment at 1000 °C, the Fe-oxides have been reduced to nanosized metallic α-Fe, while Fe_XN has withstood reduction and undergone growth; the cellulose-derived carbon has been partially graphitized attributed to an Fe-catalyzed solution-reprecipitation mechanism.
- Upon pyrolysis at 1000 °C in Ar, a similar microstructure but a notably different phase assemblage is generated with α-Fe and Fe_3C dispersed within a SiOC layer and large magnetite clusters along the fiber coating interface:
  - The overall increased carbon content and resulting generation of Fe-based carbides and some free carbon within the PDC layer is attributed to the missing carbon removal mechanism via reaction with NH_3
  - At the interface between fiber and coating, large magnetite clusters are generated, which implies a higher oxidative potential within the fiber compared to the ceramic layer
  - Regardless of the pyrolysis atmosphere, the Fe-modified papers exhibit notable ferromagnetism due to the abundance of α-Fe and/or magnetite.
- With the consecutive annealing at 1300 °C, C/Fe_XSi/SiC (Ar) and C/Fe_3Si/Si_3N_4 (N_2) microcomposites with distinct microstructures have been generated possessing an overall high degree of crystallinity:
  - Upon tempering in Ar, almost all oxygen was found removed from the system and crystalline β-SiC has been generated from the SiOC layer encasing the extensively graphitized carbon fibers
  - Tempering in N_2 on the other hand, was shown to result in PDCPs covered with a multitude of α-Si_3N_4 nanowires, occasionally decorated with Fe_3Si tips indicative of a VLS growth mechanism
  - Fe_3Si and minor Fe_5Si_3 were identified as the sole Fe-based phases and found primarily dispersed within the fibers and encased by graphitic nanostructures, substantiating an Fe-catalyzed graphitization process
  - Ferromagnetic behavior was not exhibited in the samples upon tempering, which is a result of the complete conversion of α-Fe and magnetite into soft magnetic Fe_XSi silicides.
- The results show the decisive impact of the temperature and processing atmosphere applied during PDCPs synthesis on the microstructural characteristics and phase assemblages obtained.

4.3 SiNiOC(N)-based Ceramic Papers

Similar to iron, nickel is a transition metal of outstanding importance for numerous applications such as in corrosion-resistant steel production, non-ferrous high-performance alloys, and permanent magnets. Also, nickel is frequently used in (lithium-free) rechargeable batteries, electroplating, as a binder material for hard intermetallics, and as a catalyst for hydrogenation reactions. In ceramics, nickel typically serves the purpose to increase the oxidation resistance of refractory elements in furnaces or electrical heaters, impart magnetic properties to the material, or is used as a catalytically active compound for various important reactions [100,251].

4.3.1 Pyrolysis in Inert Argon Atmosphere

Fig. 4-22 summarizes the phase assemblage generated in the PDCPs prepared with Ni-Durazane 1800 and Ni-Durazane 2250, respectively, as detected via PXRD analyses. Direct comparison between the two precursor systems reveals no notable differences in any of the processing steps besides minor discrepancies between reflex sharpness and intensities. Upon pyrolysis at 1000 °C in Ar, the XRD data primarily show discrete maxima at ≈52° and ≈61°, which can be assigned to either elemental Ni ($Fm\bar{3}m$) or cubic Ni_3Si ($Pm\bar{3}m$). In addition, some subordinate reflexes occur at ≈53.6° and ≈55.4°, indicating the presence of Ni_2Si (*Pbnm*) and Ni_5Si_2 (*P*321) but do not allow for an unambiguous assignment. As was the case in the Fe-modified papers, at ≈30.1°, a rather broad maximum with high intensity matches the (002) spacing of sp^2-hybridized graphitic carbon. The width and peak position still indicate significant disorder typical for semi-crystalline turbostratic carbon (TC); however, compared to the Fe-modified papers, the carbon appears to be much better crystallized (compare Fig. 4-15). Tempering at 1300 °C in Ar leads to very similar spectra for both precursor systems, clearly exhibiting a much higher overall crystallinity compared to the samples upon pyrolysis. Highly intense and sharp maxima (≈41.8°, ≈48.6°, and ≈71.2°) unequivocally reveal the presence of β-SiC, whereas tempering in nitrogen leads to the generation of α-Si_3N_4 and β-Si_3N_4, as it was shown to be the case in the Fe-based papers. The assemblage of Ni-based phases clearly is independent of the atmosphere and polysilazane used, as for all samples upon tempering, numerous reflexes indicate the sole presence of Ni_2Si.

Detailed TEM studies of the different Ni-modified PDCPs were conducted to characterize the micro- and nanostructure of the ceramic composites and to verify the phases identified with XRD analyses. A BF image of a fiber cross-section in the SiNiOC(N)-based ceramic papers upon pyrolysis at 1000 °C in Ar atmosphere is depicted in Fig. 4-23. The structure revealed is similar to that observed in the Fe-modified sample, albeit with some striking differences evident. Throughout the cellulose-derived carbon fiber (A), numerous Ni-based crystalline precipitates are observed that give rise to discrete reflections in the corresponding SAED pattern. The high-magnification BF image of the fiber-coating interface shows that the fiber has undergone extensive graphitization and is composed of coil- or ribbon-like graphitic nanostructures, predominately occurring around the Ni-based

crystallites. As reflected in the rather sharp concentric rings in the SAED pattern, which (from innermost to outermost) can be assigned to the (002), (100), (004), and (110) rings of turbostratic carbon, the graphitic clusters are comparably large and well-ordered. This indicates a similar degree of graphitization as in the Fe-based samples upon tempering at 1300 °C, being notably higher than in the SiFeOC(N)-based paper upon pyrolysis at 1000 °C. Also, no modulation of the d(002) ring is visible; hence, no preferential orientation of the TC lattice planes is implied.

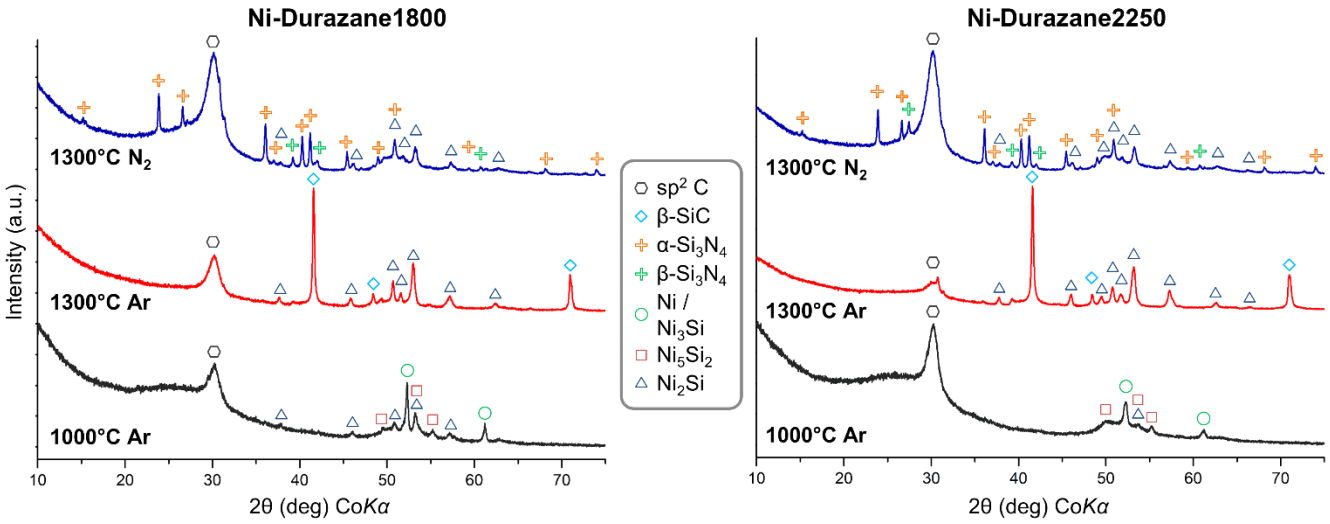

Figure 4-22: Comparison of the PXRD spectra of the Ni-modified PDCPs prepared from either precursor system and upon pyrolysis in Ar and consecutive high-temperature treatment in Ar or N_2.

The cellulose-derived carbon fiber is encased by a thin continuous PDC coating (B) that is Si(Ni)OC-based according to EDS analysis. The interface between fiber and coating is rather sharp and the ceramic layer appears to exhibit exceptional adhesion to its carbon substrate, as was the case for the Fe-based ceramic papers. Although the coating has occasionally been fragmented during the sectioning procedure, the fragments remained in place without significant delamination of the ceramic layer evident. Typically, the coating was found to be Ni-depleted, as it is shown in the overview image, whereas locally, crystalline Ni-based precipitates occur finely dispersed within an amorphous SiOC matrix being generally much smaller than the crystallites observed within the carbon fiber. In sections of the coating where Ni-based precipitates are abundant, corresponding SAED patterns, as the one shown, contain discrete reflection rings, which match the lattice parameters of either elemental Ni or several distinct Ni_XSi phases, which cannot be conclusively assigned. Also, as the BF image of the fiber-coating displays, the ceramic layer features numerous mesopores in the size range of around 2-12 nm. Their uniform distribution and isometric round shape indicate a diffusion-mediated pore formation mechanism via local enrichment of pyrolytic volatiles initiating pore nucleation [252]. A density change through partial crystallization of the coating could also play a role, but would likely lead to more irregularly shaped pores distributed heterogeneously throughout the coating.

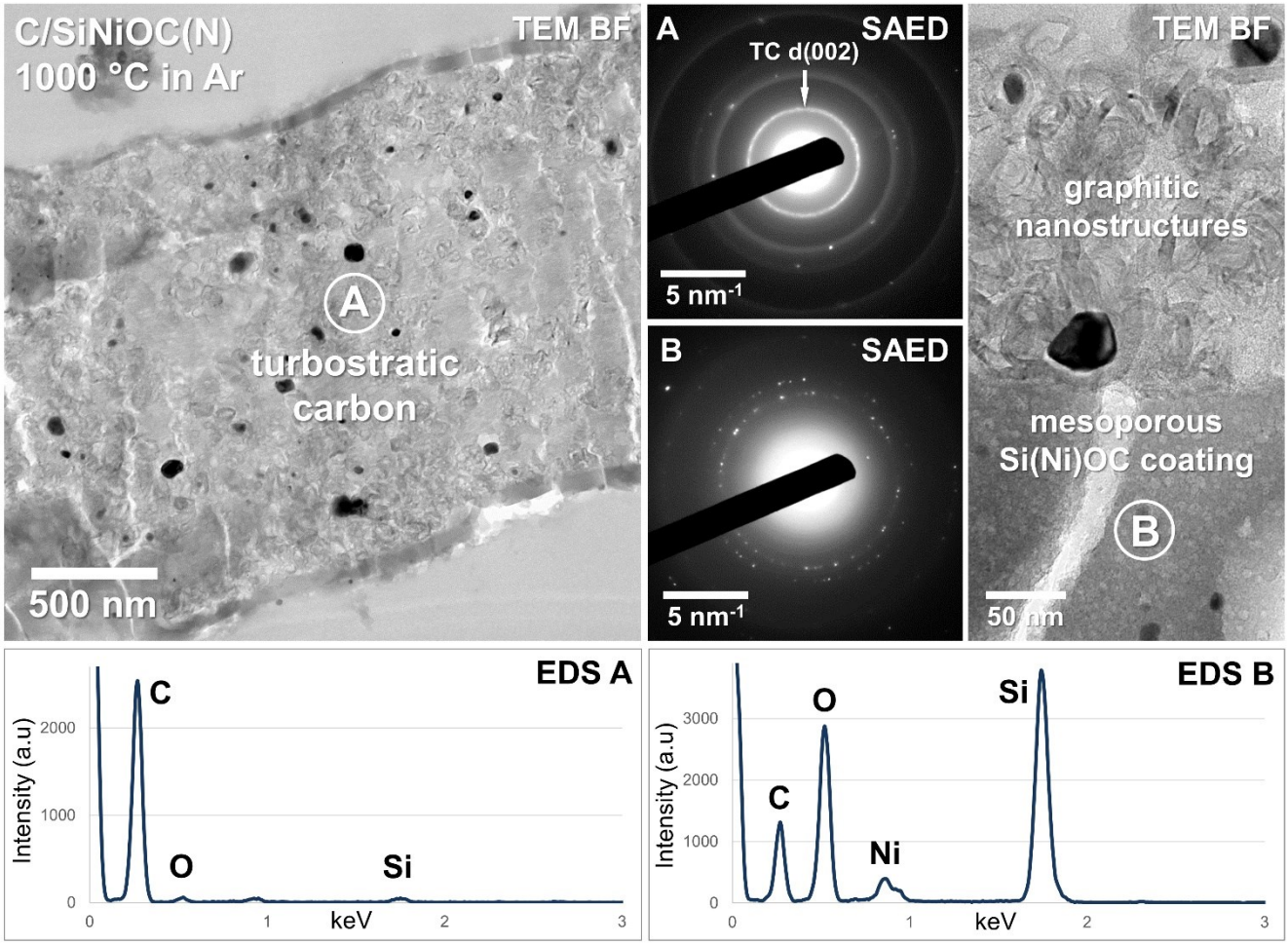

Figure 4-23: TEM BF image of a fiber cross-section in the SiNiOC(N)-based ceramic paper upon pyrolysis at 1000 °C in Ar atmosphere. An extensively graphitized cellulose-derived carbon fiber (A) is shown containing numerous Ni-based precipitates, which are always enveloped in graphitic carbon shells. Within the thin SiOC-based PDC coating continuously encasing the fiber (B), almost no precipitates are present, as seen in the high-magnification BF image of the fiber-coating interface. Please note that the PDC layer does contain numerous mesopores which are interpreted as remnants of gas-phase processes operating during pyrolysis.

In Fig. 4-24, an ADF STEM image of the same fiber is displayed, along with corresponding EDS maps revealing spatially resolved compositional data of the ceramic composite (a). As the SiOC-based ceramic layer gives rise to strong Si and O signals, it is easily distinguishable from the cellulose-derived carbon fiber that accommodates most of the Ni-based precipitates. Interestingly, while some of the crystallites show a distinct Si signal, others do not, indicating that both metallic Ni and Ni_XSi phases are coexistent. Indeed, HRTEM imaging in combination with electron diffraction revealed that at least four Ni-based phases have been generated upon pyrolysis (b-e). Elemental Ni has precipitated in the form of comparably large irregularly shaped particles, reaching sizes of up to 80 nm (b) and exclusively occurring within the carbonized fiber, being generally enveloped in graphitic carbon structures. As evident from the smeared reflections in the SAED pattern, they typically display imperfect crystallinity, which also leads to a heterogeneous contrast visible in the TEM BF image. In addition, numerous Ni_XSi precipitates were observed, which exhibit rounded polygonal or spherical shapes and are primarily located

within the carbonized fiber. Via HRTEM imaging and electron diffraction Ni_3Si, Ni_5Si_2, and Ni_2Si have been identified (c-e), verifying the phase assemblage that was concluded from the PRXD results. Although the majority of the Ni_XSi precipitates are found within the graphitized fiber enclosed by graphitic carbon structures, some are locally dispersed within the SiOC-based matrix. The crystallites enclosed within the coating typically exhibit smaller diameters and a narrower size range of around 8-35 nm, as opposed to those in the cellulose-derived fiber ranging between 15-80 nm.

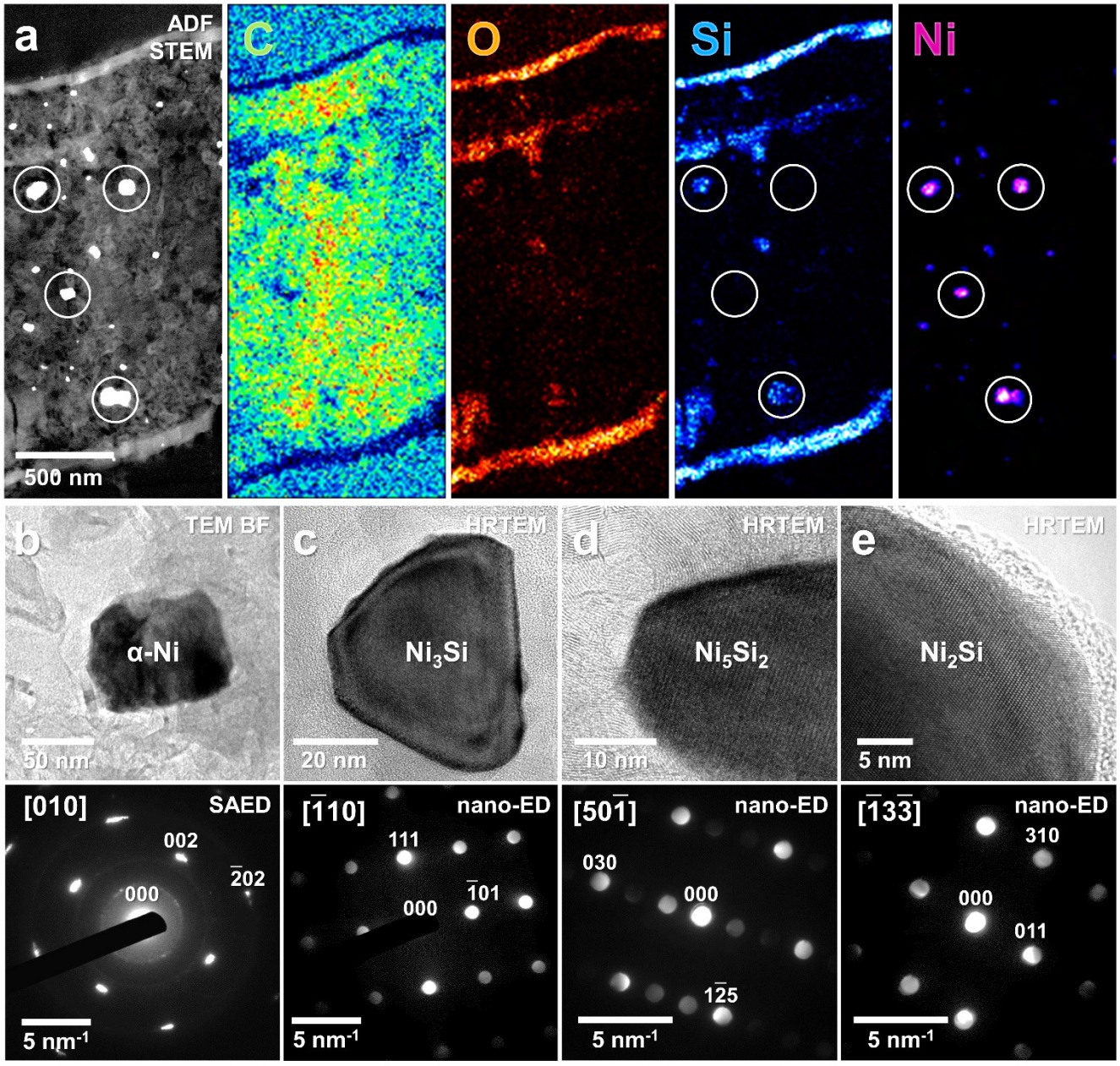

Figure 4-24: ADF STEM image and corresponding EDS maps (a) of the ceramic fiber depicted in Fig. 4-23. The maps allow for a clear distinction between the cellulose-derived carbon fiber and the SiOC-based coating. As some of the Ni-based crystallites exhibit a distinct Si signal, while others do not (white circles), the occurrence of both metallic Ni and Ni_XSi phases is implied. Studying the phase assemblage of the sample in detail via TEM imaging and electron diffraction (b-e) confirmed the existence of Ni_3Si, Ni_5Si_2, and Ni_2Si precipitates in addition to elemental Ni.

4.3.2 Tempering at 1300 °C in Argon Atmosphere

Following pyrolysis, the Ni-modified ceramic papers were tempered at 1300 °C in Ar atmosphere to assess their temperature-dependent microstructure and local phase evolution.

In the SEM image of Fig. 4-25, an as-tempered Ni-based sample is shown clearly exhibiting the typical paper morphology inherited from the template. Most fibers are decorated with numerous whisker-like structures displaying lengths of up to 20 µm while being only a few hundred nm wide. Most of the whiskers form irregularly rounded to euhedral prisms with hexagonal to trigonal symmetry, which often are terminated by spherical tips, as shown in the high-magnification inset. The tips are Ni-based, consistent with the contrast in the BSE image, and occur in diameters between 80 nm to over 1 µm. The fibers themselves exhibit a rather uniform yet grainy contrast in the element contrast image, whereas secondary electron imaging at high magnifications reveals their rough and porous surface. In the TEM BF image, a cross-section of a single cellulose-derived carbon fiber encased by a granular discontinuous coating is displayed. The carbon fiber (A) primarily consists of graphitic carbon, as shown by the high-magnification BF image and the corresponding SAED pattern revealing concentric reflection rings assignable to turbostratic graphite. The degree of graphitization, that is the ordering and size of the graphitic clusters, appears to have improved only slightly compared to the samples upon pyrolysis. In addition to the EDS spectrum featuring faint Ni and Si signals, some discrete reflections evident in the diffraction pattern indicate that the precipitates dispersed within the fiber again are crystalline Ni-Si phases, which are almost exclusively encased by graphitic carbon shells.

The amorphous PDC coating present in the paper upon pyrolysis, on the other hand, has changed considerably upon tempering, as it has been converted into a discontinuous layer comprised of numerous crystalline precipitates (B). According to the EDS spectrum, the approximately equiaxial, occasionally elongated grains are exclusively composed of Si and C, and display conspicuous streaking features along distinct directions of the grains, as shown in the close-up BF image. The numerous reflexes visible in the corresponding SAED pattern indicate that the coating consists of randomly oriented crystallites, which, in accordance with the EDS spectrum, could be identified as cubic β-SiC. The grains display sizes from around 50-200 nm, and sometimes form clusters of several crystallites, but are typically in loose contact with each other, with pores or graphitic carbon clusters between them and a diffuse interface with the cellulose-derived carbon fiber.

HRTEM imaging in conjunction with single-crystal electron diffraction was employed to elucidate the phase assemblage of the Ni-modified papers upon tempering at 1300 °C, as summarized in Fig. 4-26. The results show the occurrence of three crystalline phases, Ni_2Si, β-SiC, and α-SiC, whereas elemental Ni, Ni_3Si, or any other species have not been observed. It should be noted that the distinction between Ni_2Si and Ni_5Si_2 based on single-crystal electron diffraction alone is ambiguous in many crystallographic orientations. Nevertheless, as crystallites could always be indexed as Ni_2Si, while conclusive solutions for Ni_5Si_2 were only rarely applicable, it is clear that the majority of Ni-Si phases among the various Ni-based phases identified in the as-pyrolyzed samples, Ni_2Si (a) is prevailing upon heat-treatment at 1300 °C in Ar atmosphere. This agrees well with the diffraction data of the

present study (Fig. 4-22) and is discussed in the associated work conducted on ceramic papers, whereas the investigation of the pure precursor upon pyrolysis and consecutive tempering was shown to accommodate NiSi (*Pnma*) in addition to Ni_2Si [8], which is not the case in the corresponding PDCPs.

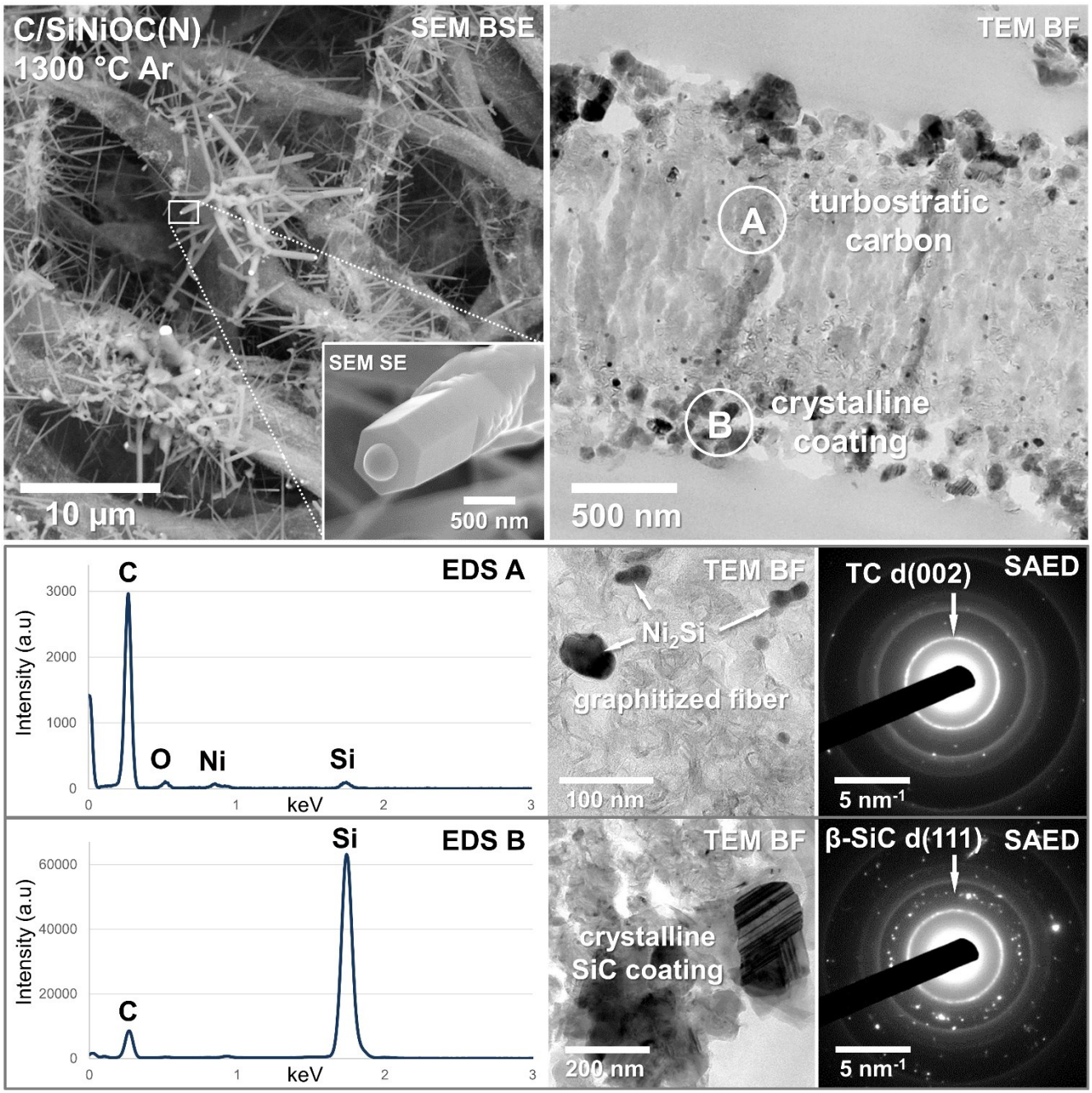

Figure 4-25: SEM image of the SiNiOC(N)-modified paper obtained upon tempering at 1300 °C in Ar atmosphere, showing fibers decorated with columnar and whisker-like structures, occasionally terminated by Ni-based particles (shown in the inset). The fiber cross-section depicted in the TEM BF image reveals a cellulose-derived carbon fiber (A) being extensively graphitized and containing numerous Ni-based precipitates according to the corresponding high-magnification BF image and SAED pattern. The fiber is coated with roughly equigranular crystallites consisting of Si and C, which give rise to discrete reflections in the diffraction pattern (B) and can be assigned to β-SiC.

As indicated by EDS analyses and electron diffraction, the polycrystalline coating encasing the fiber is composed of numerous randomly oriented β-SiC crystallites embedded within turbostratic carbon. In Fig. 4-26 b, one of the larger grains is presented exhibiting a close-to-rectangular shape with irregular crystal facets and being surrounded by smaller crystallites and graphitic carbon structures. The intrinsic lamellar features give rise to notable streaking in corresponding SAED patterns and are characteristic of SiC, originating from the disordered stacking of its various polytypes along certain crystallographic directions (being ⟨111⟩ here). Finally, TEM-based investigation of the whisker structures revealed them to be hexagonal α-SiC (6H, $P6_3mc$), occasionally decorated with round Ni_2Si tips (Fig. 4-26 c). The corresponding SAED pattern again exhibits pronounced streaking features from the disordered stacking of polytypic layers, which run exclusively along the orientation of the whisker, determined to be ⟨011⟩ in this case.

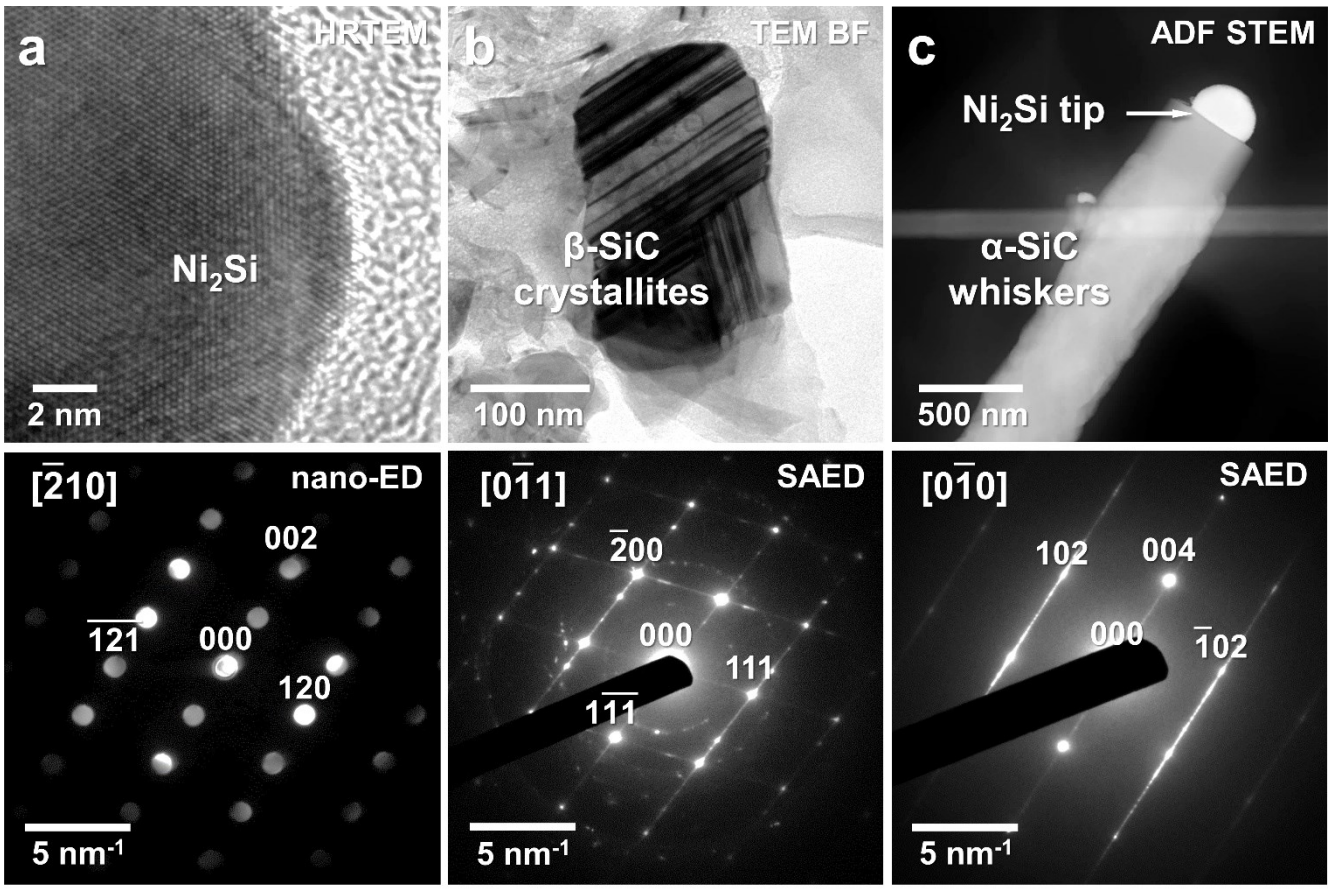

Figure 4-26: Overview of the phase assemblage observed in the SiNiOC(N)-based paper obtained upon tempering at 1300 °C in Ar atmosphere. Ni_2Si was identified to be the principal Ni-containing phase (a) within the graphitic fiber as well as at the tips of whisker structures typically reaching sizes of up to a few tens of nanometers. As indicated by electron diffraction, the coating is composed of cubic β-SiC crystallites in a size range of a few tens up to 200 nm exhibiting characteristic stacking faults along various directions (b). The whiskers on the other hand are composed of hexagonal α-SiC with stacking faults solely along their growth direction (c).

4.3.3 Tempering at 1300 °C in Nitrogen Atmosphere

Complementary characterization of as-pyrolyzed Ni-modified papers treated in a flowing N_2 atmosphere at 1300 °C were carried out to assess differences in their microstructural evolution and phase assemblage, with respect to the other transition metals.

Fig. 4-27 depicts the characteristic structure of SiNiOC(N)-based PDCPs upon tempering in N_2 as observed via low magnification SEM imaging. Again, the morphology of the paper template has been faithfully retained and, as in the Fe-modified paper, ultralong nanowires partially cover the paper surface. The wires are locally assembled in large clusters and are often decorated with metal-based tips, as shown in the inset. The internal structure of the ceramic composite is fairly comparable to that observed in the Fe-modified papers, with an extensively graphitized cellulose-derived carbon fiber (A) containing numerous crystalline precipitates, as shown in the TEM BF image. The corresponding SAED pattern reveals rather sharp reflex rings assignable to turbostratic carbon, with the d(002) ring exhibiting a spacing of just under 3.39 Å, pointing towards a comparably high degree of order in the graphitic clusters. Additional discrete reflections originate from the Ni-based crystalline nanoparticles dispersed within the fiber. At higher magnifications, coil- and ribbon-shaped graphitic nanostructures can be observed comprising the porous carbon fibers entirely. As in the samples upon pyrolysis and tempering in Ar, the Ni-based precipitates occur enveloped in these nanostructures, sometimes encased in a continuous graphitic shell. Their shape is irregularly rounded, sometimes polygonal with a size comparable to that in the other samples, ranging between 10-70 nm.

Unlike the samples tempered in Ar, no continuous crystalline coating has been generated here, but prismatic whisker structures locally encase the carbon fibers (B), as shown in the BF image. They occasionally exhibit stacking faults perpendicular to their long axis and most of them have been fragmented during the preparation procedure. Their width typically lies between a few tens up to around 300 nm and is in most cases remarkably constant, while their length can exceed hundreds of µm. According to the EDS spectrum, they are exclusively composed of Si and N, while being highly crystalline as shown by the discrete reflections in the corresponding SAED pattern.

As derived from the XRD data (Fig. 4-22), apart from the ubiquitous turbostratic carbon, two principal crystalline phases, Ni_2Si and α-Si_3N_4, alongside some minor β-Si_3N_4, have been generated in the Ni-modified papers upon tempering in N_2. Indeed, detailed TEM analyses of the phase assemblage substantiated this, as no additional Ni-based or Si-based phases could be identified. Fig. 4-28 displays one of the Si_3N_4 wires terminated by a Ni_2Si crystallite observed via TEM imaging. Compared to those investigated in the Fe-based PDCPs, the wire shown here has a larger but continuous width of 200 nm, exhibits a tip modified by {110} or {100} crystal facets, and is entirely covered with a thin shell of graphitic carbon. A polygonal faceted crystallite is visible slightly subsided within the 010 facet at the top of the wire and is entirely covered in a GC shell.

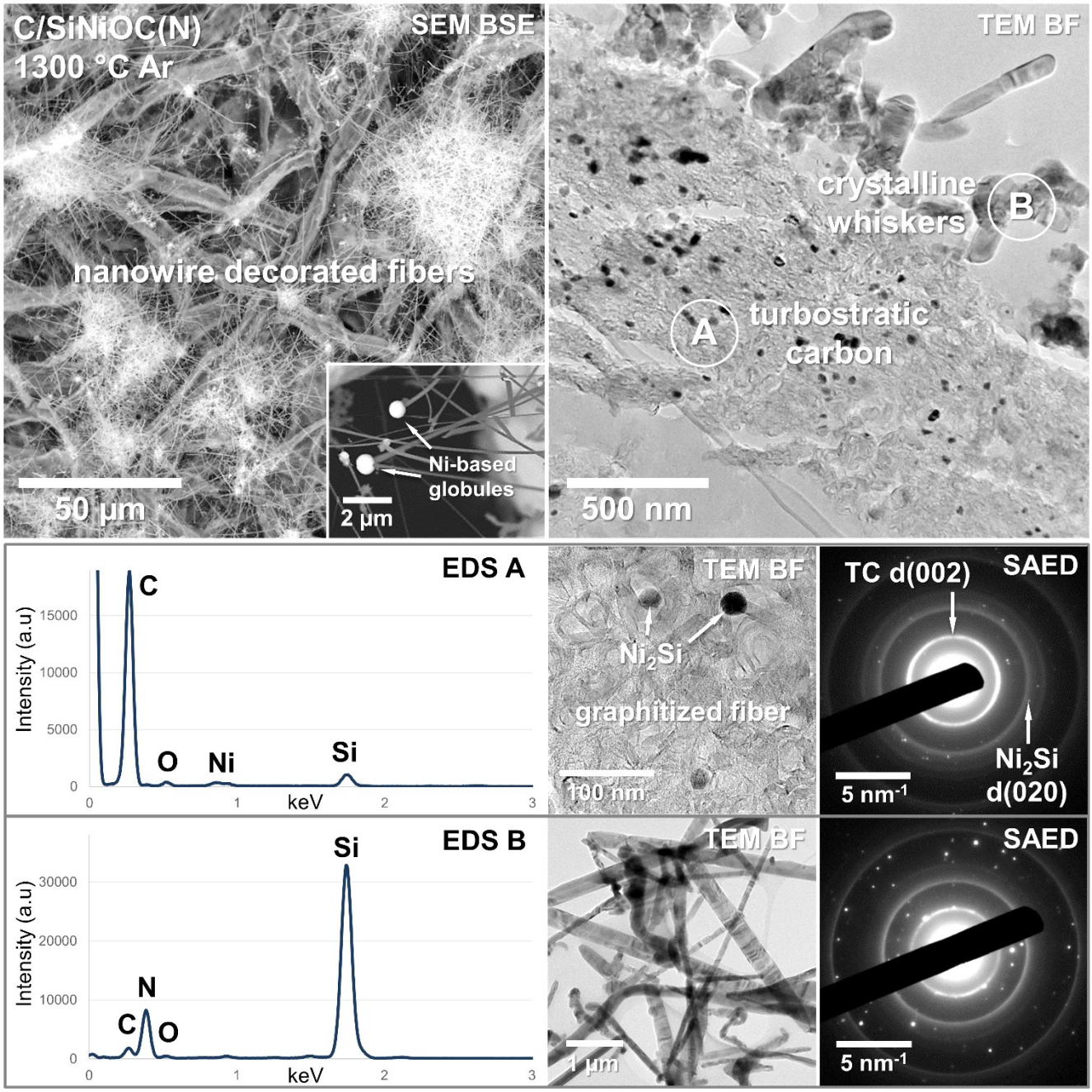

Figure 4-27: SEM image of a SiNiOC(N)-modified paper obtained upon tempering at 1300 °C in N_2 atmosphere, revealing dense clusters of nanowires covering the ceramic paper surface. In the corresponding TEM BF image, an extensively graphitized carbon fiber is shown (A), containing numerous Ni-based precipitates. The crystalline whisker and wire structures found throughout the sample (B), are composed of single-crystalline α-Si_3N_4, according to EDS analyses and electron diffraction. These high aspect-ratio wires often display stacking faults perpendicular to their growth direction and form branched and entangled clusters.

As was indicated by XRD analyses, HRTEM imaging, and ED confirmed that exclusively Ni_2Si nanoparticles (a) have been generated upon tempering, both dispersed within the graphitized carbon fiber and occasionally decorating the Si_3N_4 nanostructures. According to SAED analysis, the wire displayed has grown along ⟨010⟩ and is well-crystallized without stacking faults evident in the HRTEM image (b). Please note that in contrast to the wire shown in the Fe-modified paper (Fig. 4-21), the Ni_2Si particle is not spherical, small compared to the width

of the wire, and no planar interface with the Si_3N_4 single-crystal is present. Again, no crystallographic orientation relationship could be determined between the two phases. Please note that the majority of NW observed during SEM imaging exhibited a different appearance with large spherical catalyst tips (compare the inset of Fig. 4-27). However, different types as the one shown here occurred occasionally (c), displaying crystal facets and small Ni_2Si tips, which might indicate another growth mechanism to lead to their formation.

Overall, the characteristics observed in the Ni-modified papers upon tempering in N_2 are fairly comparable to those generated with Fe-modification of the precursor. However, as was the case in the samples processed in Ar, the characteristics of the Si-based nanostructures appear to vary with the transition metal utilized for precursor modification.

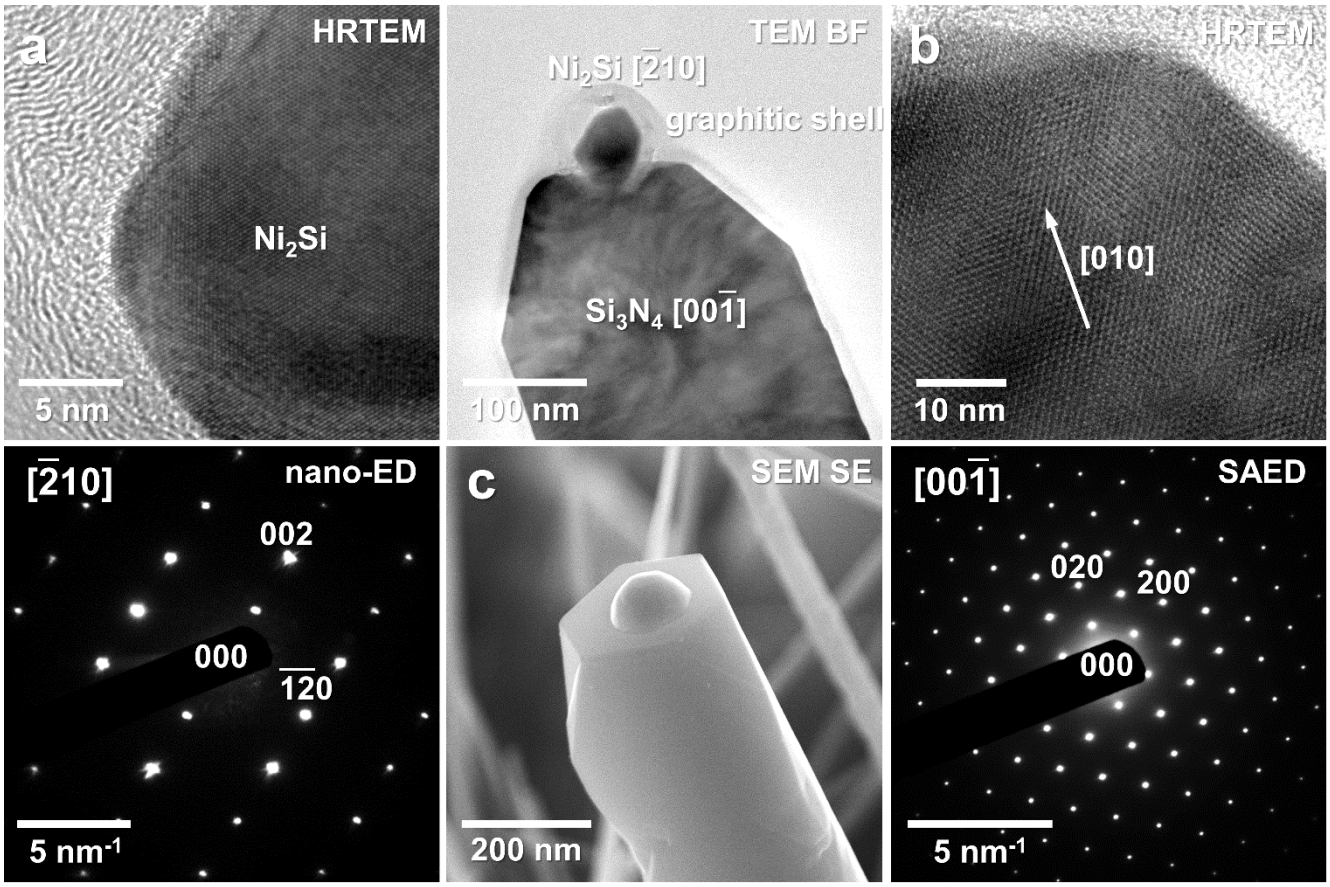

Figure 4-28: Display of a nanowire observed in the SiNiOC(N)-modified ceramic papers upon tempering at 1300 °C in N_2. The tip of the wire is decorated with a single-crystalline Ni_2Si particle (a) exhibiting well-defined crystal facets and a shell of GC extending along the edges of the nanostructure. The α-Si_3N_4 wire is also modified by surface facets and is grown along the ⟨010⟩ direction, as revealed by HRTEM imaging and ED (b). The Ni_2Si crystallite appears to be slightly subsided within the wire, which was also observed during SEM imaging (c).

4.3.4 Microstructure & Phase Evolution of SiNiOC(N)-based PDCPs

Although the morphology and bulk composition of the Fe- and Ni-modified ceramic papers were shown to be quite similar, the TEM results reveal that distinct microstructures and phase compositions can be generated depending on the transition metal utilized for precursor modification.

Upon pyrolysis at 1000 °C in Ar, the PDCPs consist of cellulose-derived carbon fibers encased by a SiOC-based PDC coating. However, in contrast to the Fe-modified papers, the majority of Ni-based precipitates is found to be dispersed within the fibers and enveloped in graphitic carbon nanostructures, while the thin ceramic layer only locally encompasses Ni-based crystallites. Moreover, instead of carbides or oxides, several distinct Ni_XSi phases between metallic Ni and Ni_2Si were identified, which highlights that the different transition metals have distinct tendencies to form certain intermetallics and phase assemblages within the complex PDCPs. Also, the coexistence of several Ni-Si phases in direct vicinity may indicate that thermodynamic equilibrium has not been established upon pyrolysis, causing a locally varying phase assemblage across the sample. Formation of metal-based nanoparticles from preceramic polymers modified with metalorganic compounds is generally considered to proceed via initial precipitation of oxide clusters, which then can be reduced towards metallic particles [23,91]. The abundance of carbon in the system can facilitate the reduction of NiO and subsequent reaction of metallic Ni with the a-SiOC coating to form silicides. Essentially, the same mechanisms are believed to be responsible for the variability in the phase assemblage as it was thoroughly discussed for the Fe-modified samples upon tempering. With the onset of catalytic graphitization, the Ni-based nanoparticles migrate into the fibers and become detached from the SiOC layer, while their Si content remains constant resulting in the generation of different silicide phases. Please note that the SiNiOC(N) papers display ferromagnetic behavior upon pyrolysis due to the presence of metallic Ni among the precipitates.

Above 1200 °C, the decomposition of the SiOC matrix generates SiO gas (Eq. 4-10), which could allow redistribution of Si throughout the system rationalizing why Ni_2Si is the sole Ni-based phase observed upon tempering at 1300 °C. As SiO is highly reactive, it will generate SiC upon interaction with free carbon (Eq. 4-11), which indeed is observed to some extent within the carbon fibers of the samples processed in Ar, indicating diffusive transport of SiO along the free volume of the porous carbon fiber. Peculiarly, in the samples treated in N_2, solely Ni_2Si has been generated without evidence of SiC formation during the transport of SiO through the carbon fiber. Thus, it remains unsolved how the transition from a variety of Ni_XSi phases in the pyrolyzed papers towards phase pure Ni_2Si in the tempered samples is realized.

Compared to the Fe-modified papers, α-SiC whisker formation was found to be substantially more pronounced in the Ni-containing samples within identical experimental conditions, which may have critical implications for potential functionalization routes. The presence of Ni_2Si globules at the tip of some whiskers indicates that a metal-catalyzed VLS mechanism facilitates their growth according to

$$SiO_{(g)} + CO_{(g)} \xrightarrow{Me_{(l)}\ cat} SiC_{(s)} + CO_{2\ (g)} \qquad \text{(Eq. 4-14)}$$

via reaction of the gaseous educts at alloy droplets [253]. However, the majority of whiskers observed was lacking a catalyst globule, and among the structures investigated several distinct types can be differentiated by their dimensions and morphologies, which could point to an additional growth mechanism to be responsible for their formation. Si_3N_4 nanowire generation, on the other hand, did not differ significantly from that observed with Fe-modified papers. Due to the presence of Ni_2Si tips on some of the wires, again, a VLS mechanism catalyzed by the metal-based phases is indicated [254]. The underlying processes of the Si-based nanostructure generation and variations arising from using different transition metals for precursor modification will be further addressed in Chapter 4.5.2.

SiNiOC(N)-based Ceramic Papers - Summary

- Upon pyrolysis of the SiNiOC(N)-modified paper templates, again, pseudomorphic PDCPs with preserved paper structure are obtained:
  - The cellulose-derived carbon fibers encompassing the majority of Ni-based precipitates have undergone extensive graphitization and are encased by a thin a-SiOC layer
  - Several Ni_XSi phases, ranging from metallic Ni to Ni_2Si, were identified occurring close to each other and are mostly enveloped by graphitic nanostructures within the fibers
  - In comparison to the Fe-modified papers, an identical macroscopic appearance but distinct microstructural characteristics and phase assemblages are generated
  - Due to the presence of metallic Ni, the papers exhibit ferromagnetic behavior.
- Annealing at 1300 °C results in the formation of crystalline C/Ni_2Si/SiC (Ar) and C/Ni_2Si/Si_3N_4 (N_2) microcomposites, with the fibers covered by Si-based whisker or wire nanostructures:
  - Upon tempering in Ar, the a-SiOC coating crystallized into β-SiC encasing the highly graphitized carbon fibers, and long α-SiC whiskers decorated with Ni_2Si globules are scattered over the papers
  - During tempering in N_2, ultra-long α-Si_3N_4 whiskers have grown on the paper surface and in the macropores, with some being terminated by Ni_2Si tips indicating a catalytic VLS growth mechanism
  - The sole Ni-based phase identified in the papers upon tempering is Ni_2Si, exclusively occurring dispersed within the carbon fiber enclosed in graphitic nanostructures
  - Upon complete conversion of metallic Ni into Ni_2Si the ferromagnetic properties are lost.
- The observations display the pivotal impact of the transition metal used for precursor modification on the microstructure and phase assemblage of PDCPs; the pronounced generation of SiC-based whisker structures upon modification with Ni could provide additional attractive functionalization options.

4.4SiPdOC(N)-based Ceramic Papers

With palladium, a third transition metal was employed for precursor modification in this study and tested for its impact on the microstructure and phase evolution of PDCPs. As a member of the precious platinum group metals, it is characterized by some sought-after properties, scarcity, and high value. Like platinum, most of the palladium produced is employed in catalytic converters, where it excels at transforming detrimental volatile compounds into harmless substances and as a catalyst for various chemical processes, such as (de)hydrogenation, petroleum cracking, C-C bonding reactions, and many more, being vastly sped up by its presence. Frequently, ceramic or carbon-based materials are employed as catalyst support, with fine-grained palladium being dispersed on porous Al_2O_3, SiO(C), other oxides, or activated carbon to maximize surface-to-mass ratios and accessibility of catalytically active sites while maintaining a long lifetime [255].

4.4.1 Pyrolysis in Inert Argon Atmosphere

Finally, the ceramic papers prepared by coating a cellulose-based template with a Pd-modified polysilazane polymer were investigated to assess their microstructure evolution and crystalline phases. Overall, the PXRD spectra shown in Fig. 4-29, display a similar trend as observed in the other systems, with PDCPs exhibiting low crystallinity upon pyrolysis and the formation of highly crystalline SiC and Si_3N_4 upon tempering at 1300 °C in Ar and N_2, respectively. Apart from some cristobalite in the Durazane 1800 sample, both precursor systems encompass metallic Pd ($Fm\bar{3}m$) in addition to Pd_2Si ($P\bar{6}2m$) upon heat treatment at 1000 °C. Although the ratios vary notably, with Durazane 2250 containing more Pd/Pd_3Si according to the reflex intensities, the overall phase composition is identical. Unlike the Fe- and Ni-modified papers upon pyrolysis, no turbostratic carbon phase is present here, as no d(002) reflex is evident at ≈30.1°. Upon tempering, however, some graphitic carbon has formed in each sample, indicating that the graphitization of the cellulose-derived carbon in the Pd-modified papers begins at higher temperatures than with Fe or Ni. Also, with increasing the temperature, the evolution of the Pd_XSi towards stoichiometric Pd_2Si has taken place, being the sole metal-based phase in the samples treated at 1300 °C, regardless of the atmosphere or precursor employed. This again agrees with the other systems featuring various metal-based phases at lower temperatures and almost exclusively Fe_3Si and Ni_2Si upon tempering.

Investigation of the Pd-modified ceramic papers via TEM was conducted analogous to the other systems, with a fiber cross-section of a SiPdOC(N)-based ceramic paper upon pyrolysis displayed in Fig. 4-30. The fibers shown in the BF image consist of a cellulose-derived carbon core (A) with fairly homogeneous contrast, which is encased by a rather thin PDC layer (B) containing numerous precipitates and evidently being much thicker at gussets between two fibers than on straight edges. Electron diffraction, EDS analyses, and HRTEM imaging of the carbon fiber show no evidence of significant porosity, crystalline precipitates, or graphitization. The carbon is entirely amorphous, with only small clusters of sp^2-hybridized carbon visible in the HRTEM image, exhibiting a lattice

distance of just under 4 Å, which is well above that of turbostratic carbon. This substantiates the XRD data indicating distinct activation temperatures of graphitization in the different PDCPs.

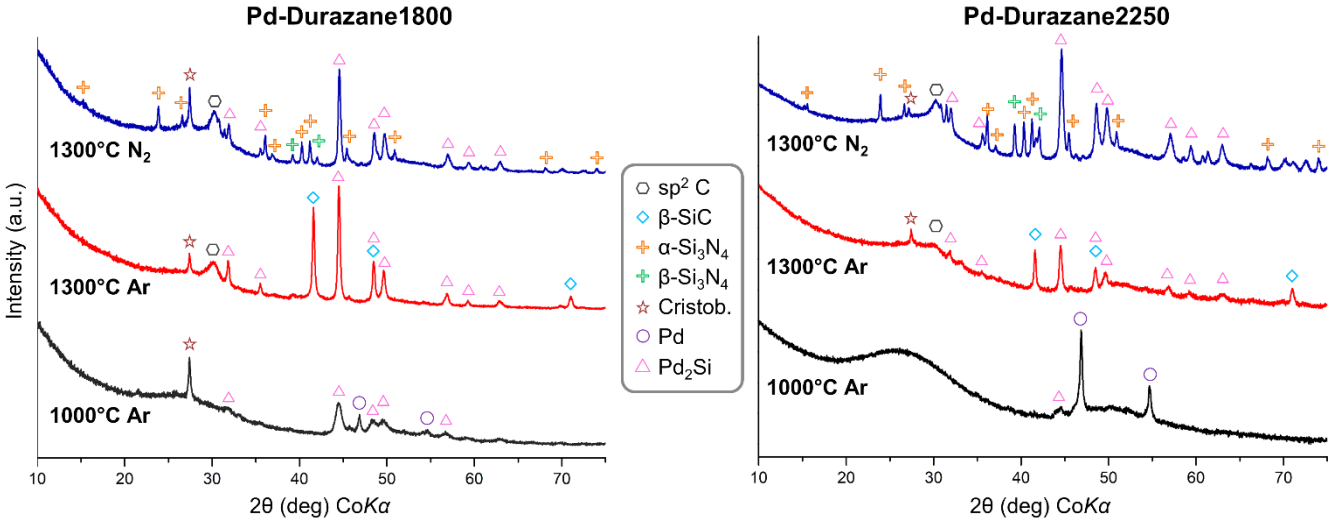

Figure 4-29: Comparison of the PXRD spectra of the Pd-modified PDCPs prepared from either precursor system and upon pyrolysis in Ar and consecutive high-temperature treatment in Ar or N_2.

The ceramic coating is SiPdOC-based according to the EDS spectrum and fairly similar to that observed in the other systems upon treatment in Ar at 1000 °C. The crystallites are homogeneously dispersed within the amorphous SiOC-based matrix and display a rather narrow size range of 5-35 nm locally as shown in the high-magnification ADF image. The BF overview, however, reveals a considerable diameter variation of the precipitates with some reaching over 120 nm. Interestingly, these larger ones have fewer other crystallites in their direct vicinity, which indicates a typical Ostwald ripening process. The discrete reflection rings in the corresponding SAED pattern can be assigned to both metallic Pd or different Pd_XSi phases, although additional reflexes do only match the latter, which points to a range of different Pd-based phases to be present, again substantiating the XRD results. Overall, the features observed are somewhat comparable to the other systems by their similar core-shell structure, the composition of the coating, and the phase assemblage generated; on the other hand, notable differences are evident, such as the absence of graphitic carbon and the fact that Pd-based phases do not occur within or in contact with the carbon fiber, but are solely found dispersed in the ceramic layer.

A closer examination of the chemical structure and phase assemblage generated upon pyrolysis was conducted via EDS mapping and localized electron diffraction with the results depicted in Fig. 4-31. The ADF image (a) shows a fiber cross-section along with the corresponding element maps, allowing for a clear distinction between the cellulose-derived carbon fiber and the SiOC-based ceramic coating. In contrast to the Ni-system, the distinction between elemental Pd and Pd_XSi cannot be made based on the mappings, as the Si-signal of the PDC layer is superimposed on that of the crystallites; hence, single-crystal electron diffraction combined with HRTEM imaging was employed for phase identification.

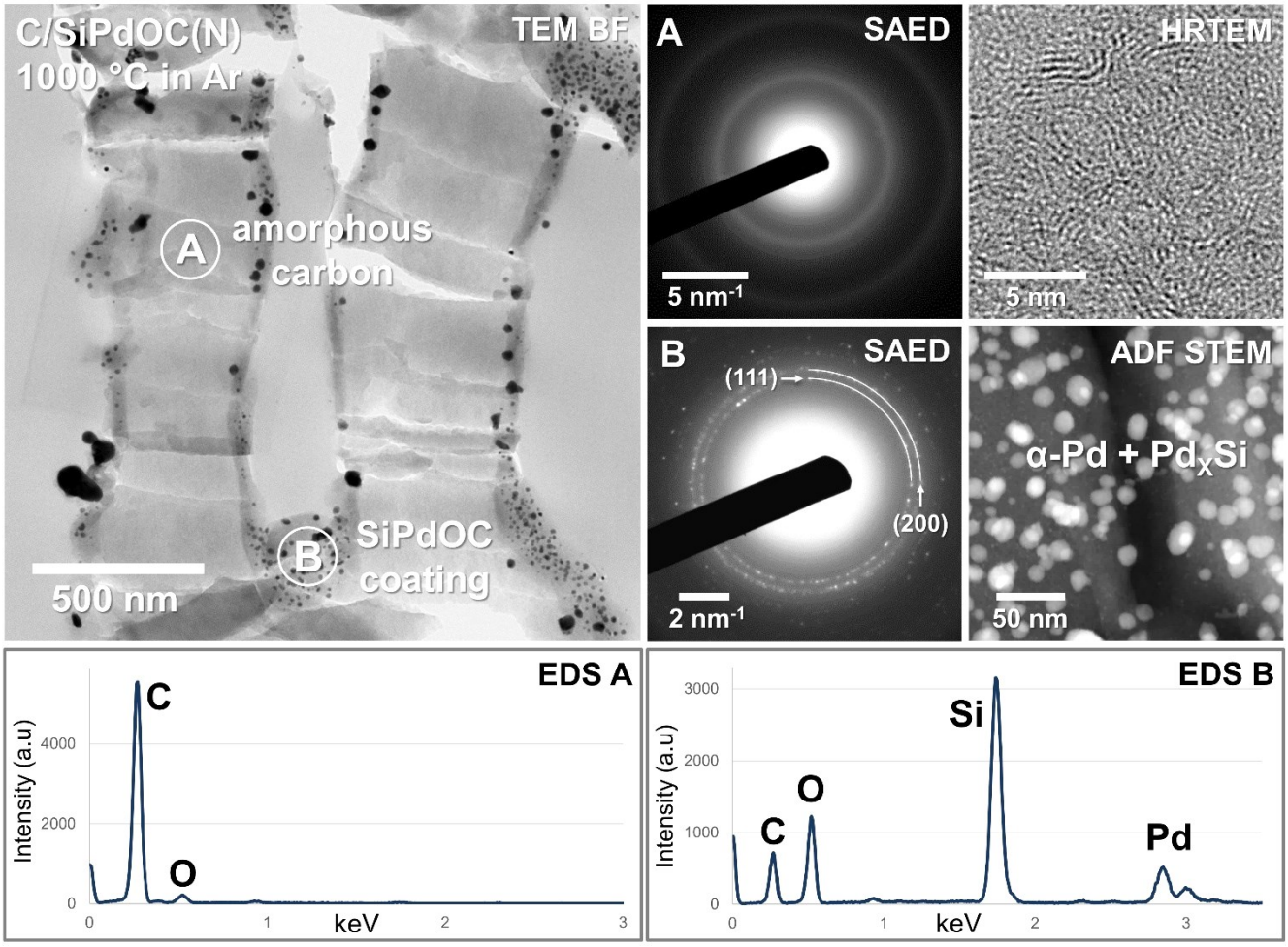

Figure 4-30: TEM BF image of a fiber cross-section in the SiPdOC(N)-based ceramic paper upon pyrolysis at 1000 °C in Ar atmosphere. The cellulose-derived carbon fibers (A) are entirely amorphous and devoid of Pd-based precipitates as shown by the corresponding SAED pattern and HRTEM image. A SiOC-based PDC coating (B) continuously encases the fibers, containing numerous crystalline precipitates, which give rise to discrete reflection rings in the SAED pattern. In addition to the rings matching metallic Pd, other reflections indicate the presence of one or more Pd-Si phases, as was also indicated by the XRD results.

Many of the larger particles, i.e. with a diameter of >30 nm, were identified as metallic Pd, some of them exhibiting rudimentary developed crystal facets (b). Although not indicated in the XRD data, TEM analyses reveal the occurrence of a stoichiometric Pd_3Si (*Pnma*) phase (c), predominately found in the population of small precipitates (<30 nm) dispersed within the coating and exhibiting spherical shapes. Associated with the Pd_3Si precipitates, hexagonal Pd_2Si nanocrystals (d) could be identified, exhibiting similarly rounded morphologies and diameters of around 5-25 nm. Moreover, among these smaller precipitates, some metallic Pd crystallites were found, which indicates that all the phases coexist in very localized assemblages in the Pd-modified PDCPs upon pyrolysis. As shown in the HRTEM images, the ceramic matrix encompassing the crystallites is amorphous, pore-free, and shows no signs of a segregated carbon phase. Also, as the XRD and TEM data show, no graphitization of the cellulose-derived carbon fiber has taken place. Thus, in terms of nano- and microstructural evolution upon pyrolysis, the Pd-modified papers investigated show specific characteristics different from the other PDCPs.

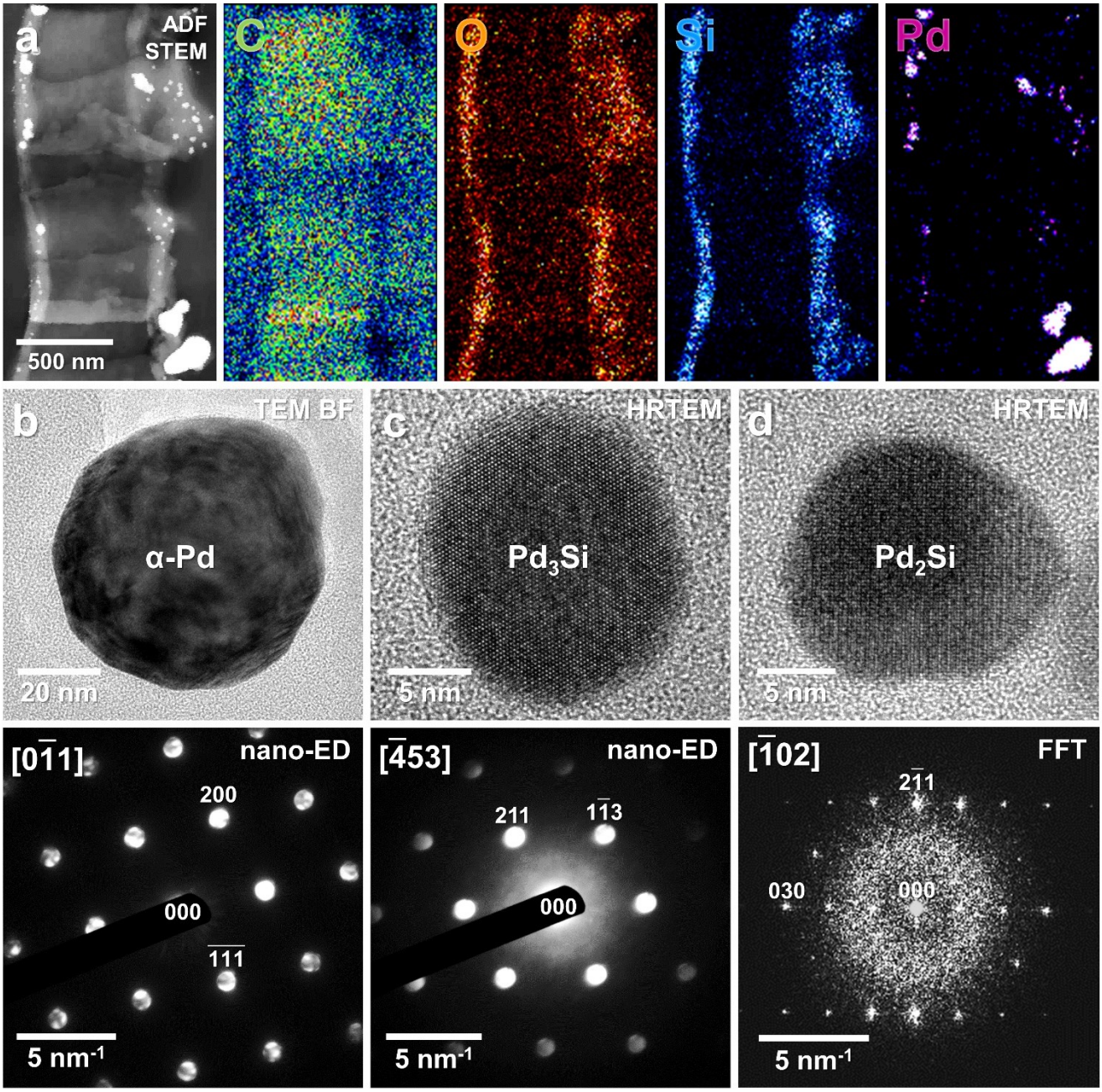

Figure 4-31: ADF STEM image and corresponding EDS maps (a) of one of the ceramic fibers depicted in the previous figure. The maps allow for a clear distinction between the cellulose-derived carbon fiber and the SiOC-based coating. Studying the phase assemblage of the sample in detail via TEM imaging and electron diffraction (b-d) confirmed the existence of Pd_3Si and Pd_2Si in addition to larger metallic Pd precipitates.

4.4.2 Tempering at 1300 °C in Argon Atmosphere

As shown in the PXRD data (Fig. 4-29), the pyrolyzed Pd-modified ceramic papers undergo extensive crystallization upon consecutive high-temperature treatment. Similar to the other systems, tempering in Ar atmosphere generates crystalline SiC in addition to metal-based silicides (Pd_2Si), whereas the formerly amorphous cellulose-derived carbon fiber undergoes notable graphitization. The SEM image of Fig. 4-32 shows that the fibrous paper structure is again well-preserved in the sample, featuring a homogeneous contrast in the BSE image. The fibers are decorated with numerous fine whisker structures, typically exhibiting diameters of a few hundred nanometers and lengths of several µm. In the high-magnification inset, one of the whiskers is shown featuring a metal-based tip encased by a thick facetted carbon shell. Overall, the paper displayed is rather similar to those generated with the other transition metals upon tempering in Ar. However, the number, size, distribution, and morphology of the whisker structures observed vary considerably across the different systems.

The TEM BF image of a fiber cross-section reveals its internal structure, with a core of amorphous carbon devoid of crystalline features and larger pores encased by a highly graphitized zone containing numerous nanosized Pd-based precipitates (A) enveloped by graphitic coil-like nanostructures. In addition, numerous larger crystallites are locally dispersed within this zone, predominately occurring close to the fiber surface and often in contact with the metal-based phases (B). According to the corresponding EDS spectrum and SAED pattern, SiC crystallized upon tempering, featuring irregularly-shaped grains with a diameter of up to around 200 nm. The TEM data show that the graphitization upon tempering detected via PXRD did not affect the whole fibers but is limited to the surface-near zone. All three phases, the Pd-base precipitates, the SiC crystallites, and the graphitic nanostructures, exclusively occur within this outer layer of the fiber and are mostly associated with each other implying a genetic relationship between these phases.

The results of the in-depth TEM analysis of the phase assemblage generated are depicted in Fig. 4-33. The nanosized Pd-based precipitates were determined to be exclusively Pd_2Si (a) exhibiting a variety of different diameters between 10-80 nm and morphologies ranging from irregularly rounded, elongated tear-shaped, to equiaxial facetted. As depicted in the HRTEM image, they are always enclosed within a coil-like shell of graphitic carbon, which often is aligned with the crystal faces. Typically, within close proximity to Pd_2Si, β-SiC crystallites occur (b), displaying irregular polygonal-rounded shapes and characteristic polytypic stacking faults along ⟨111⟩. The attributes of the SiC grains are very similar to those observed in the other systems. However, while in both Fe- and Ni-modified papers SiC was predominately generated at the surface of the fibers, here, it occurs rather homogeneously distributed throughout the graphitized zone. Moreover, the whiskers generated on the paper surface were occasionally observed during TEM imaging (c). Their structure was determined to be α-SiC, with a typical growth direction along ⟨010⟩ and, more rarely, ⟨011⟩. Although occasionally observed during SEM imaging, no metal-silicide tips were found, which could be due to most of the whiskers being fragmented upon sample preparation. On the other hand, the absence of catalyst globules could also indicate a different growth process, for instance, via a vapor-solid (VS) mechanism without a liquid phase involved.

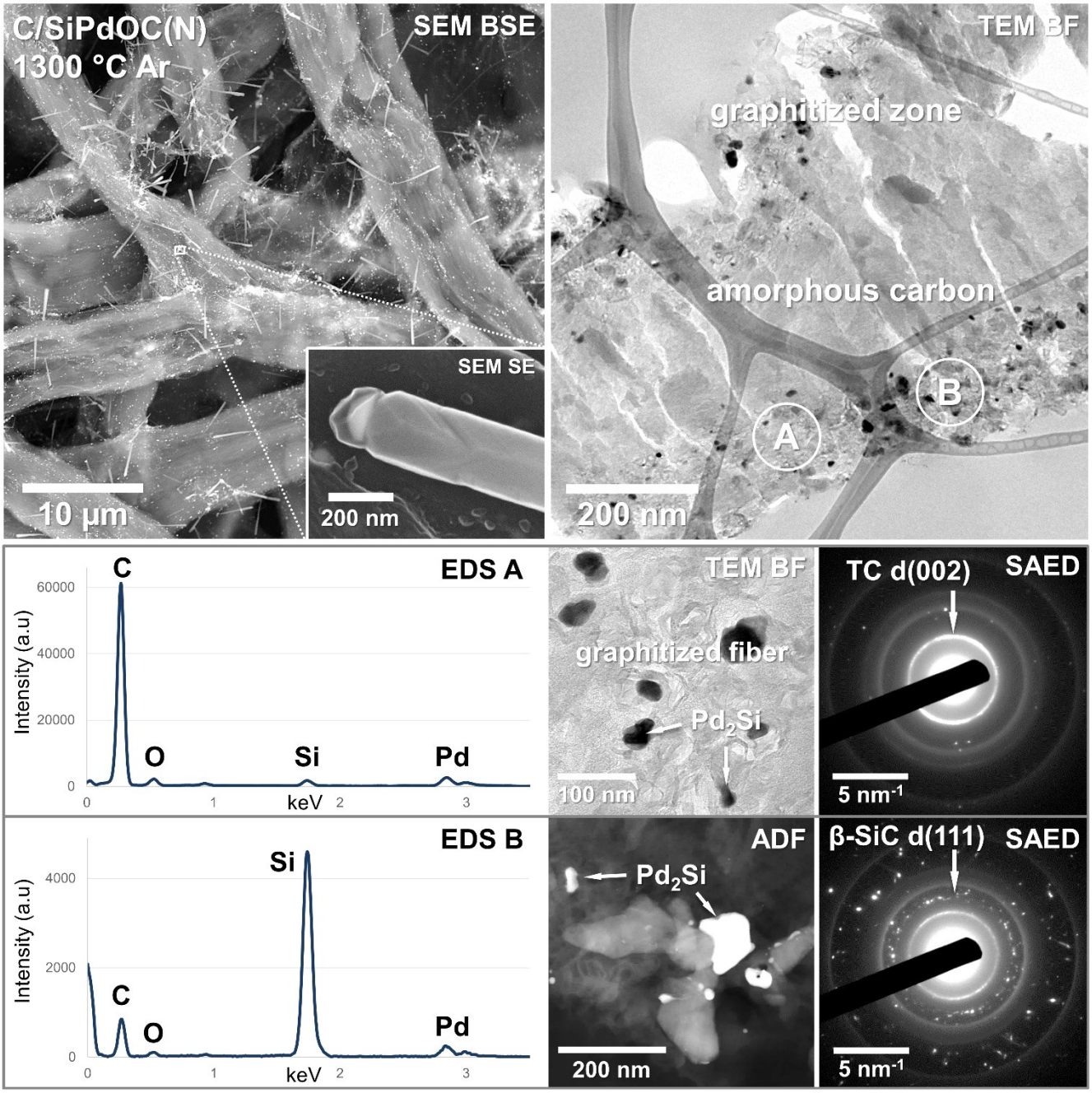

Figure 4-32: SEM image of a SiPdOC(N)-modified paper obtained upon tempering at 1300 °C in Ar atmosphere. The fibers are decorated with whisker-like structures, which are occasionally terminated by metal-based particles overgrown with a carbon shell (inset). TEM cross-sectional imaging reveals that the fibers consist of an amorphous carbon core but have undergone extensive graphitization within a surface-near zone, containing nanosized Pd-based precipitates (A) in addition to numerous β-SiC crystallites (B) enveloped by graphitic nanostructures.

Overall, the Pd-modified ceramic papers are fairly comparable to PDCPs prepared with the other transition metals upon tempering in Ar, featuring intact fibers, generation of a single type of Pd-silicides, SiC crystallization, and whisker growth. The internal structure of the ceramic composite fibers, with a large amorphous carbon core encased by an extensively graphitized outer layer, is somewhat notable in comparison with the other papers, especially as the samples upon pyrolysis revealed no signs of graphitization. The fact that graphitic nanostructures

exclusively occur in direct vicinity to the Pd-based precipitates implies a catalytic process to be responsible for the structural transformation of the carbon.

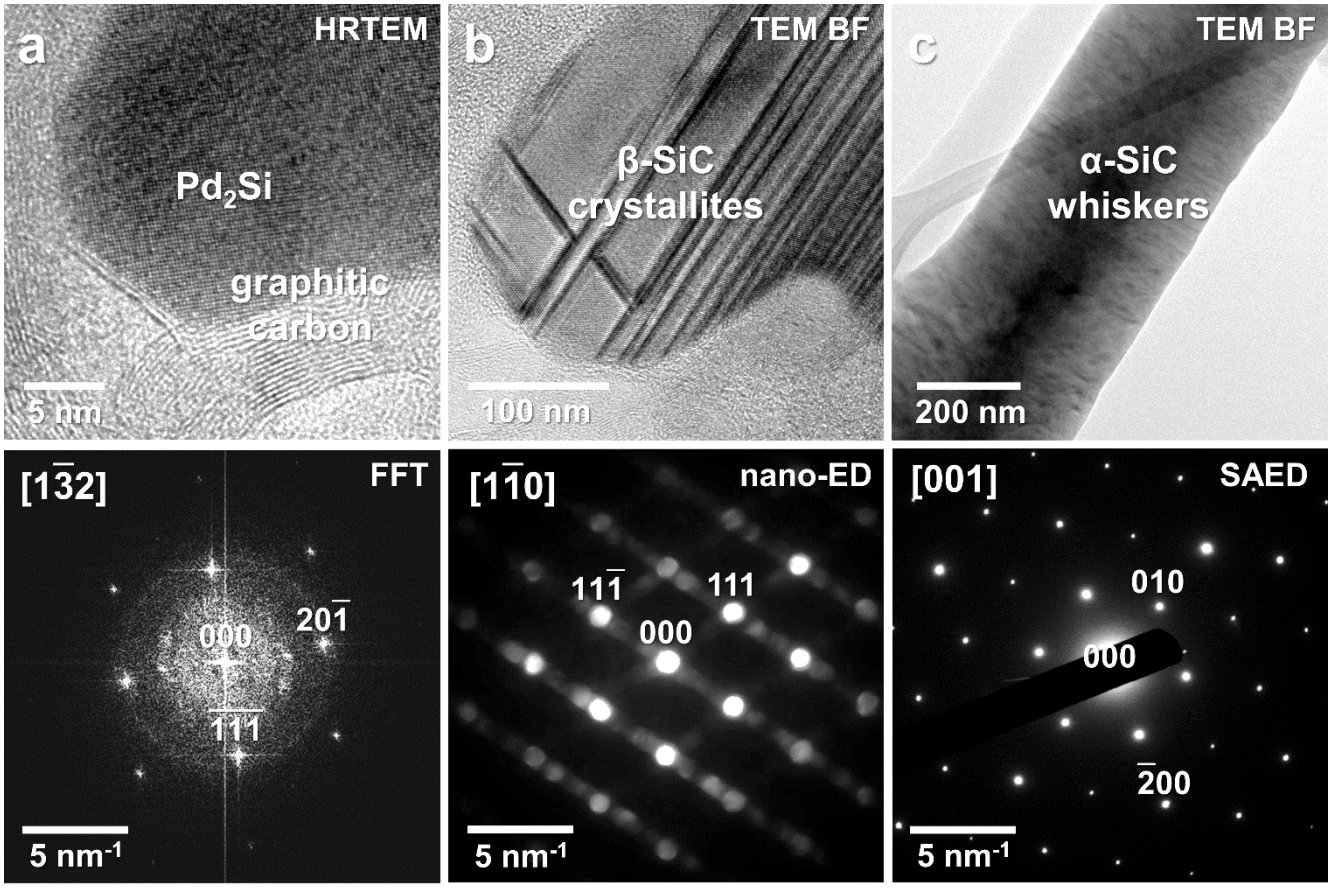

Figure 4-33: Detailed TEM analyses of the crystalline phases identified in the Pd-modified papers upon tempering at 1300 °C in Ar. The sole Pd-based phase observed is Pd_2Si (a), exclusively found enveloped in graphitic carbon nanostructures and mostly associated with β-SiC crystals exhibiting the typical polytypic stacking faults (b). Both phases occur only within the graphitized zones of the fibers near their surface, but not within the amorphous carbon core. The whiskers were identified as hexagonal α-SiC single-crystals exhibiting varying diameters and growth directions (c).

4.4.3 Tempering at 1300 °C in Nitrogen Atmosphere

Finally, SiPdOC(N)-based PDCPs were annealed at 1300 °C in N_2 and the resulting samples were investigated to assess variations with respect to the other systems. Notably, the color of the Pd-modified papers changed only slightly, with some greyish specks visible on a mostly black ceramic paper (similar to those annealed in Ar), whereas tempering in N_2 of the Fe- and Ni-modified samples resulted in light-gray to almost white PDCPs. In Fig. 4-34, the microstructure of such a C/SiPdOC(N) paper is displayed as observed via BSE imaging. The morphology of the paper template is retained upon the high-temperature treatment, and individual fibers and pores between them are visible. In contrast to the other N_2-treated samples presented earlier, ultra-long nanowires appear to be absent here. The fibers show a notably heterogeneous contrast in the BSE image, with brighter areas along fiber edges and gussets between fibers. High-magnification imaging of the fibers reveals that their surface is, in fact, scattered with small whisker and wire structures occasionally assembled into clusters of varying sizes corresponding with the lighter areas observed at low magnifications. As shown in the inset, the whiskers exhibit rather uniform and constant diameters between several tens to a few hundreds of nm, reach lengths of a few tens of µm, and are often decorated with round metal-based tips.

The intrinsic structure of the ceramic composite fibers observed during TEM imaging of the cross-sectional samples, reveals overall similar characteristics to the other PDCPs investigated. The cellulose-derived carbon fiber (A) is entirely composed of graphitic carbon in this case, as shown by the high-magnification BF image and corresponding SAED pattern exhibiting the typical diffuse turbostratic carbon rings. Numerous nanosized irregularly-shaped Pd_2Si precipitates are dispersed within the fibers encased by the graphitic carbon nanostructures displaying a comparably high degree of crystallinity. Within the core regions of some of the larger fibers, amorphous carbon is still present, again, exclusively where none of the Pd-silicides occur, which agrees with the data obtained from the samples tempered in Ar.

Primarily along the fiber surface, numerous polygonal faceted features can be observed (B). As depicted in the high-magnification BF image, they often exhibit isometric dimensions with diameters of several hundreds of nm and intermittently occur along the fibers, occasionally forming a continuous cover of the carbon fibers, whereas locally, none are evident at all. Their amplitude contrast varies drastically with orientation and electron diffraction from individual grains results in single-crystalline SAED patterns. In combination with EDS analyses, which indicate that they are exclusively composed of Si and N, the crystallites can be unequivocally identified as α-Si_3N_4. Please note that some of the crystallites appear to have been generated within the fiber, which, however, is a result of the specific cross-section shown. If a fiber is cut parallel close to its surface, the resulting slice does not show the structure generated deep within the fiber. Other cross-sections displayed a similar microstructure as that observed in the samples treated in Ar (Fig 4-32), with an inner zone composed of Pd-free amorphous carbon and an outer graphitic layer encompassing Pd-based crystallites, which is decorated with Si_3N_4 grains. Intact Si_3N_4 whisker structures attached to the fibers were only rarely observed, whereas elongated fragments and some detached whiskers are present throughout the sample slices, which is attributed to the preparation technique.

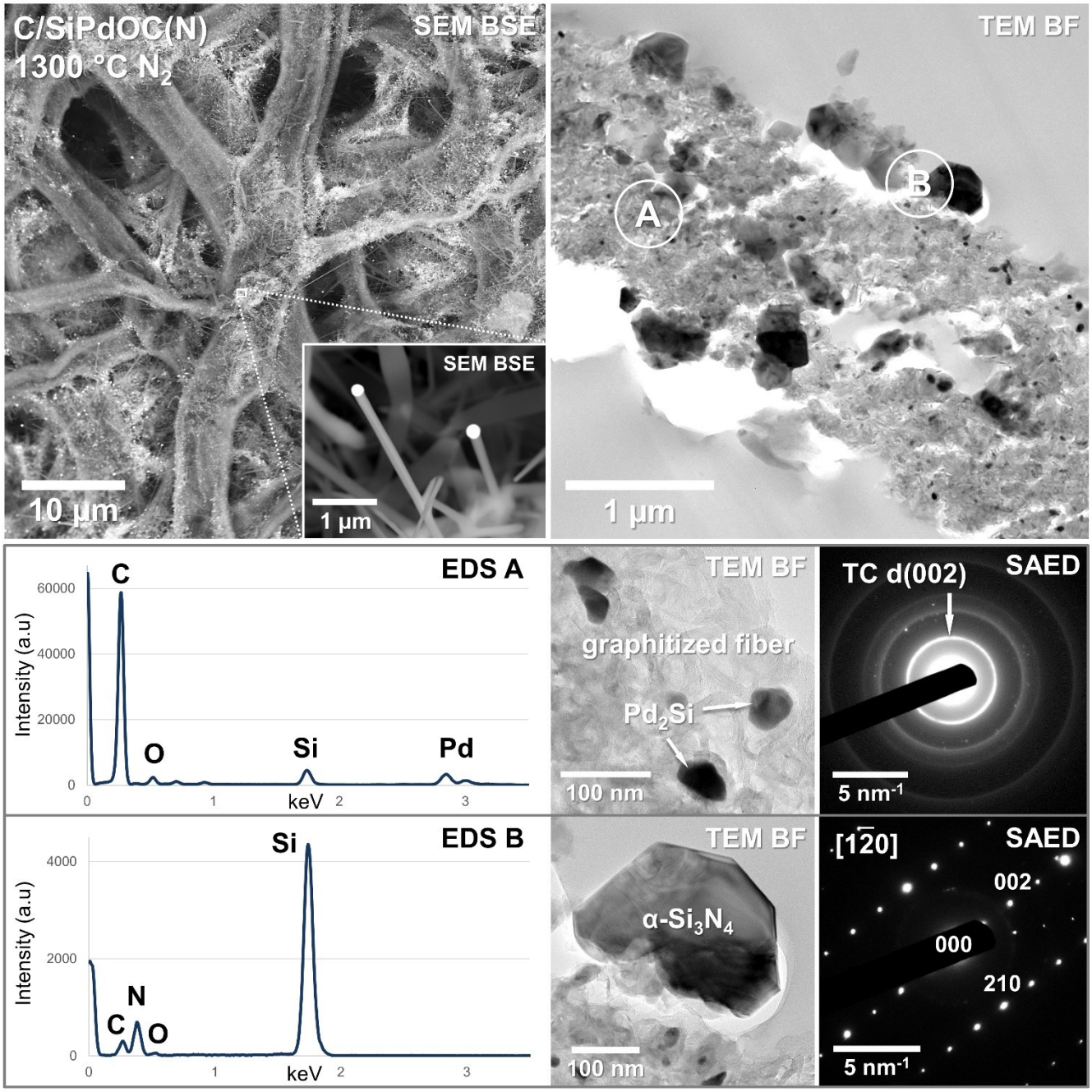

Figure 4-34: SEM image of a SiPdOC(N)-modified paper obtained upon tempering at 1300 °C in N_2. Clusters of small straight whisker structures cover most of its surface often terminated by metal-based tips, as shown in the inset. TEM imaging of fiber cross-sections shows highly graphitized fibers encompassing numerous crystalline Pd-based precipitates (A). The fiber surface is scattered with large Si_3N_4 crystallites (B), exhibiting irregular polygonal shapes.

One of the detached whiskers is displayed in Fig. 4-35, exhibiting a uniform diameter of around 150 nm and being decorated with a similarly sized metal-based globule. As previously indicated by the XRD data, all Pd-based phases in the sample examined via TEM were determined to be Pd_2Si; this was found to be the case for both the precipitates dispersed within the cellulose-derived carbon fiber as well as those atop the whisker structures, as exemplarily shown in the HAADF image (a). The atomic resolution reveals the position of the Si- and Pd atomic

columns viewed along the [001] zone axis with a single unit cell shown for comparison (generated with Vesta [256]). The whisker itself is single-crystalline α-Si_3N_4 grown along the [010] direction as shown by HRTEM imaging and ED (b). This aligns with the observations made for the other systems, showing all silicon nitride whiskers terminated by metal-silicides and to be built up along ⟨100⟩. HRTEM imaging of the contact between Pd_2Si and Si_3N_4 reveals an almost atomically sharp interface (c); however, as was the case in all other samples, no specific orientation relationship could be determined between the whiskers and the globules. Please note that a thin layer of TC was often found around the Pd_2Si crystallites, which might stem from the exsolution of carbon from the particles or adsorption and decomposition of gaseous hydrocarbon species during heat treatment [4,257]. The fact that two fundamentally different morphologies among Si_3N_4 structures have been generated (grains and whiskers) implies two distinct formation mechanisms to operate during tempering. While the isometric habit and random orientation of the silicon nitride crystallites imply an in situ formation from the a-SiOC coating, the Pd_2Si globules present at the tips of the whiskers indicate growth of the whiskers via a Pd-catalyzed VLS mechanism.

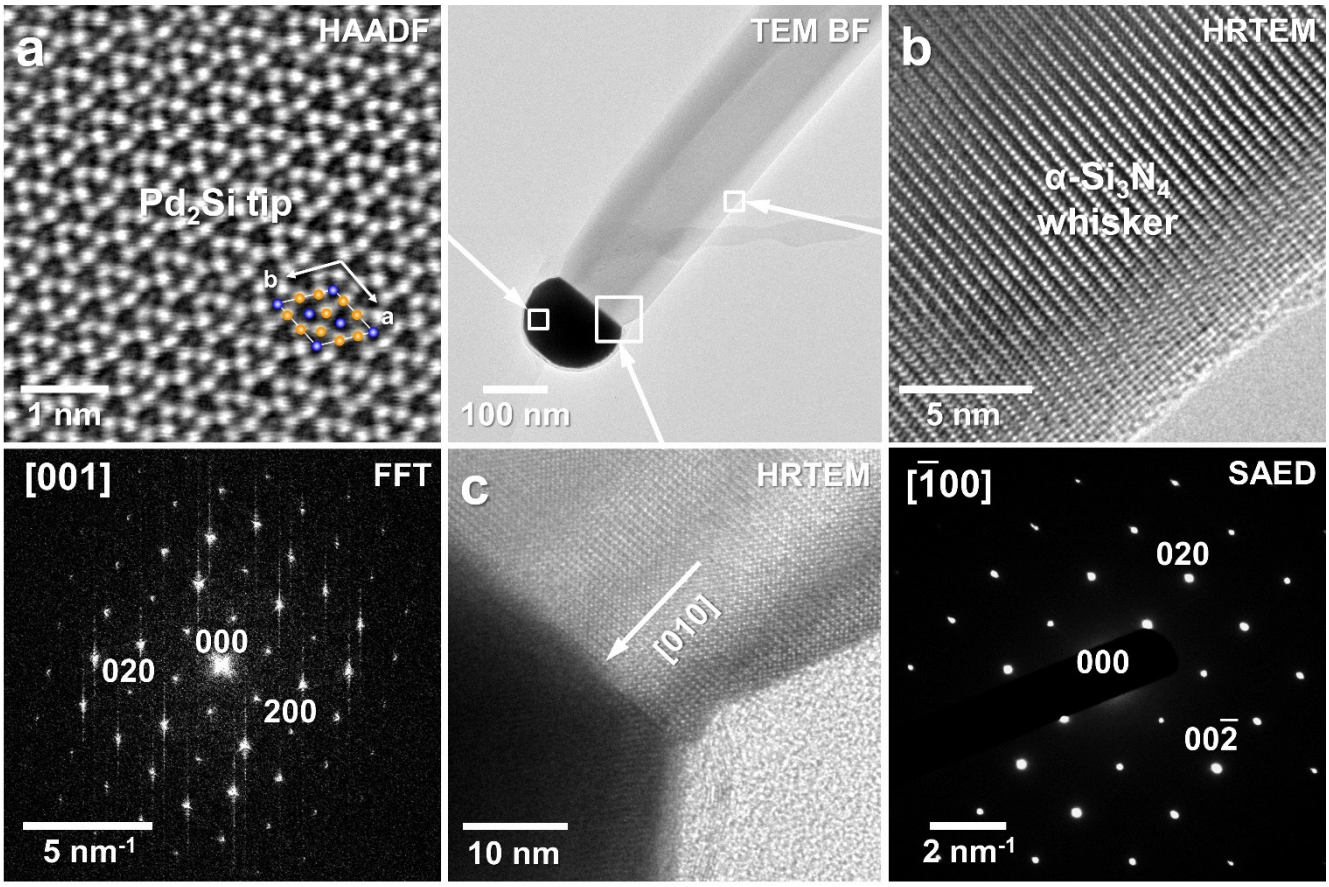

Figure 4-35: TEM analysis of a nanowire generated within the Pd-modified ceramic papers tempered in N_2 atmosphere. A Pd_2Si crystallite (a) terminates the single-crystalline α-Si_3N_4 whisker (b) grown along the [010] direction. Although no specific crystallographic orientation relationship could be determined, the silicide tip exhibits a planar interface along the tip of the wire (c).

4.4.4 Microstructure & Phase Evolution of SiPdOC(N)-based PDCPs

In most regards, the Pd-modified ceramic papers display similar characteristics upon pyrolysis as the other systems investigated. However, the cellulose-derived carbon was found to be entirely amorphous, whereas the Fe-based and Ni-modified papers in particular were shown to accommodate predominately graphitic carbon at this stage. Moreover, with Pd, the fibers are devoid of any crystalline precipitates, while Ni-based crystallites were found to be dispersed within them.

Several studies have shown that pyrolysis of preceramic polymers modified with oxygen-rich metalorganic compounds initially leads to the formation of a metal oxide phase, which then gets reduced through available carbon [23,92]. For Pd/SiOC ceramics, the formation of PdO_X clusters and subsequent reaction with carbon was proposed, resulting in CO gas and metallic Pd, which then reacts with the amorphous SiOC to form silicides [258]. According to the Pd-Si phase diagram, the region 10-34 at.-% Si. in the temperature range investigated is rather complex featuring various two-phase fields with stoichiometries between $Pd_{21}Si_4$ and Pd_2Si [259,260]. Among the Pd-Si phases, which all feature a negative Gibbs free energy of formation, ΔG_f^o, up to well over 1273 K, the latter was found to be the most favorable over a wide temperature range [261]. While Pd_2Si and Pd_3Si are adjacent and thus can coexist, elemental Pd should only be formed for very low silicon contents and only accompanied by $Pd_{21}Si_4$. Many of the Pd-rich Pd_XSi phases are deemed metastable in the literature and no reliable structure data is available. Some older studies [262,263] report on the initial formation of a metastable cubic compound $Pd_{41}Si_9$ ($Fm\bar{3}m$), which is close in stoichiometry to the $Pd_{21}Si_4$ phase and would not be distinguishable from pure Pd by the techniques employed here. Nevertheless, between this compound and Pd_3Si, several other intermediate phases should exist, such as the monoclinic Pd_5Si ($P2_1$), which, however, has not been observed. This in turn, may indicate that the phase evolution at the pyrolysis stage is governed by reaction kinetics rather than thermodynamics and that the comparably short duration and moderate temperature of pyrolysis is not sufficient to establish thermodynamic equilibrium between the Pd-based phases within the whole sample. However, in the case of pure Pd/SiCO PDCs pyrolyzed at 1100 °C, Pd_2Si was recognized as the sole crystalline phase generated [258], which was also found to be the case for the pure Pd/SiCO(N) at 1000 °C investigated for the present study [8]. This could imply that the use of a paper template somehow affects the phase evolution of the PDC layer.

Upon annealing at 1300 °C, the sole metal-based phase detected via XRD and single-crystal electron diffraction is Pd_2Si. This closely resembles the phase evolution observed within the other systems featuring a transition of several metal-based phases generated upon pyrolysis towards Fe_3Si and Ni_2Si, respectively, during high-temperature treatment. At 1300 °C, Pd_2Si is still the thermodynamically most favorable Pd_XSi phase [261] and can form from the reaction of Pd and Pd_3Si with the surrounding a-SiOC matrix. Additionally, at this temperature, SiO gas formation can enable the distribution of Si over the whole system, while the elevated temperature promotes diffusion processes, which both accelerate establishing equilibrium conditions.

Upon tempering of the Pd-modified papers, extensive graphitization of the cellulose-derived AC is observed around Pd_2Si NPs now found dispersed within the fibers. Graphitization is strictly limited to the surface-near

zones of the fibers in which the Pd-based phases are found. Although Pd-catalyzed graphitization has been reported in the literature [264], almost no information is available on the interaction with cellulosic carbon precursors. Apart from the different temperature regimes at which GC generation was observed, the well-defined coil- and ribbon-like structures generated indicate differences in the formation process upon using Pd as a catalyst. Analogous to the other systems investigated, annealing of the Pd-modified papers in Ar results in the generation of β-SiC crystallites. They exclusively occur at the surface of the fiber or within the surface-near graphitized zone associated with the Pd_2Si precipitates and are enveloped by GC nanostructures forming a local nanocomposite. In addition, in situ generation of a-SiC whiskers was observed, which however were fewer and smaller than in the Ni-modified papers. Likewise, samples annealed in N_2 were found to be decorated with α-Si_3N_4 whisker structures, occasionally exhibiting Pd_2Si tips indicating VLS growth, which has, to the best of our knowledge, not been recorded in the literature yet. Compared to the nanowires generated with Fe- or Ni-modified polymers, the whiskers are mostly straight with a uniform diameter and exhibit much smaller aspect ratios.

SiPdOC(N)-based Ceramic Papers - Summary

- Pyrolysis of the SiPdOC(N)-modified papers results in the generation of pseudomorphic PDCPs with a morphology retained from the respective template:
  - In contrast to the other systems, the cellulose-derived carbon fiber is entirely composed of AC without any signs of graphitization observable upon pyrolysis at 1000 °C
  - Nanosized metallic Pd, Pd_3Si, and Pd_2Si precipitates are exclusively found dispersed within the amorphous SiOC layer encasing the AC fibers, which themselves are devoid of Pd-based phases
  - Compared to Fe and Ni, precursor modification with Pd enables another distinct microstructure to be generated; catalytic graphitization of the fibers is entirely absent from the papers upon pyrolysis.
- During annealing at 1300 °C, crystalline C/Pd_2Si/SiC (Ar) and C/Pd_2Si/Si_3N_4 (N_2) microcomposites are generated and the fibers are decorated with a multitude of Si-based nanowhiskers:
  - Upon tempering, extensive graphitization in the outer zone of the cellulose-derived carbon fibers is observed, now encompassing Pd-based NPs enveloped by coil-like graphitic nanostructures
  - As with the other systems, XRD and TEM data indicate that Pd_2Si exclusively found within the graphitized zone of the fibers is the sole metal-silicide phase formed upon annealing of the PDCPs
  - Occurring at surface-near regions throughout the graphitized zone, β-SiC crystallites and Pd_2Si surrounded by graphitic nanostructures are generated upon tempering in Ar; the whiskers scattered over the paper surface were identified as crystalline α-SiC only infrequently exhibiting Pd_2Si tips
  - Annealing in N_2 results in the formation of separate large faceted α-Si_3N_4 crystallites and small whiskers on the surface of the fibers, which were often found terminated by Pd_2Si globules.
- The results display significant variation in the microstructural evolution of PDCPs depending on the transition metal utilized; in particular, regarding catalysis of graphitization and the size, number, and morphology of the SiC and Si_3N_4 structures generated.

4.5 Variations in Microstructure and Phase Assemblage with Transition Metal Modification

Implied by the results presented above, the choice of the transition metal used for precursor modification has considerable potential concerning designing the microstructural characteristics and phase assemblage generated within PDCPs. Specifically, the three transition metals investigated have a profound effect on the graphitization of the cellulose-derived carbon fiber, in addition to the generation and attributes of the secondary Si-based crystalline nanostructures formed upon annealing in different atmospheres. This chapter focuses on the differences observed between the ceramic papers modified with either Fe, Ni, and Pd, and aims to provide insights into the parameters that can be used to functionalize PDCPs with such nanostructures to enable future application.

4.5.1 Metal-catalyzed Generation of Graphitic Nanostructures

As pointed out previously, the thermal graphitization of amorphous carbon (precursors) typically requires substantially higher temperatures (>2000 °C) than those employed for the present synthesis of PDCPs. Nevertheless, all Fe- and Ni-modified papers showed a considerable degree of graphitization within the cellulose-derived carbon fibers, even upon pyrolysis at 1000 °C and, following the tempering step at 1300 °C, also the Pd-based papers encompass graphitic nanostructures throughout the fibers. Both the drastically reduced temperature and the fact that graphitization occurred primarily around the metal-based precipitates suggest a catalytic process to be responsible for the structural transformation observed. It is well established in the literature that various transition metals are suitable catalysts for the graphitization of amorphous carbons and carbon precursors (such as cellulose), reducing the temperatures at which graphitic structures can be generated to below 1000 °C [241,265]. Additionally, the process was shown to produce nanostructures with well-defined shapes such as nanocoils, -onions, and -ribbons, as well as bamboo-like and multi-wall nanotubes [31,266,267].

Based on the results presented, it is proposed that such catalytic graphitization processes lead to the observed structural transformation of the cellulose-derived carbon fibers in all PDCPs investigated, albeit at different temperatures and with a varying arrangement and ordering of the graphitic structures, depending on the transition metal utilized. Fig. 4-36 correlates the results obtained via TEM examination with Raman analyses of different paper samples. For reference, the Raman spectrum of a natural graphite crystal is displayed (black curve), showing the characteristics of a fully ordered sp^2-hybridized carbon sample (sharp and high-intensity G and 2D bands, low-intensity D band). No traces of graphitization were observed upon pyrolysis of pure paper samples (Cotton Linters in this case) at 1000 °C, as shown by the corresponding Raman spectrum (red) exhibiting characteristics typical for amorphous carbon, which has also been concluded from the HRTEM analyses. Upon pyrolysis of papers coated with a SiNiOC(N)-based polymer, however, the Raman spectrum (blue) reveals the presence of graphitic carbon, i.e. intensity increase and sharpening of the D and G bands, as well as a development of a sharp

2D band. Accordingly, the HRTEM data display graphitic carbon clusters with a moderate degree of order. With annealing at 1300 °C in either N_2 (green) or Ar (magenta), the graphitization progresses further as indicated by the G band displaying a higher intensity compared to the D band. The increase in ordering is also displayed in the HRTEM image revealing larger graphite clusters with increased long-range order, also reflected in the FFT. Please note that the atmosphere appears to have no effect on the graphitization observed.

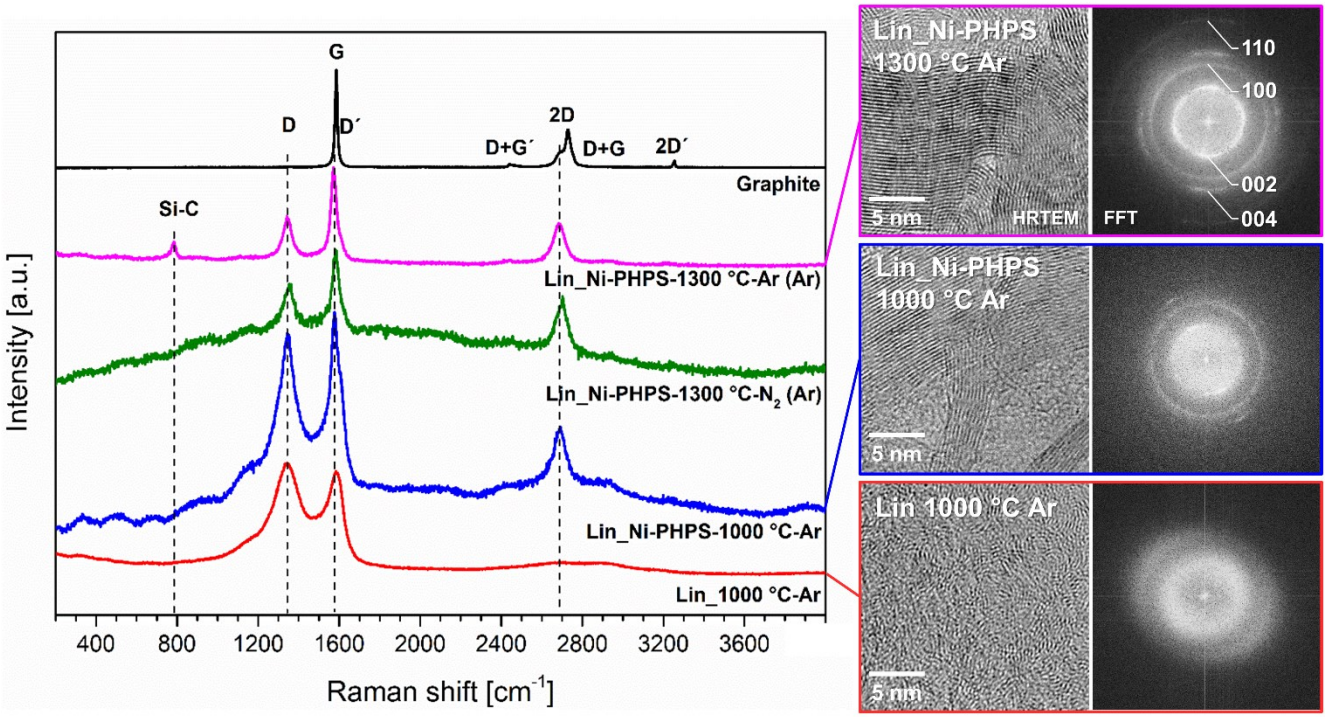

Figure 4-36: Raman analyses of different paper samples upon pyrolysis at 1000 °C in Ar. The pure Lin sample (red) shows no evidence of graphitization according to Raman analysis and HRTEM imaging, while the carbon in the Ni-PHPS modified paper (blue) has undergone structural transformation towards turbostratic carbon. Upon annealing, larger graphitic clusters with better ordering (green) are observed via HRTEM, which is also reflected by the corresponding FFT and sharpening of the G and 2D bands in the spectrum. For comparison, the Raman analysis of a well-crystallized graphite specimen is given (black). Raman data courtesy of Alexander Ott.

This strongly implies that the transition metals act as catalysts for the graphitization of the fibers, which is also supported by the fact that the extent of graphitization within the fibers appears to coincide with the distribution of the metal-based precipitates. The TEM BF image displayed in Fig. 4-37 shows a large fiber in the SiNiOC(N)-based ceramic papers upon pyrolysis cut in cross-section (a). The core of the fiber is predominately composed of amorphous feature-less carbon, while the outer layer containing Ni-based precipitates has undergone considerable graphitization extending about 500 nm into the fiber. With subsequent annealing (b), the zone of graphitization has progressed further, again coinciding with the location of the Ni-based precipitates. As shown by the SAED patterns, the core of the fibers still remained amorphous, while the outer layer is a microcomposite of nanosized Ni_2Si, β-SiC, and graphitic carbon nanostructures. This gives additional evidence of a catalytic graphitization process directly coupled to the presence of metal-based precipitates, which appear to move through the fibers

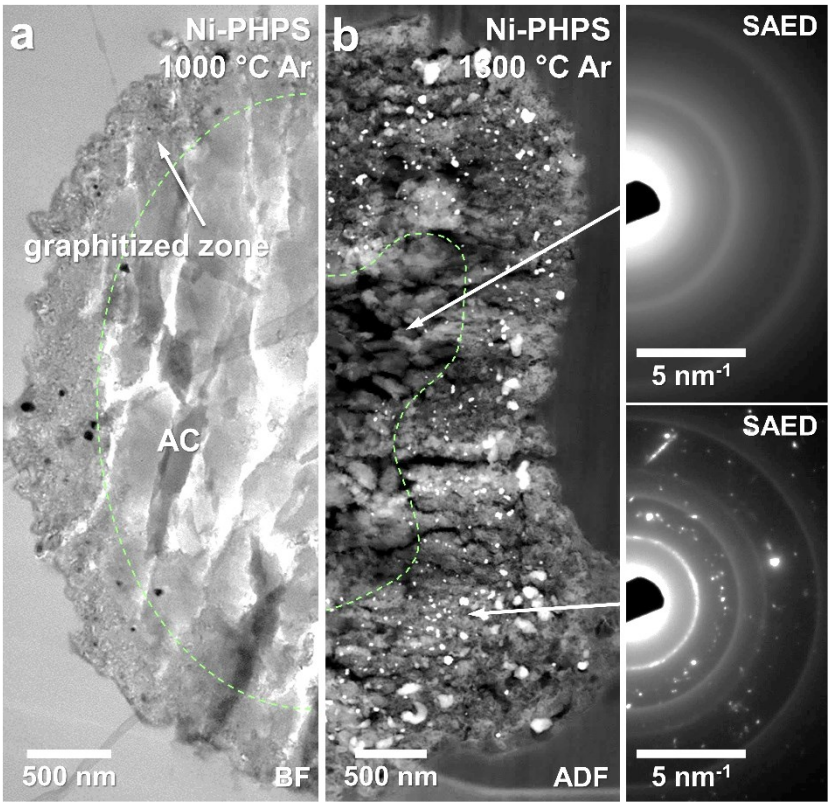

Figure 4-37: Extent of graphitization observed in a Ni-modified PDCP upon pyrolysis (a). The fiber cross-section shows a large core of amorphous carbon (AC) encased by a highly graphitized zone with numerous Ni-based particles dispersed within. Upon annealing (b), the nanoparticles have migrated within the fiber, β-SiC has crystallized, and the graphitized zone extends deeper, leaving only a small core of AC as shown by the corresponding SAED patterns.

during high-temperature treatment. According to various studies reporting on the transition metal-catalyzed graphitization of carbon, the underlying mechanism is driven by the free energy reduction through graphite formation and usually proceeds via the solution of AC (or a precursor) followed by reprecipitation as semicrystalline sp^2-hybridized carbon [241,265,266]. Many authors report on a 'liquid-like' movement of transition metal nanoparticles through the substrate, leaving a trail of graphitic nanostructures behind, which even was directly observed during in situ TEM experiments [31,241,268].

The carbon structures generated have different characteristics depending on the transition metal utilized and, as shown by the Pd-modified papers, the process starts at different temperatures. Fig. 4-38 presents a comparison of the structural state of cellulose-derived carbon in the different PDCPs investigated. Upon pyrolysis at 1000 °C, the three systems display very different degrees of graphitization depending on the metal introduced. The fibers in the Ni-modified papers have undergone extensive graphitization with individual reflection rings in the SAED pattern assignable to TC lattice planes (a), whereas Pd-modified papers accommodate exclusively AC (b). With an Fe-modified precursor, the fibers have also been converted into TC; however, compared to the Ni-based papers, the graphitic structures exhibit a slightly larger d(002) lattice plane distance (≈ 3.5 Å), more curvature of the lattice planes, and an overall lower degree of order, which is reflected in the diffuse reflection rings (c). According to several studies, the catalytic activity and details of the mechanism can vary considerably between the different transition metals, with the ability of base metals to form transient (metastable) carbides and their decomposition being proposed to play a pivotal role in the formation of graphitic nanostructures. In the case of Ni, carbide phases formed decompose rapidly as GC is thermodynamically more stable. As a result, the particles are encapsulated within a GC shell, which prevents further graphitization to occur until the shell is ruptured. The high thermal expansion of the metals, however, enables the particles to breach the shell and allow progression of the catalytic process. This typically is accompanied by the formation of large

graphitic clusters, which somewhat mimic the shape of the catalytic particle to create ribbon- and coil-like nanostructures. With an Fe catalyst, carbides generated are much more stable, and complete encapsulation does generally not occur [267]. As a result, Fe (and Fe_3C) nanoparticles are highly mobile and active for graphitization [267], but do not generate large well-ordered graphitic clusters, which aligns well with the present results.

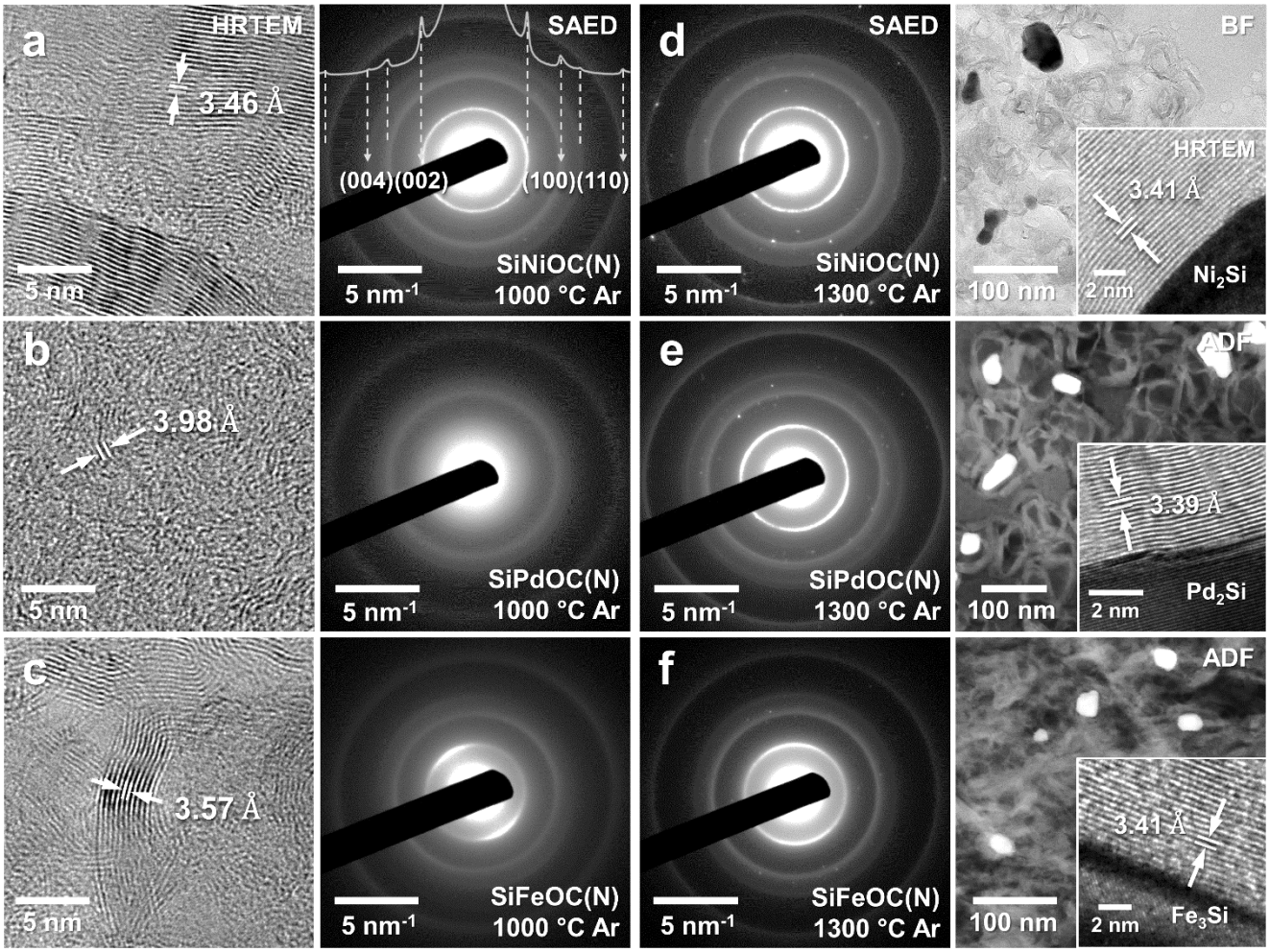

Figure 4-38: Comparison of the structural characteristics of the cellulose-derived carbon generated in the Ni- (a), Pd-, (b), and Fe-modified (c) ceramic papers. Upon pyrolysis at 1000 °C, the fibers in the three systems display very different degrees of graphitization depending on the metal introduced. Upon annealing at 1300 °C, all systems exhibit highly graphitic carbon fibers containing the majority of metal-based precipitates (d-f). Please note that the shape of the graphitic nanostructures generated is different for each transition metal; Ni and Pd in particular feature well-defined graphitic nanocoils, whereas Fe contains mainly turbostratic graphitic clusters in a disordered arrangement.

Upon tempering at 1300 °C, the degree of graphitization has increased in all samples investigated (d-f) and, most notably, even the fibers in the Pd-modified papers contain numerous graphitic nanocoils around Pd_2Si particles (e). Compared to Fe and Ni, the graphitization capability of Pd is considered inferior, although some studies have shown that it does produce GC at temperatures as low as 600 °C [268]. However, the nature of the carbon (precursor) can affect the temperature and resulting nanostructures decisively [269] and the Pd-catalyzed

graphitization of cellulose has not been investigated prior to this study [200]. In the Ni system, on the other hand, the degree of graphitization has increased only slightly, which is likely the result of the NPs becoming entrapped by thick GC shells, preventing them from being reactivated during tempering. As with the Pd-modified papers, the carbon structures generated consist of large ribbon- to coil-like clusters, typical for carbide decomposition. Upon tempering of the Fe-modified samples, the GC structures are still comparably disordered and turbostratic, again implying that the process is largely driven by solution and reprecipitation [241].

The results show that the nanostructure of the cellulose-derived carbon fibers within PDCPs can be controlled through metal modification of the precursor. Nanostructured carbon materials have become increasingly important for a variety of applications in the last decades, including but not limited to energy storage, structural materials, sensors, and many others [270–272]. Hence, their in situ generation within the ceramic papers investigated is an attractive feature adding to the options of designing the properties of these complex ceramic composites. Adjusting the preceramic polymers could be used to affect the type, order, and morphology of the GC nanostructures through the controlled formation of transition metal NPs, which, however, demands further investigation of the underlying processes.

4.5.2 Growth of SiC and Si_3N_4-based Nanostructures

Functionalization of PDCPs with in situ generated SiC- and Si_3N_4-based nanostructures exhibiting well-defined morphologies is another highly attractive feature of PDCPs concerning a variety of potential applications. Often, such nanostructures exhibit interesting novel or superior properties compared to traditional materials, and hence, their investigation and establishment of economic synthesis routes have attracted widespread interest in the scientific community.

Upon tempering at 1300 °C in Ar, in each ceramic paper investigated, crystallization of the a-SiOC coating generated upon pyrolysis has been observed and β-SiC was identified as the principal Si-based phase. Regardless of the transition metal modification, the cubic polymorph was shown to have precipitated as irregularly shaped crystallites close to the surface of the carbon fibers associated with and enveloped in turbostratic GC. This process is induced by the devitrification of amorphous SiOC at high temperatures and the subsequent reaction of SiO_2 domains with free carbon resulting in the generation of SiO gas and, finally, the formation of SiC along with CO. Additionally, the growth of SiC-based whisker structures has been observed in all system, albeit with significant variations concerning their number, distribution, dimensions, and morphology, depending on the transition metal utilized. As comparatively displayed in the light micrographs of Fig. 4-39, the surface of a SiNiOC(N)-based paper (a) is scattered with a multitude of SiC whiskers arranged in radiating clusters upon tempering in Ar. The Fe-modified paper (b) on the other hand, is almost devoid of whiskers and predominately encompasses β-SiC

coated fibers, whereas, within the Pd-modified paper (c), whiskers too small to be observable in the light micrographs have been generated.

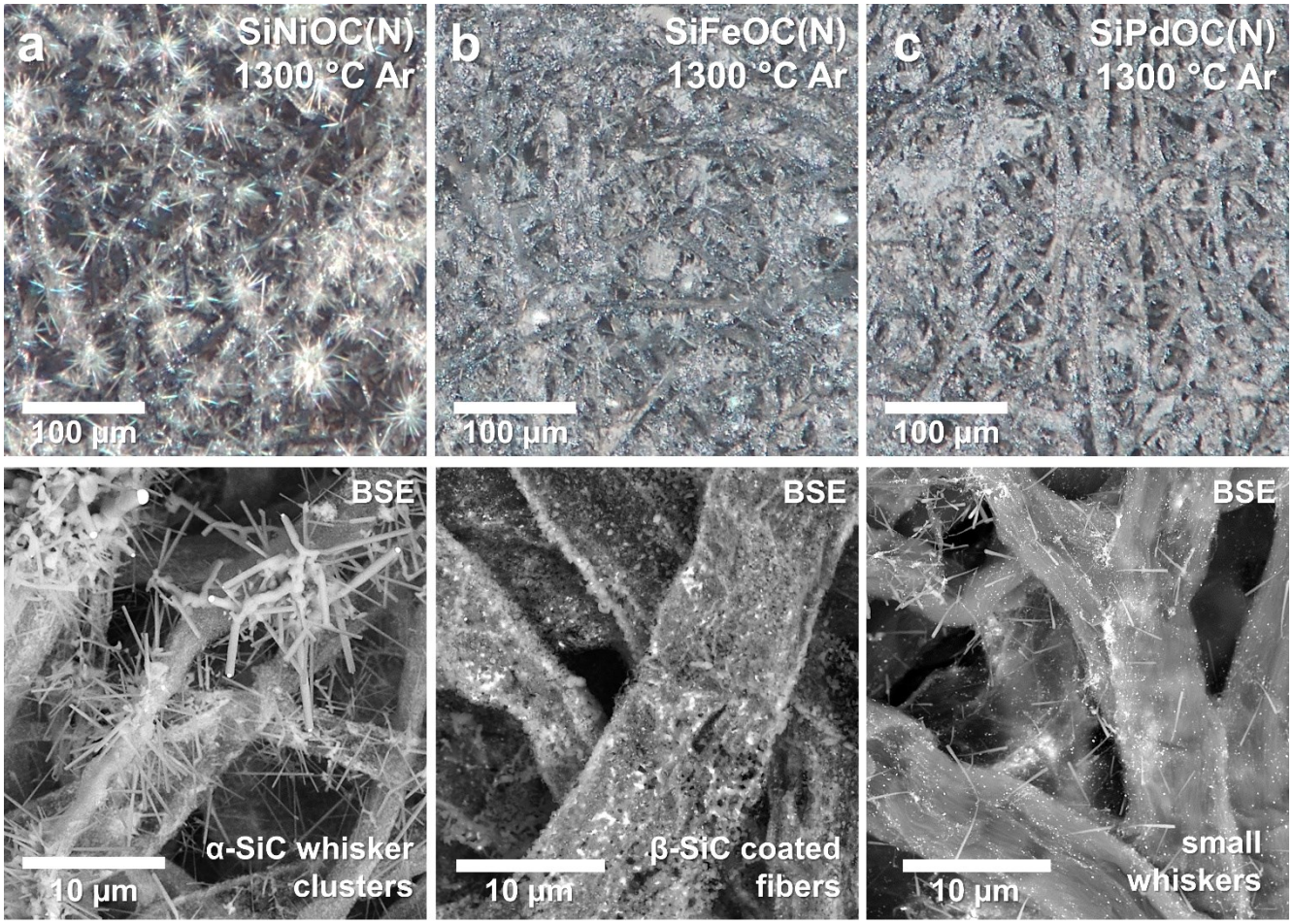

Figure 4-39: Comparison of the SiC whisker growth observed in the different systems investigated. The Ni-modified papers (a) have been extensively surface-modified with clusters of α-SiC whiskers, whereas with Fe-modification, almost no such nanostructures have been generated (b). In the Pd-modified paper (c), only very tiny whiskers have grown, which are too small to be seen in the light micrographs. Focus stacked composite images acquired with a Zeiss AxioZoom.V16 using annular illumination and high dynamical range (HDR) processing.

According to the literature, different mechanisms can lead to the growth of SiC nanowires and whisker structures, and a variety of different synthesis routes and experimental setups have been studied. Among other options vapor-liquid-solid (VLS), vapor-solid (VS), and solid-liquid-solid (SLS) processes have been proposed to be the underlying principles of whisker formation in numerous cases [253]. VLS growth is based on the adsorption of gaseous educts at liquid catalyst droplets until supersaturation is reached, which is then followed by crystal growth. The catalyst enables fast growth and inherent control over the diameter, length, and growth location of the SiC wires, which are characteristically decorated with catalyst globules. The VS mechanism, on the other hand, can generate NW without a catalyst present through the reaction of Si- or C-containing gases with nanometric nuclei within a solid substrate. While a variety of different experimental configurations and educts

have been investigated, in many cases, SiO_2 has been successfully employed as a substrate for SiC NW growth via VS [273]. Finally, SLS denotes NW growth from a stationary catalyst particle remaining on the substrate, which provides both the C and Si needed [274]. SLS-grown wires do not exhibit metal-based tips but the catalysts are found at their root within the substrate.

The results of the present research provide an indication for each of the three mechanisms to contribute to the growth of SiC nanostructures. Obviously, the VLS mechanism is responsible for the whiskers found decorated with metal-catalyst globules in all of the systems but was especially pronounced in the Ni-modified papers. As shown in Fig. 4-40, these whiskers exhibit variable dimensions and overall high diameters (up to more than 1 µm), which appear to correlate with the size of the catalyst particles (a). Moreover, some of them have well-defined crystal facets, have a conical shape with varying diameters, and can be kinked or branched. Additionally, another type of whisker is present in large quantities, exhibiting much smaller diameters (30-200 nm), needle-like facet-less morphologies, and lack catalyst globules entirely. Their generation is likely realized through the VS process, i.e. reaction of CO or SiO gas with solid SiO_2 or carbon domains, respectively. This is substantiated by the rather homogenous distribution throughout the sample and the fact that in situ crystallization of SiC on the fiber surface upon tempering provides the nucleation sites needed to initiate whisker growth [253]. The CO gas produced upon crystallization of the a-SiOC coating (Eq. 4-9) is then available as the C-containing educt needed for VLS, VS, or vapor phase growth of the whiskers.

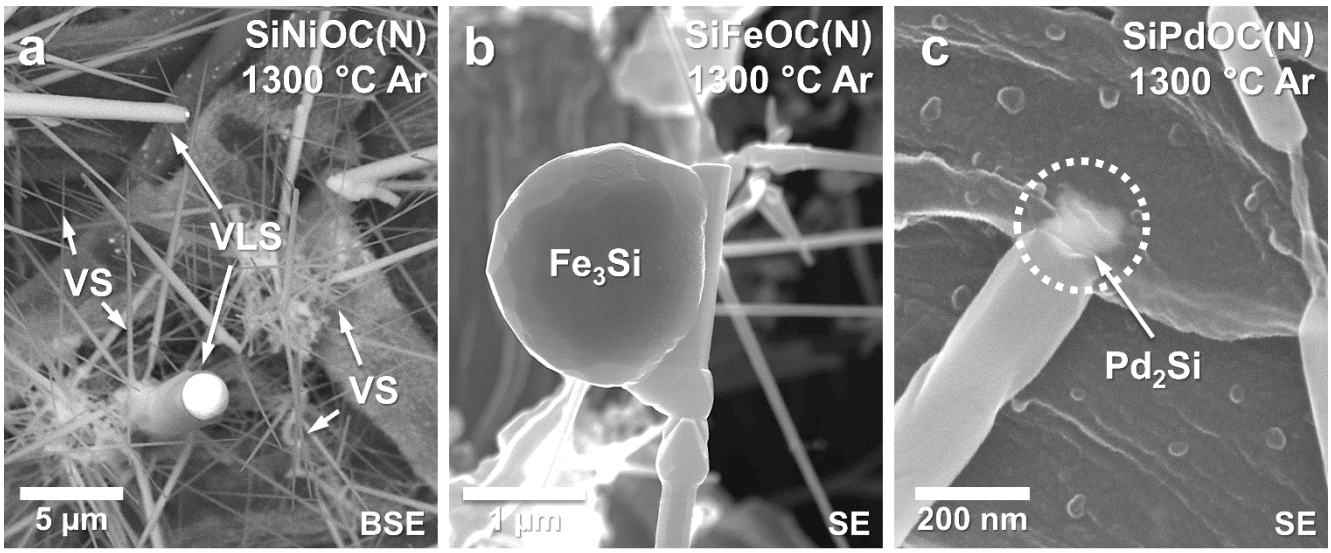

Figure 4-40: Comparison of different SiC whiskers grown in situ on the PDCPs investigated. The characteristics of the whiskers in the Ni-modified papers indicate at least two distinct types of growth mechanisms, i.e. VLS for the thick whiskers exhibiting catalyst tips and VS for needle-like, low-diameter structures (a). The few whiskers found in the Fe-modified papers display complex shapes and large Fe_3Si globules attached to their side faces (b). Pd_2Si at the root of some whiskers generated in the Pd-modified papers implies formation via SLS growth (c).

Meanwhile, PDCPs modified with Fe display almost no whisker structures upon tempering in Ar. Although the fibers are coated with β-SiC crystallites, only the local formation of small SiC whisker clusters was observed.

This is also reflected in the results of QMID analysis of SiFeOC(N)-modified papers upon TGA from room temperature up to 1400 °C (App. B, Fig. B-1), displaying a sudden rise of CO detected beyond 1200 °C, which indicates the crystallization of SiC, whereas no increase in the CO_2 signal was observed [8]. This implies that no substantial VLS growth (Eq. 4-14) operates during tempering. Among the few SiC whiskers found in the Fe-modified papers, some peculiarly shaped structures have been generated (b). The small-diameter whiskers exhibit a well-defined hexagonal habit with prismatic facets, branching, kinks, and growth nodes and are decorated with comparably large Fe-based globules, which are attached to the sides of the whiskers instead of at their tip. Although they can be assigned to VLS growth, their habit differs drastically from the structures generated upon Ni-modification.

In the Pd-modified papers, most whiskers generated display rather uniform diameters of around 80-150 nm, lengths of up to 2 µm, and a rather homogeneous distribution over the surface of the fibers, while only a few are decorated with Pd_2Si tips. Hence, VS growth appears to be the underlying mechanism for whisker generation. However, some whiskers are rooted in Pd-based phases on the fibers (compare Fig. 4-40,c), which indicates growth according to an SLS process. It is not clear, whether this is the prevailing growth mechanism or to which extent VS and VLS have contributed to whisker formation (at least some of the whiskers exhibited Pd_2Si tips; compare Fig. 4-32), and based on the existing results, no clear conclusion can be drawn here.

It is important to note that the vast majority of publications have reported on the generation of cubic β-SiC nanowires [253], whereas the present TEM data indicate that primarily hexagonal α-SiC whiskers have formed. The few papers reporting on α-SiC whisker formation typically used doping with Al powder, which was shown to stabilize the hexagonal phase [275,276]. In fact, although no Al was added to the PDCPs and none was detected by EDS analyses, trace amounts could originate from the ash content of the paper templates employed. Also please note that the orientation of the structures was reported to be either [210] or [212], whereas [011] and [010] were identified in the present case [275,276]. Generally, NW growth takes place along the energetically most favorable direction, which may change depending on the diameter of the structure [277].

In conclusion, the exact mechanisms that led to the generation of SiC nanostructures within metal-modified PDCPs are not well understood, and comparison with the existing literature is problematic due to the widely varying synthesis approaches and experimental setups deployed. Moreover, the heterogenous nature of PDCPs and the complexity of possible reactions, especially concerning local variations, make it impossible to determine reasons for the variation in whisker growth observed. For instance, it remains unresolved why the capabilities of Fe-modified papers to generate SiC whiskers are inferior to those of Ni-based PDCPs and why the shape of the VLS-grown structures differs significantly between the two systems. Also, based on the existing data, it is not clear to which extent the mechanisms discussed proceed simultaneously or consecutively and which factors determine the mode of growth and the characteristics of the resulting SiC structures. To address these questions, additional investigation of model systems has to be conducted to establish a fundamental understanding of the processes that allow the controlled generation of specific SiC-based nanostructures and expand the functionalization options of PDCPs.

In situ generation of α-Si_3N_4 NW on the other hand, has already been reported once in the context of PDCPs and the growth mechanism for this specific case was intensively discussed [4]. Here, C/SiFeN(O)-based ceramic papers, generated upon ammonolysis at 1000 °C, were subjected to consecutive tempering at 1300 °C in N_2 resulting in the formation of a multitude of ultra-long Si_3N_4 NW on the surface and in the macropores of the paper, as displayed in Fig. 4-41 a. Due to the presence of iron silicide tips, the growth was attributed to the VLS mechanism involving the reaction of SiO, CO, and N_2 at the liquid Fe-Si droplets, which was further substantiated by TGA coupled with QMID analysis (compare Fig. 4-41 b). The sudden increase in CO generation at around 1200 °C coincides with the maximum of SiO, which both drop rapidly beyond 1400 °C. At the same time, CO_2 emission remains at a high level, in line with the proposed growth mechanism (Eq. 4-12), consuming CO and SiO to generate α-Si_3N_4 and CO_2. Shells of turbostratic GC found enveloping the catalyst globules were attributed to the decomposition of cellulose-derived pyrolytic hydrocarbons at the metal catalyst tips.

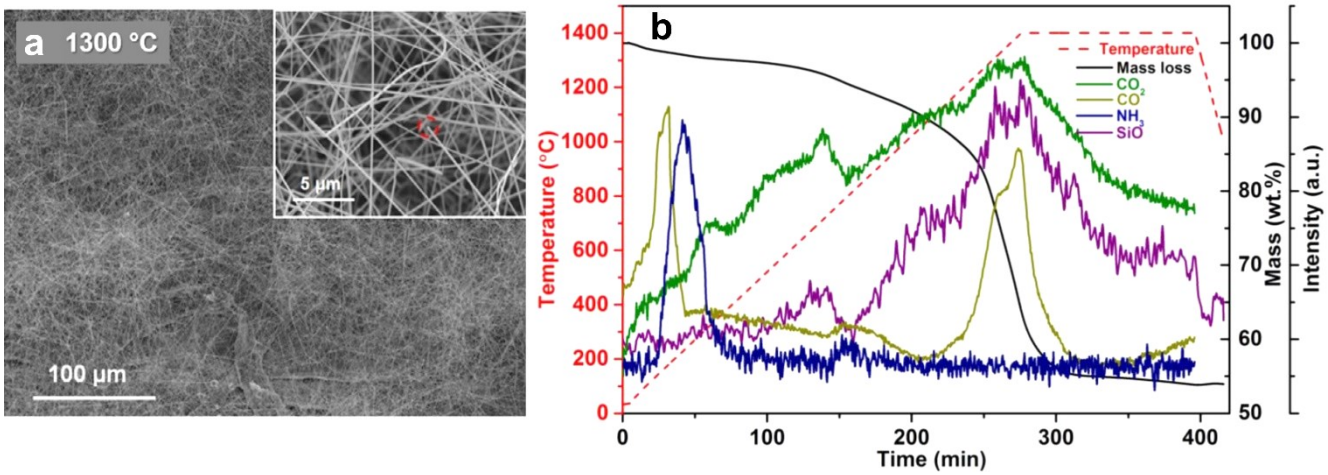

Figure 4-41: SEM micrograph depicting a C/SiFeN(O)-based paper prepared by reactive ammonolysis at 1000 °C and consecutive annealing at 1300 °C in N_2 (a). The surface and macropores are covered by numerous ultra-long α-Si_3N_4 NW, occasionally exhibiting catalyst globules at their tips (inset). TGA coupled with QMID analysis of the paper during tempering (b) reveals a sudden increase in CO and SiO generation beyond 1200 °C attributed to Fe-catalyzed VLS growth of the NW. Reproduced from [4,5].

It stands to reason that the same principles apply to the samples of the present work, as all three transition metals investigated displayed very similar Si_3N_4 nanostructures decorated with metal silicide tips. However, again some variations with the metal modification were observed, as comparatively depicted in Fig. 4-42. The Ni-modified paper shown (a) is extensively covered with furry clusters of fine Si_3N_4 NW, which often are found being decorated with Ni_2Si catalyst tips, as depicted in the SEM image. Introducing Fe into the precursor results in the generation of ultra-long wires coating the whole paper surface (b) occasionally exhibiting catalyst tips, similar to the results reported in [4]. Within Pd-modified papers annealed in N_2, the fibers are densely scattered with short Si_3N_4 whiskers displaying rather uniform dimensions (c). Please note that, while Pd is known to facilitate the growth of NW structures from SiO_X and GaN [278,279], the VLS mechanism indicated by the Pd_2Si tips has, to the best of our knowledge, not been reported in the literature for the case of Si_3N_4 generation. The distinct

morphology obtained compared to those generated with the other metals could provide options to control the morphology of the in situ generated nanostructures by variation of the metal modification.

Generation of α-Si_3N_4 NW from preceramic polymers was first reported almost two decades ago, via pyrolysis of $FeCl_2$-modified polysilazanes in N_2 [280]. The metal was shown to catalyze NW generation and in the following years, other metals, such as Ni or Co, were successfully tested for their ability to facilitate the growth of 1D nanostructures [254,281]. Often, VLS is proposed to be the underlying mechanism for NW growth, but as with SiC, VS, SLS, and other processes were discussed as well. In the present case, the macropores of the paper template are assumed to play a pivotal role in the local enrichment of gaseous educts promoting gas-phase reactions to take place and facilitating the growth of the NW. As most of the wires were found lacking a catalyst globule, NW growth could also be realized by the VS mechanism at Si_3N_4 nuclei formed within the a-SiOC coating upon tempering (Eq. 4-13) [282].

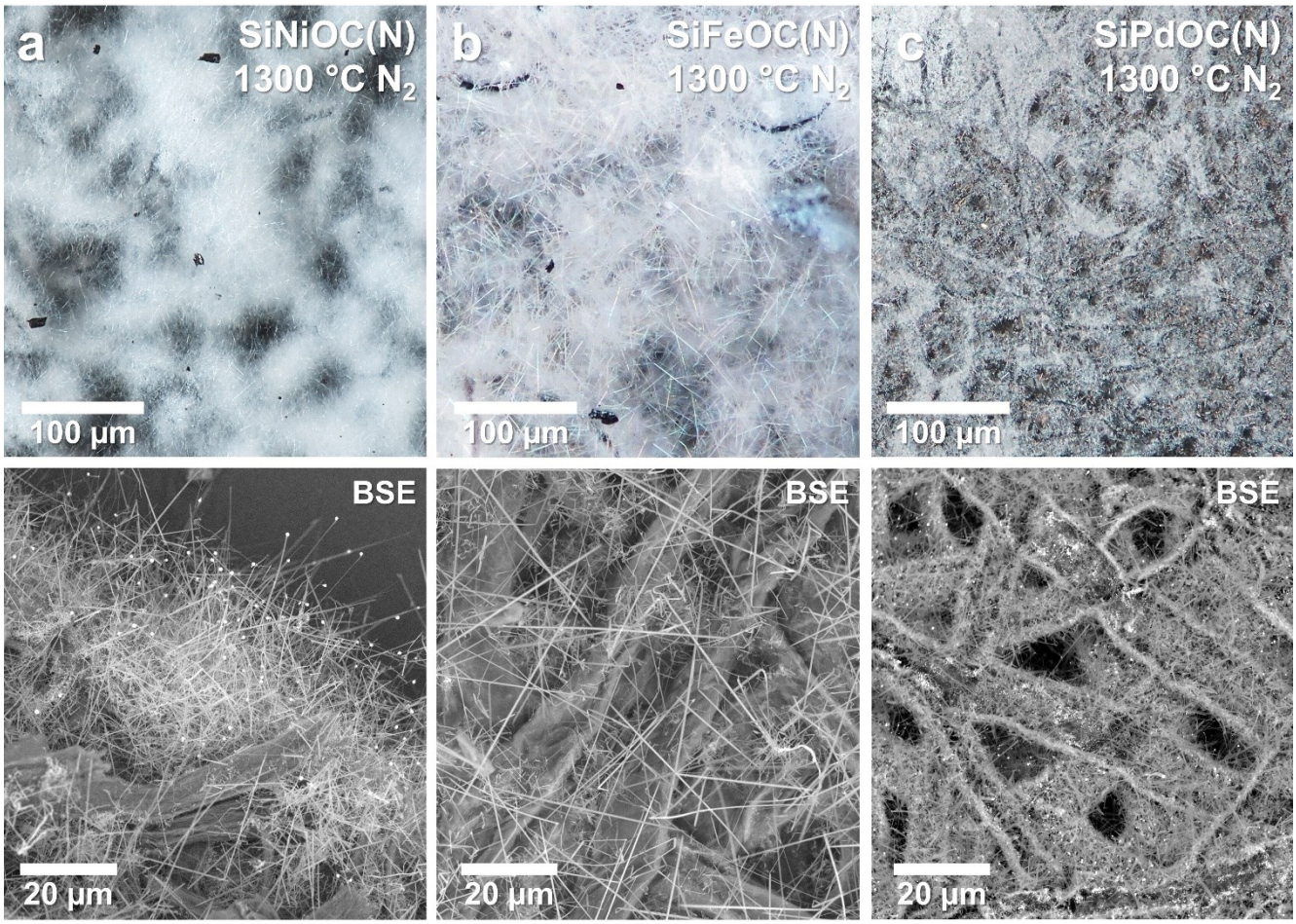

Figure 4-42: Comparison of the Si_3N_4 NW growth observed in the PDCPs investigated. With a Ni-modified precursor, dense clusters of fine entangled NW are obtained with many exhibiting Ni_2Si globules at their tips (a). Fe-modification results in the formation of ultra-long straight NW with exceptionally high aspect ratios (b); catalyst tips were only infrequently observed. The Si_3N_4 structures generated in the Pd-modified papers display generally low aspect ratios with a rather uniform size distribution and are often found being decorated with Pd_2Si (c).

The in situ decoration of PDCPs with Si-based nanostructures potentially allows convenient modification of a wide range of properties such as electrical conductivity, permeability, appearance, and mechanical properties. Using different transition metals for precursor modification and atmospheres during annealing decisively affects the number, dimensions, and morphologies of the nanostructures. Detailed investigation of the interplay between these factors could enable control of their characteristics and expand the tools to design PDCPs to the needs of future applications.

Variations with Transition Metal Modification - Summary

- The cellulose-derived carbon fibers in all metal-modified PDCPs investigated undergo extensive graphitization upon heat treatment, as indicated by the TEM data and complementary Raman analyses:
  - The generation of GC at temperatures as low as < 1000 °C is attributed to catalytic graphitization by the metal-based NPs via solution of AC followed by precipitation of TC nanostructures
  - While Fe- and Ni- modified papers undergo extensive graphitization upon pyrolysis, Pd-catalyzed generation of graphitic carbon is only observed upon tempering at 1300 °C
  - Different nanostructures such as coils, ribbons, and onions were identified varying with the transition metal introduced, which might be attributed to mechanistic differences in the graphitization process
  - Tailoring the structural characteristics of the cellulose-derived carbon fibers via metal modification offers interesting possibilities to affect the properties of PDCPs.
- Upon tempering at 1300 °C, in situ growth of crystalline α-SiC whisker (Ar) or α-Si_3N_4 (N_2) NW on the surface and in the macropores of the metal-modified ceramic papers was observed:
  - Generation of α-SiC whiskers varied considerably depending on the transition metal utilized; Ni was shown to facilitate extensive whisker growth, whereas Fe generated almost no such structures
  - In each case, the presence of catalyst globules implies that some of the whiskers are generated via VLS growth; however, indications for other mechanisms such as VS and SLS were observed as well
  - In line with earlier studies, tempering of Fe-modified PDCPs in N_2 results in the in situ generation of α-Si_3N_4 NW exhibiting exceptionally high aspect ratios; the same is the case with Ni-modification
  - Although Pd catalyzed formation of α-Si_3N_4 nanostructures has not been recognized in the literature, introducing Pd into the precursor generates a cover of short whiskers often decorated with Pd_2Si tips
  - As many NW are decorated with metal-based tips, a VLS mechanism is proposed to facilitate their growth; NW without a catalyst globule on the other hand could indicate VS growth on Si_3N_4 nuclei.
- Introducing different transition metals into PDCPs has a crucial impact on the in situ generation of graphitic and SiC/Si_3N_4-based nanostructures; however, the complexity of PDCP materials make it difficult to determine the exact mechanisms that lead to their generation and additional studies are paramount to enable control of their targeted synthesis.

5 Conclusions & Outlook

For this study, regular cellulose-based papers were infiltrated with transition metal-modified polysilazane polymers and heat-treated in different atmospheres to produce pseudomorphic polymer-derived ceramic papers with a paper-like structure. A variety of synthesis parameters, such as the type of the paper template employed, the carbon content of the precursor, the modification of the precursors with different transition metals, and the influence of consecutive high-temperature treatment in either nitrogen or argon atmosphere, were tested for their impact on the micro-/nanostructure and phase assemblage generated within the ceramic composites.

The morphology of the ceramic composites was shown to be directly dependent on the paper template employed, with even fine structural details inherited upon heat treatment. Other parameters, such as the precursor used, the processing temperature and atmosphere, as well as the modification with transition metals had no notable impact on the morphological feature transfer. Meanwhile, upon pyrolysis at 1000 °C, the majority of nitrogen is removed from the system and C/SiMOC-based (M = Fe, Ni, Pd) ceramics are generated, which is attributed to reactions between the pyrolysis products of the H_2O-rich cellulose and the oxidation sensitive precursor. Hence, employing cellulose as template material is a useful approach to conveniently generating pseudomorphic ceramics with complex structures, but the effects of the organic papers on the composition of the resulting material have to be considered.

TEM analyses of cross-sectional samples revealed that the papers upon pyrolysis have a complex composite structure with cellulose-derived porous carbon fibers encased by a ceramic nanocomposite layer. The PDC coating exhibits excellent adhesion to the fibers, which is attributed to chemical bonding upon reaction of the polysilazanes with the hydroxy surface groups of the cellulose substrate, as indicated by FT-IR measurements. Dispersed within the SiOC-based ceramic layer, depending on the metal modification, a distinct phase assemblage of nanosized metal-based precipitates is generated, ranging from a variety of silicides in the Ni- and Pd-based samples to metals, carbides, and oxides upon Fe-modification. Reactive ammonolysis at 500-1000 °C of the latter revealed the low-temperature phase evolution, beginning with the precipitation of $Fe_{(1-X)}O$ at 700 °C and simultaneous generation of Fe_XN at the fiber coating interface. Upon 1000 °C treatment, the oxides get reduced resulting in metallic α-Fe, whereas the nitrides withstand reduction and have grown, revealing a distinct nitriding potential within the fibers. This is attributed to the retention of N_2 produced from the thermal decomposition of NH_3 diffusing through the porous carbon, demonstrating the effect of the pyrolysis atmosphere on the phase assemblage generated. Moreover, the respective transition metal affects the micro- and nanostructural characteristics of the ceramic papers, with varying degrees of fiber graphitization and distinct distribution of the metal-based precipitates within the composites observable. The different papers and polysilazane base-precursors on the other hand, had no noteworthy influence on the microstructural characteristics of the PDCPs.

Upon tempering at 1300 °C in either Ar or N_2 atmosphere, most of the oxygen present is removed from the papers via carbothermal reduction and associated CO_X formation. The PDC coatings crystallize forming either SiC or Si_3N_4, depending on the atmosphere employed, and the phase equilibrium is shifted towards the thermodynamically favorable silicides, regardless of the metal modification. In addition, the cellulose-derived carbon fibers have now undergone extensive graphitization in all papers, revealing different temperature ranges for catalytic carbon graphitization for the different metals and resulting in the generation of C/M/SiC (Ar) and C/M/Si_3N_4 (N_2) microcomposites (M = Fe_3Si, Ni_2Si, Pd_2Si) with overall very similar microstructures. On the surface of the ceramic papers, a multitude of crystalline whisker- and wire-like Si-based nanostructures with high-aspect ratios is generated, which is attributed to a VLS process reacting gaseous SiO and CO or N_2 at catalytic transition metal sites forming the one-dimensional nanostructures. Hence, upon high-temperature annealing, some macroscopic characteristics of the papers, such as their color, mechanical properties, and ferromagnetism, change notably.

In summary, within the pseudomorphic ceramic papers inheriting the morphology of the paper template used, a variety of phase assemblages, microstructural characteristics, and functional properties can be generated by controlling certain synthesis parameters. In addition, the concept could enable the convenient production of ceramics with well-defined and specialized morphologies through preforming of paper templates and subsequent conversion into ceramic materials. The results highlight that, besides using different transition metals for precursor modification, the attributes of PDCPs can be conveniently adjusted by controlling temperature and atmosphere during processing. However, optimization of the parameters discussed is a necessity for the production of applicable functionalized ceramics prepared by the organic template-assisted approach, paving the way for future pseudomorphic ceramic composites with potentially designable properties. Some of the key questions and subjects of interest remaining open for future investigation include but are not limited to:

I) The use of different polymeric precursors and transition metals to assess their general suitability for producing PDCPs and differences compared to polysilazane-based SSPs

II) Optimization of synthesis routes, to obtain homogeneous phase distribution, uniform, and more predictable microstructures, as well as precisely adjust the phase assemblage

III) Conversion of paper templates with complex structures (e.g. corrugated cardboard, paper-based electronics, anisotropic papers, cellulose-sponges) advancing the template-assisted approach towards generation of ceramics with designable morphologies for application

IV) Utilization of the findings obtained from the present study to adjust phases, micro-, and nanostructural details, as well as macroscopic properties within PDCPs for specific applications fields

V) Testing of functional capabilities of PDCPs, such as mechanical properties, electric properties, catalytic activities, and electromagnetic shielding, and correlation with the findings presented.

Bibliography

[1] X. Dai, Z. Guo, The gorgeous transformation of paper: from cellulose paper to inorganic paper to 2D paper materials with multifunctional properties, J. Mater. Chem. A. 10 (2022) 122–156. https://doi.org/10.1039/D1TA08410K.

[2] G. Wen, Z. Guo, A paper-making transformation: from cellulose-based superwetting paper to biomimetic multifunctional inorganic paper, J. Mater. Chem. A. 8 (2020) 20238–20259. https://doi.org/10.1039/D0TA07518C.

[3] W. Wang, T. Xue, Z. Jin, G. Qiao, Preparation and characterization of morph-genetic aluminum nitride/carbon composites from filter paper, Materials Research Bulletin. 43 (2008) 939–945. https://doi.org/10.1016/j.materresbull.2007.04.033.

[4] C. Zhou, C. Fasel, R. Ishikawa, M. Gallei, Y. Ikuhara, S. Lauterbach, H.-J. Kleebe, R. Riedel, E. Ionescu, One-pot synthesis of a C/SiFeN(O)-based ceramic paper with in-situ generated hierarchical micro/nano-morphology, Journal of the European Ceramic Society. 37 (2017) 5193–5203. https://doi.org/10.1016/j.jeurceramsoc.2017.03.007.

[5] C. Zhou, Ternary Si-Metal-N Ceramics: Single-Source-Precursor Synthesis, Nanostructure and Properties Characterization, PhD Thesis, Technische Universität Darmstadt, 2017.

[6] A. Ott, J. Peter, L. Wiehl, V. Potapkin, U.I. Kramm, H.-J. Kleebe, R. Riedel, E. Ionescu, Conversion of a polysilazane-modified cellulose-based paper into a C/SiFe(N,C)O ceramic paper via thermal ammonolysis, International Jounal of Applied Ceramic Technology. 19 (2022) 838–846. https://doi.org/10.1111/ijac.13869.

[7] J. Peter, A. Ott, R. Riedel, E. Ionescu, H. Kleebe, Micro-/nanostructure evolution of C/SiFeO(N,C) polymer-derived ceramic papers pyrolyzed in a reactive ammonia atmosphere, Journal of the American Ceramic Society. 105 (2022) 2334–2348. https://doi.org/10.1111/jace.18237.

[8] A. Ott, Conversion of Cellulose-based Papers into Functional Ceramic Papers, PhD Thesis, Technische Universität Darmstadt, 2022. https://tuprints.ulb.tu-darmstadt.de/id/eprint/21595 (accessed October 28, 2022).

[9] J.R. Blum, Die Pseudomorphosen des Mineralreichs, E. Schweizerbart'sche Verlagshandlung, 1843.

[10] A. Putnis, Mineral Replacement Reactions, Reviews in Mineralogy and Geochemistry. 70 (2009) 87–124. https://doi.org/10.2138/rmg.2009.70.3.

[11] F. Ainger, J. Herbert, The preparation of phosphorus-nitrogen compounds as non-porous solids, Special Ceramics. (1960) 168–182.

[12] P.G. Chantrell, P. Popper, Inorganic Polymers and Ceramics, Special Ceramics. (1965) 87–103.

[13] W. Verbeek, Production of shaped articles of homogeneous mixtures of silicon carbide and nitride, (1974).

[14] S. Yajima, J. Hayashi, M. Omori, Continuous silicon carbide fiber of high tensile strength, Chem. Lett. 4 (1975) 931–934. https://doi.org/10.1246/cl.1975.931.

[15] S. Yajima, Y. Hasegawa, K. Okamura, T. Matsuzawa, Development of high tensile strength silicon carbide fibre using an organosilicon polymer precursor, Nature. 273 (1978) 525–527. https://doi.org/10.1038/273525a0.

[16] B.C. Mutsuddy, Use of organometallic polymer for making ceramic parts by plastic forming techniques, Ceramics International. 13 (1987) 41–53. https://doi.org/10.1016/0272-8842(87)90037-X.

[17] T. Zhang, J.R.G. Evans, J. Woodthorpe, Injection moulding of silicon carbide using an organic vehicle based on a preceramic polymer, Journal of the European Ceramic Society. 15 (1995) 729–734. https://doi.org/10.1016/0955-2219(95)00049-Z.

[18] R.M. da Rocha, P. Greil, J.C. Bressiani, A.H. de A. Bressiani, Complex-shaped ceramic composites obtained by machining compact polymer-filler mixtures, Mat. Res. 8 (2005) 191–196. https://doi.org/10.1590/S1516-14392005000200019.

[19] P. Colombo, G. Mera, R. Riedel, G.D. Sorarù, Polymer-Derived Ceramics: 40 Years of Research and Innovation in Advanced Ceramics: Polymer-Derived Ceramics, Journal of the American Ceramic Society. (2010) 1805–1837. https://doi.org/10.1111/j.1551-2916.2010.03876.x.
[20] R. Riedel, G. Mera, R. Hauser, A. Klonczynski, Silicon-Based Polymer-Derived Ceramics: Synthesis Properties and Applications-A Review: Dedicated to Prof. Dr. Fritz Aldinger on the occasion of his 65th birthday, Nippon Seramikkusu Kyokai Gakujutsu Ronbunshi. 114 (2006) 425–444. https://doi.org/10.2109/jcersj.114.425.
[21] G. Mera, A. Navrotsky, S. Sen, H.-J. Kleebe, R. Riedel, Polymer-derived SiCN and SiOC ceramics – structure and energetics at the nanoscale, J. Mater. Chem. A. 1 (2013) 3826. https://doi.org/10.1039/c2ta00727d.
[22] Z.-C. Wang, F. Aldinger, R. Riedel, Novel Silicon-Boron-Carbon-Nitrogen Materials Thermally Stable up to 2200°C, Journal of the American Ceramic Society. 84 (2004) 2179–2183. https://doi.org/10.1111/j.1151-2916.2001.tb00984.x.
[23] M. Hojamberdiev, R.M. Prasad, C. Fasel, R. Riedel, E. Ionescu, Single-source-precursor synthesis of soft magnetic Fe_3Si- and Fe_5Si_3-containing SiOC ceramic nanocomposites, Journal of the European Ceramic Society. 33 (2013) 2465–2472. https://doi.org/10.1016/j.jeurceramsoc.2013.04.005.
[24] E. Ionescu, H.-J. Kleebe, R. Riedel, Silicon-containing polymer-derived ceramic nanocomposites (PDC-NCs): preparative approaches and properties, Chem. Soc. Rev. 41 (2012) 5032. https://doi.org/10.1039/c2cs15319j.
[25] W. Duan, X. Yin, Q. Li, L. Schlier, P. Greil, N. Travitzky, A review of absorption properties in silicon-based polymer derived ceramics, Journal of the European Ceramic Society. 36 (2016) 3681–3689. https://doi.org/10.1016/j.jeurceramsoc.2016.02.002.
[26] L. Zhang, Y. Wang, Y. Wei, W. Xu, D. Fang, L. Zhai, K.-C. Lin, L. An, A Silicon Carbonitride Ceramic with Anomalously High Piezoresistivity, Journal of the American Ceramic Society. 91 (2008) 1346–1349. https://doi.org/10.1111/j.1551-2916.2008.02275.x.
[27] R. Riedel, L. Toma, E. Janssen, J. Nuffer, T. Melz, H. Hanselka, Piezoresistive Effect in SiOC Ceramics for Integrated Pressure Sensors, Journal of the American Ceramic Society. 93 (2010) 920–924. https://doi.org/10.1111/j.1551-2916.2009.03496.x.
[28] E.I. Ricohermoso, High-temperature giant piezoresistivity of microstructured SiOC-based strain gauges, PhD Thesis, Technische Universität Darmstadt, 2022. https://tuprints.ulb.tu-darmstadt.de/id/eprint/22468 (accessed April 4, 2023).
[29] Y. Guo, Y. Sugahara, Polymer-derived ceramics for electrocatalytic energy conversion reactions, International Journal of Applied Ceramic Technology. 20 (2023) 8–23. https://doi.org/10.1111/ijac.14262.
[30] C. Vakifahmetoglu, E. Pippel, J. Woltersdorf, P. Colombo, Growth of One-Dimensional Nanostructures in Porous Polymer-Derived Ceramics by Catalyst-Assisted Pyrolysis. Part I: Iron Catalyst, Journal of the American Ceramic Society. 93 (2010) 959–968. https://doi.org/10.1111/j.1551-2916.2009.03448.x.
[31] M. Scheffler, P. Greil, A. Berger, E. Pippel, J. Woltersdorf, Nickel-catalyzed in situ formation of carbon nanotubes and turbostratic carbon in polymer-derived ceramics, Materials Chemistry and Physics. 84 (2004) 131–139. https://doi.org/10.1016/j.matchemphys.2003.11.003.
[32] H.-J. Kleebe, Y.D. Blum, SiOC ceramic with high excess free carbon, Journal of the European Ceramic Society. 28 (2008) 1037–1042. https://doi.org/10.1016/j.jeurceramsoc.2007.09.024.
[33] Y.D. Blum, D.B. MacQueen, H.-J. Kleebe, Synthesis and characterization of carbon-enriched silicon oxycarbides, Journal of the European Ceramic Society. 25 (2005) 143–149. https://doi.org/10.1016/j.jeurceramsoc.2004.07.019.
[34] Y. Abe, T. Gunji, Oligo- and polysiloxanes, Progress in Polymer Science. 29 (2004) 149–182. https://doi.org/10.1016/j.progpolymsci.2003.08.003.
[35] J.M. Schwark, M.J. Sullivan, Isocyanate-Modified Polysilazanes: Conversion to Ceramic Materials, MRS Proc. 271 (1992) 807. https://doi.org/10.1557/PROC-271-807.
[36] Y. Blum, R.M. Laine, Catalytic methods for the synthesis of oligosilazanes, Organometallics. 5 (1986) 2081–2086. https://doi.org/10.1021/om00141a026.
[37] F. Babonneau, G.D. Soraru, K.J. Thorne, J.D. Mackenzie, Chemical Characterization of Si-Al-C-O Precursor and Its Pyrolysis, Journal of the American Ceramic Society. 74 (1991) 1725–1728. https://doi.org/10.1111/j.1151-2916.1991.tb07172.x.

[38] Y. Iwamoto, K. Kikuta, S. Hirano, Synthesis of Poly-Titanosilazanes and Conversion into Si_3N_4-TiN Ceramics., J. Ceram. Soc. Japan. 108 (2000) 350–356. https://doi.org/10.2109/jcersj.108.1256_350.
[39] B. Papendorf, K. Nonnenmacher, E. Ionescu, H.-J. Kleebe, R. Riedel, Strong Influence of Polymer Architecture on the Microstructural Evolution of Hafnium-Alkoxide-Modified Silazanes upon Ceramization, Small. 7 (2011) 970–978. https://doi.org/10.1002/smll.201001938.
[40] R. Hauser, A. Francis, R. Theismann, R. Riedel, Processing and magnetic properties of metal-containing SiCN ceramic micro- and nano-composites, Journal of Materials Science. 43 (2008) 4042–4049. https://doi.org/10.1007/s10853-007-2143-3.
[41] L. Biasetto, A. Francis, P. Palade, G. Principi, P. Colombo, Polymer-derived microcellular SiOC foams with magnetic functionality, J Mater Sci. 43 (2008) 4119–4126. https://doi.org/10.1007/s10853-007-2224-3.
[42] E. Ionescu, S. Bernard, R. Lucas, P. Kroll, S. Ushakov, A. Navrotsky, R. Riedel, Polymer-Derived Ultra-High Temperature Ceramics (UHTCs) and Related Materials, Adv. Eng. Mater. 21 (2019) 1900269. https://doi.org/10.1002/adem.201900269.
[43] K. Sato, Fabrication and pressure testing of a gas-turbine component manufactured by a preceramic-polymer-impregnation method, Composites Science and Technology. 59 (1999) 853–859. https://doi.org/10.1016/S0266-3538(99)00015-9.
[44] T.P. Smirnova, A.M. Badalian, L.V. Yakovkina, V.V. Kaichev, V.I. Bukhtiyarov, A.N. Shmakov, I.P. Asanov, V.I. Rachlin, A.N. Fomina, SiCN alloys obtained by remote plasma chemical vapour deposition from novel precursors, Thin Solid Films. 429 (2003) 144–151. https://doi.org/10.1016/S0040-6090(03)00408-5.
[45] R. Melcher, P. Cromme, M. Scheffler, P. Greil, Centrifugal Casting of Thin-Walled Ceramic Tubes from Preceramic Polymers, Journal of the American Ceramic Society. 86 (2003) 1211–1213. https://doi.org/10.1111/j.1151-2916.2003.tb03451.x.
[46] J. Zeschky, T. Höfner, C. Arnold, R. Weißmann, D. Bahloul-Hourlier, M. Scheffler, P. Greil, Polysilsesquioxane derived ceramic foams with gradient porosity, Acta Materialia. 53 (2005) 927–937. https://doi.org/10.1016/j.actamat.2004.10.039.
[47] N. Janakiraman, F. Aldinger, Fabrication and characterization of fully dense Si–C–N ceramics from a poly(ureamethylvinyl)silazane precursor, Journal of the European Ceramic Society. 29 (2009) 163–173. https://doi.org/10.1016/j.jeurceramsoc.2008.05.028.
[48] M. Schulz, M. Börner, J. Göttert, T. Hanemann, J. Haußelt, G. Motz, Cross Linking Behavior of Preceramic Polymers Effected by UV- and Synchrotron Radiation, Adv. Eng. Mater. 6 (2004) 676–680. https://doi.org/10.1002/adem.200400082.
[49] J. Lipowitz, Infusible Preceramic Polymers via Plasma Treatment, U.S. Patent 4,743,662, 1988.
[50] Y. Hasegawa, Si-C fiber prepared from polycarbosilane cured without oxygen, Journal of Inorganic and Organometallic Polymers. 2 (1992) 161–169. https://doi.org/10.1007/BF00696543.
[51] T. Friedel, N. Travitzky, F. Niebling, M. Scheffler, P. Greil, Fabrication of polymer derived ceramic parts by selective laser curing, Journal of the European Ceramic Society. 25 (2005) 193–197. https://doi.org/10.1016/j.jeurceramsoc.2004.07.017.
[52] P. Colombo, ed., Polymer derived ceramics: from nano-structure to applications, DEStech Publications, Lancaster, Pa, 2010.
[53] E. Kroke, Y.-L. Li, C. Konetschny, E. Lecomte, C. Fasel, R. Riedel, Silazane derived ceramics and related materials, Materials Science and Engineering: R: Reports. 26 (2000) 97–199. https://doi.org/10.1016/S0927-796X(00)00008-5.
[54] J. Seitz, J. Bill, N. Egger, F. Aldinger, Structural investigations of Si/C/N-ceramics from polysilazane precursors by nuclear magnetic resonance, Journal of the European Ceramic Society. 16 (1996) 885–891. https://doi.org/10.1016/0955-2219(96)00007-6.
[55] L.-A. Liew, R.A. Saravanan, V.M. Bright, M.L. Dunn, J.W. Daily, R. Raj, Processing and characterization of silicon carbon-nitride ceramics: application of electrical properties towards MEMS thermal actuators, Sensors and Actuators A: Physical. 103 (2003) 171–181. https://doi.org/10.1016/S0924-4247(02)00330-8.
[56] S.H. Yu, R.E. Riman, S.C. Danforth, R.Y. Leung, Pyrolysis of Titanium-Metal-Filled Poly(siloxane) Preceramic Polymers: Effect of Atmosphere on Pyrolysis Product Chemistry, Journal of the American Ceramic Society. 78 (1995) 1818–1824. https://doi.org/10.1111/j.1151-2916.1995.tb08894.x.

[57] G.D. Soraru, A. Ravagni, R. Campostrini, F. Babonneau, Synthesis and Characterization of β'-SiAlON Ceramics from Organosilicon Polymers, Journal of the American Ceramic Society. 74 (1991) 2220–2223. https://doi.org/10.1111/j.1151-2916.1991.tb08288.x.
[58] Y. Li, Z. Zheng, C. Reng, Z. Zhang, W. Gao, S. Yang, Z. Xie, Preparation of Si-C-N-Fe magnetic ceramics from iron-containing polysilazane, Appl. Organometal. Chem. 17 (2003) 120–126. https://doi.org/10.1002/aoc.400.
[59] C. Zhou, A. Ott, R. Ishikawa, Y. Ikuhara, R. Riedel, E. Ionescu, Single-source-precursor synthesis and high-temperature evolution of novel mesoporous SiVN(O)-based ceramic nanocomposites, Journal of the European Ceramic Society. 40 (2020) 6280–6287. https://doi.org/10.1016/j.jeurceramsoc.2019.11.021.
[60] P. Colombo, T.E. Paulson, C.G. Pantano, Atmosphere effects in the processing of silicon carbide and silicon oxycarbide thin films and coatings, Journal of Sol-Gel Science and Technology. 2 (1994) 601–604. https://doi.org/10.1007/BF00486317.
[61] D. Bahloul, M. Pereira, P. Goursat, N.S.C.K. Yive, R.J.P. Corriu, Preparation of Silicon Carbonitrides from an Organosilicon Polymer: I, Thermal Decomposition of the Cross-linked Polysilazane, Journal of the American Ceramic Society. 76 (1993) 1156–1162. https://doi.org/10.1111/j.1151-2916.1993.tb03734.x.
[62] G. Barroso, Q. Li, R.K. Bordia, G. Motz, Polymeric and ceramic silicon-based coatings – a review, J. Mater. Chem. A. 7 (2019) 1936–1963. https://doi.org/10.1039/C8TA09054H.
[63] J. Cordelair, P. Greil, Electrical Characterization of Polymethylsiloxane/$MoSi_2$-Derived Composite Ceramics, Journal of the American Ceramic Society. 84 (2004) 2256–2259. https://doi.org/10.1111/j.1151-2916.2001.tb00998.x.
[64] O. Dernovsek, J.C. Bressiani, A.H.A. Bressiani, W. Acchar, P. Greil, Reaction bonded niobium carbide ceramics from polymer-filler mixtures, Journal of Materials Science. 35 (2000) 2201–2207. https://doi.org/10.1023/A:1004766607619.
[65] P. Greil, M. Seibold, Modelling of dimensional changes during polymer-ceramic conversion for bulk component fabrication, Journal of Materials Science. 27 (1992) 1053–1060. https://doi.org/10.1007/BF01197660.
[66] D. Suttor, H.-J. Kleebe, G. Ziegler, Formation of Mullite from Filled Siloxanes, Journal of the American Ceramic Society. 80 (2005) 2541–2548. https://doi.org/10.1111/j.1151-2916.1997.tb03156.x.
[67] E. Bernardo, E. Tomasella, P. Colombo, Development of multiphase bioceramics from a filler-containing preceramic polymer, Ceramics International. 35 (2009) 1415–1421. https://doi.org/10.1016/j.ceramint.2008.07.003.
[68] E. Bernardo, P. Colombo, S. Hampshire, Advanced ceramics from a preceramic polymer and nano-fillers, Journal of the European Ceramic Society. 29 (2009) 843–849. https://doi.org/10.1016/j.jeurceramsoc.2008.07.011.
[69] Y. Katsuda, P. Gerstel, J. Narayanan, J. Bill, F. Aldinger, Reinforcement of precursor-derived Si–C–N ceramics with carbon nanotubes, Journal of the European Ceramic Society. 26 (2006) 3399–3405. https://doi.org/10.1016/j.jeurceramsoc.2005.10.014.
[70] J.-H. Eom, Y.-W. Kim, I.-H. Song, H.-D. Kim, Microstructure and properties of porous silicon carbide ceramics fabricated by carbothermal reduction and subsequent sintering process, Materials Science and Engineering: A. 464 (2007) 129–134. https://doi.org/10.1016/j.msea.2007.03.076.
[71] Y.-W. Kim, S.-H. Kim, H.-D. Kim, C.B. Park, Processing of closed-cell silicon oxycarbide foams from a preceramic polymer, Journal of Materials Science. 39 (2004) 5647–5652. https://doi.org/10.1023/B:JMSC.0000040071.55240.85.
[72] P. Colombo, Engineering porosity in polymer-derived ceramics, Journal of the European Ceramic Society. 28 (2008) 1389–1395. https://doi.org/10.1016/j.jeurceramsoc.2007.12.002.
[73] B. Ceron-Nicolat, T. Fey, P. Greil, Processing of Ceramic Foams with Hierarchical Cell Structure, Adv. Eng. Mater. 12 (2010) 884–892. https://doi.org/10.1002/adem.201000114.
[74] X. Wang, J. Liu, F. Hou, X. Lu, X. Sun, Y. Zhou, Manufacture of porous SiC/C ceramics with excellent damage tolerance by impregnation of LPCS into carbonized pinewood, Journal of the European Ceramic Society. 35 (2015) 1751–1759. https://doi.org/10.1016/j.jeurceramsoc.2014.12.033.
[75] R.A. White, J.N. Weber, E.W. White, Replamineform: A New Process for Preparing Porous Ceramic, Metal, and Polymer Prosthetic Materials, Science. 176 (1972) 922–924. https://doi.org/10.1126/science.176.4037.922.

[76] G. Barroso, Thermal barrier coating by polymer-derived ceramic technique for application in exhaust systems, 1st ed., Cuvillier Verlag, Göttingen, 2018.
[77] H. Gleiter, Nanocrystalline Materials, in: W.G.J. Bunk (Ed.), Advanced Structural and Functional Materials, Springer Berlin Heidelberg, Berlin, Heidelberg, 1991: pp. 1–37. https://doi.org/10.1007/978-3-642-49261-7_1.
[78] R.E. Newnham, D.P. Skinner, L.E. Cross, Connectivity and piezoelectric-pyroelectric composites, Materials Research Bulletin. 13 (1978) 525–536. https://doi.org/10.1016/0025-5408(78)90161-7.
[79] K. Niihara, A. Nakahira, T. Sekino, New Nanocomposite Structural Ceramics, MRS Proc. 286 (1992) 405. https://doi.org/10.1557/PROC-286-405.
[80] R. Riedel, H.-J. Kleebe, H. Schönfelder, F. Aldinger, A covalent micro/nano-composite resistant to high-temperature oxidation, Nature. 374 (1995) 526–528. https://doi.org/10.1038/374526a0.
[81] C. Haluschka, C. Engel, R. Riedel, Silicon carbonitride ceramics derived from polysilazanes Part II. Investigation of electrical properties, Journal of the European Ceramic Society. 20 (2000) 1365–1374. https://doi.org/10.1016/S0955-2219(00)00009-1.
[82] S. Trassl, G. Motz, E. Rössler, G. Ziegler, Characterisation of the free-carbon phase in precursor-derived SiCN ceramics, Journal of Non-Crystalline Solids. 293–295 (2001) 261–267. https://doi.org/10.1016/S0022-3093(01)00678-0.
[83] A. Saha, R. Raj, D.L. Williamson, A Model for the Nanodomains in Polymer-Derived SiCO, Journal of the American Ceramic Society. 89 (2006) 2188–2195. https://doi.org/10.1111/j.1551-2916.2006.00920.x.
[84] S.J. Widgeon, S. Sen, G. Mera, E. Ionescu, R. Riedel, A. Navrotsky, ^{29}Si and ^{13}C Solid-State NMR Spectroscopic Study of Nanometer-Scale Structure and Mass Fractal Characteristics of Amorphous Polymer Derived Silicon Oxycarbide Ceramics, Chem. Mater. 22 (2010) 6221–6228. https://doi.org/10.1021/cm1021432.
[85] S. Schempp, J. Dürr, P. Lamparter, J. Bill, F. Aldinger, Study of the Atomic Structure and Phase Separation in Amorphous Si-C-N Ceramics by X-Ray and Neutron Diffraction, Zeitschrift Für Naturforschung A. 53 (1998) 127–133. https://doi.org/10.1515/zna-1998-3-405.
[86] E. Radovanovic, M.F. Gozzi, M.C. Gonçalves, I.V.P. Yoshida, Silicon oxycarbide glasses from silicone networks, Journal of Non-Crystalline Solids. 248 (1999) 37–48. https://doi.org/10.1016/S0022-3093(99)00101-5.
[87] M. Harris, T. Chaudhary, L. Drzal, R.M. Laine, Silicon oxycarbide coatings on graphite fibers: chemistry, processing, and oxidation resistance, Materials Science and Engineering: A. 195 (1995) 223–236. https://doi.org/10.1016/0921-5093(94)06522-5.
[88] G. Mera, R. Riedel, F. Poli, K. Müller, Carbon-rich SiCN ceramics derived from phenyl-containing poly(silylcarbodiimides), Journal of the European Ceramic Society. 29 (2009) 2873–2883. https://doi.org/10.1016/j.jeurceramsoc.2009.03.026.
[89] G. Mera, A. Tamayo, H. Nguyen, S. Sen, R. Riedel, Nanodomain Structure of Carbon-Rich Silicon Carbonitride Polymer-Derived Ceramics, Journal of the American Ceramic Society. 93 (2010) 1169–1175. https://doi.org/10.1111/j.1551-2916.2009.03558.x.
[90] H. Störmer, H.-J. Kleebe, G. Ziegler, Metastable SiCN glass matrices studied by energy-filtered electron diffraction pattern analysis, Journal of Non-Crystalline Solids. 353 (2007) 2867–2877. https://doi.org/10.1016/j.jnoncrysol.2007.06.003.
[91] E. Ionescu, B. Papendorf, H.-J. Kleebe, F. Poli, K. Müller, R. Riedel, Polymer-Derived Silicon Oxycarbide/Hafnia Ceramic Nanocomposites. Part I: Phase and Microstructure Evolution During the Ceramization Process, Journal of the American Ceramic Society. (2010). https://doi.org/10.1111/j.1551-2916.2010.03765.x.
[92] E. Ionescu, B. Papendorf, H.-J. Kleebe, H. Breitzke, K. Nonnenmacher, G. Buntkowsky, R. Riedel, Phase separation of a hafnium alkoxide-modified polysilazane upon polymer-to-ceramic transformation—A case study, Journal of the European Ceramic Society. 32 (2012) 1873–1881. https://doi.org/10.1016/j.jeurceramsoc.2011.09.003.
[93] A. Saha, S.R. Shah, R. Raj, Oxidation Behavior of SiCN-ZrO_2 Fiber Prepared from Alkoxide-Modified Silazane, Journal of the American Ceramic Society. 87 (2004) 1556–1558. https://doi.org/10.1111/j.1551-2916.2004.01556.x.

[94] N. Thor, J. Bernauer, N.-C. Petry, E. Ionescu, R. Riedel, A. Pundt, H.-J. Kleebe, Microstructural evolution of Si(Hf_xTa_{1-x})(C)N polymer-derived ceramics upon high-temperature anneal, Journal of the European Ceramic Society. 43 (2023) 1417–1431. https://doi.org/10.1016/ j.jeurceramsoc.2022.11.060.
[95] C. Linck, E. Ionescu, B. Papendorf, D. Galuskova, D. Galusek, P. Šajgalík, R. Riedel, Corrosion behavior of silicon oxycarbide-based ceramic nanocomposites under hydrothermal conditions, International Journal of Materials Research. 103 (2012) 31–39. https://doi.org/10.3139/146.110625.
[96] C. Liu, C. Hong, X. Wang, J. Han, High temperature structure evolution of SiBZrOC quinary polymer derived ceramics, RSC Adv. 12 (2022) 8154–8159. https://doi.org/10.1039/D1RA08208F.
[97] C. Wu, F. Lin, X. Pan, Z. Cui, Y. He, G. Chen, X. Liu, G. He, Q. Chen, D. Sun, Z. Hai, TiB_2 -Modified Polymer-Derived Ceramic SiCN Double-Layer Thin Films Fabricated by Direct Writing for High-Temperature Application, Adv Eng Mater. 24 (2022) 2200228. https://doi.org/10.1002/adem.202200228.
[98] C. Zhou, S. Li, Z. Yu, Polymer-derived Fe_xSi_y/SiC@SiOC ceramic nanocomposites with tunable microwave absorption behavior, International Journal of Applied Ceramic Technology. 19 (2022) 813–827. https://doi.org/10.1111/ijac.13850.
[99] J. Wang, A. Gili, M. Grünbacher, S. Praetz, J.D. Epping, O. Görke, G. Schuck, S. Penner, C. Schlesiger, R. Schomäcker, A. Gurlo, M.F. Bekheet, Silicon oxycarbonitride ceramic containing nickel nanoparticles: from design to catalytic application, Mater. Adv. 2 (2021) 1715–1730. https://doi.org/ 10.1039/D0MA00917B.
[100] H.P. Macedo, R.L.B.A. Medeiros, J. Ilsemann, D.M.A. Melo, K. Rezwan, M. Wilhelm, Nickel-containing hybrid ceramics derived from polysiloxanes with hierarchical porosity for CO_2 methanation, Microporous and Mesoporous Materials. 278 (2019) 156–166. https://doi.org/10.1016/j.micromeso.2018.11.006.
[101] M. Schubert, M. Wilhelm, S. Bragulla, C. Sun, S. Neumann, T.M. Gesing, P. Pfeifer, K. Rezwan, M. Bäumer, The Influence of the Pyrolysis Temperature on the Material Properties of Cobalt and Nickel Containing Precursor Derived Ceramics and their Catalytic Use for CO_2 Methanation and Fischer–Tropsch Synthesis, Catalysis Letters. 147 (2017) 472–482. https://doi.org/10.1007/s10562-016-1919-y.
[102] Y. Feng, Z. Yu, J. Schuch, S. Tao, L. Wiehl, C. Fasel, W. Jaegermann, R. Riedel, Nowotny phase $Mo_{3+2x}Si_3C_{0.6}$ dispersed in a porous SiC/C matrix: A novel catalyst for hydrogen evolution reaction, Journal of the American Ceramic Society. 103 (2020) 508–519. https://doi.org/10.1111/jace.16731.
[103] J. Blechschmidt, Taschenbuch der Papiertechnik: mit 85 Tabellen, 2nd ed., Fachbuchverlag Leipzig im Carl Hanser Verlag, München, 2010.
[104] Pulp & paper market size globally 2021-2029, Statista. (n.d.). https://www.statista.com/statistics/1073451/ global-market-value-pulp-and-paper/ (accessed May 16, 2023).
[105] M. Hubbe, Paper's resistance to wetting - A review of internal sizing chemicals and their effects, BioResources. 2 (2006) 106–145.
[106] H. Sixta, Handbook of Pulp, 1st ed., John Wiley & Sons, Weinheim : Chichester, 2006.
[107] R.M. Rowell, Handbook of Wood Chemistry and Wood Composites, 1st ed., CRC Press, 2005. https://doi.org/10.1201/9780203492437.
[108] D. Mboowa, A review of the traditional pulping methods and the recent improvements in the pulping processes, Biomass Conv. Bioref. (2021). https://doi.org/10.1007/s13399-020-01243-6.
[109] H. Holik, Handbook of paper and board, 1st ed., John Wiley & Sons, Weinheim, 2006.
[110] M.A. Dulany, G.L. Batten, M.C. Peck, C.E. Farley, Papermaking Additives, in: John Wiley & Sons, Inc. (Ed.), Kirk-Othmer Encyclopedia of Chemical Technology, 5th ed., John Wiley & Sons, Hoboken, NJ, USA, 2011. https://doi.org/10.1002/0471238961. 1601160504211201.a01.pub2.
[111] H. Choi, Y.C. Choi, Setting characteristics of natural cellulose fiber reinforced cement composite, Construction and Building Materials. 271 (2021) 121910. https://doi.org/10.1016/j.conbuildmat. 2020.121910.
[112] P. Dalmay, A. Smith, T. Chotard, P. Sahay-Turner, V. Gloaguen, P. Krausz, Properties of cellulosic fibre reinforced plaster: influence of hemp or flax fibres on the properties of set gypsum, Journal of Materials Science. 45 (2010) 793–803. https://doi.org/10.1007/s10853-009-4002-x.
[113] M. Jakob, A.R. Mahendran, W. Gindl-Altmutter, P. Bliem, J. Konnerth, U. Müller, S. Veigel, The strength and stiffness of oriented wood and cellulose-fibre materials: A review, Progress in Materials Science. 125 (2022) 100916. https://doi.org/10.1016/j.pmatsci.2021.100916.

[114] H. Sehaqui, A. Liu, Q. Zhou, L.A. Berglund, Fast Preparation Procedure for Large, Flat Cellulose and Cellulose/Inorganic Nanopaper Structures, Biomacromolecules. 11 (2010) 2195–2198. https://doi.org/10.1021/bm100490s.
[115] M.A.S. Azizi Samir, F. Alloin, A. Dufresne, Review of Recent Research into Cellulosic Whiskers, Their Properties and Their Application in Nanocomposite Field, Biomacromolecules. 6 (2005) 612–626. https://doi.org/10.1021/bm0493685.
[116] H. Tu, M. Zhu, B. Duan, L. Zhang, Recent Progress in High-Strength and Robust Regenerated Cellulose Materials, Adv. Mater. 33 (2021). https://doi.org/10.1002/adma.202000682.
[117] H. Mohit, V. Arul Mozhi Selvan, A comprehensive review on surface modification, structure interface and bonding mechanism of plant cellulose fiber reinforced polymer based composites, Composite Interfaces. 25 (2018) 629–667. https://doi.org/10.1080/09276440.2018.1444832.
[118] J. Fan, S. Zhang, F. Li, Y. Yang, M. Du, Recent advances in cellulose-based membranes for their sensing applications, Cellulose. 27 (2020) 9157–9179. https://doi.org/10.1007/s10570-020-03445-7.
[119] X. Li, K.Y. Wang, B. Helmer, T.-S. Chung, Thin-Film Composite Membranes and Formation Mechanism of Thin-Film Layers on Hydrophilic Cellulose Acetate Propionate Substrates for Forward Osmosis Processes, Ind. Eng. Chem. Res. 51 (2012) 10039–10050. https://doi.org/10.1021/ie2027052.
[120] S. Glatzel, Z. Schnepp, C. Giordano, From Paper to Structured Carbon Electrodes by Inkjet Printing, Angew. Chem. Int. Ed. 52 (2013) 2355–2358. https://doi.org/10.1002/anie.201207693.
[121] E. Fortunato, N. Correia, P. Barquinha, L. Pereira, G. Goncalves, R. Martins, High-Performance Flexible Hybrid Field-Effect Transistors Based on Cellulose Fiber Paper, IEEE Electron Device Lett. 29 (2008) 988–990. https://doi.org/10.1109/LED.2008.2001549.
[122] L.J. Gibson, The hierarchical structure and mechanics of plant materials, J. R. Soc. Interface. 9 (2012) 2749–2766. https://doi.org/10.1098/rsif.2012.0341.
[123] C. Chen, L. Hu, Nanoscale Ion Regulation in Wood-Based Structures and Their Device Applications, Adv. Mater. 33 (2021) 2002890. https://doi.org/10.1002/adma.202002890.
[124] C. Ververis, K. Georghiou, N. Christodoulakis, P. Santas, R. Santas, Fiber dimensions, lignin and cellulose content of various plant materials and their suitability for paper production, Industrial Crops and Products. 19 (2004) 245–254. https://doi.org/10.1016/ j.indcrop.2003.10.006.
[125] A. Ebringerová, Z. Hromádková, T. Heinze, Hemicellulose, in: T. Heinze (Ed.), Polysaccharides I, Springer-Verlag, Berlin/Heidelberg, 2005: pp. 1–67. https://doi.org/10.1007/b136816.
[126] L. Donaldson, Cellulose microfibril aggregates and their size variation with cell wall type, Wood Science and Technology. 41 (2007) 443. https://doi.org/10.1007/s00226-006-0121-6.
[127] W. Boerjan, J. Ralph, M. Baucher, Lignin Biosynthesis, Annu. Rev. Plant Biol. 54 (2003) 519–546. https://doi.org/10.1146/annurev.arplant.54.031902.134938.
[128] J. Blechschmidt, S. Heinemann, H. Putz, G.G. Duffy, Fibrous Materials for Paper and Board Manufacture, in: H. Holik (Ed.), Handbook of Paper and Board, 1st ed., John Wiley & Sons, 2013: pp. 33–108. https://doi.org/10.1002/9783527652495.ch2.
[129] M.K. Misra, K.W. Ragland, A.J. Baker, Wood ash composition as a function of furnace temperature, Biomass and Bioenergy. 4 (1993) 103–116. https://doi.org/10.1016/0961-9534(93)90032-Y.
[130] Y.-C. Lin, J. Cho, G.A. Tompsett, P.R. Westmoreland, G.W. Huber, Kinetics and Mechanism of Cellulose Pyrolysis, J. Phys. Chem. C. 113 (2009) 20097–20107. https://doi.org/10.1021/jp906702p.
[131] M.M. Tang, R. Bacon, Carbonization of cellulose fibers—I. Low temperature pyrolysis, Carbon. 2 (1964) 211–220. https://doi.org/10.1016/0008-6223(64)90035-1.
[132] D. Klemm, B. Heublein, H.-P. Fink, A. Bohn, Cellulose: Fascinating Biopolymer and Sustainable Raw Material, Angew. Chem. Int. Ed. 44 (2005) 3358–3393. https://doi.org/10.1002/anie.200460587.
[133] H. Yang, R. Yan, H. Chen, D.H. Lee, C. Zheng, Characteristics of hemicellulose, cellulose and lignin pyrolysis, Fuel. 86 (2007) 1781–1788. https://doi.org/10.1016/j.fuel.2006.12.013.
[134] J. Lédé, Cellulose pyrolysis kinetics: An historical review on the existence and role of intermediate active cellulose, Journal of Analytical and Applied Pyrolysis. 94 (2012) 17–32. https://doi.org/10.1016/j.jaap.2011.12.019.
[135] D. Mohan, C.U. Pittman, P.H. Steele, Pyrolysis of Wood/Biomass for Bio-oil: A Critical Review, Energy Fuels. 20 (2006) 848–889. https://doi.org/10.1021/ef0502397.
[136] C. Zhang, L. Chao, Z. Zhang, L. Zhang, Q. Li, H. Fan, S. Zhang, Q. Liu, Y. Qiao, Y. Tian, Y. Wang, X. Hu, Pyrolysis of cellulose: Evolution of functionalities and structure of bio-char versus temperature,

Renewable and Sustainable Energy Reviews. 135 (2021) 110416. https://doi.org/10.1016/j.rser.2020.110416.
[137] J.B. Wooten, J.I. Seeman, M.R. Hajaligol, Observation and Characterization of Cellulose Pyrolysis Intermediates by ^{13}C CPMAS NMR. A New Mechanistic Model, Energy Fuels. 18 (2004) 1–15. https://doi.org/10.1021/ef0300601.
[138] F. Shafizadeh, Introduction to pyrolysis of biomass, Journal of Analytical and Applied Pyrolysis. 3 (1982) 283–305. https://doi.org/10.1016/0165-2370(82)80017-X.
[139] J. Lehto, A. Oasmaa, Y. Solantausta, M. Kytö, D. Chiaramonti, Review of fuel oil quality and combustion of fast pyrolysis bio-oils from lignocellulosic biomass, Applied Energy. 116 (2014) 178–190. https://doi.org/10.1016/j.apenergy.2013.11.040.
[140] Z. Wang, F. Wang, J. Cao, J. Wang, Pyrolysis of pine wood in a slowly heating fixed-bed reactor: Potassium carbonate versus calcium hydroxide as a catalyst, Fuel Processing Technology. 91 (2010) 942–950. https://doi.org/10.1016/j.fuproc.2009.09.015.
[141] M. Safar, B.-J. Lin, W.-H. Chen, D. Langauer, J.-S. Chang, H. Raclavska, A. Pétrissans, P. Rousset, M. Pétrissans, Catalytic effects of potassium on biomass pyrolysis, combustion and torrefaction, Applied Energy. 235 (2019) 346–355. https://doi.org/10.1016/ j.apenergy.2018.10.065.
[142] N.H. Phan, S. Rio, C. Faur, L. Le Coq, P. Le Cloirec, T.H. Nguyen, Production of fibrous activated carbons from natural cellulose (jute, coconut) fibers for water treatment applications, Carbon. 44 (2006) 2569–2577. https://doi.org/10.1016/j.carbon.2006.05.048.
[143] J.-H. Kim, S.-C. Jung, H.-M. Lee, B.-J. Kim, Comparison of Pore Structures of Cellulose-Based Activated Carbon Fibers and Their Applications for Electrode Materials, International Journal of Molecular Sciences. 23 (2022) 3680. https://doi.org/10.3390/ijms23073680.
[144] B.-Q. Lu, Y.-J. Zhu, F. Chen, Highly Flexible and Nonflammable Inorganic Hydroxyapatite Paper, Chem. Eur. J. 20 (2014) 1242–1246. https://doi.org/10.1002/chem.201304439.
[145] N. Travitzky, H. Windsheimer, T. Fey, P. Greil, Preceramic Paper-Derived Ceramics, Journal of the American Ceramic Society. 91 (2008) 3477–3492. https://doi.org/10.1111/j.1551-2916.2008.02752.x.
[146] W. Zhou, R. Yin, L. Long, H. Luo, W. Hu, Y. Ding, Y. Li, SiC nanofibers modified Si_3N_4 ceramics for improved electromagnetic interference shielding in X-band, Ceramics International. 44 (2018) 2249–2254. https://doi.org/10.1016/j.ceramint.2017.10.183.
[147] L. Yang, S. Cheng, Y. Ding, X. Zhu, Z.L. Wang, M. Liu, Hierarchical Network Architectures of Carbon Fiber Paper Supported Cobalt Oxide Nanonet for High-Capacity Pseudocapacitors, Nano Lett. 12 (2012) 321–325. https://doi.org/10.1021/nl203600x.
[148] G. Li, J. Ma, G. Peng, W. Chen, Z. Chu, Y. Li, T. Hu, X. Li, Room-Temperature Humidity-Sensing Performance of SiC Nanopaper, ACS Appl. Mater. Interfaces. 6 (2014) 22673–22679. https://doi.org/10.1021/am5067496.
[149] J. Yuan, X. Liu, O. Akbulut, J. Hu, S.L. Suib, J. Kong, F. Stellacci, Superwetting nanowire membranes for selective absorption, Nature Nanotech. 3 (2008) 332–336. https://doi.org/10.1038/nnano.2008.136.
[150] S. Miura, Y. Umemura, Y. Shiratori, T. Kitaoka, In situ synthesis of Ni/MgO catalysts on inorganic paper-like matrix for methane steam reforming, Chemical Engineering Journal. 229 (2013) 515–521. https://doi.org/10.1016/j.cej.2013.06.052.
[151] C. Jia, Y. Liu, L. Li, J. Song, H. Wang, Z. Liu, Z. Li, B. Li, M. Fang, H. Wu, A Foldable All-Ceramic Air Filter Paper with High Efficiency and High-Temperature Resistance, Nano Lett. 20 (2020) 4993–5000. https://doi.org/10.1021/acs.nanolett.0c01107.
[152] B.N. Tepekiran, M.D. Calisir, Y. Polat, Y. Akgul, A. Kilic, Centrifugally spun silica (SiO_2) nanofibers for high-temperature air filtration, Aerosol Science and Technology. 53 (2019) 921–932. https://doi.org/10.1080/02786826.2019.1613514.
[153] B. Lan, L. Yu, T. Lin, G. Cheng, M. Sun, F. Ye, Q. Sun, J. He, Multifunctional Free-Standing Membrane from the Self-assembly of Ultralong MnO_2 Nanowires, ACS Appl. Mater. Interfaces. 5 (2013) 7458–7464. https://doi.org/10.1021/am401774r.
[154] F.-F. Chen, Y.-J. Zhu, F. Chen, L.-Y. Dong, R.-L. Yang, Z.-C. Xiong, Fire Alarm Wallpaper Based on Fire-Resistant Hydroxyapatite Nanowire Inorganic Paper and Graphene Oxide Thermosensitive Sensor, ACS Nano. 12 (2018) 3159–3171. https://doi.org/10.1021/acsnano.8b00047.

[155] L.-Y. Dong, Y.-J. Zhu, A New Kind of Fireproof, Flexible, Inorganic, Nanocomposite Paper and Its Application to the Protection Layer in Flame-Retardant Fiber-Optic Cables, Chem. Eur. J. 23 (2017) 4597–4604. https://doi.org/10.1002/chem.201604552.
[156] F. Chen, J. Zhang, N. Li, C. Zhang, B. Ji, L. Hu, T. Zhao, Z. Wang, S. Zhang, Heat insulating, fire retardant and flexible inorganic nanocomposite paper, Materials & Design. 144 (2018) 281–289. https://doi.org/10.1016/j.matdes.2018.02.039.
[157] W. Dai, L. Lv, J. Lu, H. Hou, Q. Yan, F.E. Alam, Y. Li, X. Zeng, J. Yu, Q. Wei, X. Xu, J. Wu, N. Jiang, S. Du, R. Sun, J. Xu, C.-P. Wong, C.-T. Lin, A Paper-Like Inorganic Thermal Interface Material Composed of Hierarchically Structured Graphene/Silicon Carbide Nanorods, ACS Nano. (2019) acsnano.8b07337. https://doi.org/10.1021/acsnano.8b07337.
[158] L. Li, F. Wang, J. Zhu, W. Wu, The facile synthesis of layered Ti_2C MXene/carbon nanotube composite paper with enhanced electrochemical properties, Dalton Trans. 46 (2017) 14880–14887. https://doi.org/10.1039/C7DT02688A.
[159] Y. Li, H. Zhou, G. Zhu, C. Shao, H. Pan, X. Xu, R. Tang, High efficient multifunctional Ag_3PO_4 loaded hydroxyapatite nanowires for water treatment, Journal of Hazardous Materials. 299 (2015) 379–387. https://doi.org/10.1016/j.jhazmat.2015.06.032.
[160] Z.-C. Xiong, Z.-Y. Yang, Y.-J. Zhu, F.-F. Chen, R.-L. Yang, D.-D. Qin, Ultralong hydroxyapatite nanowire-based layered catalytic paper for highly efficient continuous flow reactions, J. Mater. Chem. A. 6 (2018) 5762–5773. https://doi.org/10.1039/C7TA11215G.
[161] F.E. Tuler, E.D. Banús, M.A. Zanuttini, E.E. Miró, V.G. Milt, Ceramic papers as flexible structures for the development of novel diesel soot combustion catalysts, Chemical Engineering Journal. 246 (2014) 287–298. https://doi.org/10.1016/j.cej.2014.02.083.
[162] F.-F. Chen, Y.-J. Zhu, Z.-C. Xiong, T.-W. Sun, Y.-Q. Shen, R.-L. Yang, Inorganic Nanowires-Assembled Layered Paper as the Valve for Controlling Water Transportation, ACS Appl. Mater. Interfaces. 9 (2017) 11045–11053. https://doi.org/10.1021/acsami.7b01326.
[163] C. Jia, Z. Xu, D. Luo, H. Xiang, M. Zhu, Flexible Ceramic Fibers: Recent Development in Preparation and Application, Adv. Fiber Mater. 4 (2022) 573–603. https://doi.org/10.1007/s42765-022-00133-y.
[164] P. Baldus, M. Jansen, D. Sporn, Ceramic Fibers for Matrix Composites in High-Temperature Engine Applications, Science. 285 (1999) 699–703. https://doi.org/10.1126/ science.285.5428.699.
[165] H. Ichikawa, Polymer-Derived Ceramic Fibers, Annu. Rev. Mater. Res. 46 (2016) 335–356. https://doi.org/10.1146/annurev-matsci-070115-032127.
[166] G. Li, M. Zhu, W. Gong, R. Du, A. Eychmüller, T. Li, W. Lv, X. Zhang, Boron Nitride Aerogels with Super-Flexibility Ranging from Liquid Nitrogen Temperature to 1000 °C, Adv. Funct. Mater. 29 (2019) 1900188. https://doi.org/10.1002/adfm.201900188.
[167] M. Sadat-Shojai, M.-T. Khorasani, E. Dinpanah-Khoshdargi, A. Jamshidi, Synthesis methods for nanosized hydroxyapatite with diverse structures, Acta Biomaterialia. 9 (2013) 7591–7621. https://doi.org/10.1016/j.actbio.2013.04.012.
[168] J. Chen, X. Liao, M. Wang, Z. Liu, J. Zhang, L. Ding, L. Gao, Y. Li, Highly flexible, nonflammable and free-standing SiC nanowire paper, Nanoscale. 7 (2015) 6374–6379. https://doi.org/10.1039/C5NR00776C.
[169] H. Koga, H. Ishihara, T. Kitaoka, A. Tomoda, R. Suzuki, H. Wariishi, NO_x reduction over paper-structured fiber composites impregnated with Pt/Al_2O_3 catalyst for exhaust gas purification, Journal of Materials Science. 45 (2010) 4151–4157. https://doi.org/10.1007/s10853-010-4504-6.
[170] J. Nowak, M. Florek, W. Kwiatek, J. Lekki, P. Chevallier, E. Zięba, N. Mestres, E.M. Dutkiewicz, A. Kuczumow, Composite structure of wood cells in petrified wood, Materials Science and Engineering: C. 25 (2005) 119–130. https://doi.org/10.1016/j.msec.2005.01.018.
[171] H. Sieber, C. Hoffmann, H. Kaindl, P. Greil, Biomorphic Cellular Ceramics, Advanced Engineering Materials. 2 (2000) 105–109.
[172] H. Sieber, C. Zollfrank, N. Popovska, D. Almeida, H. Gerhard, Gas Phase Processing of Porous, Biomorphous TiC-Ceramics, Key Engineering Materials. 264–268 (2004) 2227–2230. https://doi.org/10.4028/www.scientific.net/KEM.264-268.2227.
[173] T. Ota, M. Imaeda, H. Takase, M. Kobayashi, N. Kinoshita, T. Hirashita, H. Miyazaki, Y. Hikichi, Porous Titania Ceramic Prepared by Mimicking Silicified Wood, Journal of the American Ceramic Society. 83 (2000) 1521–1523. https://doi.org/10.1111/j.1151-2916.2000.tb01421.x.

[174] J. Cao, C.R. Rambo, H. Sieber, Preparation of Porous Al_2O_3 -Ceramics by Biotemplating of Wood, Journal of Porous Materials. 11 (2004) 163–172. https://doi.org/10.1023/B:JOPO. 0000038012.58705.c9.
[175] C.R. Rambo, J. Cao, H. Sieber, Preparation and properties of highly porous, biomorphic YSZ ceramics, Materials Chemistry and Physics. 87 (2004) 345–352. https://doi.org/10.1016/j.matchemphys. 2004.05.031.
[176] A. Ruffini, S. Sprio, A. Tampieri, Study of the hydrothermal transformation of wood-derived calcium carbonate into 3D hierarchically organized hydroxyapatite, Chemical Engineering Journal. 217 (2013) 150–158. https://doi.org/10.1016/j.cej.2012.11.107.
[177] A. Tampieri, S. Sprio, A. Ruffini, G. Celotti, I.G. Lesci, N. Roveri, From wood to bone: multi-step process to convert wood hierarchical structures into biomimetic hydroxyapatite scaffolds for bone tissue engineering, J. Mater. Chem. 19 (2009) 4973. https://doi.org/10.1039/b900333a.
[178] P. Greil, E. Vogli, T. Fey, A. Bezold, N. Popovska, H. Gerhard, H. Sieber, Effect of microstructure on the fracture behavior of biomorphous silicon carbide ceramics, Journal of the European Ceramic Society. 22 (2002) 2697–2707. https://doi.org/10.1016/S0955-2219(02)00135-8.
[179] J. Ramírez-Rico, J. Martínez-Fernandez, M. Singh, Biomorphic ceramics from wood-derived precursors, International Materials Reviews. 62 (2017) 465–485. https://doi.org/10.1080/09506608.2017.1354429.
[180] Y. Shin, C. Wang, G.J. Exarhos, Synthesis of SiC Ceramics by the Carbothermal Reduction of Mineralized Wood with Silica, Adv. Mater. 17 (2005) 73–77. https://doi.org/10.1002/adma.200400371.
[181] C.R. Rambo, J. Cao, O. Rusina, H. Sieber, Manufacturing of biomorphic (Si, Ti, Zr)-carbide ceramics by sol–gel processing, Carbon. 43 (2005) 1174–1183. https://doi.org/10.1016/ j.carbon.2004.12.009.
[182] L. Qian, R. Li, L. Zhou, Y. Liu, M. Yu, F. Xiong, S. Liu, X. Hao, Preparation of Biomorphic TiO_2 Ceramics from Rattan Templates, BioResources. 10 (2015) 4391–4402. https://doi.org/10.15376/biores.10.3.4391-4402.
[183] R.C. Pullar, P. Marques, J. Amaral, J.A. Labrincha, Magnetic wood-based biomorphic $Sr_3Co_2Fe_{24}O_{41}$ Z-type hexaferrite ecoceramics made from cork templates, Materials & Design. 82 (2015) 297–303. https://doi.org/10.1016/j.matdes.2015.03.047.
[184] N. Popovska, E. Alkhateeb, A.P. Fröba, A. Leipertz, Thermal conductivity of porous SiC composite ceramics derived from paper precursor, Ceramics International. 36 (2010) 2203–2207. https://doi.org/10.1016/j.ceramint.2010.05.028.
[185] N. Popovska, D.A. Streitwieser, C. Xu, H. Gerhard, Paper derived biomorphic porous titanium carbide and titanium oxide ceramics produced by chemical vapor infiltration and reaction (CVI-R), Journal of the European Ceramic Society. 25 (2005) 829–836. https://doi.org/10.1016/j.jeurceramsoc.2004.04.007.
[186] D.A. Streitwieser, N. Popovska, H. Gerhard, G. Emig, Application of the chemical vapor infiltration and reaction (CVI-R) technique for the preparation of highly porous biomorphic SiC ceramics derived from paper, Journal of the European Ceramic Society. 25 (2005) 817–828. https://doi.org/10.1016/ j.jeurceramsoc.2004.04.006.
[187] N. Popovska, D. Almeida-Streitwieser, C. Xu, H. Gerhard, H. Sieber, Kinetic Analysis of the Processing of Porous Biomorphic Titanium Carbide Ceramics by Chemical Vapor Infiltration, Chem. Vap. Deposition. 11 (2005) 153–158. https://doi.org/10.1002/cvde.200306319.
[188] H. Ghanem, H. Gerhard, N. Popovska, Paper derived SiC–Si_3N_4 ceramics for high temperature applications, Ceramics International. 35 (2009) 1021–1026. https://doi.org/10.1016/j.ceramint. 2008.04.020.
[189] S.L. Stares, M.C. Fredel, P. Greil, N. Travitzky, Paper-derived hydroxyapatite, Ceramics International. 39 (2013) 7179–7183. https://doi.org/10.1016/j.ceramint.2013.02.062.
[190] H. Windsheimer, N. Travitzky, A. Hofenauer, P. Greil, Laminated Object Manufacturing of Preceramic-Paper-Derived Si-SiC Composites, Adv. Mater. 19 (2007) 4515–4519. https://doi.org/10.1002/ adma.200700789.
[191] B. Gutbrod, D. Haas, N. Travitzky, P. Greil, Preceramic Paper Derived Alumina/Zirconia Ceramics, Adv. Eng. Mater. 13 (2011) 494–501. https://doi.org/10.1002/adem.201100017.
[192] T. Fan, X. Li, J. Ding, D. Zhang, Q. Guo, Synthesis of biomorphic Al_2O_3 based on natural plant templates and assembly of Ag nanoparticles controlled within the nanopores, Microporous and Mesoporous Materials. 108 (2008) 204–212. https://doi.org/10.1016/j.micromeso.2007.03.050.
[193] S. Silvestri, B. Szpoganicz, D. Hotza, J.A. Labrincha, Synthesis of biomorphic paper-derived anatase, Materials Letters. 141 (2015) 275–279. https://doi.org/10.1016/j.matlet.2014.11.125.

[194] D. Jia, K. Wang, J. Huang, Filter paper derived nanofibrous silica–carbon composite as anodic material with enhanced lithium storage performance, Chemical Engineering Journal. 317 (2017) 673–686. https://doi.org/10.1016/j.cej.2017.02.109.
[195] M. Wang, S. Li, Y. Zhang, J. Huang, Hierarchical SnO_2 /Carbon Nanofibrous Composite Derived from Cellulose Substance as Anode Material for Lithium-Ion Batteries, Chem. Eur. J. 21 (2015) 16195–16202. https://doi.org/10.1002/chem.201502833.
[196] D. Jia, X. Li, J. Huang, Bio-inspired sandwich-structured carbon/silicon/titanium-oxide nanofibers composite as an anode material for lithium-ion batteries, Composites Part A: Applied Science and Manufacturing. 101 (2017) 273–282. https://doi.org/10.1016/ j.compositesa.2017.06.028.
[197] Z. Lin, J. Huang, Hierarchical nanostructures derived from cellulose for lithium-ion batteries, Dalton Trans. 48 (2019) 14221–14232. https://doi.org/10.1039/C9DT02986A.
[198] C.R. Rambo, H. Sieber, Manufacturing of cellular β-SiAlON/β-SiC composite ceramics from cardboard, Journal of Materials Science. 41 (2006) 3315–3322. https://doi.org/10.1007/s10853-005-5428-4.
[199] H. Sieber, P. Greil, Ceramic Composites from Bioorganic Derived Materials, in: G. Müller (Ed.), Ceramics - Processing, Reliability, Tribology and Wear, John Wiley & Sons, Weinheim, 2006: pp. 45–49. https://doi.org/10.1002/3527607293.ch8.
[200] J. Peter, E. Ionescu, H.-J. Kleebe, Tailoring the micro- and nanostructure of polymer-derived ceramic papers, Journal of the European Ceramic Society. (2023) 3969–3980. https://doi.org/10.1016/ j.jeurceramsoc.2023.02.071.
[201] J. Peter, Microstructural Characterization of Ceramic SiFeN/OC Papers – Morphology Transfer and Phase Evolution, Master's Thesis, Technische Universität Darmstadt, 2020.
[202] G. McMahon, T. Malis, Ultramicrotomy of nanocrystalline materials, Microsc. Res. Tech. 31 (1995) 267–274. https://doi.org/10.1002/jemt.1070310403.
[203] G. Miehe, Program for interpreting electron diffraction patterns (PIEP), (2017).
[204] Y. Seto, M. Ohtsuka, *ReciPro* : free and open-source multipurpose crystallographic software integrating a crystal model database and viewer, diffraction and microscopy simulators, and diffraction data analysis tools, Journal of Applied Crystallography. 55 (2022) 397–410. https://doi.org/10.1107/ S1600576722000139.
[205] D.B. Williams, C.B. Carter, Transmission electron microscopy: a textbook for materials science, 2. ed, Springer, New York, 2009.
[206] A.-K. Fetzer, M. Trapp, S. Lauterbach, H.-J. Kleebe, Introduction to Transmission Electron Microscopy; The Basics, in: Encyclopedia of Materials: Technical Ceramics and Glasses, Elsevier, 2021: pp. 578–599. https://doi.org/10.1016/B978-0-12-818542-1.00036-9.
[207] C. Kisielowski, B. Freitag, M. Bischoff, H. van Lin, S. Lazar, G. Knippels, P. Tiemeijer, M. van der Stam, S. von Harrach, M. Stekelenburg, M. Haider, S. Uhlemann, H. Müller, P. Hartel, B. Kabius, D. Miller, I. Petrov, E.A. Olson, T. Donchev, E.A. Kenik, A.R. Lupini, J. Bentley, S.J. Pennycook, I.M. Anderson, A.M. Minor, A.K. Schmid, T. Duden, V. Radmilovic, Q.M. Ramasse, M. Watanabe, R. Erni, E.A. Stach, P. Denes, U. Dahmen, Detection of Single Atoms and Buried Defects in Three Dimensions by Aberration-Corrected Electron Microscope with 0.5-Å Information Limit, Microscopy and Microanalysis. 14 (2008) 469–477. https://doi.org/10.1017/S1431927608080902.
[208] J. Peter, M. Trapp, S. Lauterbach, P. Gollé-Leidreiter, U. Kolb, H.-J. Kleebe, Exomorphism of jacobsite precipitates in bixbyite single crystals from the Thomas Range in Utah, American Mineralogist. 106 (2021) 1163–1171. https://doi.org/10.2138/am-2021-7715CCBYNCND.
[209] D. Amouzou, L. Fourdrinier, F. Maseri, R. Sporken, Formation of Me–O–Si covalent bonds at the interface between polysilazane and stainless steel, Applied Surface Science. 320 (2014) 519–523. https://doi.org/10.1016/j.apsusc.2014.09.109.
[210] L. Picard, P. Phalip, E. Fleury, F. Ganachaud, Chemical adhesion of silicone elastomers on primed metal surfaces: A comprehensive survey of open and patent literatures, Progress in Organic Coatings. 80 (2015) 120–141. https://doi.org/10.1016/j.porgcoat.2014.11.022.
[211] G. Barroso, M. Döring, A. Horcher, A. Kienzle, G. Motz, Polysilazane-Based Coatings with Anti-Adherent Properties for Easy Release of Plastics and Composites from Metal Molds, Adv. Mater. Interfaces. 7 (2020) 1901952. https://doi.org/10.1002/admi.201901952.

[212] G.S. Barroso, W. Krenkel, G. Motz, Low thermal conductivity coating system for application up to 1000 °C by simple PDC processing with active and passive fillers, Journal of the European Ceramic Society. 35 (2015) 3339–3348. https://doi.org/10.1016/j.jeurceramsoc.2015.02.006.
[213] T. Bleith, L.H. Gade, Mechanism of the Iron(II)-Catalyzed Hydrosilylation of Ketones: Activation of Iron Carboxylate Precatalysts and Reaction Pathways of the Active Catalyst, J. Am. Chem. Soc. 138 (2016) 4972–4983. https://doi.org/10.1021/jacs.6b02173.
[214] E. Buitrago, F. Tinnis, H. Adolfsson, Efficient and Selective Hydrosilylation of Carbonyl Compounds Catalyzed by Iron Acetate and *N*-Hydroxyethylimidazolium Salts, Adv. Synth. Catal. 354 (2012) 217–222. https://doi.org/10.1002/adsc.201100606.
[215] H. Kanda, N. Shibayama, A.J. Huckaba, Y. Lee, S. Paek, N. Klipfel, C. Roldán-Carmona, V.I.E. Queloz, G. Grancini, Y. Zhang, M. Abuhelaiqa, K.T. Cho, M. Li, M.D. Mensi, S. Kinge, M.K. Nazeeruddin, Band-bending induced passivation: high performance and stable perovskite solar cells using a perhydropoly(silazane) precursor, Energy Environ. Sci. 13 (2020) 1222–1230. https://doi.org/10.1039/C9EE02028D.
[216] Z. Zhang, Z. Shao, Y. Luo, P. An, M. Zhang, C. Xu, Hydrophobic, transparent and hard silicon oxynitride coating from perhydropolysilazane: Silicon oxynitride coating from perhydropolysilazane, Polym. Int. 64 (2015) 971–978. https://doi.org/10.1002/pi.4871.
[217] P.H. Mutin, Control of the Composition and Structure of Silicon Oxycarbide and Oxynitride Glasses Derived from Polysiloxane Precursors, Journal of Sol-Gel Science and Technology. 14 (1999) 27–38. https://doi.org/10.1023/A:1008769913083.
[218] N.S. Choong Kwet Yive, R.J.P. Corriu, D. Leclercq, P.H. Mutin, A. Vioux, Thermogravimetric analysis/mass spectrometry investigation of the thermal conversion of organosilicon precursors into ceramics under argon and ammonia. 2. Poly(silazanes), Chem. Mater. 4 (1992) 1263–1271. https://doi.org/10.1021/cm00024a028.
[219] T. Ogawa, Y. Ogata, R. Gallage, N. Kobayashi, N. Hayashi, Y. Kusano, S. Yamamoto, K. Kohara, M. Doi, M. Takano, M. Takahashi, Challenge to the Synthesis of α''-$Fe_{16}N_2$ Compound Nanoparticle with High Saturation Magnetization for Rare Earth Free New Permanent Magnetic Material, Appl. Phys. Express. 6 (2013) 073007. https://doi.org/10.7567/APEX.6.073007.
[220] L. Dai, S. Xie, M. Yu, L. Ci, Fabrication and electromagnetic properties of carbon-based iron nitride composite, Journal of Magnetism and Magnetic Materials. 466 (2018) 22–27. https://doi.org/10.1016/j.jmmm.2018.06.046.
[221] Z. Ye, P. Zhang, X. Lei, X. Wang, N. Zhao, H. Yang, Iron Carbides and Nitrides: Ancient Materials with Novel Prospects, Chem. Eur. J. 24 (2018) 8922–8940. https://doi.org/10.1002/chem.201706028.
[222] G. Serghiou, G. Ji, N. Odling, H.J. Reichmann, D.J. Frost, J.P. Wright, Synthesis and high-resolution study distinguishing between very similar interstitial iron nitride structures, High Pressure Research. 35 (2015) 28–36. https://doi.org/10.1080/08957959.2014.996561.
[223] D.-Y. Kim, Y. Nishiyama, M. Wada, S. Kuga, Graphitization of highly crystalline cellulose, Carbon. 39 (2001) 1051–1056. https://doi.org/10.1016/S0008-6223(00)00221-9.
[224] S. Welz, M.J. McNallan, Y. Gogotsi, Carbon structures in silicon carbide derived carbon, Journal of Materials Processing Technology. 179 (2006) 11–22. https://doi.org/10.1016/ j.jmatprotec.2006.03.103.
[225] A.G. Dumanli, A.H. Windle, Carbon fibres from cellulosic precursors: a review, Journal of Materials Science. 47 (2012) 4236–4250. https://doi.org/10.1007/s10853-011-6081-8.
[226] K.H. Jack, The iron–nitrogen system: the crystal structures of ε-phase iron nitrides, Acta Cryst. 5 (1952) 404–411. https://doi.org/10.1107/S0365110X52001258.
[227] L.S. Darken, R.W. Gurry, The System Iron-Oxygen. I. The Wüstite Field and Related Equilibria, J. Am. Chem. Soc. 67 (1945) 1398–1412. https://doi.org/10.1021/ja01224a050.
[228] X. Zhao, N. Xu, X. Li, Y. Gong, K. Huang, Long Term Stability Study of a Solid Oxide Metal-Air Battery, ECS Trans. 45 (2013) 113–121. https://doi.org/10.1149/04529.0113ecst.
[229] E. Ionescu, C. Terzioglu, C. Linck, J. Kaspar, A. Navrotsky, R. Riedel, Thermodynamic Control of Phase Composition and Crystallization of Metal-Modified Silicon Oxycarbides, J. Am. Ceram. Soc. 96 (2013) 1899–1903. https://doi.org/10.1111/jace.12327.
[230] H. Liu, W. Han, C. Huo, Y. Cen, Development and application of wüstite-based ammonia synthesis catalysts, Catalysis Today. 355 (2020) 110–127. https://doi.org/10.1016/j.cattod.2019.10.031.

[231] J. Tseng, D. Gu, C. Pistidda, C. Horstmann, M. Dornheim, J. Ternieden, C. Weidenthaler, Tracking the Active Catalyst for Iron-Based Ammonia Decomposition by *In Situ* Synchrotron Diffraction Studies, ChemCatChem. 10 (2018) 4465–4472. https://doi.org/10.1002/ cctc.201800398.
[232] B.M. Eick, J.P. Youngblood, Carbothermal reduction of metal-oxide powders by synthetic pitch to carbide and nitride ceramics, Journal of Materials Science. 44 (2009) 1159–1171. https://doi.org/10.1007/s10853-009-3249-6.
[233] R.J. Longbottom, O. Ostrovski, J. Zhang, D. Young, Stability of Cementite Formed from Hematite and Titanomagnetite Ore, Metallurgical and Materials Transactions B. 38 (2007) 175–184. https://doi.org/10.1007/s11663-006-9005-2.
[234] J. Hunt, A. Ferrari, A. Lita, M. Crosswhite, B. Ashley, A.E. Stiegman, Microwave-Specific Enhancement of the Carbon–Carbon Dioxide (Boudouard) Reaction, J. Phys. Chem. C. 117 (2013) 26871–26880. https://doi.org/10.1021/jp4076965.
[235] M.N. Abu Tahari, F. Salleh, T.S. Tengku Saharuddin, A. Samsuri, S. Samidin, M.A. Yarmo, Influence of hydrogen and carbon monoxide on reduction behavior of iron oxide at high temperature: Effect on reduction gas concentrations, International Journal of Hydrogen Energy. 46 (2021) 24791–24805. https://doi.org/10.1016/j.ijhydene.2020.06.250.
[236] T.S.T. Saharuddin, A. Samsuri, F. Salleh, R. Othaman, M.B. Kassim, M.W. Mohamed Hisham, M.A. Yarmo, Studies on reduction of chromium doped iron oxide catalyst using hydrogen and various concentration of carbon monoxide, International Journal of Hydrogen Energy. 42 (2017) 9077–9086. https://doi.org/10.1016/j.ijhydene.2016.08.151.
[237] Y. Liu, Y. Wang, Z. You, X. Lv, Reduction and Nitridation of Iron/Vanadium Oxides by Ammonia Gas: Mechanism and Preparation of $FeV_{45}N$ Alloy, Metals. 10 (2020) 356. https://doi.org/10.3390/ met10030356.
[238] A. Hao, X. Wan, X. Liu, R. Yu, J. Shui, Inorganic microporous membranes for hydrogen separation: Challenges and solutions, Nano Research Energy. 1 (2022) e9120013. https://doi.org/ 10.26599/NRE.2022.9120013.
[239] D. Grainger, M.-B. Hägg, Evaluation of cellulose-derived carbon molecular sieve membranes for hydrogen separation from light hydrocarbons, Journal of Membrane Science. 306 (2007) 307–317. https://doi.org/10.1016/j.memsci.2007.09.005.
[240] M. Hou, L. Li, Z. He, R. Xu, Y. Lu, T. Wang, High hydrogen permselective carbon molecular sieve membrane and its structural formation mechanism, Carbon. 205 (2023) 194–206. https://doi.org/10.1016/ j.carbon.2023.01.035.
[241] R.D. Hunter, J. Ramírez-Rico, Z. Schnepp, Iron-catalyzed graphitization for the synthesis of nanostructured graphitic carbons, J. Mater. Chem. A. 10 (2022) 4489–4516. https://doi.org/10.1039/ D1TA09654K.
[242] Z.C. Eckel, C. Zhou, J.H. Martin, A.J. Jacobsen, W.B. Carter, T.A. Schaedler, Additive manufacturing of polymer-derived ceramics, Science. 351 (2016) 58–62. https://doi.org/10.1126/science.aad2688.
[243] D. Erb, K. Lu, Effect of additive structure and size on SiO_2 formation in polymer-derived SiOC ceramics, Journal of the American Ceramic Society. 101 (2018) 5378–5388. https://doi.org/10.1111/jace.15876.
[244] P. Greil, Near Net Shape Manufacturing of Polymer Derived Ceramics, Journal of the European Ceramic Society. 18 (1998) 1905–1914. https://doi.org/10.1016/S0955-2219(98)00129-0.
[245] Y. Tang, J. Wang, X. Li, W. Li, H. Wang, X. Wang, Thermal stability of polymer derived SiBNC ceramics, Ceramics International. 35 (2009) 2871–2876. https://doi.org/10.1016/ j.ceramint.2009.03.043.
[246] K. Lu, Porous and high surface area silicon oxycarbide-based materials—A review, Materials Science and Engineering: R: Reports. 97 (2015) 23–49. https://doi.org/10.1016/ j.mser.2015.09.001.
[247] H. Bréquel, J. Parmentier, S. Walter, R. Badheka, G. Trimmel, S. Masse, J. Latournerie, P. Dempsey, C. Turquat, A. Desmartin-Chomel, L. Le Neindre-Prum, U.A. Jayasooriya, D. Hourlier, H.-J. Kleebe, G.D. Sorarù, S. Enzo, F. Babonneau, Systematic Structural Characterization of the High-Temperature Behavior of Nearly Stoichiometric Silicon Oxycarbide Glasses, Chem. Mater. 16 (2004) 2585–2598. https://doi.org/10.1021/cm049847a.
[248] C.J. Thambiliyagodage, S. Ulrich, P.T. Araujo, M.G. Bakker, Catalytic graphitization in nanocast carbon monoliths by iron, cobalt and nickel nanoparticles, Carbon. 134 (2018) 452–463. https://doi.org/10.1016/ j.carbon.2018.04.002.

[249] H. Marsh, D. Crawford, D.W. Taylor, Catalytic graphitization by iron of isotropic carbon from polyfurfuryl alcohol, 725–1090 K. A high resolution electron microscope study, Carbon. 21 (1983) 81–87. https://doi.org/10.1016/0008-6223(83)90160-4.
[250] A.W. Weimer, G.A. Eisman, D.W. Susnitzky, D.R. Beaman, J.W. McCoy, Mechanism and Kinetics of the Carbothermal Nitridation Synthesis of α-Silicon Nitride, Journal of the American Ceramic Society. 80 (1997) 2853–2863. https://doi.org/10.1111/j.1151-2916.1997.tb03203.x.
[251] C. Harman, B. King, Applications of Nickel Compounds in Ceramics, Industrial and Engineering Chemistry. 44 (1952) 1015–1017.
[252] M.R. O'Masta, E. Stonkevitch, K.A. Porter, P.P. Bui, Z.C. Eckel, T.A. Schaedler, Additive manufacturing of polymer-derived ceramic matrix composites, Journal of the American Ceramic Society. 103 (2020) 6712–6723. https://doi.org/10.1111/jace.17275.
[253] K. Zekentes, K. Rogdakis, SiC nanowires: material and devices, J. Phys. D: Appl. Phys. 44 (2011) 133001. https://doi.org/10.1088/0022-3727/44/13/133001.
[254] Dan Liu, Tielin Shi, Lei Zhang, Shuang Xi, Zirong Tang, Xiaoping Li, Wuxing Lai, Bulk synthesis of long silicon nitride nanowires on silicon wafer, in: 2011 IEEE Nanotechnology Materials and Devices Conference, IEEE, Jeju, 2011: pp. 512–516. https://doi.org/10.1109/NMDC.2011.6155280.
[255] M.L. Toebes, J.A. Van Dillen, K.P. De Jong, Synthesis of supported palladium catalysts, Journal of Molecular Catalysis A: Chemical. 173 (2001) 75–98. https://doi.org/10.1016/S1381-1169(01)00146-7.
[256] K. Momma, F. Izumi, VESTA: a three-dimensional visualization system for electronic and structural analysis, Journal of Applied Crystallography. 41 (2008) 653–658. https://doi.org/10.1107/S0021889808012016.
[257] S.H. Tsai, C.L. Lee, C.W. Chao, H.C. Shih, A novel technique for the formation of carbon-encapsulated metal nanoparticles on silicon, Carbon. 38 (2000) 781–785. https://doi.org/10.1016/S0008-6223(00)00018-X.
[258] K. Papakollu, N. Moharana, K.C. Hari Kumar, S. Lauterbach, H.-J. Kleebe, E. Ionescu, R. Kumar, Synthesis and temperature-dependent evolution of the phase composition in palladium-containing silicon oxycarbide ceramics, Journal of the European Ceramic Society. 42 (2022) 4825–4834. https://doi.org/10.1016/j.jeurceramsoc.2022.05.032.
[259] H. Okamoto, Pd-Si (Palladium-Silicon), Journal of Phase Equilibria and Diffusion. 28 (2007) 231–232. https://doi.org/10.1007/s11669-007-9039-4.
[260] Z. Du, C. Guo, X. Yang, T. Liu, A thermodynamic description of the Pd–Si–C system, Intermetallics. 14 (2006) 560–569. https://doi.org/10.1016/j.intermet.2005.09.008.
[261] E. Njoroge, J.T. Kabini, M. Mlambo, T. Ntsoane, T. Hlatshwayo, J. Malherbe, Investigation of Solid State Reactions of Pd Films on Single-Crystal 6H-SiC, in: 2018 Open Innovations Conference (OI), IEEE, Johannesburg, 2018: pp. 107–114. https://doi.org/10.1109/OI.2018.8535764.
[262] R.O. Suzuki, K. Osamura, SAXS study on crystallization of an amorphous $Pd_{76}Au_6Si_{18}$ alloy, Journal of Materials Science. 19 (1984) 1476–1485. https://doi.org/10.1007/BF00563042.
[263] T. Masumoto, R. Maddin, The mechanical properties of palladium 20 a/o silicon alloy quenched from the liquid state, Acta Metallurgica. 19 (1971) 725–741. https://doi.org/10.1016/0001-6160(71)90028-9.
[264] R. Lamber, N. Jaeger, G. Schulz-Ekloff, Electron microscopy study of the interaction of Ni, Pd and Pt with carbon, Surface Science. 227 (1990) 15–23. https://doi.org/10.1016/0039-6028(90)90386-M.
[265] Oleg P. Krivoruchko, V.I. Zaikovskii, A new phenomenon involving the formation of liquid mobile metal–carbon particles in the low-temperature catalytic graphitisation of amorphous carbon by metallic Fe, Co and Ni, Mendeleev Commun. 8 (1998) 97–99. https://doi.org/10.1070/MC1998v008n03ABEH000944.
[266] M. Sevilla, A.B. Fuertes, Graphitic carbon nanostructures from cellulose, Chemical Physics Letters. 490 (2010) 63–68. https://doi.org/10.1016/j.cplett.2010.03.011.
[267] J. Hoekstra, A.M. Beale, F. Soulimani, M. Versluijs-Helder, J.W. Geus, L.W. Jenneskens, Base Metal Catalyzed Graphitization of Cellulose: A Combined Raman Spectroscopy, Temperature-Dependent X-ray Diffraction and High-Resolution Transmission Electron Microscopy Study, J. Phys. Chem. C. 119 (2015) 10653–10661. https://doi.org/10.1021/acs.jpcc.5b00477.
[268] M. Boudart, W.L. Holstein, R.D. Moorhead, H. Poppa, In situ electron microscopy study of the palladium-amorphous carbon interaction in carbon dioxide and oxygen atmospheres, Applied Catalysis. 11 (1984) 117–122. https://doi.org/10.1016/S0166-9834(00)84045-2.

[269] N. Maksimova, O. Krivoruchko, G. Mestl, V. Zaikovskii, A. Chuvilin, A. Salanov, E. Burgina, Catalytic synthesis of carbon nanostructures from polymer precursors, Journal of Molecular Catalysis A: Chemical. 158 (2000) 301–307. https://doi.org/10.1016/S1381-1169(00)00095-9.
[270] R. Mendes, P. Wróbel, A. Bachmatiuk, J. Sun, T. Gemming, Z. Liu, M. Rümmeli, Carbon Nanostructures as a Multi-Functional Platform for Sensing Applications, Chemosensors. 6 (2018) 60. https://doi.org/10.3390/chemosensors6040060.
[271] O. Mykhailiv, H. Zubyk, M.E. Plonska-Brzezinska, Carbon nano-onions: Unique carbon nanostructures with fascinating properties and their potential applications, Inorganica Chimica Acta. 468 (2017) 49–66. https://doi.org/10.1016/j.ica.2017.07.021.
[272] O.A. Shenderova, V.V. Zhirnov, D.W. Brenner, Carbon Nanostructures, Critical Reviews in Solid State and Materials Sciences. 27 (2002) 227–356. https://doi.org/10.1080/ 10408430208500497.
[273] M. Bechelany, A. Brioude, P. Stadelmann, G. Ferro, D. Cornu, P. Miele, Very Long SiC-Based Coaxial Nanocables with Tunable Chemical Composition, Adv. Funct. Mater. 17 (2007) 3251–3257. https://doi.org/10.1002/adfm.200700110.
[274] Y.J. Xing, Q.L. Hang, H.F. Yan, H.Y. Pan, J. Xu, D.P. Yu, Z.H. Xi, Z.Q. Xue, S.Q. Feng, Solid–liquid–solid (SLS) growth of coaxial nanocables: silicon carbide sheathed with silicon oxide, Chemical Physics Letters. 345 (2001) 29–32. https://doi.org/10.1016/S0009-2614(01)00768-0.
[275] F. Gao, W. Yang, H. Wang, Y. Fan, Z. Xie, L. An, Controlled Al-Doped Single-Crystalline 6*H*-SiC Nanowires, Crystal Growth & Design. 8 (2008) 1461–1464. https://doi.org/10.1021/ cg701227n.
[276] G. Wei, W. Qin, G. Wang, J. Sun, J. Lin, R. Kim, D. Zhang, K. Zheng, The synthesis and ultraviolet photoluminescence of 6H–SiC nanowires by microwave method, J. Phys. D: Appl. Phys. 41 (2008) 235102. https://doi.org/10.1088/0022-3727/41/23/235102.
[277] S.A. Fortuna, X. Li, Metal-catalyzed semiconductor nanowires: a review on the control of growth directions, Semicond. Sci. Technol. 25 (2010) 024005. https://doi.org/10.1088/0268-1242/25/2/024005.
[278] S. Sankaranarayanan, P. Kandasamy, R. Raju, S. Gengan, B. Krishnan, Controlled growth of gallium nitride nanowires on silicon and their utility in high performance Ultraviolet-A photodetectors, Sensors and Actuators A: Physical. 332 (2021) 113189. https://doi.org/10.1016/j.sna.2021.113189.
[279] R. Esterina, X.M. Liu, C.A. Ross, A.O. Adeyeye, W.K. Choi, Synthesis of silicon oxide nanowires and nanotubes with cobalt-palladium or palladium catalysts, Journal of Applied Physics. 112 (2012) 024312. https://doi.org/10.1063/1.4737593.
[280] W. Yang, Z. Xie, J. Li, H. Miao, L. Zhang, L. An, Ultra-Long Single-Crystalline α-Si_3N_4 Nanowires: Derived from a Polymeric Precursor, Journal of the American Ceramic Society. 88 (2005) 1647–1650. https://doi.org/10.1111/j.1551-2916.2005.00270.x.
[281] T. Kusunose, T. Yagi, S.H. Firoz, T. Sekino, Fabrication of epoxy/silicon nitride nanowire composites and evaluation of their thermal conductivity, J. Mater. Chem. A. 1 (2013) 3440–3445. https://doi.org/10.1039/c3ta00686g.
[282] F. Chen, Z. Wang, Q. Shen, Z. Huang, L. Zhang, Synthesis of Single-Crystalline Silicon Nitride (α-Si_3N_4) Nanowires with Controlled Diameters by Nitriding Cryomilled Nanocrystalline Silicon Powder, MRS Proc. 1279 (2010) 21. https://doi.org/10.1557/PROC-1279-21.

Appendix

Appendix A: Tables listing all samples investigated in the present study and the corresponding synthesis materials and synthesis parameters employed.

Table A-1: Overview of the PDCPs prepared using Fe-modified polysilazanes.

Designation	Polymer	Metal Precursor	Template	Pyrolysis	Tempering
Sar_Fe-PHPS_500-NH_3	Durazane 2250	Fe(III)$acac_3$	Sartorius	500 °C NH_3	-
Sar_Fe-PHPS_700-NH_3	Durazane 2250	Fe(III)$acac_3$	Sartorius	700 °C NH_3	-
Sar_Fe-PHPS_1000-NH_3	Durazane 2250	Fe(III)$acac_3$	Sartorius	1000 °C NH_3	-
Lin_Fe-PHPS_1000-NH_3	Durazane 2250	Fe(III)$acac_3$	‚Cotton Linters'	1000 °C NH_3	-
Euc_Fe-PHPS_1000-NH_3	Durazane 2250	Fe(III)$acac_3$	‚Eucalyptus'	1000 °C NH_3	-
Lin_Fe-PHPS_1000-Ar	Durazane 2250	Fe(III)$acac_3$	‚Cotton Linters'	1000 °C Ar	-
Lin_Fe-PHPS_1300-Ar	Durazane 2250	Fe(III)$acac_3$	‚Cotton Linters'	1000 °C Ar	1300 °C Ar
Lin_Fe-PHPS_1300-N_2	Durazane 2250	Fe(III)$acac_3$	‚Cotton Linters'	1000 °C Ar	1300 °C N_2
Euc_Fe-PHPS_1000-Ar	Durazane 2250	Fe(III)$acac_3$	‚Eucalyptus'	1000 °C Ar	-
Euc_Fe-PHPS_1300-Ar	Durazane 2250	Fe(III)$acac_3$	‚Eucalyptus'	1000 °C Ar	1300 °C Ar
Euc_Fe-PHPS_1300-N_2	Durazane 2250	Fe(III)$acac_3$	‚Eucalyptus'	1000 °C Ar	1300 °C N_2
Lin_Fe-Dur_1000-Ar	Durazane 1800	Fe(III)$acac_3$	‚Cotton Linters'	1000 °C Ar	-
Lin_Fe-Dur_1300-Ar	Durazane 1800	Fe(III)$acac_3$	‚Cotton Linters'	1000 °C Ar	1300 °C Ar
Lin_Fe-Dur_1300-N_2	Durazane 1800	Fe(III)$acac_3$	‚Cotton Linters'	1000 °C Ar	1300 °C N_2
Euc_Fe-Dur_1000-Ar	Durazane 1800	Fe(III)$acac_3$	‚Eucalyptus'	1000 °C Ar	-
Euc_Fe-Dur_1300-Ar	Durazane 1800	Fe(III)$acac_3$	‚Eucalyptus'	1000 °C Ar	1300 °C Ar
Euc_Fe-Dur_1300-N_2	Durazane 1800	Fe(III)$acac_3$	‚Eucalyptus'	1000 °C Ar	1300 °C N_2

Table A-2: Overview of the PDCPs prepared using Ni-modified polysilazanes.

Designation	Polymer	Metal Precursor	Template	Pyrolysis	Tempering
Lin_Ni-PHPS_1000-Ar	Durazane 2250	Ni(II)acac2	‚Cotton Linters'	1000 °C Ar	-
Lin_Ni-PHPS_1300-Ar	Durazane 2250	Ni(II)acac2	‚Cotton Linters'	1000 °C Ar	1300 °C Ar
Lin_Ni-PHPS_1300-N2	Durazane 2250	Ni(II)acac2	‚Cotton Linters'	1000 °C Ar	1300 °C N_2
Euc_Ni-PHPS_1000-Ar	Durazane 2250	Ni(II)acac2	‚Eucalyptus'	1000 °C Ar	-
Euc_Ni-PHPS_1300-Ar	Durazane 2250	Ni(II)acac2	‚Eucalyptus'	1000 °C Ar	1300 °C Ar
Euc_Ni-PHPS_1300-N2	Durazane 2250	Ni(II)acac2	‚Eucalyptus'	1000 °C Ar	1300 °C N_2
Lin_Ni-Dur_1000-Ar	Durazane 1800	Ni(II)acac2	‚Cotton Linters'	1000 °C Ar	-
Lin_Ni-Dur_1300-Ar	Durazane 1800	Ni(II)acac2	‚Cotton Linters'	1000 °C Ar	1300 °C Ar
Lin_Ni-Dur_1300-N2	Durazane 1800	Ni(II)acac2	‚Cotton Linters'	1000 °C Ar	1300 °C N_2
Euc_Ni-Dur_1000-Ar	Durazane 1800	Ni(II)acac2	‚Eucalyptus'	1000 °C Ar	-
Euc_Ni-Dur_1300-Ar	Durazane 1800	Ni(II)acac2	‚Eucalyptus'	1000 °C Ar	1300 °C Ar
Euc_Ni-Dur_1300-N2	Durazane 1800	Ni(II)acac2	‚Eucalyptus'	1000 °C Ar	1300 °C N_2

Table A-3: Overview of the PDCPs prepared using Pd-modified polysilazanes.

Designation	Polymer	Metal Precursor	Template	Pyrolysis	Tempering
Lin_Pd-PHPS_1000-Ar	Durazane 2250	Pd(II)$acac_2$	‚Cotton Linters'	1000 °C Ar	-
Lin_Pd-PHPS_1300-Ar	Durazane 2250	Pd(II)$acac_2$	‚Cotton Linters'	1000 °C Ar	1300 °C Ar
Lin_Pd-PHPS_1300-N_2	Durazane 2250	Pd(II)$acac_2$	‚Cotton Linters'	1000 °C Ar	1300 °C N_2
Euc_Pd-PHPS_1000-Ar	Durazane 2250	Pd(II)$acac_2$	‚Eucalyptus'	1000 °C Ar	-
Euc_Pd-PHPS_1300-Ar	Durazane 2250	Pd(II)$acac_2$	‚Eucalyptus'	1000 °C Ar	1300 °C Ar
Euc_Pd-PHPS_1300-N_2	Durazane 2250	Pd(II)$acac_2$	‚Eucalyptus'	1000 °C Ar	1300 °C N_2
Lin_Pd-Dur_1000-Ar	Durazane 1800	Pd(II)$acac_2$	‚Cotton Linters'	1000 °C Ar	-
Lin_Pd-Dur_1300-Ar	Durazane 1800	Pd(II)$acac_2$	‚Cotton Linters'	1000 °C Ar	1300 °C Ar
Lin_Pd-Dur_1300-N_2	Durazane 1800	Pd(II)$acac_2$	‚Cotton Linters'	1000 °C Ar	1300 °C N_2
Euc_Pd-Dur_1000-Ar	Durazane 1800	Pd(II)$acac_2$	‚Eucalyptus'	1000 °C Ar	-
Euc_Pd-Dur_1300-Ar	Durazane 1800	Pd(II)$acac_2$	‚Eucalyptus'	1000 °C Ar	1300 °C Ar
Euc_Pd-Dur_1300-N_2	Durazane 1800	Pd(II)$acac_2$	‚Eucalyptus'	1000 °C Ar	1300 °C N_2

Table A-4: Overview of miscellaneous samples investigated.

Designation	Polymer	Metal Precursor	Template	Pyrolysis	Tempering
Sar_PHPS_1000-NH_3	Durazane 2250	-	‚Sartorius‘	1000 °C NH_3	-
Sar_PHPS_1300-N_2	Durazane 2250	-	‚Sartorius‘	1000 °C NH_3	1300 °C N_2
Sar_1000-NH_3	-	-	‚Sartorius‘	1000 °C NH_3	-
Sar_1000-Ar	-	-	‚Sartorius‘	1000 °C Ar	-
Sar_1300-Ar	-	-	‚Sartorius‘	1000 °C Ar	1300 °C Ar
Lin_1000-Ar	-	-	‚Cotton Linters‘	1000 °C Ar	-
Lin_1300-Ar	-	-	‚Cotton Linters‘	1000 °C Ar	1300 °C Ar
Euc_1000-Ar	-	-	‚Eucalyptus‘	1000 °C Ar	-
Euc_1300-Ar	-	-	‚Eucalyptus‘	1000 °C Ar	1300 °C Ar

Appendix B: Additional data and complementary results.

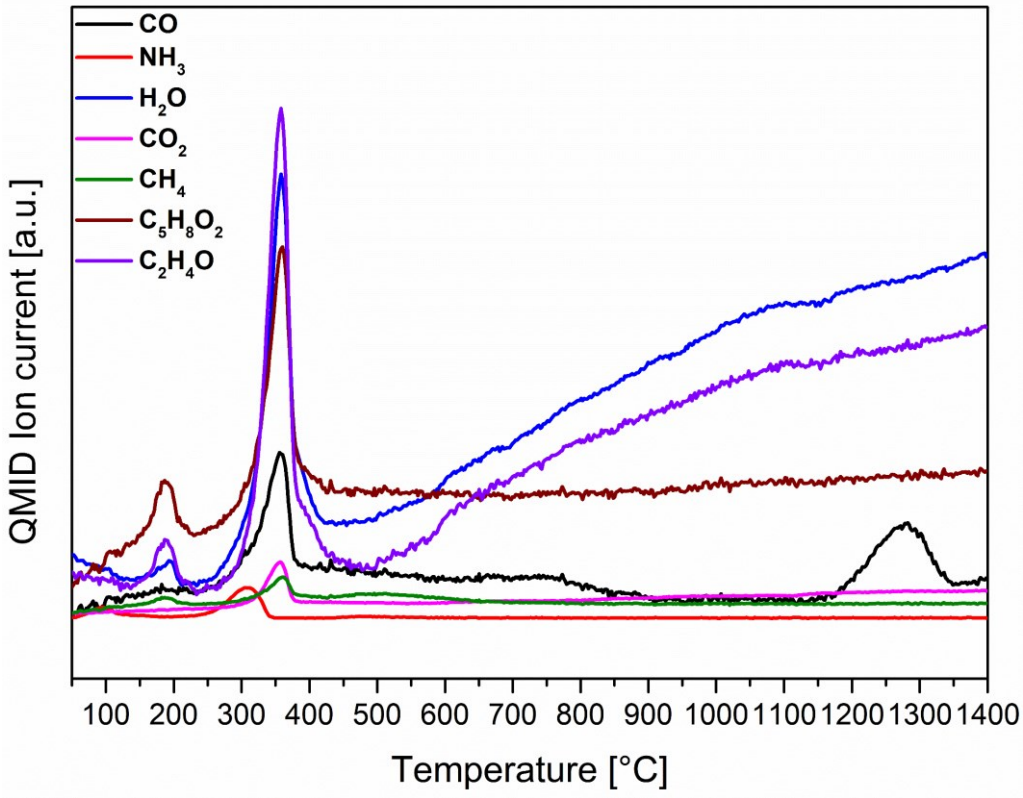

Figure B-1: QMID analysis of SiFeOC(N)-modified ceramic papers upon pyrolysis in Ar atmosphere. A sudden increase in CO emission (black curve) between 1200-1350 °C indicates a reaction of SiO_2 with free carbon forming crystalline SiC. Reproduced from [8].

List of Figures

List of Tables